Chapter 3 The novel oscillatory flow reactor designs

The "conventional" oscillatory flow reactor (OFR) geometry was re-designed to suit some of the bioprocess applications requirements. Similarly to Belhouse (1978), the sharp baffles were smoothed, thus reducing the high shear regions that may be crucial to some cell cultures. The straight tube and the smooth periodic constrictions (SPCs) are incorporated as a single piece, thus making it easy for sterilisation. Based on this new SPC geometry, two novel oscillatory flow reactor configurations were developed and are herein presented. Further experimental materials and methods particular to each chapter are described in the respective Materials and Methods section.

3.1 The novel SPC tube geometry

The novel geometry is based on two concentric tubes, where the inner tube presents Smooth Periodic Constrictions (SPCs) and has a 4.4 mm internal diameter (d) as shown in Figure 3-1. The mean spacing between consecutive constrictions (L) is ~13 mm (approximately $3d$) and the constriction length (δ) is ~6 mm. The internal tube diameter in the constrictions (d_0) is 1.6 mm, representing 13 % of the cross-sectional area α, where $\alpha = d_0^2/d^2$, being considerably lower than the typical α = 50 % used in conventional OFRs. A cooling/heating fluid may circulate in the free spacing between the two concentric tubes.

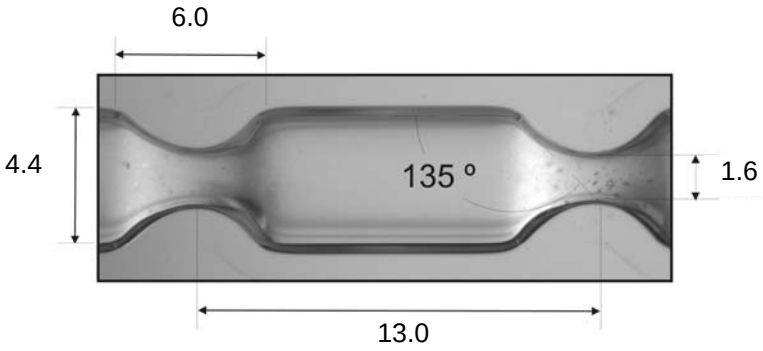

Figure 3-1. Novel SPC tube geometry. All dimensions are in mm.

3.2 The novel micro-bioreactor

The firstly developed design was the micro-bioreactor. It consists in one single jacketed glass SPC tube, with 350 mm of length (Figure 3-2). The micro-bioreactor is suitable for vertical operation and due to the small volume of c.a. 4.5 ml it is envisaged for screening purposes, supporting batch and continuous operation modes. Several micro-bioreactor tubes may be stacked side-to-side in a single unit, assuming a high throughput (HTP) screening configuration.

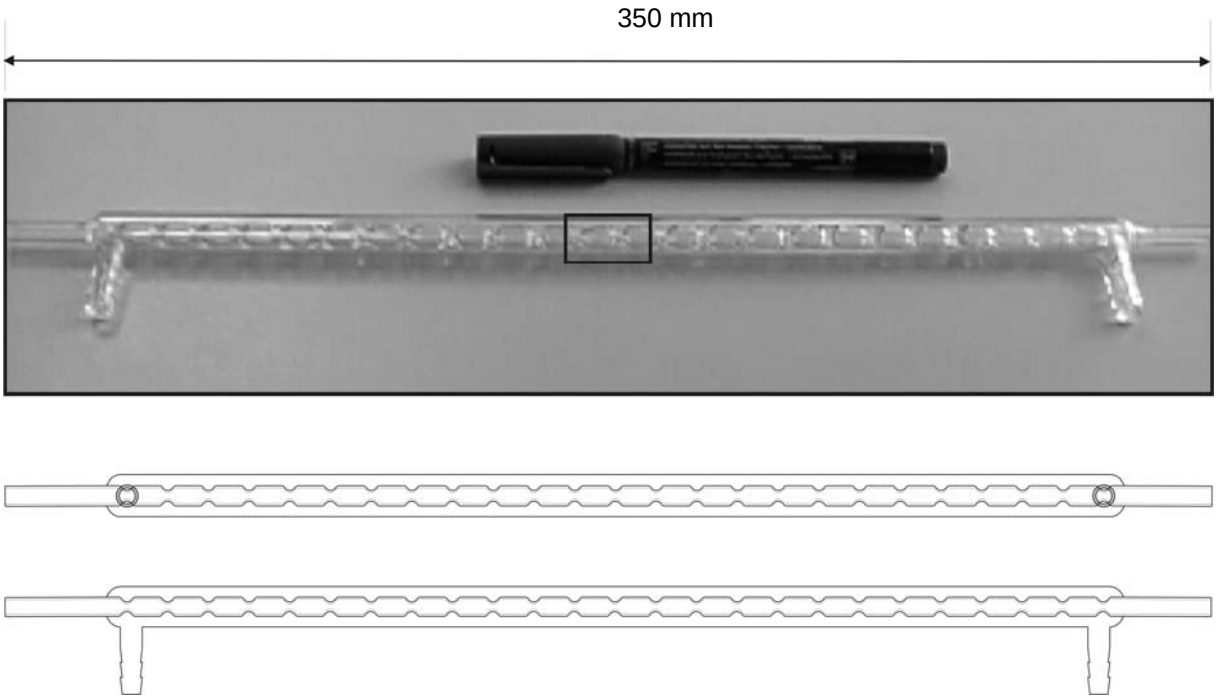

Figure 3-2. Geometry of the SPC tube composing the novel micro-bioreactor.

Fluid oscillations within the micro-bioreactor are achieved by a rotative ceramic piston pump (CKCRH0, Fluid Metering Inc., New York, USA), working in close-loop, connected to the bottom of the SPC tube. Good sinusoidal fluid oscillations are usually obtained with this system. The control of fluid oscillation amplitude centre-to-peak (x_0 from 0 to 3 mm) is made by turning an easy-grip flow control ring in the pump head. The fluid oscillation frequency (f) is controlled by the rotation speed of the ceramic piston. In all, a precise control of both x_0 and f is obtained. Bioreaction temperature may be easily controlled by passing a cooling/heating fluid through the tube's jacket.

3.3 The novel continuous oscillatory flow meso-reactor

The second configuration is adjusted to the continuous operation mode. It is an array of 10 SPC tubes of ~800 mm length near-horizontally positioned (Figure 3-3). Tubes are connected with fittings and U-bends provided with constrictions and with sampling/measurement points.

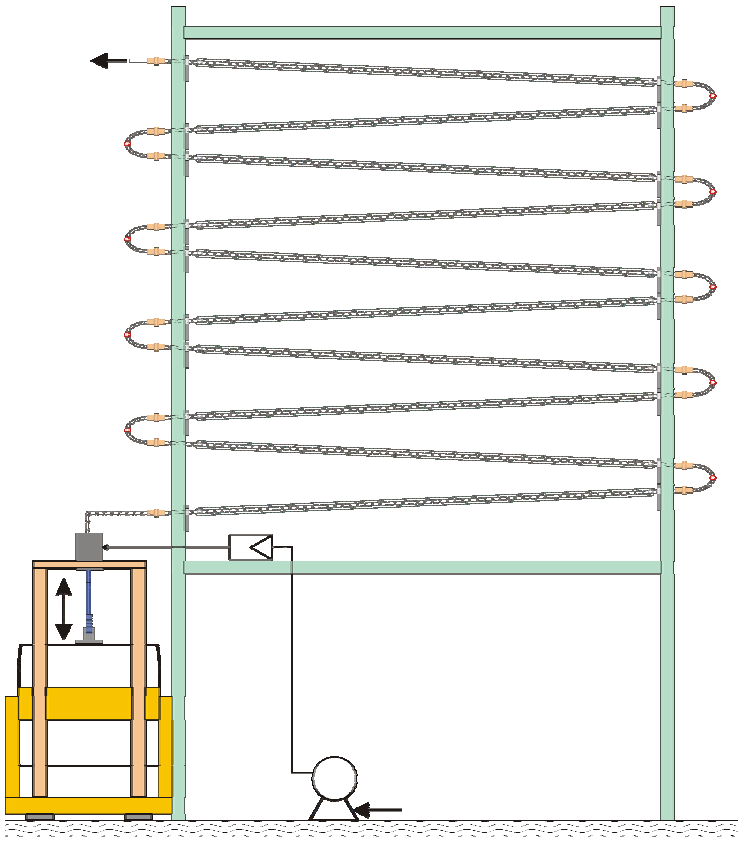

Figure 3-3. Simplified scheme of the novel continuous oscillatory flow meso-reactor.

Fluid is oscillated using a piston moved up- and down-stroke through an electromagnetic oscillator. The piston moves a membrane fixed in a 'mixing chamber' which connects to the base of the SPC tube array. A signal generator and an amplifier control the piston f and x_o. Fluid oscillation frequencies between 0 and 50 Hz and amplitudes between 0 and 20 mm (centre-to-peak) are possible, but the apparatus could not provide both high f and high x_o values. Typically f values of 1 - 15 Hz and x_o values of 0 - 4 mm could be obtained with this system. The x_o is monitored by reading the liquid level in a scaled glass tube, connected to the top of the SPC tube, but also in line checked by a displacement transducer. Temperature may be controlled by running a heating/cooling fluid through the tubes' jackets.

Fluids are pumped into the meso-reactor using syringe pumps connected to the mixing chamber via a non-return valve. All the system is pressurised (0.5 bar) to reduce the formation of bubbles from the gas dissolved in the liquid. The small inclination (ca. 10 ° from the horizontal position) of the SPC tubes allows overcoming an eventual gas inlet. The total internal volume of the system (i.e. SPC tubes more the mixing chamber) is ~137 mL.

Chapter 4 Fluid mechanics and catalyst particle suspension within the novel micro-bioreactor

The novel, continuous, oscillatory flow screening reactor (micro-bioreactor), described in the previous chapter, is presented as a new option for small-scale reaction engineering applications, particularly those involving the screening of solid catalysts. Experimental studies using particle image velocimetry have demonstrated that this reactor provides excellent fluid mixing, and is able to suspend catalyst particles with a wide range of sedimentation velocities. Results from 2-D and 3-D CFD simulations exhibit semi-quantitative agreement with the experimental data, and will aid in the design of future reactors. Potential application areas for this reactor are specialist chemical manufacture and high-throughput screening. Unlike conventional screening devices, the flow patterns in this reactor can be reproduced at larger scales, therefore results obtained in the laboratory can be related directly to larger scale production.

Keywords: continuous screening reactor; CFD; PIV; oscillatory flow; screening; catalyst particle suspension.

4.1 Introduction

Since the early 1990s, studies have shown that tubes containing periodically-spaced orifice baffles, when subjected to a net flow with a reversing oscillatory component of the correct magnitude, can exhibit efficient fluid mixing and a narrow residence time distribution (Brunold *et al.*, 1989; Dickens *et al.*, 1989; Howes *et al.*, 1991; Mackley and Ni, 1991, 1993, Stonestreet and van der Veeken, 1995). The baffle edges promote eddy formation, which increases the radial mixing in the tube, leading to radial velocities of the same order of magnitude as the axial velocities (e.g. Mackley, 1990; Mackley and Ni, 1991; Ni and Pereira, 2000). These "oscillatory flow reactors" (OFRs) can be operated continuously in horizontal or vertical tubes containing liquid or multiphase flows. The fluid is oscillated in the axial direction by means of diaphragms, bellows or pistons, at one or both ends of the tube, or by moving a set of baffles up and down from the top of the tube (Ni *et al.*, 2002).

At Re_o values of 100-300, vortex rings are symmetrically generated within each baffle cavity during each oscillation of the fluid. At higher Re_o*s*, the flow becomes more intensely mixed and chaotic, leading to increased axial mixing such that the OFR's mixing increasingly resembles that of a stirred tank (Ni *et al.*, 1999, 2002). The generation of vortices is no longer axi-symmetrical (Ni *et al.*, 2002). These phenomena remain the same between reactors of different diameters, indicating that the fluid mechanical conditions in an OFR can be linearly scaled up (Brunold *et al.*, 1989; Dickens *et al.*, 1989; Ni *et al.*, 1995b). The fluid mechanics of OFRs at millimetre scales, however, have not previously been studied.

Experiments by Smith *et al.* (1993) and flow visualisation studies by Ni *et al.* (1995a) show that fluid oscillation in an OFR is an efficient method of uniformly suspending particles. The performance of the OFR as a heterogeneous catalytic reactor has been demonstrated for the suspension of titania particles acting as catalysts to oxidise waste water contaminants (Fabiyi and Skelton, 2000). The OFR has also been shown to be an effective particle separator (Mackley *et al.*, 1993).

The formation and dissipation of eddies in the OFR results in significant enhancement of processes such as heat transfer (Mackley *et al.*, 1990; Mackley and Stonestreet, 1995), mass transfer (Hewgill *et al.,* 1993; Ni *et al.*, 1995a, 1995b; Ni and Gao, 1996), particle mixing and separation (Mackley *et al.*, 1993), liquid-liquid reaction (Ni and Mackley, 1993), polymerization (Ni *et al.*, 1998, 1999) and flocculation (Gao *et al.*, 1998). The OFR increases the hold-up time of bubbles and particles, and is an effective method of controlling drop and bubble size distributions. Other phenomena that have been investigated in the OFR

include: its fluid mechanics (Brunold *et al.*, 1989; Mackley and Ni, 1991, 1993), local velocity profiles and shear rate distribution (Ni *et al.*, 1995c), residence time distribution (Dickens *et al.*, 1989; Mackley and Ni, 1991, 1993; Ni, 1994), dispersion (Howes, 1988; Howes and Mackley, 1990), velocity profiles (Liu *et al.*, 1995) and scale-up correlations (Ni and Gao, 1996). A full review of the applications of oscillatory flow technology is presented in Baird *et al.* (2003).

This work describes the evaluation of a novel, oscillatory flow screening reactor (micro-bioreactor), using Particle Image Velocimetry (PIV), combined with Computational Fluid Dynamics (CFD). The scale of this novel reactor is smaller than that used before and the geometry includes smooth periodic constrictions, rather than sharp-edged baffles.

4.2 Materials and methods

Operation of the experimental rig

In these trials a single 350-mm-long, smooth periodic constricted (SPC) tube (micro-bioreactor) was usually positioned vertically, and the fluid oscillated using a piston fitted on an electromagnetic oscillator, connected to the base of the tube by means of a 5 mm internal diameter PVC tube. A signal generator and amplifier controlled the piston oscillation frequency (f) and amplitude (x_o). Fluid oscillation frequencies between 0 and 50 Hz and amplitudes between 0 and 20 mm (centre-to-peak) were possible, but the apparatus could not provide both high frequency and high amplitude. The fluid oscillation amplitude was monitored by reading the liquid level in a 2.0 mm internal diameter scaled glass tube, connected to the top of the SPC tube, the smaller internal diameter of the measuring tube increasing the resolution of amplitude measurement approximately tenfold. The fluid used was tap water at room temperature (20 °C), pumped into the reactor using a peristaltic pump connected to the bottom of the reactor via a non-return valve. All experiments were conducted in batch mode.

Particle Image Velocimetry apparatus

In order to minimise optical distortion, a rectangular Perspex optical box was fitted around the centre of the reactor tube and filled with glycerol (which has a refractive index similar to Perspex and glass) (Figure 4-1). The glass jacket of the reactor tube was also filled with glycerol. The light source was a Nd:YAG dual

pulsed laser, with a wavelength of 532 nm and a maximum power intensity of 40 mJ. The beam was diverged into a vertical light sheet, ~1 mm thick, and positioned to cross the middle of the flow field.

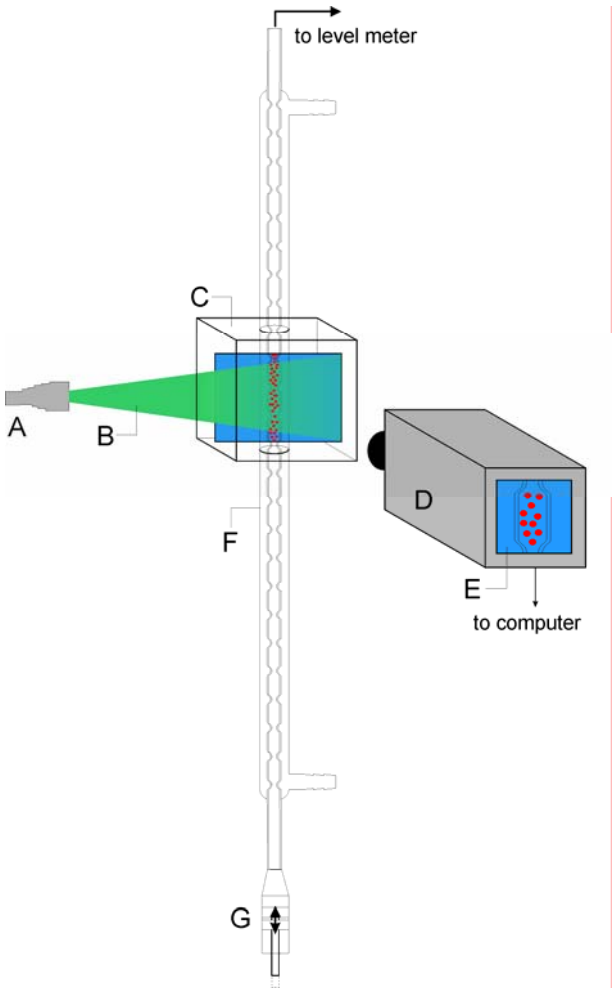

Figure 4-1. Experimental setup used in experimental PIV. A. Laser source. B. Laser sheet. C. Optical box made of Perspex. D. CCD camera. E. captured image-pair. F. SPC tube. G. Oscillation unit. The optical box (C) and the jacket of SPC tube (F) were filled with glycerol to avoid optical distortions.

A CCD camera (1000 x 1200 pixels, PCO Sensicam) was located perpendicularly to the laser sheet (Figure 4-1). As the camera used was limited to low image acquisition frequencies (1 to 4 Hz), a phase difference of 0.1 Hz was imposed between the frequencies of camera capture and oscillator unit to obtain the velocity profiles at different piston positions. This allowed 10 equally spaced phase images per cycle. The phase angle of a picture was determined by either reading the level meter captured at the same

moment with a second digital camera, or by analysis of the average axial velocity profile. The cameras were synchronised with the laser source using an ILA synchroniser (ILA, Juelich, Germany). The reactor was seeded with neutrally buoyant silvered "microspheres" with a mean particle diameter of 10 μm, at a seeding to liquid ratio of 10^{-5}:1, as recommended by Elgobashi (1994). The seeded fluid was oscillated for 5 minutes before image acquisition was initiated, to ensure that the seeding was well-dispersed. All experiments were performed at room temperature (ca. 20 °C).

The results were processed using VidPIV® software (ILA, Juelich, Germany) and plotted using TECPLOT® software. In each experiment 30 images were acquired, permitting three equal phase images for each phase angle. The instantaneous velocity vector maps were constructed for each image, as well as averaged maps for each phase angle. Experiments were carried out at fifteen amplitude-frequency combinations, corresponding to Re_o values between 12 and 1335, covering the expected axisymmetric and non-axisymmetric regimes (Mackley and Ni, 1991; Mackley, 1990; Howes *et al.*, 1991; Mackley, 1991).

The following conditions were used, to provide a wide range of Re_os, as well as to investigate the effects of both amplitude and frequency individually:

Table 4-1: Experimental Conditions

Amplitude [mm]	Frequency [Hz]	Oscillatory Re_o [-]
0.2	2.1	12
0.3	2.1	17
1	4.1	113
1	5.1	141
1	10.1	279
1	11.1	307
1	15.1	417
1	20.1	556
3	2.1	174
5	2.1	290
4	1.1	122
11	1.1	335

Two further series of experiments were performed to investigate the effect of gravity on the fluid mechanics and particle suspensions: at oscillation frequencies of i) 4.1 Hz and ii) 12.1 Hz and fluid amplitudes between 3 and 4 mm, the reactor was positioned at 90°, 45° or 10° to the horizontal.

Computational Fluid Dynamics

The CFD package used was "Fluent" 5.5 (1998). Meshes were created using Gambit 1.2.2 software. In Fluent, the velocity profiles in the inlet and outlet of the SPC had to be matched. This condition was imposed on "Fluent" by using periodic boundary conditions, but it should be noted that such conditions can only be used if the number and location of nodes is similar in both periodic zones (inlet and outlet). 2-D planar, 2-D with axisymmetric and 3-D meshes were constructed and used to simulate flow patterns within the SPC tube. Firstly, mesh size independency was studied for the 2-D planar model at continuous flow. Then, 2-D axisymmetric and 3-D geometries were meshed using the minimum cell size required for mesh independency of the results (from the 2-D planar results), so that computational times were minimised. The number of cells were 6,820 and 110,772, respectively. The grid used in 3-D simulations is presented in Figure 2. Details of the meshing can be found in Table 4-2.

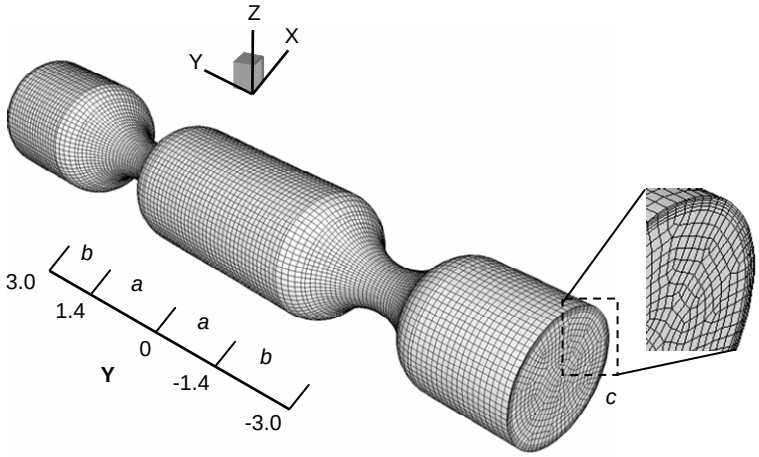

Figure 4-2. Mesh for 3-D numerical simulations (units are radii of the tube, R). A detail of mesh in zones a, b and c may be found in Table 4-2.

Table 4-2: Details of mesh used for 3-D numerical simulations presented in Figure 2

Mesh function	Meshing details
Axial mesh (zones a and b)	linear spacing of 0.20 mm
Radial mesh (zone c)	uniform boundary layer, 4 rows, growth factor of 1.2 meshed face: quad elements, map scheme, uniform spacing of 0.20 mm
Mesh volume (all zones)	hex/wedge elements, cooper scheme, spacing of 0.20 mm with projected radial boundary layer along the axial distance total cells number: 110,772

For continuous flow, the mean flow velocity was specified as a constant and set as one of the "Fluent" boundary conditions. For oscillatory flow, the displacement of oscillation, *x(t),* and the oscillation velocity, *u(t),* were defined as follows:

$$x(t) = x_0 \sin(2\pi f t) \tag{4.1}$$

$$u(t) = 2\pi f x_0 \cos(2\pi f t) \tag{4.2}$$

However, at unsteady conditions the mass flow rate had to be used, expressed as:

$$\dot{m}(t) = \rho.u(t).A \tag{4.3}$$

where *u(t)* is the velocity ($m.s^{-1}$) and *A* is the cross-sectional area (m^2). For a 3-D mesh, the cross-sectional area used was the cross-section of the mesh at the inlet/outlet point. For a 2-D axisymmetric mesh, the cross-section was based on unit depth at the inlet.

The software did not allow the definition of unsteady inlet boundary conditions. This was overcome by discretising a sinusoidal oscillation cycle into many equal time steps, depending on the oscillation frequency (usually, 200 intervals per cycle). At each time step, the oscillation mass flow rate was introduced via a "Fluent" journal file. Non-slip conditions were used as the wall boundary conditions. To ensure that the solution was independent of the initial conditions, the solver was allowed to run until the results were essentially the same from one oscillation to the next. The governing equations were solved sequentially using the segregated method solver. Under-relaxation was used to control the change of scalar variables in every iteration. The discretization scheme for pressure was second-order, and those for

momentum and turbulence were second-order upwind schemes. The SIMPLEC algorithm was employed in the pressure-velocity coupling scheme.

Comparison of PIV and CFD results

Qualitative analysis. A qualitative comparison of the two sets of data was performed by analysing the vortex behaviour, based on the vorticity, *w*, for a 2-D flow, in the *x-y* plane (Perry, 2001):

$$w = \frac{1}{2}\left(\frac{\delta u_y}{\delta x} - \frac{\delta u_x}{\delta y}\right) \tag{4.4}$$

For PIV and 2-D numerical simulations, all the points were coplanar, making the calculation of vorticity trivial. For 3-D simulations, points on the *x-y* plane were selected and the calculation of *w* was made by the same method. However, since the flow in 3-D simulations was expected to be non-axisymmetric, it should be stated that the *x-y* plane is not necessarily representative of the vorticity in all other planes crossing the centre of the grid. The number, position and size of vortex rings were analysed, to allow the agreement between the experimental and computer-generated results to be assessed.

Vorticities were compared using the following procedure:

a) values of w corresponding to points with y-coordinate between -6.5 and 6.5 mm were selected (i.e. 1 single cavity length)
b) w values below 15 % of the maximum vorticity in the centre of the cavity (straight zone) were filtered out for each time instant. Only the straight-walled section of the cavity was considered, as, due to the high curvature of the constriction and pronounced radial profiles of axial velocity, the higher w values near the constrictions and the walls of the cavity did not necessarily represent vortices
c) the points where vorticity presents a local maximum/minimum were considered to be the centre of each vortex
d) the size of each eddy was calculated by approximating the geometry of the filtered regions (from b)) of each vortex to an elliptical shape and considering it to have a length, a, and a width, b. The vortex area could therefore be expressed as:

$$A_{vortex} = \frac{\pi.a.b}{4} \tag{4.5}$$

Quantitative analysis. To compare the results quantitatively, mixing intensity was calculated by quantifying the axial and radial velocities in the cavity, using an Excel spreadsheet. To compare the PIV results with the 2-D numerical simulations, the axial and radial velocities in the *x-y* plane were used, but the velocity values in all the cells had to be used for the 3-D mesh. The calculation was made for each velocity vector map ($1/10^{th}$ of an oscillation cycle), and the parameters determined using the follow procedures:

a) **Instantaneous averaged (axial or radial) velocities** were determined by a mass balance across the surface (Perry, 2001):

$$\bar{u}(t) = \frac{1}{A}\int_A u(t)dA \tag{4.6}$$

where A is the flow cross-section. For the 2-D axisymmetric grid, the cells are not of a uniform size, so the velocities were integrated in the axial and radial directions:

$$\bar{u}(t) = \frac{1}{A_{total}}\sum_{i=1}^{n}\sum_{j=1}^{m} u(t)_{ij}.A_{ij} \tag{4.7}$$

where i and j represent the axial and radial components, respectively, $u(t)_{ij}$ is the component (radial or axial) of the velocity in the element of area, A_{ij}, and A_{total} is the total area of the cross-section, calculated by summing all the A_{ij} elements of the *x-y* plane. The cross-sectional area is presented by "Fluent" as a 2-D cell volume, i.e. the cross-section multiplied by π radians, and has area units. However, it should be noted that the value of averaged velocity in equation (9) is expressed in relation to the mean diameter of the grid, i.e. about 3.82 mm ($d_{average}$) rather than 4.40 mm (d - diameter of the tube in the straight zone). Therefore, equation (9) must be multiplied by a factor of $(d_{average}/d)^2$ in order to obtain the average velocity expressed to the inlet cross section (with diameter d).

For the 3-D grid, since cells in a specific plane (e.g. the *x-y* plane) have different cross-sections and the cross-sectional areas of the cells were not available in "Fluent", values of volume-averaged velocities were determined as follows:

$$\bar{u}(t) = \frac{1}{V_{total}}\sum_{i=1}^{n}\sum_{j=1}^{m}\sum_{k=1}^{p} u(t)_{ijk}.V_{ijk} \tag{4.8}$$

where $u(t)_{ijk}$ is the value of axial or radial velocity in the centre of the cell grid of unit volume V_{ijk} and V_{total} is the sum of all V_{ijk} elements. The average volume in equation (10) is again expressed in terms of the mean cross-section and the same factor as equation (9) must be used to calculate the average velocity in the straight zone (with diameter d).

b) **Standard deviations, σ:** of instantaneous area- or volume-averaged axial and radial velocities were calculated as follows:

$$\sigma(t) = \sqrt{\frac{\sum_{i=1}^{n} n_i . u(t)_i^{\,2}}{N} - \bar{u}(t)^2} \qquad (4.9)$$

where n_i is the height of the cross-sectional area or volume of the cell, *i*, and was determined by dividing the cross-section by the minimal cross-section of the 2-D grid or, for the 3-D mesh, as the ratio of the volume of each cell by the smallest cell volume in the grid. *u(t)* is the velocity value in the cell, *i*, and $\bar{u}(t)$ is the area or volume-averaged velocity value at the time instant, *t*.

c) **Average values of positive and negative components:** were calculated at each time instant by the global value method presented in equations (9) and (10), by considering only the positive or negative velocity values. Again, the factor of $(d_{average}/d)^2$ must be used in order to express the area- or volume-averaged velocity components to the inlet cross section.

d) **Full cycle average values:** of axial and radial velocities were determined by averaging the values over a full cycle in the simulations, or over 3 oscillation cycles for the experimental PIV data, using equations (4.7) and (4.8). Full cycle standard deviations were determined using equation (4.9).

Particle and bubble suspension experiments

When investigating the particle suspension performance of the screening reactor, particles were injected at the top of the tube and oscillated until a steady concentration distribution was achieved. The three different kinds of particles used were: *a)* ion exchange resin, *b)* polyamine resin and *c)* silica resin. The particles' sedimentation velocities were determined by measuring the distance and time travelled by a particle in a 500 ml test tube, filled with water. The sedimentation velocities for particles *a)* to *c)* were 23.0, 1.5 and 2.5 $mm.s^{-1}$ respectively. The silica resin and polyamine particles were in the size range 40 – 75 μm and the ion exchange resin particles were in the range 150 – 180μm. A polyethylene fibre mesh was fitted to the bottom of the tube to prevent particles settling into the piston cavity when oscillation ceased. The volume fraction used in each set of experiments was determined by decreasing the fluid

oscillations to specific conditions at which the particles sediment to the bottom of the tube. The height of the bed was then measured and the volume fraction expressed as the "*particle bed height/ tube height x 100*". The mass fraction was determined by drying the particles in a microwave oven and measuring the dry weight.

For bubble retention experiments, ~1 ml of air was injected through a syringe, under constant oscillation conditions, leading to the random formation of bubbles (i.e. mean size and size distributions of the bubbles were a function of the fluid oscillation conditions). Bubble suspension experiments were recorded visually at the centre of the tube, through the installed optical box, using a Samsung digital video camera at 25 frames per second, illuminated from above by a 50W lamp.

4.3 Results and analyses

Several PIV and CFD simulations were carried out at different combinations of fluid oscillation amplitudes and frequencies (for further details see section Materials and Methods). Observations across this range of conditions are reported here, but a case study has been focused for the typical set of conditions: Re_o = 348, x_o = 1.1 mm and f = 11.1 Hz.

Particle Image Velocimetry (PIV)

Experimental analysis of flow patterns within a single SPC tube and the effect of fluid oscillation conditions on fluid mixing were studied by PIV. In constricted tubes under oscillatory flow, two critical Re_os are usually used to represent obtained flow patterns: the first one (at a lower Re_o) is with the point at which flow separation occurs, and the second one (at a higher Re_o) represents the Re_o at which flow symmetry breaks.

In this study it was found that symmetrical eddy structures were in evidence at the lowest Re_o*s* attainable with this oscillator unit (Re_o = 12, at f = 2.1 Hz, x_o = 0.2). Therefore the lower critical Re_o is below this value.

The axisymmetry of the vortex rings was broken at approximately Re_o = 100 (when operating at f = 1.1 Hz; x_o = 3.8 mm), leading to greater axial mixing. The dependence of the flow patterns on fluid oscillation amplitude was observed to differ from the dependence on oscillation frequency because the oscillation amplitude controls the eddy length detachment. This was also concluded by Ni et al. (1997) in studies on conventional larger OFRs with sharp-edged baffles, but conflicts with behaviour reported in further works (e.g., Ni and Pereira, 2000; Mackley and Ni, 1993). In the present study, flow patterns observed at similar Re_os (117 and 116), but at oscillation conditions of 4.1 Hz/1.0 mm and 1.1 Hz/3.8 mm, differ significantly: at high frequency, the eddy structures were generally axisymmetrical, but at high amplitude axisymmetry was clearly broken at a Re_o near 100.

Typical observed flow patterns are shown in the instantaneous velocity vector maps in Figure 3 below, corresponding to three different points of the oscillation cycle:

a) the point of maximum upward piston velocity (start of oscillation cycle);
b) point of near-zero piston velocity (before flow reverses downwards)
c) the point of minimum downward piston velocity, after flow reversal

The flow structures presented in Figure 4-3 may be interpreted as follows: at the lower constriction in Figure 4-3a) there is flow separation, generating an upward-travelling vortex ring. The vortex ring emerges from the near-wall region and grows through Figure 4-3b) and Figure 4-3c) to occupy most of the cross-sectional area of the tube, before colliding with the previous vortex ring. It should be noted that the non-axisymmetry at the point of flow separation is related only to the non-axisymmetric separation near the expansion (which is difficult to avoid in the tube's manufacture). Maximum non-axisymmetry was observed in the velocity vector maps when $u(t)$ was near its maximum value (point a) of the oscillation cycle), while for points at lower axial velocities (e.g. in Figure 4-3*b* and Figure 4-3*c*), the vortex rings become more axisymmetric and more centrally located.

In Figure 4-3, the average residence time of each vortex ring was between 1.0 and 1.2 oscillation cycles. Each vortex ring was able to travel, on average, about half a cavity length. It should be noted that the point at which the vortex rings collide in Figure 4-3 is not in the middle. This is due to slightly different velocities of the piston in the upward and downward directions. Apart from the initial asymmetry during flow separation, due to the asymmetry of the tube at the constriction, the mixing patterns observed in this reactor are essentially the same as those observed for larger, sharp-baffled OFRs. Therefore we can expect

to achieve the same uniformity and efficiency of mixing, as well as particle suspension and bubble hold-up as has been observed in those reactors.

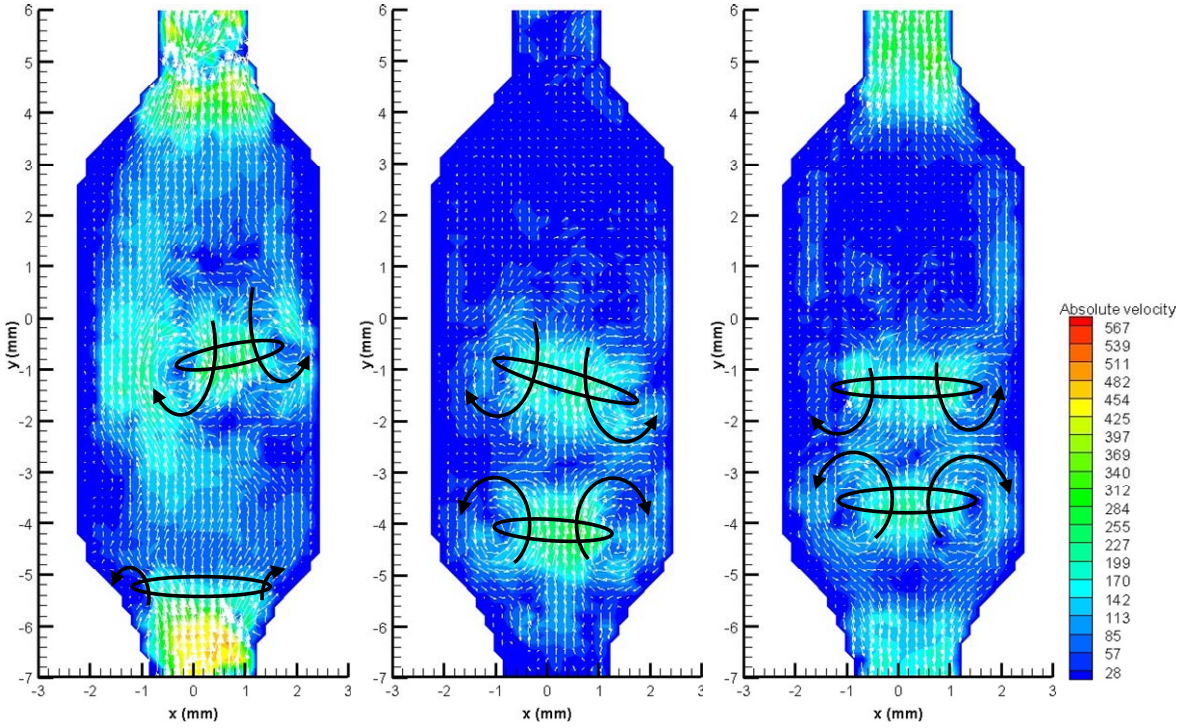

Figure 4-3. Instantaneous velocity vector maps at Re_o = 348, x_0 = 1.1 mm, f = 11.1 Hz coloured by absolute velocity magnitude (mm/s) and different phase angles (black vortex rings and arrows added to aid visualization):

a) beginning of cycle;

b) 1/5th way through cycle, i.e. before flow reversing;

c) 3/10th way through cycle, i.e. after flow reversing.

Figure 4-4, below, shows that the flow structures become considerably more asymmetrical at higher Re_os, as is the case in conventional OFRs. At Re_o = 1350, it is clear that symmetry is completely broken: it can be clearly seen that there are two vortex rings travelling in the same direction in Figure 4-4b), and in Figure 4-4c), it can be seen that although the rings are travelling in opposite directions they are highly asymmetrical. Clearly the SPC tube should not be operated at such high Re_os if plug flow is required, as there is a high degree of axial dispersion.

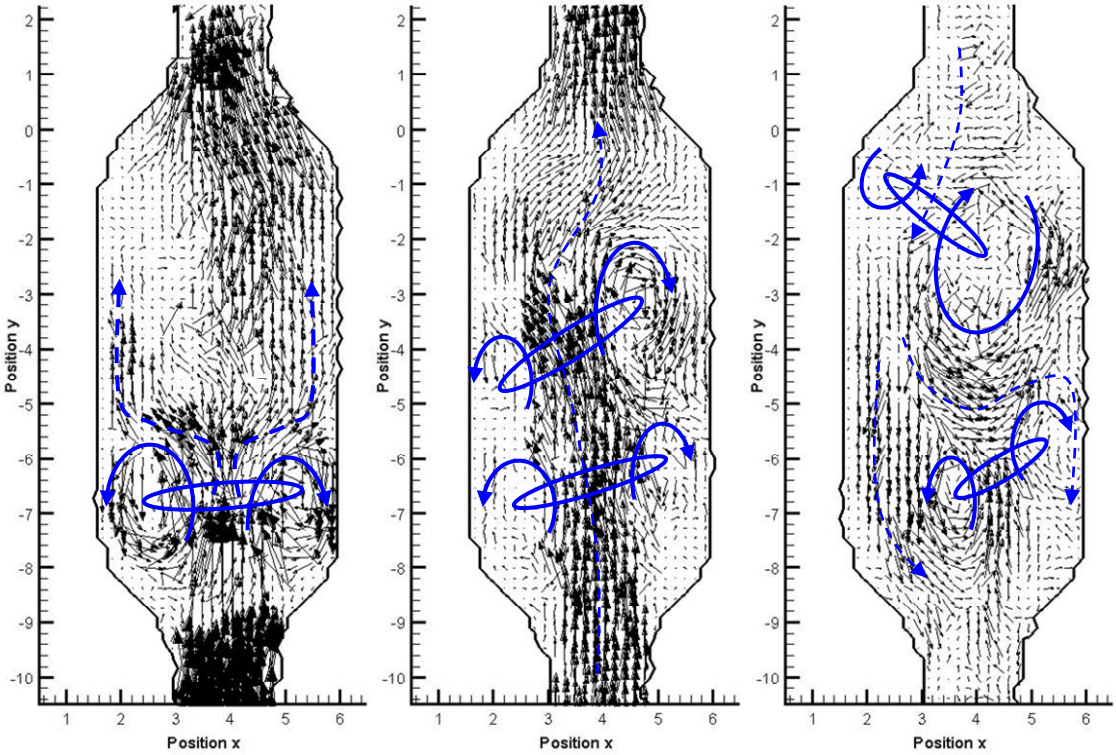

Figure 4-4. Instantaneous velocity vector maps at Re_o = 1,350, x_0 = 4 mm, f = 12.1 Hz and different phase angles (blue vortex rings and arrows added to aid visualization):

a) start of a new cycle;

b) 1/5th way through cycle, i.e. before flow reversing;

c) 3/10th way through cycle, i.e. after flow reversing.

To ensure suspension of high concentrations of catalyst particles the oscillation frequencies must be increased, as intensive eddy structures will be required at *all phase angles*, as in Figure 4-4.

PIV analysis led to the conclusion that the critical Re_os for the screening reactor are lower than that for the conventional OFR. This is summarised in Table 4-3 below. Flow separation was observed at $Re_o \approx 10$ for the first case. This is approximately five times lower than the minimum value reported for the conventional OFR and it is probably related to the greater constriction ratio of the SPC geometry.

Table 4-3: Minimum critical Re_o observed for the screening reactor and comparison with some reported values for the conventional OFR

Vortex rings geometry	Reactor mixing conditions	Screening reactor	Conventional OFR	
Axisymmetrical	Low axial mixing (or near plug flow behaviour at continuous flow)	$Re_o > 10$	$Re_o > 50$ $Re_o > 75$	Mackley and Ni, 1991 Mackley, 1990
Non-axisymmetrical	Stirred tank behaviour	$Re_o > 100$	$Re_o > 300$ $Re_o > 400$	Howes et al., 1991 Mackley, 1991

CFD Simulations

Sensitivity of the solution to numerical parameters. The number of numerical parameters involving the numerical scheme is large, but the principal parameters are the grid size, the time-step and the error allowed for the velocities. The influence of these parameters was studied for a continuous flow (in the absence of fluid oscillations) at a Reynolds number of 100.

A grid size independent solution is necessary for validation of results. It was found that the solution was qualitatively independent of the grid used. Quantitative analysis was accomplished by analysing the recirculation strength, which is defined as the difference between the maximum value of the stream function and its value at the wall ($w_{max} - w_{wall}$). The effect of varying the grid size was checked with the 2-D planar model and is depicted, qualitatively, in Figure 4-5. The solution was found to be mesh-independent for a mean cell size of 0.20 mm or less.

The time-step length was found to have no significant influence on the solution, once the convergence of the momentum and velocity equations was assured. Its typical value was around 0.005, i.e. about 200 time steps per simulated oscillation cycle. Values of the residual in the range 0.001 to 0.0001s were adjudged to represent convergence. Further reduction of the allowed error increased the CPU time required, without altering the solution.

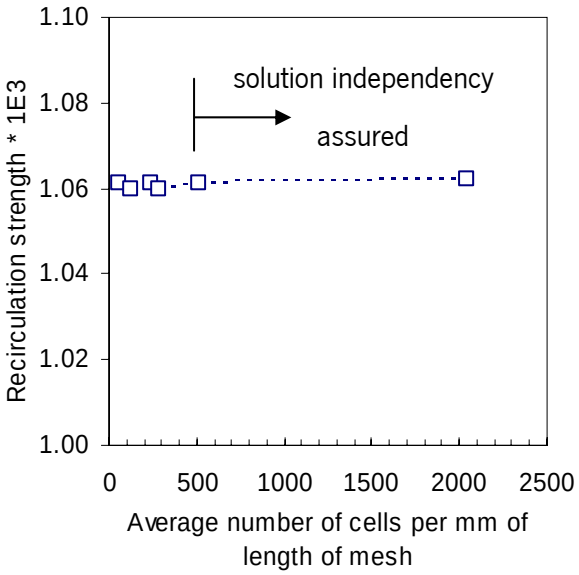

Figure 4-5. Influence of the grid size on the recirculation strength of steady state solution, w_{max} - w_{wall}, for continuous net flow, based on 2-D planar model results (Re = 100).

Simulated flow patterns. Figure 4-6 shows the results of a 2-D laminar axisymmetric model simulation at low axial mixing conditions (Re_o = 11), corresponding to conditions at which flow separation was observed by PIV. Flow separation was not observed when $u(t)$ is at its maximum (Figure 4-6*a*), but when the following deceleration leads to formation of an eddy (Figure 4-6*b*). Initially, flow is well-distributed radially, but as the axial velocity decreases, the flow moves preferentially to the centre of the tube. In Figure 4-6c), as the flow then reverses, it instead passes along the walls, as the vortex ring moves to the centre of the tube. This flow pattern would ensure good radial mixing due to the movement of flow between the centre and the walls of the cavity. The vortex structures are not as intensive as at higher Re_os, but this demonstrates a mechanism by which good radial mixing can be achieved at relatively low Re_os.

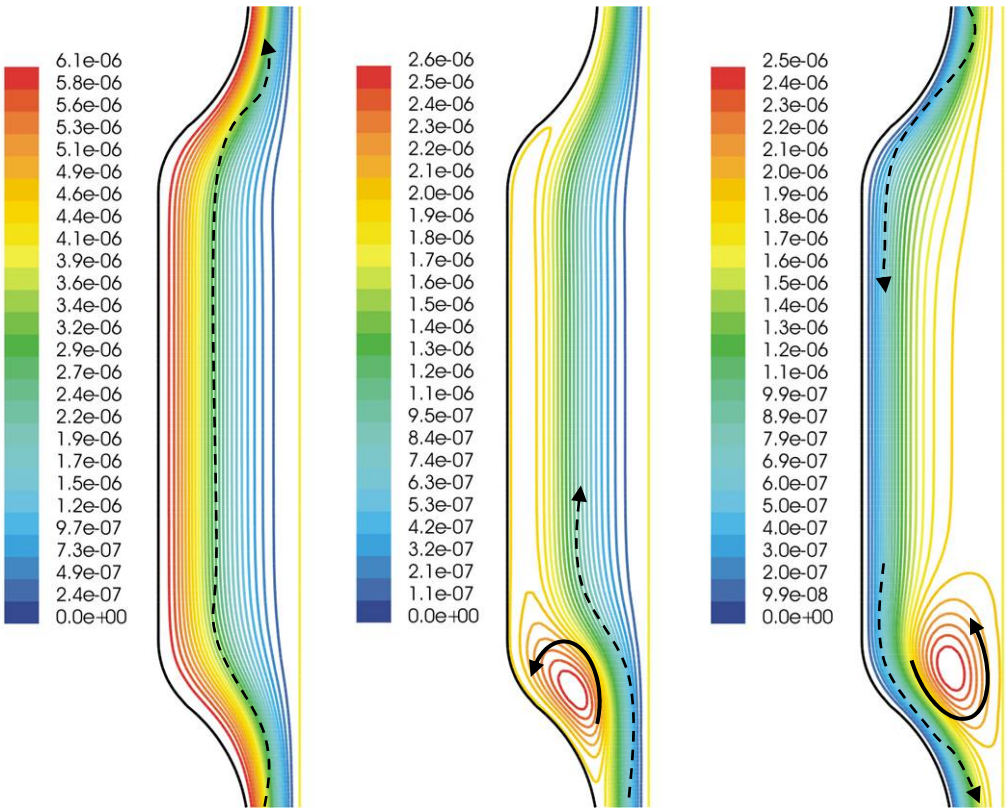

Figure 4-6. Simulated flow patterns for Re_o = 11, x_0 = 0.2 mm, f = 2 Hz, no net flow, using a 2-D axisymmetric laminar model, after 2 simulation cycles. Contours of stream functions (kg s^{-1}) at:

a) start of cycle, i.e. maximum upward velocity;

b) 1/5th of an oscillation cycle, i.e. before flow reversing;

c) 3/10th of an oscillation cycle, i.e. after flow reversing.

The flow patterns produced by the numerical simulations using the 2-D axisymmetric laminar model at low oscillation amplitudes (below 1 mm) generally exhibited good agreement with the PIV results. An example is presented in Figure 4-7, below, at a Re_o = 348 (11.1 Hz and 1.1 mm), which matches the case study. The simulated flow patterns qualitatively agree with the PIV measurements made at similar oscillation conditions (Re_o = 348, x_0 = 1.1 mm, f = 11.1 Hz) shown in Figure 4-3. There is vortex mixing in the entire cavity, and the "wall flushing" effect of oscillatory flow can be clearly seen. Again, it should be stated that the mixing here is essentially the same as that occurring in larger, sharp-baffled, conventional OFRs.

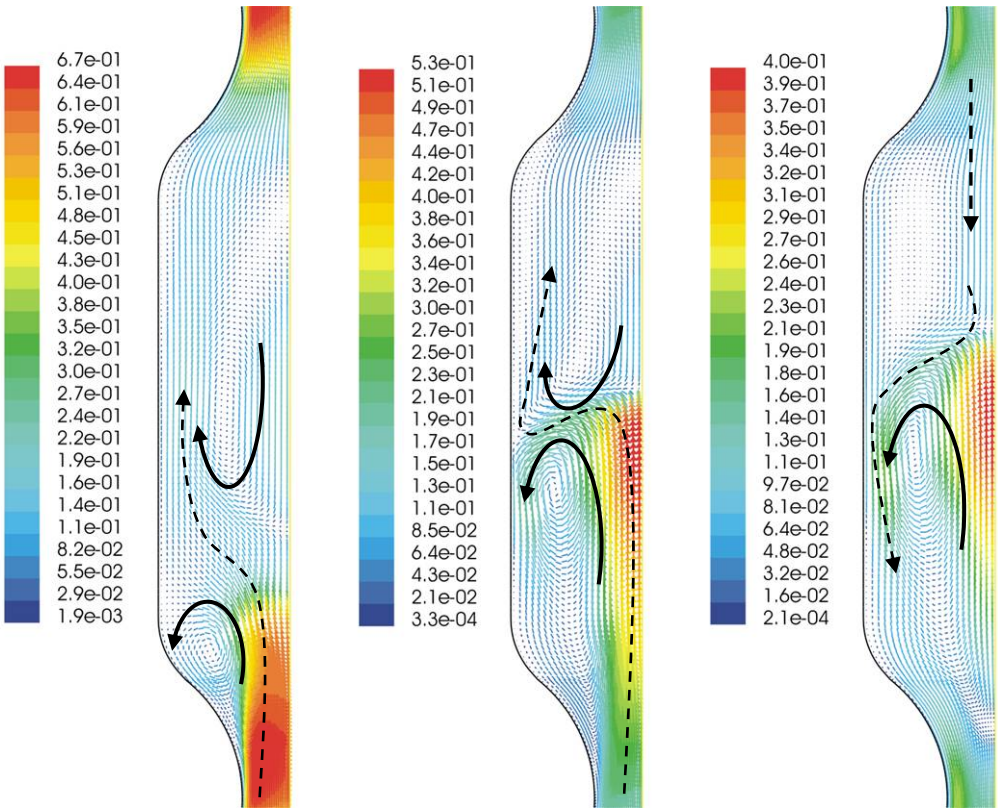

Figure 4-7. Simulated flow patterns for Re_o = 348, x_0 = 1.1 mm, f = 11.1 Hz, using a 2-D axisymmetric laminar model, after 12 simulation cycles, no net flow. Velocity vectors coloured by velocity magnitude (m/s) at:

a) start of cycle, i.e. maximum upward velocity;

b) 1/5th of an oscillation cycle;

c) 3/10th of an oscillation cycle.

To allow non-axisymmetry to be simulated it was necessary to move to a 3D mesh. It was possible to simulate asymmetric flows using a laminar model, provided there were enough cells in the mesh, although simulation by LES required less computational time (as per Schluter, 2001), as it required fewer cells. The laminar simulations below again exhibit good agreement with experimentally observed phenomena (see Figure 4-8) and are now able, in a three dimensional model, to generate non-axisymmetrical vortices.

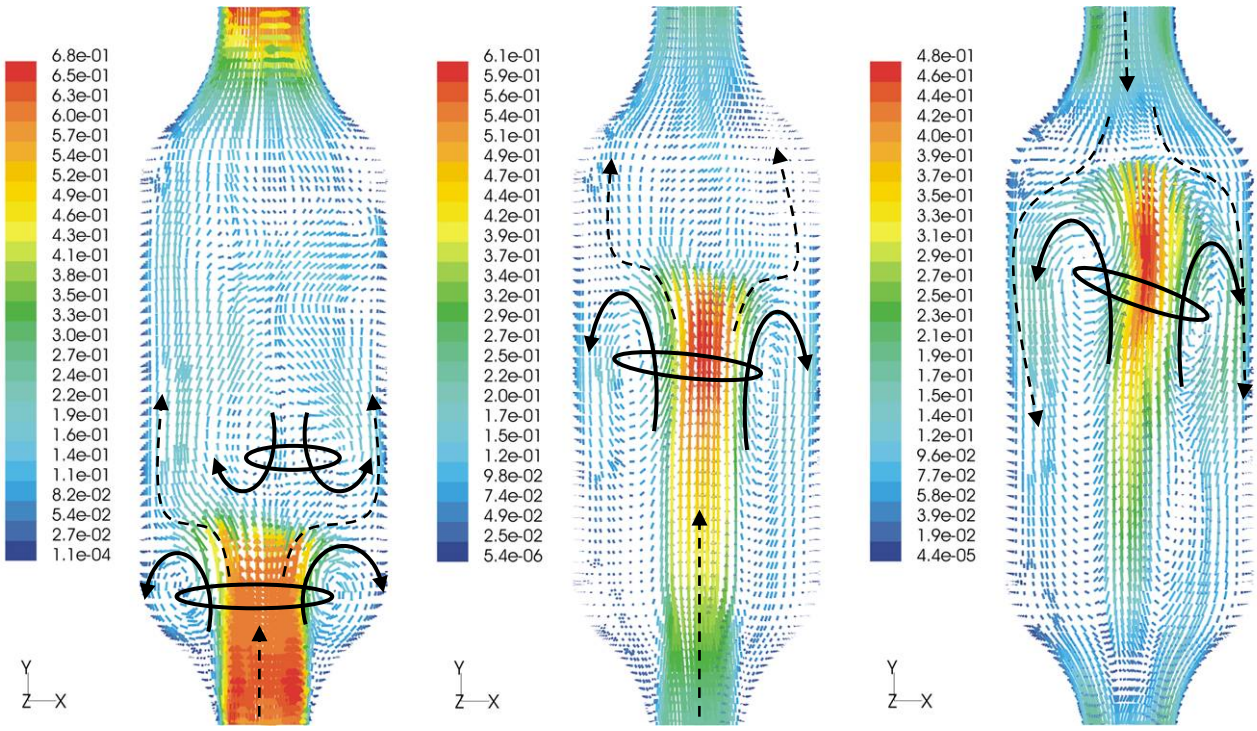

Figure 4-8. Simulated flow patterns for Re_o = 348, x_o = 1.1 mm, f = 11.1 Hz, using a 3-D laminar model, after 26 simulation cycles. Velocity vectors coloured by velocity magnitude (m/s), on plane z = 0, (black arrows added to aid visualization) at:

d) start of cycle, i.e. maximum upward velocity;

e) 1/5th of an oscillation cycle, i.e. before flow reversing;

f) 3/10th of an oscillation cycle, i.e. after flow reversing.

Model matching using the case study. It was necessary to determine quantifiable properties of the flow to allow the simulations to be validated and ranked. One such property is the total vortex area. The sum of the area occupied by all vortices through a complete oscillation cycle is represented in Figure 4-9 below. No comparison with results from 2-D planar model is presented since it did not accurately represent the fluid mechanics within a single SPC tube in the main range of fluid oscillation conditions in study.

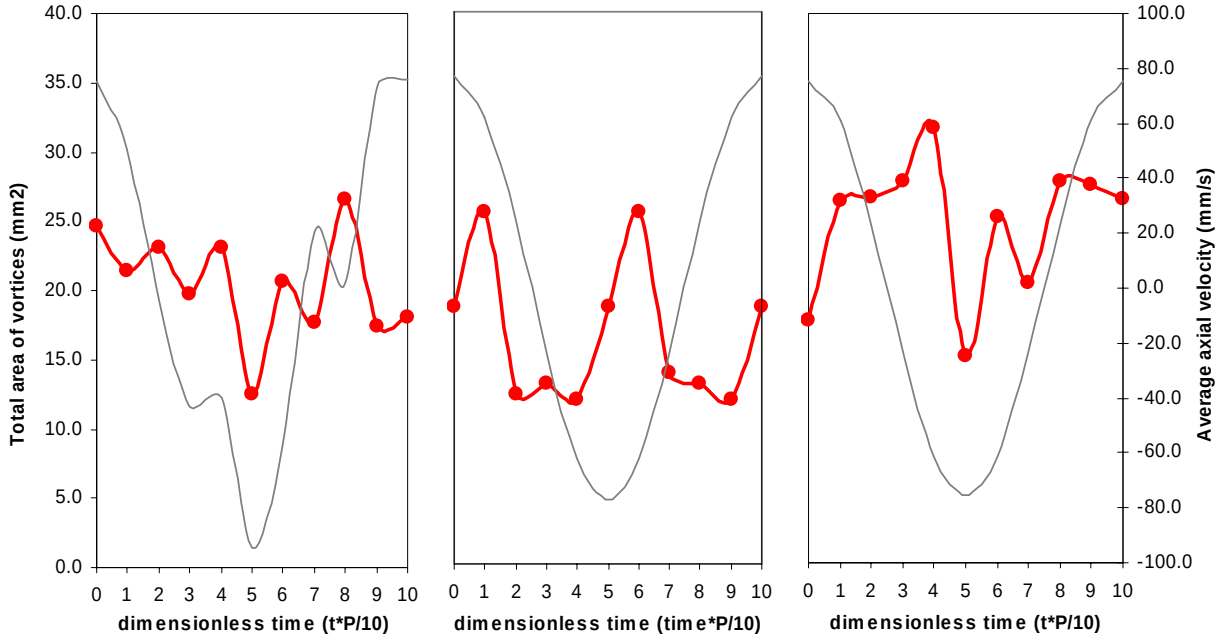

Figure 4-9. Comparison of the total areas occupied by the vortices (●) in different instants of the oscillation cycle (Re_o = 348, x_0 = 1.1 mm, f = 11.1 Hz; no net flow, i.e. Re_n = 0) for:

a) experimental PIV data;

b) 2-D axisymmetric laminar numerical simulations;

c) 3-D laminar numerical simulations.

It is clear that there is a good agreement between the vortex areas in the 3-D and 2-D simulations and the experimental PIV results. It should be noted that some differences are unavoidable, due to the imperfect action of the oscillation unit in the PIV experiments.

Average axial and radial velocities were also determined in order to compare the sets of data:

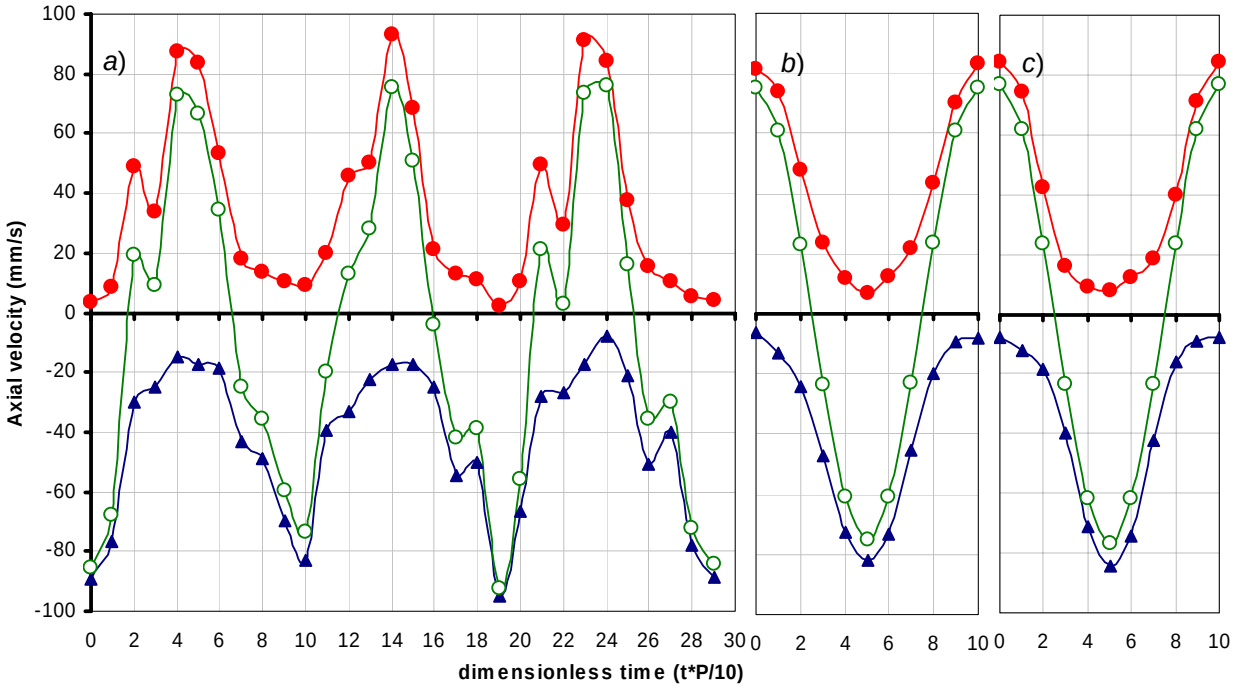

Figure 4-10. Average of axial velocities through the oscillation cycle at Re_o = 348, f = 12.1 Hz, x_o = 1.2 mm, using *a)* experimental data from PIV, *b)* data from numerical modelling using a 2-D laminar axisymmetric model and *c)* data from numerical modelling using a 3-D laminar model. (○) global averaged axial velocity; (●) average of positive values of axial velocity; (▲) average of negative values of axial velocities.

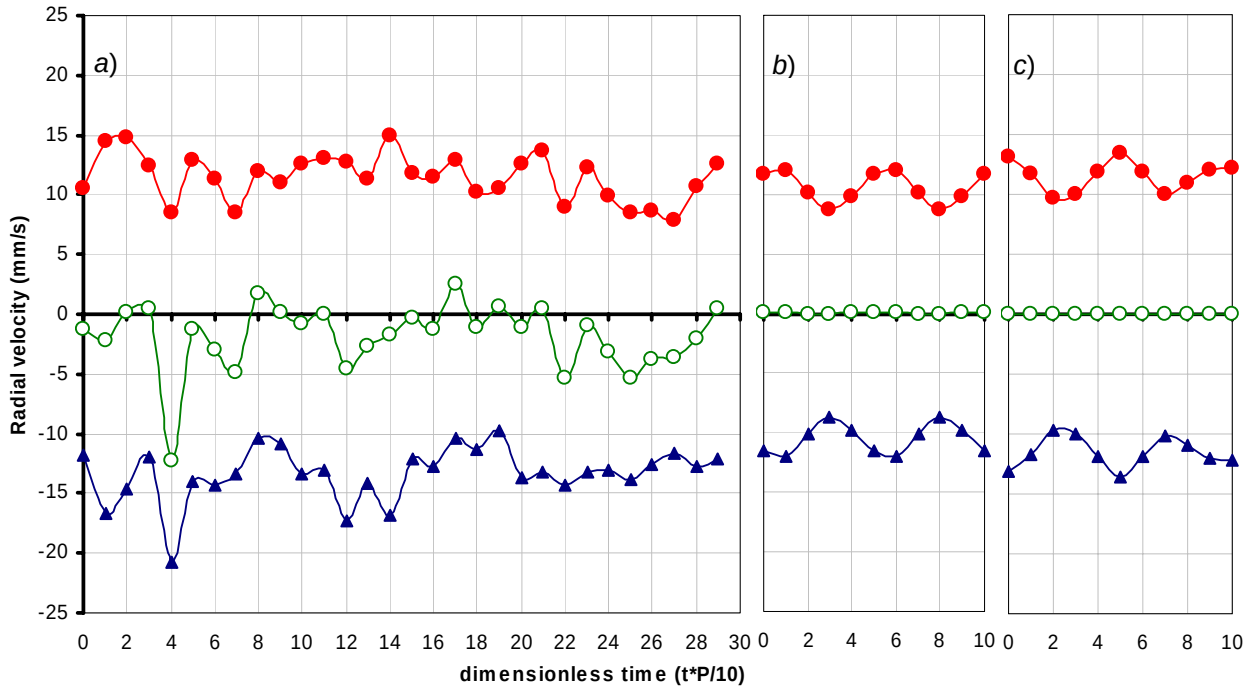

Figure 4-11. Average of radial velocities through the oscillation cycle using *a)* experimental data from PIV, *b)* data from numerical modelling using a 2-D laminar axisymmetric model and *c)* data from numerical modelling using a 3-D laminar model using cells at plane z = 0. (○) global averaged radial velocity; (●) average of positive values of radial velocity; (▲) average of negative values of radial velocities. Connection lines just intend to represent a tendency. Re_o = 348; f = 12.1 Hz, x_o = 1.2 mm.

Again a good degree of agreement was observed, for both the axial and radial velocities, indicating that the simulations are good models of the flow in the screening reactor. There is little difference between the 2D and 3D laminar simulations, although the 3D velocities are always slightly larger and therefore slightly closer to the experimentally observed velocities. For low axial mixing conditions, i.e. a Re_o below 100, there was a complete agreement between the PIV results and the numerical simulations with the 2-D axisymmetric laminar model in terms of location, number and size of vortices (results not shown here). At these oscillation conditions, the flow contains non-axisymmetric vortex rings that the 2-D axisymmetric model is inherently unable to simulate, but there is still semi-quantitative agreement with the PIV results, as the non-axisymmetry is mild. In strongly non-axisymmetric flows our evaluation criteria would show clear differences.

The numerical simulations helped to confirm that oscillation frequency affects the flow more significantly than the oscillation amplitude, because the use of small amplitudes leads to an increase in eddy intensity (smaller eddy size). Conversely, the use of high oscillation amplitudes increases the eddy size and decreases the number of visible eddy structures at any given phase angle of an oscillation cycle.

In the case study of Figure 4-7 and Figure 4-8 the 2-D axisymmetric simulations shown a better fit to the PIV data than results from planar simulations, as the size of eddy structures given by the planar model tend to be exaggerated and of too low intensity. The 3-D laminar model is an improvement as it is able to simulate non-axisymmetry, but is very dependent on the mesh resolution.

No significant mesh dependence was observed for the 3-D LES model. The results are in agreement with Ni *et al.* (2002), who claimed that the uniform mixing in an OFR is independent of turbulent intensity, and is instead due to "laminar instabilities". It was found that, due to nature of the LES model, similar results to the 3-D laminar model (with a fine mesh) may be achieved with lower CPU times.

The 2-D axisymmetric model also exhibited better agreement with the vortex behaviour than the 3-D laminar model (results not shown here). It is not clear why the number of simulated vortex rings is, on average, lower in the 3-D modeling than in the experimental results, or why the total distance traveled by eddy structures is overestimated in the 3D modeling. The 2-D axisymmetric model presents a good estimation of the vortex trail, but does not predict vortex dissipation time well. One explanation could be the existence of a tangential (swirl) flow, or the non-zero averaged axial velocity in the experimental data could be due to experimental error. The 2-D axisymmetric model cannot simulate a tangential flow, but it is possible in the 3-D laminar mode, but was not predicted (the averaged value of the tangential velocity component is also zero). It is difficult to say whether this result represents the true flow inside the SPC tube, or is a result of mesh dependency. The use of the periodic boundary layer in the numerical simulations should also be considered, as the flow patterns are constrained by the imposed periodicity of flow patterns in the next baffle cavity.

The comparison of the cycle average values (presented in Table 4-4 and Table 4-5, below) for a Re_o of 388, f = 11.1 Hz and x_o = 1.1 mm, demonstrates that simulation of the mixing intensity using the 3-D laminar model is slightly closer to the experimental data than the results from the 2-D axisymmetric simulations.

Table 4-4: Comparison of cycle average axial, radial (and tangential) velocities measured by PIV with the results from numerical simulations, using 2-D axisymmetric and 3-D laminar models; Re_o = 348, f = 11.1 Hz, x_0 = 1.1. Re_n = 0.

		Axial velocity [mm s^{-1}]			Radial velocity [mm s^{-1}]			Tangential velocity [mm s^{-1}]		
		Global	V_{axial}^{+}	V_{axial}^{-}	Global	V_{radial}^{+}	V_{radial}^{-}	Global	V_{tang}^{+}	V_{tang}^{-}
Without flow reversing (1)	Average	0.0	24.4	-24.4	-	-	-	-	-	-
	σ	54.5	-	-	-	-	-	-	-	-
	Min	-76.7	-	-	-	-	-	-	-	-
	Max	76.7	-	-	-	-	-	-	-	-
experimental PIV	Average	-8.8	34.4	-43.2	-1.9	11.5	-13.3	-	-	-
	σ	115.2	-	-	37.2	-	-	-	-	-
	Min	-595.6	-	-	-321.9	-	-	-	-	-
	Max	539.6	-	-	90.1	-	-	-	-	-
2-D axisymmetric laminar model	Average	0.0	37.5	-37.5	0.0	10.5	-10.4	-	-	-
	σ	105.6	-	-	32.2	-	-	-	-	-
	Min	-668.2	-	-	-136.7	-	-	-	-	-
	Max	668.2	-	-	256.3	-	-	-	-	-
3-D laminar model	Average	0.0	39.3	-39.3	-0.01	11.5	-11.5	-0.0	9.9	-9.9
	σ	112.9	-	-	33.2	-	-	29.1	-	-
	Min	-681.5	-	-	-318.0	-	-	-346.6	-	-
	Max	679.3	-	-	358.4	-	-	285.3	-	-

(1) Assuming fluid oscillated at same oscillation conditions in a smooth pipe.

Table 4-5:. Comparison of measured mixing intensity by PIV with the results from numerical simulations, using 2-D axisymmetric and 3-D laminar models; Re_o = 348, f = 11.1 Hz, x_0 = 1.1 mm

	Average ratio V_{radial}/V_{axial}	Averaged axial circulation rate [mm s^{-1}]	Predicted mixing time [s]
PIV	0.32	0.59	0.25
2-D axisymmetric laminar model	0.28	0.57	0.26
3-D laminar model	0.29	0.60	0.25
STR[(1)]	-	0.02	3.65

(1) data from Rase (1977), assuming a STR with same d/L ratio as a single SPC cavity.

Effect of the concentration of particles. In order to investigate particle suspension in the screening reactor, experiments were performed using three kinds of particles with distinct sizes and sedimentation velocities: silica resin, polyamine resin and ion exchange resin. Figure 4-12 below shows the relationship between the oscillation conditions and the maximum suspended concentration of ion exchange resin particles when the SPC tube was oriented vertically.

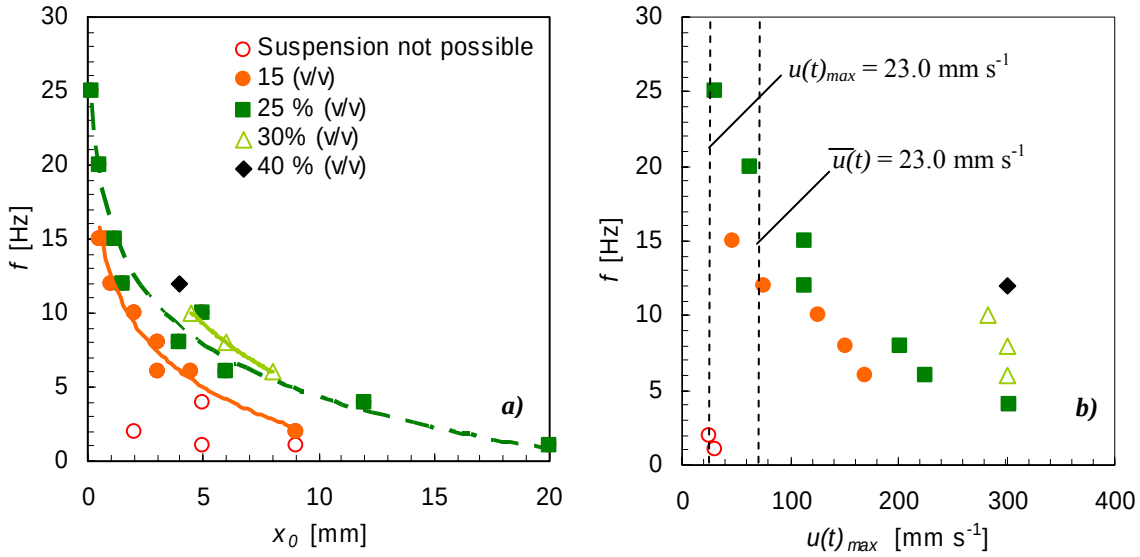

Figure 4-12. a) maximum concentration of ion exchange resin particles completely suspended at different fluid oscillations frequencies and amplitudes for a vertically fixed SPC tube; b) minimum $u(t)_{max}$ (maximum oscillation velocities) for complete suspension of particles, at different fluid oscillation frequencies.

Note that the values shown in Figure 4-12 are expressed in terms of volume of particles per available internal volume of a SPC tube. For larger ion exchange resin particles these units were used because they were considered to accurately reflect the ion exchange resin particle suspension performance of the reactor, as this suspension represented a significant fraction of the available volume of the tube occupied. The maximum concentration of ion exchange resin particles (40 % v/v, equivalent to 16 % w/w) in well-mixed conditions was achieved at 12.1 Hz and 4 mm, with the SPC tube vertically oriented (Figure 4-12a). Oscillation conditions at other combinations of amplitude and frequency (for a similar Re_o) were,

unfortunately, impossible to achieve due to the limitations of the oscillator unit. Consequently, these were the most suitable oscillation conditions that could be achieved for suspension of such large particles.

It was found that it was easier to suspend particles at high frequencies and low amplitudes than at low frequencies and high amplitudes. This observation is in agreement with the findings of the PIV and is supported by Figure 4-12b). The $u(t)_{max}$ required for complete suspension of particles (at constant particle concentration) exponentially decreases with the increase of f, approaching the value of sedimentation velocity of ion exchange resin particles (23.0 mm s^{-1}). When operating at low f (and consequently at high x_0), the $u(t)_{max}$ necessary for complete suspension of particles may be up to ten to fifteen times of the value of sedimentation velocity of particles, implying that the reactor has a lower energetic efficiency for particle suspension applications at these fluid oscillation conditions.

At the optimal oscillation conditions (12.1 Hz and 4 mm), it was also possible to keep 15 % (w/w) of small diameter particles (polyamine particles) completely suspended within the SPC tube and to re-suspend these particles after settling within a few seconds.

PIV was conducted whilst catalyst particles were present. In Figure 4-13a) and b) below the flow structures are essentially unaffected by the presence of the catalyst particles, but in Figure 4-13c) (at a different point in the oscillation) a certain degree of stratification of the particles has occurred, and has caused the flow to be pushed to one side of the tube. This may have to be taken into account in design of these reactors: that use of larger particles may necessitate increasing the axial dispersion of the flow.

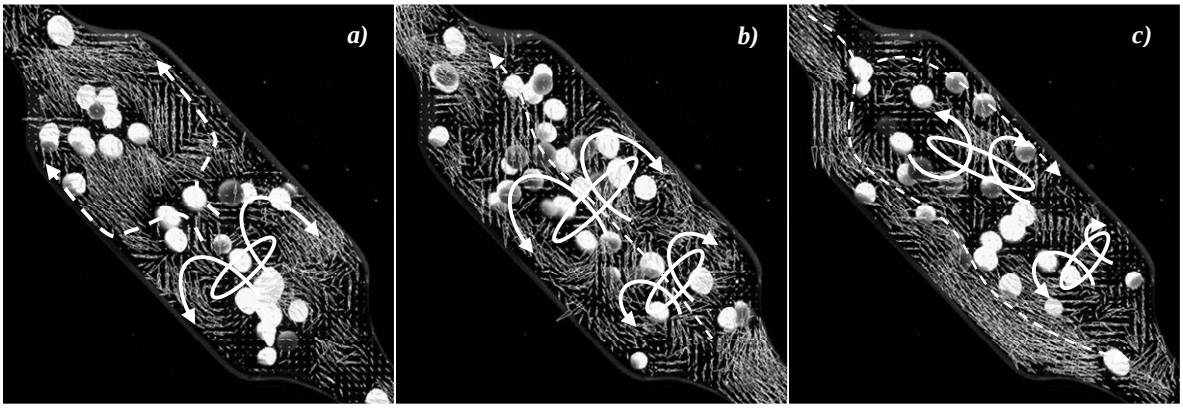

Figure 4-13. Instantaneous velocity vector maps of fluid phase at Re_o = 990, x_0 = 3 mm, f = 12.1 Hz and 45° of tube position in the presence of a small amount of ion exchange resin particles:

a) start of cycle, i.e. maximum upward velocity;

b) 1/5th of an oscillation cycle, i.e. before flow reversing;

c) 3/10th of an oscillation cycle, i.e. after flow reversing.

Effect of Reactor Orientation on Particle and Bubble Suspensions: In Figure 4-14, below, the suspension of ion exchange resin particles is shown for different angles of a SPC tube, between the horizontal (0 degrees) and the vertical (90 degrees). The oscillation conditions presented correspond to the minimum necessary oscillation amplitude, at 12.1 Hz, to keep all the particles suspended. Ion exchange resin particles were used as they are relatively easy to observe, due to their relatively large particle diameter.

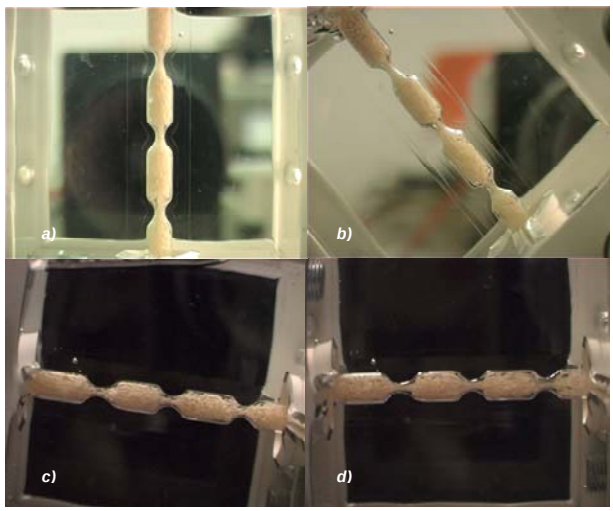

Figure 4-14 Complete suspension of 40 % v/v of ion exchange resin particles at varying angles and similar oscillation conditions: *(a)* vertical position, f = 12.1 Hz, x_0 = 4 mm; *(b)* 45°, f = 12.1 Hz, x_0 = 4 mm; *(c)* 10°, f = 12.1 Hz, x_0 = 3 mm; *(d)* horizontal position, f = 12.1 Hz, x_0 = 3 mm. In *b)*, *c)* and *d)*, the right hand side corresponds to the bottom of the tube.

When SPC tube orientation was switched from vertical to horizontal, it was observed that it was easier to keep particles suspended when the reactor was in the horizontal rather than the vertical position. For example, at 12.1 Hz, amplitude of 3 mm is enough to keep 40 % (v/v) of ion exchange resin particles completely suspended with the tube positioned horizontally, but oscillation amplitude of 4 mm is needed to keep the same quantity of particles completely suspended when the tube is held vertically. This means a considerable decrease on the required power input to keep the same amount of particles completely suspended with the swap of tube orientation from the vertical to the horizontal position. This may be due to differences of pressure drop between the two situations: when the SPC tube is positioned vertically, the particles in the bottom are at a higher static pressure than those at the top of the tube, due to the height of the particle "bed". Thus, a higher power input is required in order to suspend the same amount of particles.

Bubble Retention: Due to the small scale of the SPC geometry the problem of gas washout must be considered during reactor design. Therefore, the effect of reactor angle on bubble washout was investigated, at the optimal oscillation conditions given above (a frequency of 12.1 Hz and amplitude

between 3 and 4 mm, depending on the tube orientation). It was observed that the screening reactor had a self-cleaning capacity at angles above 45° at batch mode, i.e. washout of bubbles naturally occurs at tube orientations above 45 ° thus gas retention in the cavities is avoided. At smaller angles (near horizontal) small diameter (<1.6mm) bubbles were retained inside each cavity. The washout of these small diameter bubbles is the most important parameter in determining the reactor's angle.

In practice, an angle smaller than 45° will allow reactor tubes to be arranged in series (Figure 4-15). Thus, the optimal minimum angle for the reactor was determined to be 10°. This position does not limit the natural washout of large (>1.6mm) bubbles (even in batch mode), and may be a useful result, if the screening reactor is operated at low bubble breakage conditions. If a high power input is required (which may lead to significant bubble breakage) the small bubbles can be cleaned from the system by imposing a cyclic net flow of 14 ml/min (corresponding to a residence time of 20 s) for less than 1 minute, per SPC tube.

A significant increase in the mean residence time of the bubbles was observed when the fluid was oscillated at the optimal conditions (12 Hz and 4 mm), even when the tube was positioned vertically. This means that the operation of SPC tube under oscillatory conditions may lead to higher bubble contact time, which has the potential to enhance mass transfer processes, such as air-water oxygen mass transfer coefficient.

4.4 Discussion and conclusions

This work has presented PIV data for a millimetre-scale oscillatory flow screening reactor (micro-bioreactor) geometry with smooth periodic constrictions. The results demonstrate that the mixing previously observed at larger scales (e.g. in "conventional" oscillatory flow), with sharp baffles, can be reproduced at this, smaller scale in a reactor with smooth constrictions. It has also been shown that, as in larger oscillatory flow reactors, it is possible to keep high concentrations of polymer-supported catalyst beads suspended in the screening reactor, whilst maintaining uniform fluid mixing. The effect of tube orientation was investigated in relation to the movement of trapped air bubbles within the reactor tube, resulting in the finding that, for a tube oriented at ten degrees or greater to the horizontal, air bubbles

would migrate along the tube when subjected to appropriate oscillation conditions, rather than being trapped within the reactor.

Matching numerical simulations were performed and, in general, a high degree of correlation was observed between the simulations with 3D large eddy simulation (LES) and laminar models and the experimental PIV observations. This should aid in future design of these reactors. For reactors which operate at a Re_o below 100, a simple 2-D axisymmetric laminar simulation will fully describe the flow, and for most aspects of design will be good enough for higher Re_os (up to 1,200).

The data presented here is the basis for a concept design of a continuous small-scale reactor, to be used in speciality chemicals manufacture and high-throughput screening. A schematic of a prototype is shown in Figure 4-15. The reactor will have the capability to perform sequential reactions, by keeping different solid particles or reactants in separate tubes. A significant advantage of the system is that the mixing conditions achieved in the laboratory can easily be achieved at larger scales (Harvey and Stonestreet, 2001), as scale-up is predictable.

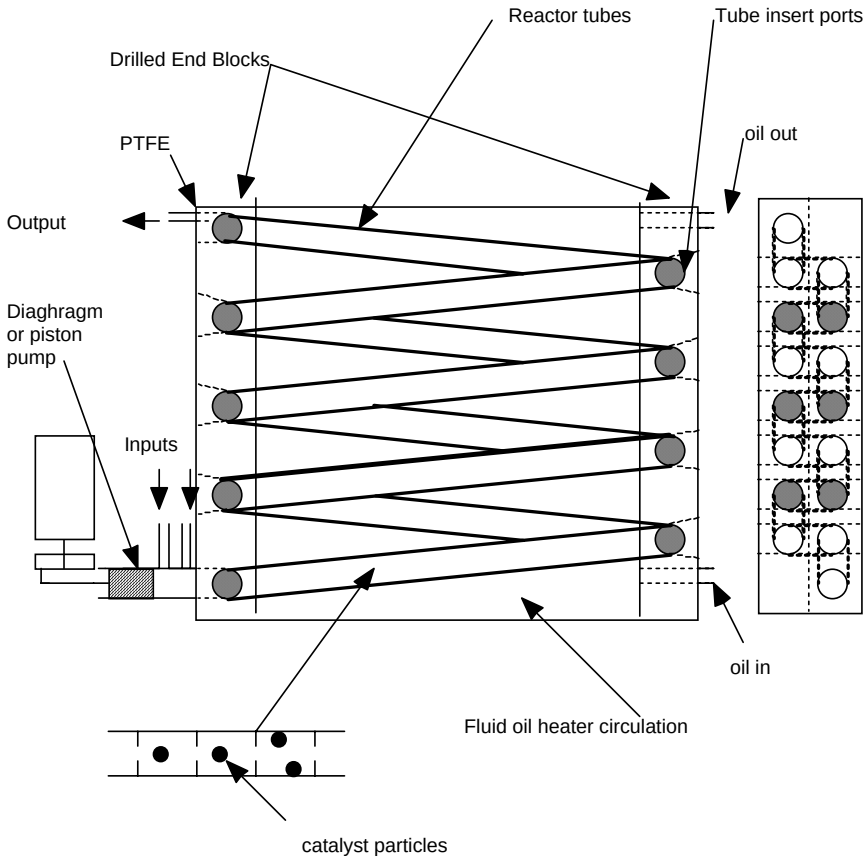

Figure 4-15. Proposed "in series" configuration for a single screening reactor unit.

4.5 Nomenclature

A_{ij}	*Area of element (m^2)*
A_{total}	*Cross-sectional area (m^2)*
A_{vortex}	*Vortex area (m^2)*
B	*Particle weight percentage (%)*
$d_{average}$	*Average diameter (m)*
d	*Diameter (m)*
d_0	*Orifice diameter (m)*
f	*Frequency (Hz)*
f_c	*Critical frequency (Hz)*
i, j, k	*Co-ordinates*
$m(t)$	*Mass flow rate ($kg\ s^{-1}$)*
n_i	*Height of the cross-sectional area or volume of the cell, i (m)*
Re_o	*Oscillatory Reynolds Number*
Re_n	*Net Flow Reynolds Number*
Str	*Strouhal Number*
t	*Time (s)*
$u(t)$	*Velocity ($m\ s^{-1}$)*
u_y	*Y-velocity ($m\ s^{-1}$)*
u_x	*X-velocity ($m\ s^{-1}$)*
V_{total}	*Total volume (m^3)*
w	*Vorticity ($1\ s^{-1}$)*
x	*x co-ordinate (m)*
x_0	*Amplitude (centre-to-peak) (m)*
y	*y co-ordinate (m)*
Greek letters	
ρ	*liquid density ($kg\ m^{-3}$)*
$\Delta\rho$	*difference of density between the particles and the liquid ($kg\ m^{-3}$)*
μ	*viscosity ($kg\ m^{-1}\ s^{-1}$)*
σ	*standard deviation*
υ	*kinematic viscosity ($m^2\ s^{-1}$)*

4.6 References

Baird, M.H.I. and Stonestreet, P., 1995, Energy-dissipation in oscillatory flow within a baffled tube, *Chem Eng Res Des*, 73: 503-511.

Brunold, C.R., Hunns, J.C.B., Mackley, M.R. and Thompson, J.W., 1989, Experimental-observations on flow patterns and energy-losses for oscillatory flow in ducts containing sharp edges, *Chem Eng Sci*, 44: 1227-1244.

Dickens, A.W., Mackley, M.R. and Williams, H.R., 1989, Experimental residence time distribution measurements for unsteady-flow in baffled tubes, *Chem Eng Sci*, 44: 1471-1479.

Elgobashi, S., 1994, On prediction particle-laden turbulent flows, *App Sci Res*, 52: 309-329.

Fabiyi ME and Skelton RL, 2000, Photocatalytic mineralisation of methylene blue using buoyant TiO2-coated polystyrene beads. *J Photochem and Photobiol A – Chem*, 132(1-2):121-128.

Gao, S., Ni, X., Cumming, R.H., Greated, C.A. and Norman, P., 1998, Experimental investigation of bentonite flocculation in a batch oscillatory baffled column, Separ Sci Technol, 33: 2143-2157.

Hewgill, M.R., Mackley, M.R., Pandit, A.B. and Pannu, S.S., 1993, Enhancement of gas-liquid mass-transfer using oscillatory flow in a baffled tube, *Chem Eng Sci*, 48: 799-809.

Howes, T., 1988, *On the Dispersion of Unsteady Flow in Baffled Tubes*, Ph.D. thesis, (Department of Chemical Engineering, Cambridge University, Cambridge, UK).

Howes, T. and Mackley, M.R., 1990, Experimental axial-dispersion for oscillatory flow through a baffled tube, *Chem Eng Sci*, 45: 1349-1358.

Howes, T., Mackley, M.R. and Roberts, E.P.L., 1991, The simulation of chaotic mixing and dispersion for periodic flows in baffled channels, *Chem Eng Sci*, 46: 1669-1677.

Liu, S., Ni, X., Greated, C.A. and Fryer, P.J., 1995, Measurements of velocities of single particles for steady and oscillatory flows in plain and baffled tubes, *Chem Eng Res Des*, 73: 727-732.

Mackley, M.R., 1991, Process innovation using oscillatory flow within baffled tubes, *Chem Eng Res Des*, 69: 197-199.

Mackley, M.R. and Ni, X., 1991, Mixing and dispersion in a baffled tube for steady laminar and pulsatile flow, *Chem Eng Sci*, 46: 3139-3151.

Mackley, M.R. and Ni, X., 1993, Experimental fluid dispersion measurements in periodic baffled tube arrays, *Chem Eng Sci*, 48: 3293-3305.

Mackley, M.R., Smith, K.B. and Wise, N.P., 1993, The mixing and separation of particle suspensions using oscillatory flow in baffled tubes, *Chem Eng Res Des*, 71: 649-656.

Mackley, M.R. and Stonestreet, P., 1995, Heat-transfer and associated energy-dissipation for oscillatory flow in baffled tubes, *Chem Eng Sci*, 50: 2211-2224.

Mackley, M.R., Tweddle, G.M. and Wyatt, I.D., 1990, Experimental heat-transfer measurements for pulsatile flow in baffled tubes, *Chem Eng Sci*, 45: 1237-1242.

Ni, X. and Gao, S., 1996, Scale-up correlation for mass transfer coefficients in pulsed baffled reactors, *J Chem Eng*, 63: 157-166.

Ni, X., Gao, S., Cumming, R.H. and Pritchard, D.W., 1995b, A comparative-study of mass-transfer in yeast for a batch pulsed baffled bioreactor and a stirred-tank fermenter, *Chem Eng Sci*, 50: 2127-2136.

Ni, X. and Gough, P., 1997, On the discussion of the dimensionless groups governing oscillatory flow in a baffled tube, *Chem Eng Sci*, 52: 3209-3212.

Ni, X., Jian, H. and Fitch, A.W., 2002, Computational fluid dynamic modelling of flow patterns in an oscillatory baffled column, *Chem Eng Sci*, 57: 2849-2862.

Ni, X., Liu, S., Grewal, P.S. and Greated, C.A., 1995c, A study of velocity vector profile and strain rate distribution for laminar and oscillatory flows in a baffled tube using particle imaging velocimetry, *J Flow Visual Image Proc*, 2: 135-147.

Ni, X. and Mackley, M.R., 1993, Chemical-reaction in batch pulsatile flow and stirred-tank reactors, *Chem Eng J Bioch Eng*, 52: 107-114.

Ni, X., Zhang, Y. and Mustafa, I., 1998, An investigation of droplet size and size distribution in methylmethacrylate suspensions in a batch oscillatory-baffled reactor, *Chem Eng Sci*, 53: 2903-2919.

Ni, X., Zhang, Y. and Mustafa, I., 1999, Correlation of polymer particle size with droplet size in suspension polymerisation of methylmethacrylate in a batch oscillatory-baffled reactor, *Chem Eng Sci*, 54: 841-850.

Ni, X.W., 1994, Residence time distribution measurements in a pulsed baffled tube bundle, *J Chem Technol Biot*, 59: 213-221.

Ni, X.W., Gao, S.W. and Pritchard, D.W., 1995a, Study of mass-transfer in yeast in a pulsed baffled bioreactor, *Biotechnol Bioeng*, 45: 165-175.

Ni, X.W. and Pereira, N.E., 2000, Parameters affecting fluid dispersion in a continuous oscillatory baffled tube, *J AIChE*, 46: 37-45.

Perry, R.P., Green, D.W. and Maloney, J.O., 2002, *Perry's Chemicals Engineer*, Platinum edition (McGraw-Hill, New York, USA).

Rase, H.F., 1997, Chemical reactor design for process plants, Volume one: principles and techniques, (Willey-Interscience, New York, USA).

Schlüter, J.U., 2000, Large Eddy Simulations of flow and mixing in jets and swirl flows: applications to gas turbines, Ph.D. thesis, (CERFACS, Toulousse, France).

Scragg, A.H., 1988, Biotechnology for Engineers: Biological Systems in Technological Processes (Ellis Horwood Limited, West Sussex, England).

Stonestreet, P. and Harvey, A.P., 2002, A mixing-based design methodology for continuous oscillatory flow reactors, *Chem Eng Res Des*, 80: 31-44.

Stonestreet P. and van der Veeken P.M.J. The effects of oscillatory flow and bulk flow components on the residence time distribution in baffled tube reactors. *Trans IChemE, Part A*, Vol. 77, pp671-684, November 1999.

Chapter 5 Mixing times and residence time distribution of liquid phase within the SPC geometry

The mixing times and residence time distributions within the 350-mm-long SPC tube (micro-bioreactor) and the meso-reactor are herein presented, through four working stages.

In a first part, the characterisation and flow modelling through liquid residence time distribution (RTD) of the micro-bioreactor under oscillatory flow mixing (OFM) was performed. The macroscopic flow patterns were determined by introducing a step-down injection at the tube inlet, while fibre optic micro-probes were used to monitor the RTD at several combinations of frequency (f) and amplitude centre-to-peak (x_0) (0 to 20 Hz and 0 to 3 mm, respectively).

The macroscopic fluid mixing was quantified by comparison of the real system response with the ideal flow cases of either completely back-mixed or plug flow reactors, and with various, non-ideal, single-phase flow models: tanks-in-series with and without backflow, axial dispersion model and a combined model (composed of an ideal plug flow reactor (PFR) and an ideal continuous stirred tank reactor (CSTR) in series). Non-ideal flow models parameters (N_{tis}, G, P_D and V_p/V, respectively) were estimated through diverse methods and the reproduction of an ideal step function at the inlet was confirmed. Estimated parameters values at different OFM conditions were standardised with those estimated for the laminar, steady flow, and showed that the balance between the convective and dispersive flow is controlled by both x_0 and f. In particular, the approach to an ideal flow situation of PFR is revealed by a 3.1-fold, 4.2-fold and 1.6-fold increase, respectively, of N_{tis}, P_D and V_p/V, and a decrease of 87 % in G (extracted using Laplace transfer functions) in comparison with the steady flow situation. The selected OFM conditions are relevant to chemical synthesis with residence times up to several minutes, thus RTD were applied in the prediction of conversion ($\overline{X}$) in a first order homogenous and isothermal reaction in the SPC tube. For a reference value of $k\bar{t}$ = 4 it was concluded that $\overline{X}$ in a continuous system based on SPC geometry may be approached to $\overline{X}$ obtained in a tubular reactor with a deviation as small as 1.2 %.

In a second stage, the effect of v (2.28 to 27.40 ml/min) on the RTD in the SPC tube geometry was studied at unsteady flow conditions by running a further set of experiments in the continuous meso-reactor. The increase of v was found to drive the RTD towards the PFR (making the RTD narrower), which was considered to be due to reducing of backflow usually observed at increased x_0 values (above 1 mm).

The third part of this work is concerned with the study of (batch) mixing performance of the micro-bioreactor system. Using fibre optic probes, a mixing coefficient k_m is determined for the system as a function of the applied f and x_0. The mixing coefficient k_m was found to increase with the increase of both f and x_0, and an empirical correlation for k_m is herein presented.

In the fourth part, numerical simulations of steady flow in the micro-bioreactor for increasing values of v were performed. A poor agreement was obtained between the numerically predicted backflow parameter G (using a 2-D axisymmetric laminar model) and the experimentally estimated G, as the numerical simulations with a 2D-axisymmetric model tend to over-estimate the mean residence time of the tracer.

Keywords: SPC geometry; meso-reactor; oscillatory flow mixing; fluid mechanics; dispersion; mixing; numerical simulations; batch; continuous.

5.1 Introduction

Chemical and biochemical engineers are concentrated on developing small-scale systems to support the actual high demand of high-throughput screening experiments of e.g. catalyst particles and biocatalysts. Such systems have the main advantage of reducing labour and reagents requirements, as several reactions may be run at the same time using small volumes. The continuous systems provide further advantages over the batch, by e.g. allowing the integration of upstream and downstream operations, running series of reactions, presenting improved reaction yields, allowing to obtain data that is not otherwise possible to obtain in a batch system (e.g. in the case of biocatalysts).

While dimensions of scale-down systems may be small, time-scales of molecular processes (such as diffusion times in liquid systems) may remain large, thus deviations from ideal flow are frequent. Consequently, the study of macroscopic flow patterns has become important for successful modelling, design and optimization of microscale systems. That is the case of the novel continuous screening meso-reactor recently presented (Reis et al. 2005), composed by a 4.4 mm internal diameter jacketed tube featuring smooth periodic constrictions (SPCs). SPC geometry is envisaged for application to e.g. screening of homogeneous catalysts, multiphase flows such as those formed in heterogeneous catalysis or those inducing particle nucleation phenomena for particle generation or biocatalyst screening. Previous work with CFDs (Reis et al. 2005) suggested that operation of SPC geometry under oscillatory flow mixing (OFM) improves the radial mixing and drives the macroscopic flow patterns to either the ideal flow cases of plug flow reactor (PFR) or completely back-mixed reactors. This is done to maximize reactor productivity (e.g. optimal volume/time yield) or to offset non-ideal effects, such as non-isothermal behaviour, that otherwise might occur. In particular, flow patterns may allow the establishment of reliable comparisons between e.g. conversion and selectivity of catalyst performance data or the efficient contact between different phases (in multiphase systems). Thus, it is necessary to identify combinations of process conditions (net flow rate and oscillatory flow conditions) that drive the macroscopic flow patterns within the SPC geometry towards the ideal flow cases of PFR or completely back-mixed limits.

For continuous processing devices, the tracer injection and response method has been widely used to study mixing characteristics of reactors through residence time distribution (RTD) (Lu et al. 1994). Techniques such as the moment, (Hatch 1973) weighted moment (Andersse and White 1971), Laplace and Fourier transform domain analysis (Gangwal et al. 1971) and time domain analysis (Mills and

Dudukovic 1989; Verlaan et al. 1989) have been employed to analyse the tracer response data. A good discussion of advantages and disadvantages of each technique may be found elsewhere (Froment and Bischoff 1990). Time domain analysis of RTD in baffled tubes such as conventional (50-mm-i.d) oscillatory flow reactors (OFRs) has been reported by several authors (Mackley and Ni 1991; Mackley and Ni 1993; Ni et al. 2002; Ni et al. 1995; Ni and Pereira 2000) using conventional techniques, e.g. conductivity measurement. The main problem with such technique is the effect of the tracer density (solution of NaCl or KNO_2) which affects the sensitivity of the determination. More recently a non-intrusive state-of-the-art laser induced fluorescence technique (Fitch and Ni 2003) was applied (using a dye that fluoresces when induced by a laser) to study the RTD in conventional OFRs, being concluded that intrusive experiments using conductivity probes can have mass transfer associated problems into the membranes of the probes, originating misleading results. In most of the studies available, two different models were used to determine dispersion coefficients: *i*) plug-flow with axial dispersion and *ii*) series of CSTRs with backflow. Similar results were achieved with both methods.

Briens et al. (1995) demonstrated that significant differences can exist between the real RTD curve and a concentration profile measured by a "through the wall" technique (instead of "mixed cup" concentrations) when flow behaviour is far from plug flow. This usually leads to errors in the determination of liquid residence times by the tracer injection technique. Thus, a correct specification of the system boundaries is of vital importance.

This study is divided into four sections. In the present part, a 350-mm-long SPC tube (micro-bioreactor) is used for the assessment of the deviation from tubular flow in SPC geometry by monitoring the RTD of liquid phase at increasing net flow rates (v), fluid oscillation frequency (f) and amplitude centre-to-peak (x_o). Due to the small-scale SPC tube geometry, refined techniques are required for an accurate measurement of RTD, thus optical fibre micro-probes are used for tracer detection, additionally allowing eliminating some of the pitfalls of unsteady tracer injection technique mentioned elsewhere (Boyer et al. 2002). Four models representing non-ideal flow in macro-scale reactor were used in the modelling of RTD curves. Deviations from the ideal flow cases of either plug flow reactors or completely back-mixed reactor are quantified by the respective model parameters estimated through various methods from the non-ideal cumulative washout tracer concentration, $W(t)$, according to the appropriate system boundaries (open or closed system). The consequences of such deviations from tubular flow are quantified by predicting the conversion for a first-order homogenous, isothermal, chemical reaction based on the experimental RTDs.

In a second part, the effect of ν on the continuous RTD was assessed by operating the meso-reactor at various combinations of Re_o numbers and ν, and the mean number of tanks-in-series (N_{ts}) estimated for the various flow situations.

In the third part, the batch operation of the 350-mm-long SPC tube (micro-bioreactor) is foreseen, thus the mixing times of the liquid phase are determined for various combinations of f and x_o using the conventional unsteady tracer injection

In a fourth part, CFD technique is assessed for prediction (modelling) of RTD in SPC geometry, at steady flow conditions (i.e., in the absence of fluid oscillations).

5.2 Experimental

5.2.1 RTD of liquid phase in the novel micro-bioreactor

RTD experiments in the 350-mm-long SPC tube (micro-bioreactor) were performed using imperfect pulse response experiments with a dye tracer. A schematic of the experimental setup is illustrated in Figure 5-1.

A 350-mm-long SPC tube (Reis et al. 2005) was fixed vertically and mounted according to Figure 5-1. A steady, continuous fluid flow rate was supplied with a peristaltic pump. Flow from the peristaltic pump was passed through a reservoir in order to cut off the propagation of fluid pulsations. Oscillations of the liquid inlet flow rate were achieved by a rotative ceramic piston pump (CKCRH0, Fluid Metering Inc., New York), working in closed-loop. The design of such pump (valveless rotating and reciprocating piston) allowed good sinusoidal oscillations of the fluid. The control of oscillation amplitude centre-to-peak (x_o) of the fluid was made by turning an easy-grip flow control ring in the pump head. The relation between piston position (h_p) and x_o was: $x_0 = 7.307 \times 10^{-1} \times h_P$. Values of x_o of 0 - 3 mm were achievable with this system (x_o represents the centre-to-peak oscillation of the fluid in the maximum internal tube diameter zone, d = 4.4 mm). The oscillation frequency (f) was controlled by the angular rotation of the motor. In this work, the range of interest for f was 0 to 20 Hz, as this is the typical range of f reported for OFRs. In all, a precise control of both x_o and f was obtained within the referred limits.

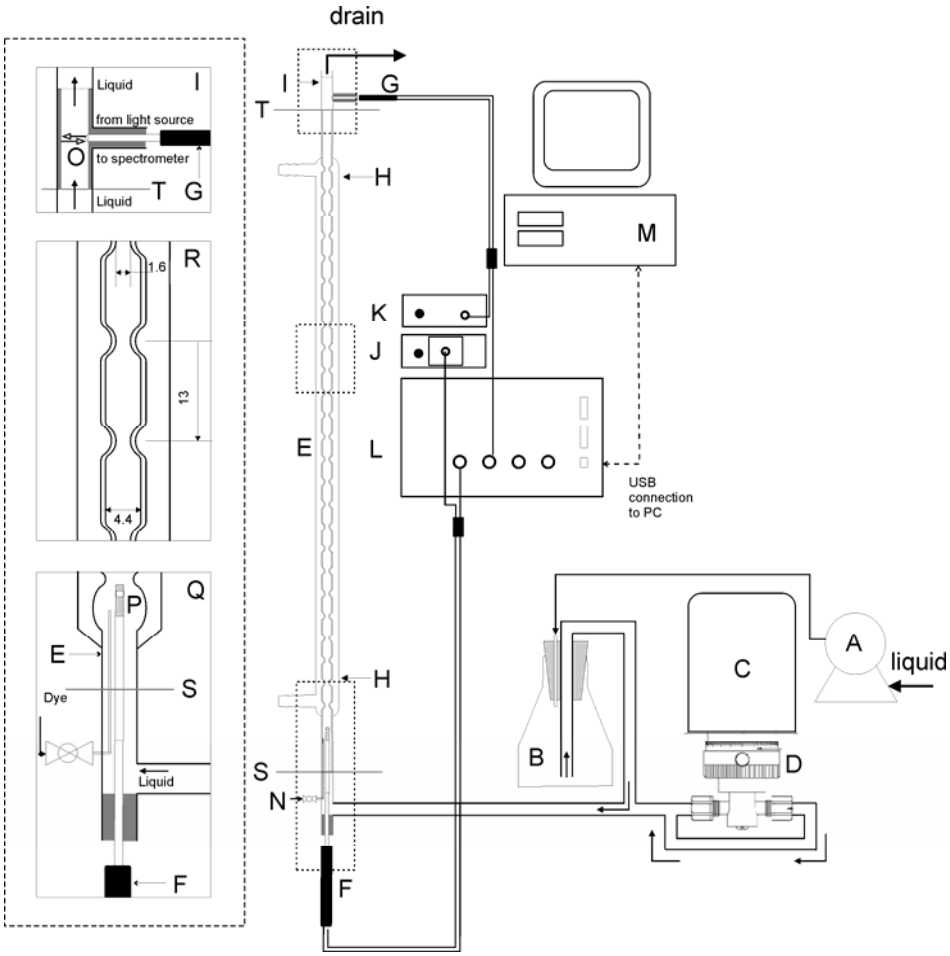

Figure 5-1. Experimental setup. A: Peristaltic pump; B: Reservoir; C: Electric motor; D: Piston pump; E: 350-mm-long SPC tube; F: Micro transmission dip optical probe; G: Reflection optical probe; H: Aluminium foil; I: In-line cell; J: Tungsten halogen light source; K: 475 nm LED light source; L: Multi-channel fibre optic spectrometer; M: Personal computer; N: Tracer injection; O: Optical path of reflection probe; P: Optical path of transmission probe (2 mm); Q: section of dye injection; R: detail of SPC geometry (all units are in millimetres); S: inlet tube; T: outlet tube.

The dye tracer used in the experiments was an aqueous solution of Indigo carmine obtained from Merck (Darmstadt, Germany). This substance was selected, as it did not adsorb to both the installation pipes and the SPC tube walls. The maximum optical absorption of Indigo carmine is 610 - 612 nm.

In-line tracer concentration was obtained from the optical density (OD) measured via two optical micro-probes connected to a multi-channel optic spectrometer system (Avantes, Eerbeek, The Netherlands). Due to the geometry of the SPC tube, two different probes were used. A micro transmission dip optical probe

(micro-probe 1) (FDP-UV-micro-1), with 2 mm optical length, was used to monitor the (local) tracer concentration inside the first cavity of the SPC tube (Figure 5-1, part Q) at an axial distance of 15 mm from the inlet. At the outlet (axial distance of 358 mm from the inlet point), a reflection probe (micro-probe 2) (FCR-7UV200-1,5x100-2) with a small tip (1.5 mm) was installed perpendicularly to the flow direction, into a 5 mm internal diameter in-line flow cell with white walls (Figure 5-1, part I), measuring the cross averaged (through-the-wall) concentration. The SPC tube was covered with an aluminium foil to reduce the noise due to environmental light. Both optical probes were provided with SMA connectors.

Inlet tube (step-down injection point) and outlet tube (micro-probe 2 location) boundaries were located in plain pipe sections, where the generated flow patterns are different from those in the constricted tube section, mainly when operating under OFM. Moreover, both boundaries were positioned far enough (> 3.5d) from the nearest constriction such that no flow inversion occurs across them. Thus, boundaries conditions were considered as 'closed-closed', allowing obtaining the true RTD in the control volume (Nauman and Buffham 1983).

Reading of power radiation (P) coming from both probes was done *on-line* and simultaneously using slave1 and slave2 channels of a 4-channel optical spectrometer AvaLights-2048 (Figure 5-1, L), detecting the intensity for a wavelength scan. The CCD detector was connected to an electronic board with 14 bit AD converter and USB/RS-232 interface. Data transfer from the optic spectrometer to a personal computer was controlled by AvaSoft full software. A function $S = \int_{585\,nm}^{635\,nm} A(\lambda)\,\mathrm{d}\lambda$ (where λ is the wavelength and $A(\lambda)$ is the light absorbance) was monitored for both slave1 and slave2 channels using an optimised integration time (i.e. which allows a maximum accuracy of CCD detector). Readings of S were taken every 1/9th of a second and each three consecutive readings were averaged resulting in experimental points available at each 1/3rd of a second. This resulted in highly linear tracer concentrations (x) up to 0.2 kg/m^3 for both micro-probes.

Procedure and data analysis

The optical response of micro-probes was calibrated by running several water-solutions through the system at increasing concentrations of Indigo carmine (x = 0 - 1 kg/m^3). These solutions were sequentially pumped directly to the bottom of the SPC tube at a high flow rate (ν) ($\nu \approx$ 18 ml/min). The first 50 - 100

millilitres of each standard solution were rejected and the remnant was recirculated for 10 - 15 minutes, until stabilisation of the intensity for a wavelength scan for both micro-probes signals. Finally, S was monitored for 1 minute and the mean P found by averaging S in this time interval. Light absorbance (A = log (P_0/ P)) was found highly linear for both micro-probes at $x \leq 0.2$ kg/m^3, as seen in Figure 5-2.

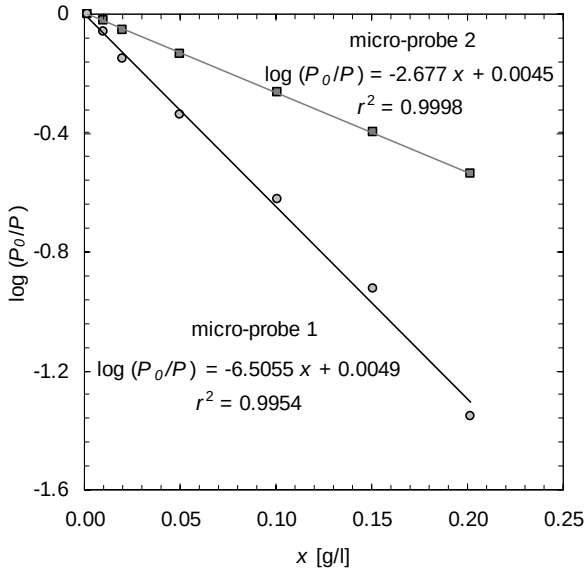

Figure 5-2. Relation between absorbance (A = log (P_0/ P)) measured by optical micro-probes and the tracer concentration (x).

The complete procedure for acquisition of RTD was as follows. After washout (Figure 5-3, phase I) of the system with distilled water, an aqueous solution of Indigo carmine (inlet concentration, x_{in}, equal to 0.2 kg/m^3, thus with a density very close to that of water) was continuously injected (Figure 5-3, phase II) in the SPC tube through a tracer injection port (see Figure 5-1, part Q). Once the concentration was stable (Figure 5-3, phase III) the dye tracer injection was stopped. Fresh water was subsequently pumped (Figure 5-3, phase IV) through the inlet of the SPC tube (creating a step-down injection) by switching on the peristaltic pump (the starting point of the experiments, i.e. t = 0) until the concentration of tracer becomes null at the exit. The step input injection method was applied since it is relatively easy to generate experimentally. The step-down variant (washout probability function, $W(t)$) was applied as it drastically reduces the required amounts of tracer to achieve the final 'lined out' response. However, the step-down concentrations were converted into a positive-step response by considering the linear relation between the

cumulative washout probability function, $W(t)$, and the cumulative distribution function, $F(t)$, i.e. $W(t) = 1 - F(t)$, which simplified some of the mathematical manipulation of data (results not shown). All experiments were performed at room temperature (20 °C) and using distilled water as main fluid.

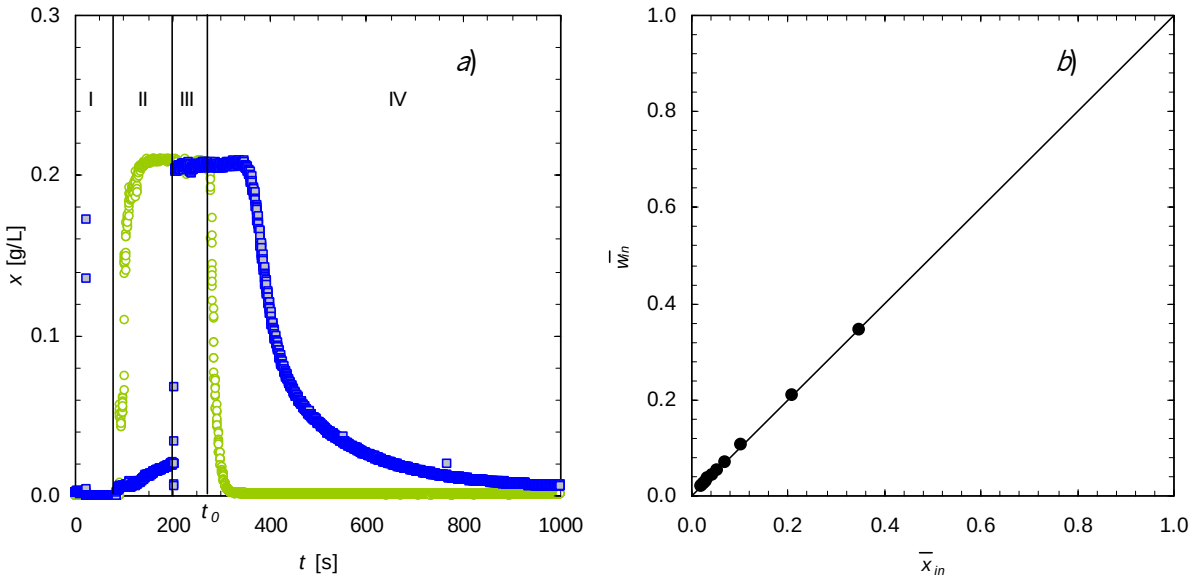

Figure 5-3. (a) Response of micro-probes during the consecutive phases of a complete RTD experiment; (b) comparison of generated Laplace step-down function ('generated $\bar{x}_{in}$') found by deconvolution of x measured by micro-probe 1 (located downstream the injection point) with a perfect Laplace input step function ('perfect $\bar{x}_{in}$'). Example is given for an experiment at steady, continuous flow (Re_o = 0 and ν = 1.94 ml/min). I: system cleaning; II: feeding of the system with the tracer; III: stabilisation of concentration in the system through the recirculation and oscillatory mixing; IV: RTD experiment running. ○ micro-probe 1 response, ■ micro-probe 2 response. Line in (b) represents: 'generated $\bar{x}_{in}$' = 'perfect $\bar{x}_{in}$'.

For a perfect pulse disturbance the RTD can be expressed (Nauman and Buffham 1983; Wen and Fan 1975) by means of the cumulative distribution function evaluated from the tracer response at the exit (x_{out}) of the SPC tube

$$F_t = 1 - \frac{x_{out}(t)}{x_{in}} \qquad F_\theta = 1 - \frac{x_{out}(\theta)}{x_{in}} \tag{5.1}$$

Where θ is the dimensionless residence time and is give by $t/\bar{t}$. The reduced distribution function results from derivation

$$E_t = \frac{\mathrm{d}F_t}{\mathrm{d}t} \qquad E_\theta = E_t\,\bar{t} \tag{5.2}$$

Moments are used to characterise RTD functions in terms of statistical parameters. The mean residence time ($\bar{t}$) is given by the first moment of the distribution function

$$\bar{t} = \int_0^{x_{in}} t \frac{1}{x_{in}} \mathrm{d}x \tag{5.3}$$

and the spread in residence time (characterised by the variance, σ^2) is given by (Westerterp et al. 1963)

$$\sigma^2 = \int_0^{x_{in}} t^2 \frac{1}{x_{in}} \mathrm{d}x - \bar{t}^2 \tag{5.4}$$

RTD curves were interpreted/modelled in this study by direct comparison with responses of four different single-phase models (derived from the mass balance to the reactor system), representing intermediate mixing behaviours: (1) series of CSTRs without interactions (Levenspiel 1972), (2) plug flow with axial dispersion (differential reactor (Mecklenburgh and Hartland 1976)), (3) series of CSTRs with backflow (stagewise reactor (Mecklenburgh and Hartland 1976)) and (4) PFR and CSTR in series (Levenspiel 1972). The plug flow with axial dispersion and the tanks-in-series with backflow models consider the backflow of fluid, which is absent in the other two models. The characteristic model parameters are: number of tanks-in-series (N_{tis}), dimensionless axial dispersion number (P_D), backmixing coefficient (G) and volume-fraction of PFR (V_R/V), respectively. In particular, the stagewise reactor model is appreciated to represent the RTD due to its natural physical analogy with the SPC geometry. In an ideal situation (good radial mixing and no axial dispersion), each cavity would behave as a small CSTR, thus N_{sw} (the number of stages, as described in Mecklenburgh and Hartland (1976)) was defined as equal to 26 (the number of cavities in the 350-mm-long SPC tube).

Analytical solutions for RTD are simply derived from the mass balance equation in the Laplace domain. Furthermore, as shown in more detail in the text, the integral convolution of non-ideal washout response

(i.e. transformation to Laplace's domain) is a direct prediction of the system conversion ($\overline{X}$) for a single-phase reaction. Model parameters are also easily extracted if a direct comparison is done in Laplace's domain, where the system response can be simplified as illustrated in Figure 5-4; z_1 and z_2 are the dimensionless distances of probes to inlet and equal to 0.04 and 1.0, respectively.

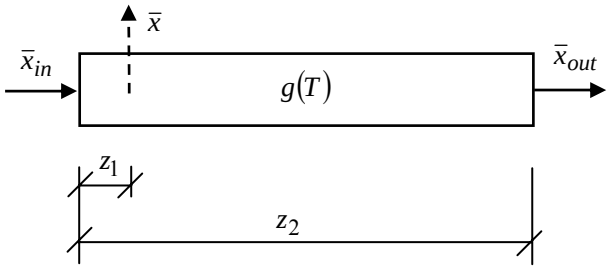

Figure 5-4. Schematic of the SPC configuration for RTD experiments, as seen in Laplace's domain.

The Laplace inlet, step injection function ('generated $\bar{x}_{in}$', determined from deconvolution of the integral convolution, $\bar{x}$, of the tracer concentration measured with micro-probe 1, i.e. measured at z_1 = 0.04) was confirmed to reproduce faithfully the ideal step function for all tested values of v, as demonstrated in Figure 5-3(b) (the 'generated $\bar{x}_{in}$' fits the ideal pulse, i.e. $\bar{x}_{in} = C_0/T$, with a deviation lower than 0.04 % and cross-correlation coefficient r^2 = 0.9999). Because different methods for estimation of model parameters may lead to significant differences of best-fitted model parameters (Froment and Bischoff 1990), two methods were used in these study: (*i*) fitting of the moments ($\bar{t}$ and σ^2) with the moments of the function $\bar{x}_{out}$; (*ii*) best-fitting of the numerical Laplace transform $g(T)$ to the experimental transfer function $g_{out}(T)$, where $g_{out}(T) = \bar{x}_{out}/\bar{x}_{in}$ and $\bar{x}_{in} = C_0/T$ (perfect step function). Transfer functions for each single-phase model may be found elsewhere (Mecklenburgh and Hartland 1976). For comparison purposes, values of P_D and N_{tis} were also estimated by direct nonlinear regression to time domain solutions (F_θ-diagram) of plug flow with axial dispersion model and tanks-in-series model (both defined by Levenspiel 1972), respectively. All these and further methods for estimation of model parameters are discussed in detailed elsewhere (Froment and Bischoff 1990).

Best fitting of F_θ-diagrams consisted in the minimization (least squares) of the difference Δ_1 between the theoretical response (F_θ) and the experimental response (F_θ^{out})

$$\Delta_1 = \int_0^{\infty} \left\{ F_\theta - F_\theta^{out} \right\}^2 \mathrm{d}\theta \tag{5.5}$$

while the best-fitting of the numerical Laplace transfer functions was based on the minimization of difference Δ_2

$$\Delta_2 = \int_{0.5\,T_{ref}}^{2T_{ref}} \left\{ g(T) - g_{out}(T) \right\}^2 \mathrm{d}T \tag{5.6}$$

The selected value for T_{ref} was 2.0, after a study of its effect over the values of the parameters to be estimated (results not shown).

5.2.2 RTD of liquid phase in the novel meso-reactor

The experimental rig used for study of RTD within the continuous meso-reactor is shown in Figure 5-5. A continuous liquid-flow rate was supplied with a syringe pump (allowing a very precise, steady flow) into the mixing chamber, through a non-return valve. Reactor volume was kept under pressure (differential pressure = 0.5 bar) to avoid formation of bubbles which could limit the RTD measurements.

Experiments were run in the meso-reactor at four hydraulic residence times (τ), comprising τ = 5 to 60 minutes – see

Table **5-1**) and at four fixed situations of OFM: *i*) steady flow, i.e. Re_o = 0; *ii*) 10 Hz and 1.0 mm, Re_o = 312; *iii*) 10 Hz and 2 mm, Re_o = 625; *iv*) 6 Hz and 3.5 mm, Re_o = 657.

Through-the-wall OD of single-phase flow was monitored via three reflectance optical micro-probes (FCR-7UV200, the same as micro-probe 2) connected to a multi-channel optic spectrometer system (Avantes, Eerbeek, The Netherlands). Micro-probes were fitted to three sampling ports in U-bends, along the reactor length, perpendicularly to the liquid pass. Backplane was provided with a clear-white background, which together with a perpendicular light (passed from a Halogen light source through a set of optical fibres) allowed monitoring the OD of single-phase in an optical flow cell like configuration.

An injection port installed in the mixing chamber allowed a sharp pulse (Dirac delta function, δ(t)) of dye tracer (Indigo carmine, x_{in} = 0.2 kg/m^3) near the physically closed-inlet tube boundary. For each

experiment, 0.2 mL of dye tracer was injected for 2 seconds, giving a maximum relative injection time of 0.7 %. In the context of overall RTD, this approximates the ideal Dirac-δ function. Generally, the injection pulses were remarkably reproducible (injection amount of tracer as well as shape of the inlet pulse).

Dye tracer concentration was determined from the detected intensity of OD for a wavelength scan. Light absorbance (A) measured by each of the three micro-probes was calibrated at six increasing concentrations of tracer in the range of x = 0 - 20 mg/l. The linear relationship A versus x obtained for each probe is summarised in Figure 5-6. Distilled water and room temperature (20 °C) were used in all experiments.

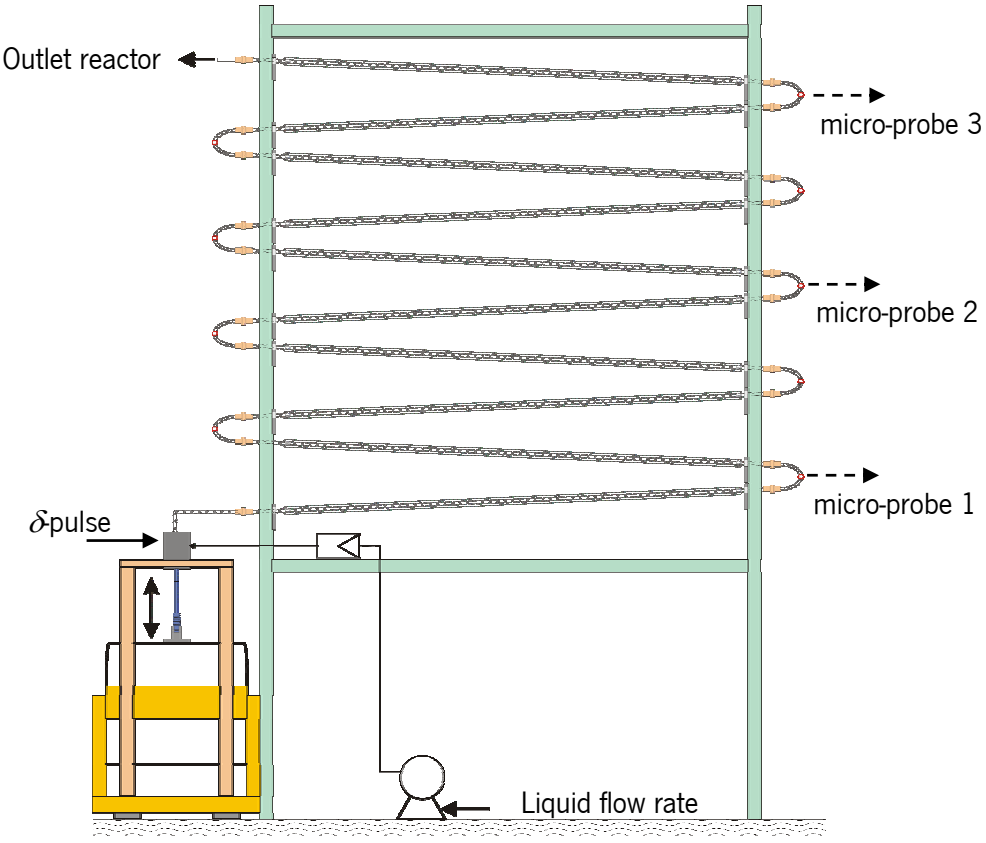

Figure 5-5. Experimental apparatus used for RTD studies in the novel continuous meso-reactor.

Table 5-1: Conversion between mean flow rate (ν), superficial liquid velocity (u_{LS}), net flow Reynolds number (Re_n) and hydraulic residence time (τ) for the meso-reactor experiments.

v [ml/min]	2.28	4.57	13.70	27.40
u_s [cm/s]	0.19	0.39	1.16	2.33
Re_o [-]	9	19	56	113
τ [min]	60	30	10	5

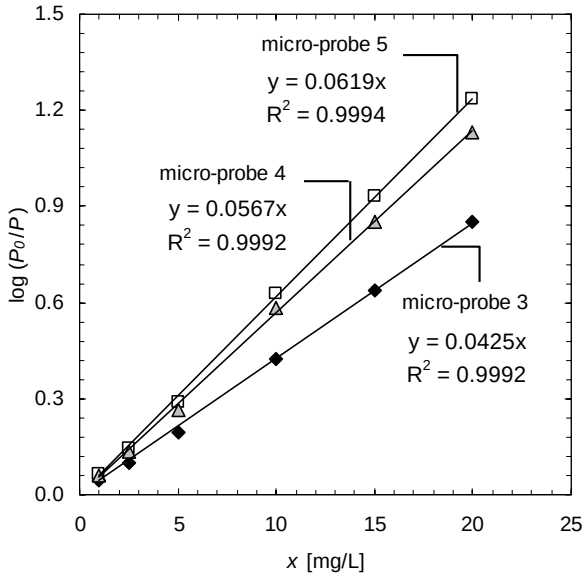

Figure 5-6. Light absorbance (A = log (P_o/ P)) measured by micro-probes 3, 4 and 5 at dye tracer concentration (x) of 0 to 10 mg/L.

5.2.3 Mixing times for batch operation of the novel micro-bioreactor

A batch 350-mm-long SPC tube (micro-bioreactor) was fixed vertically and 0.2 ml of the tracer with a concentration of 0.5 kg/m^3 of Indigo carmine was injected at the top of the reactor. Operational volume was about 4.5 ml. Fluid oscillation was started (at time t = 0) and the tracer concentration inside the SPC tube was on-line monitored at the top cavity (the same cavity where injection was performed) using the transmission dip optical micro-probe until a steady (constant) value was attained. The optical probes were connected to a multi-channel optic spectrometer (AvaLight-2048, Avantes, Eerbeek, The Netherlands). Readings were made at each 1/9th of a second and each three consecutive readings were averaged resulting in experimental points available at each 1/3rd of a second. The response of the fibre-optical system was highly linear in the used range of tracer concentrations. The time required to achieve a specified level of uniformity, U, where 0<U<1, was defined as the mixing time, t_U.

5.2.4 Numerical simulations of RTD for steady flow in the SPC tube geometry

Numerical simulations with the Computational Fluid Dynamics (*CFD*) technique were performed where an accurate prediction of the distribution of residence times was sought. It has been previously reported by Reis et al. (2005) and Harvey et al. (2003) that a 2D-axisymmetric model may show a good agreement of simulated flow patterns at smooth oscillation conditions (low fluid oscillation amplitudes). For further details about CFD model please refer Reis et al. (2005). The ability of such model to predict the RTD of the liquid phase was tested at steady flow and different continuous flow rates (v), using Fluent software (Fluent Inc, New York, USA).

5.3 Results and discussion

5.3.1 Analysis of RTD of liquid phase in the micro-bioreactor

Several experiments were run at increasing net flow rate (v) in order to test the effect of v on the RTD within the SPC tube. The intended mean residence times for future applications are in the order of minutes to hours. This requires very small v, namely in the order of few millilitres per minute. Thus, RTD was studied for superficial liquid velocities (u_{LS}) (where $u_{LS} = 4v/\pi d^2$) of 0.18 to 2.34 cm/s, or net flow Reynolds numbers (Re_n) of 8 to 102. Correspondence between v, $u_{LS} = 4v/\pi d^2$ and $Re_n = u_{LS}\,\rho\, d/\mu$ is shown in Table 5-2.

Table 5-2: Correspondence between superficial liquid velocity (u_{LS}), liquid flow rate (v) and net flow Reynolds number (Re_n). All values are based on d = 4.4 mm.

v [ml/min]	1.67	1.93	2.98	5.60	10.83	21.30
u_{LS} [cm/s]	0.18	0.21	0.33	0.61	1.19	2.34
approx. Re_n [-]	8	9	14	27	52	102

Figure 5-7 represents the normalised through-the-wall distribution (i.e. E_θ versus θ) for increasing u_{LS}. Comparison with RTD for pure-convective laminar flow (Danckwerts 1953) (such flow is obtained in very viscous fluids) is also presented, which is given by:

$$E(\theta) = \frac{1}{2\theta^3} \tag{5.7}$$

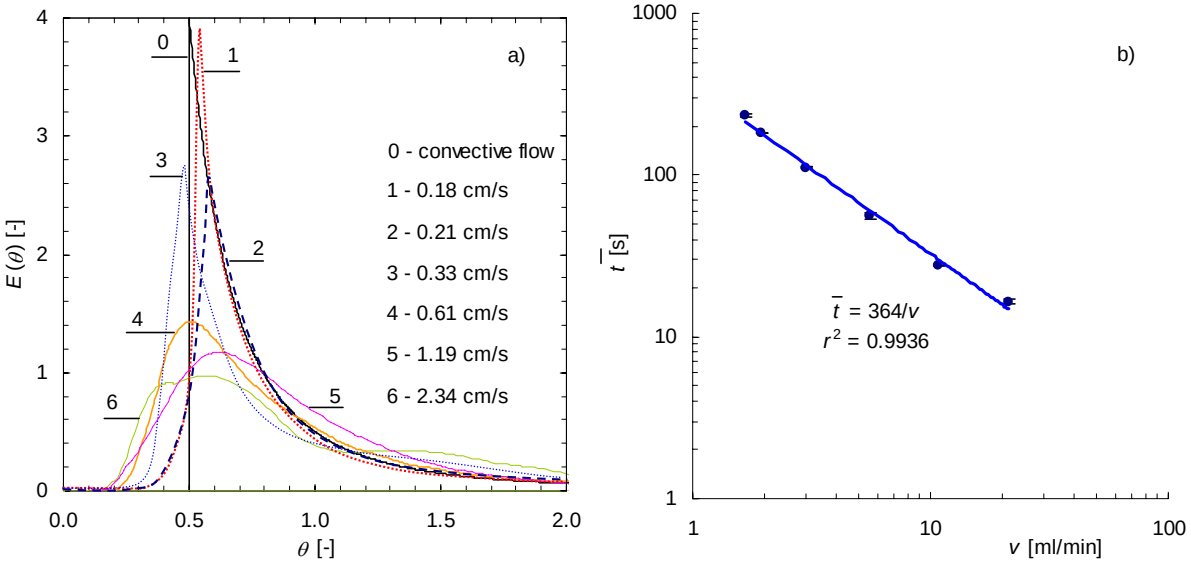

Figure 5-7. (a) Reduced RTD curves for different superficial liquid tube velocities (u_{Ls}) (in cm/s) and comparison with the pure-convective flow (Danckwerts 1953); (b) mean tracer residence time ($\bar{t}$) as a function of inlet liquid flow rate (v).

Figure 5-7a shows that laminar liquid flow in SPC tube is convective at very small u_{LS}, namely at a u_{LS} = 0.18 cm/s (i.e. Re_n = 8), considering a perfect step-down input. At such flow conditions, the reduced RTD curves are very to the residence distribution given by Equation (5-7). Nevertheless, increase of u_{LS} for values above 0.21 cm/s (i.e. Re_n > 9) leads to wider E_θ-distributions, with significant deviations from convective laminar flow. In such cases, a significant part of the fluid elements leaves the SPC tube at a θ < 0.5, while another substantial fraction of fluid elements stays in the tube for longer times than the mean dimensionless residence time, i.e. θ > 1. These conclusions are supported by the observation of longer

tails in Figure 5-7a and also by the observed 'short-circuits', which are related with the fact that the most part of tracer flows (at high ν) through the central streamlines of SPC tube (results not shown).

The reduced distribution functions shown in Figure 5-7a were normalised by the mean residence time, $\bar{t}$, which was found to be inversely proportional to ν in the form of $\bar{t} \propto 1/\nu^{1.0}$, as seen in Figure 5-7b thus being proportional to τ (because $\tau \propto 1/\nu$). This demonstrates that $\bar{t}$ is not significantly affected by the nature (convective or dispersive) of flow generated within the SPC tube at steady, laminar flow conditions.

The improvement of RTD through the OFM

Improvement of RTD in the SPC tube was sought through oscillatory flow mixing (OFM). Several experiments were run at 20 different combinations of f and x_o, between 0-20 Hz and 0-3 mm, respectively, and a fixed ν = 1.94 ml/min. All experiments were repeated and demonstrated (Figure 5-8a) very good agreement between them. The minimum Re_o tested (excluding the experiments at Re_o = 0) was 41, with f = 3 Hz and x_o = 0.5 mm.

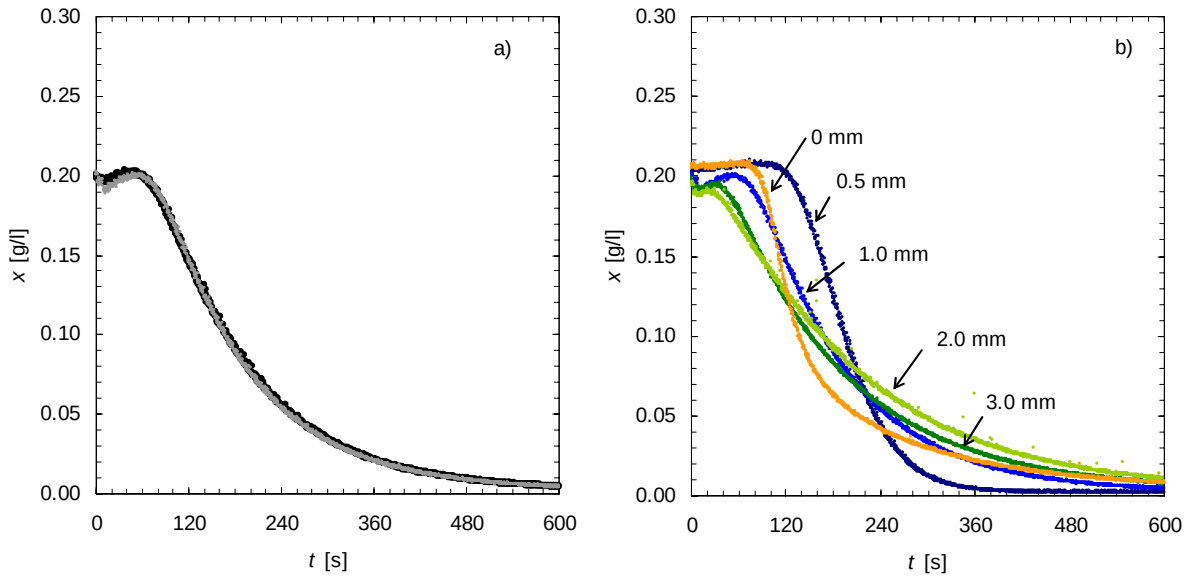

Figure 5-8. Tracer response curves at the outlet of a 350-mm-long SPC tube at f = 20 Hz and ν = 1.94 ml/min. (a) Repeatability of two different experiments (x_o = 1 mm); (b) Experimental data for x_o of 0, 0.5, 1.0, 2.0 and 3.0 mm.

Figure 5-8b demonstrates the very stable signal obtained at increasing x_o, at a constant f = 20 Hz and v = 1.94 ml/min. Some fluctuations of micro-probe signal were observed mainly at high f and x_o due to bubbles interference. The reciprocal fluid motion promoted the release of dissolved gas in the water stream with the consequent formation of bubbles. However, such fluctuations did not affect the quality of data.

It has been observed in the experiments under OFM (results not shown) that the through-the-wall concentration measured with the micro-probe 2 is in fact a flux-averaged concentration (i.e. mixing cup) due to the improvement of radial mixing achieved with the OFM. Moreover, as the reciprocating fluid motion improves the mixing within each cavity of the SPC tube, the local tracer measurements with the micro-probe 1 turn out into flux-averaged measurements (i.e. mixing-cup). According to Nauman and Buffham (1983) only the mixing-cup measurements provide the true residence time distribution, thus this experimental setup allows the acquisition of true RTDs in SPC tube. Such mixing, however, is not occurring across the system boundaries, therefore keeping intact the assumption of closed-closed boundaries.

None of the four single-phase flow models are in fact of the same type as (accordingly Briens et al. 1995) none of them attempt to describe the actual flow structure but, instead, characterises the velocity fluctuations and the backflow by using two parameters: the average residence time ($\bar{t}$) and a characteristic number (model parameter). Figure 5-9 shows $\bar{t}$ determined for all the tested combinations of x_o and f, using Equation (5) discretised according to the Simpson's rule. It was found that $\bar{t}$ is approximately constant for all tested combinations of x_o and f (mean $\bar{t}$ = 200 $\pm$ 7), with a small enhancement (8 - 10 %) for the higher tested Re_o (i.e., x_o = 3 mm and f = 15-20 Hz). This means $\bar{t}$ is not variable in the SPC geometry for the different tested combinations of f and x_o and the fixed value of v, making possible the direct correlation of each model parameters found at different OFM conditions.

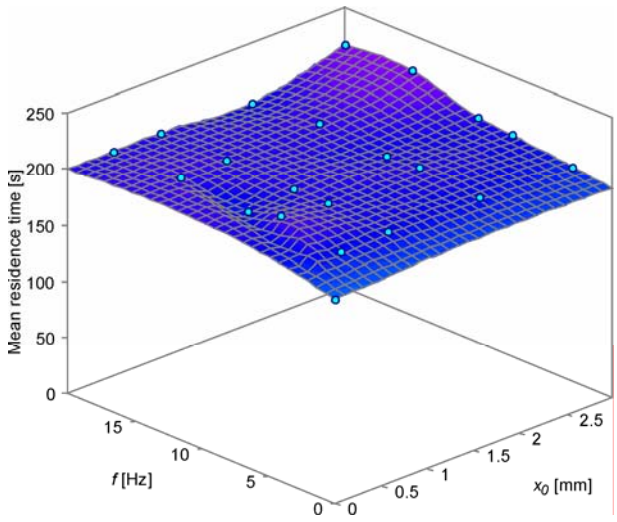

Figure 5-9. Average mean residence times of the tracer in a 350-mm-long SPC tube as a function of fluid oscillation frequency (f) and amplitude(x_0) for a net flow rate (ν) of 1.94 ml/min.

Figure 5-10a and Figure 5-10b show the evolution of cumulative dimensionless concentration of tracer (F_θ-diagrams) detected in the internal location (with the micro-probe 1) and at the tube outlet (with the micro-probe 2) with the experimental θ, for two experiments performed at the lower (41) and higher (1,629) values of Re_o, respectively (estimated values of N_{tis} and P_D for both Re_o situations are also presented). Figure 5-10c and Figure 5-10d presents the fitting of non-ideal outlet response to the transfer functions of the considered models (with parameters N_{tis}, P_D, G and V_R/V) for the experiments represented of Figure 5-10a and Figure 5-10b, respectively. Model parameters (in particular N_{tis} and P_D) demonstrated to be sensitive to the estimation method. Differences were more evident for highly back-mixed flow (Figure 5-10b and Figure 5-10d).

It is observed in Figure 5-10 that operation of SPC tube at very smooth fluid oscillation conditions (low x_0 and f) makes the RTD narrower (Figure 5-10a), with the system flow approaching the ideal flow case of a PFR. On the other hand, the increase of f and x_0 to 20 Hz and 3 mm (Figure 5-10b), respectively, makes the RTD moving towards the ideal flow case of completely back-mixed reactor (i.e., a CSTR). The approach to PFR behaviour is related with the generation of vortex rings due to flow separation on the constriction-walls of SPC tube in comparison with the steady flow situation (with a consequent improvement of radial mixing, thus minimizing fluid dispersion), whereas the approach to CSTR behaviour is related with the convective mixing in the direction of flow (Westerterp et al. 1963) (produced by the axial propagation of

vortex rings), in accordance with the previous fluid mechanics studies on the same SPC tube (Reis et al. 2005).

The combined effects of SPC tube geometry, v, f and x_0 on flow patterns modification was captured by a new dimensionless parameter, I. For the case of axial dispersion model (with the respective model parameter P_D), the parameter I_{PD} is defined as

$$I_{P_D} = \frac{P_{D,osc}}{P_{D,0}} \tag{5.8}$$

In this particular case, I_{PD} quantifies the improvement of estimated value of P_D for each experiment performed under OFM (i.e., $P_{D,osc}$), in relation to the mean-value of P_D obtained in the experiments at a steady flow (i.e., $P_{D,0}$) in the SPC tube; the later is used as the reference to measure that improvement. Thus, values of $I_{PD} > 1$ mean an increase of convection in relation to dispersion (i.e. towards the ideal flow in a PFR) in reference to the steady flow reference, while $I_{PD} < 1$ represents a decrease in convection/dispersion ratio (in the direction of ideal flow in a CSTR).

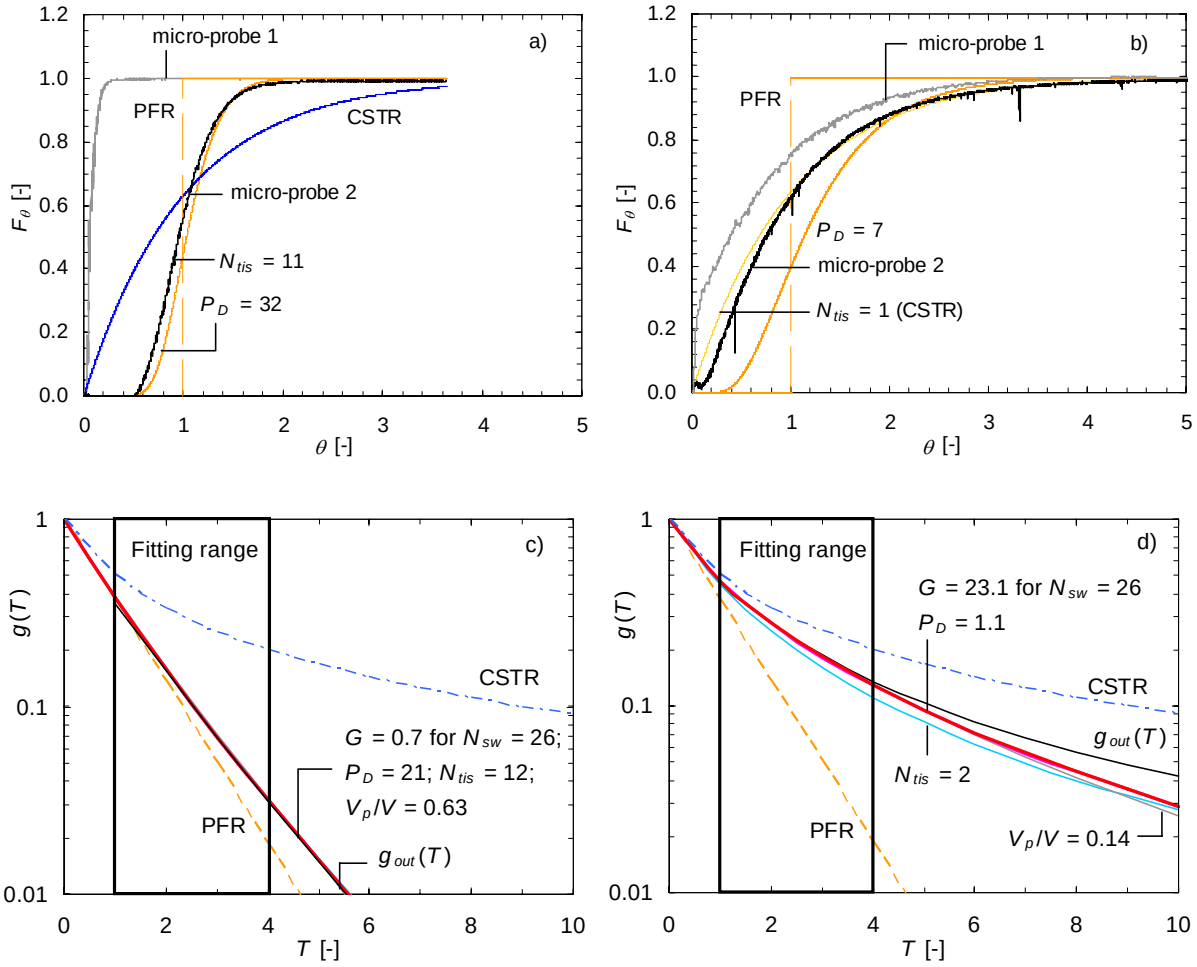

Figure 5-10. Details of best-fitting of cumulative dimensionless concentration of tracer (F_θ-diagram) and transfer function $g(T)$ to single-flow models. (a) and (b) shows parameters N_{tis} and D_P estimated through direct comparison of F_θ-diagrams (Levenspiel 1972) and using best-fitting criteria of Equation (5-5); (c) and (d) shows model parameters estimated by best-fitting (with Equation (5-6) of transfer function $g_{out}(T)$ to transfer function $g(T)$ derived by mass balance of single-phase models. Fluid oscillated at: (a) and (c) 3 Hz and 0.3 mm; (b) and (d) 20 Hz and 3 mm. Net flow rate of 1.94 ml/min. Note that some curves are coincident. The fitting range refers to the integration intervals in Equation (5-6).

Figure 5-11 shows maps of I_{PD} calculated for different tested combinations of f and x_0, using values of P_D estimated through various methods.

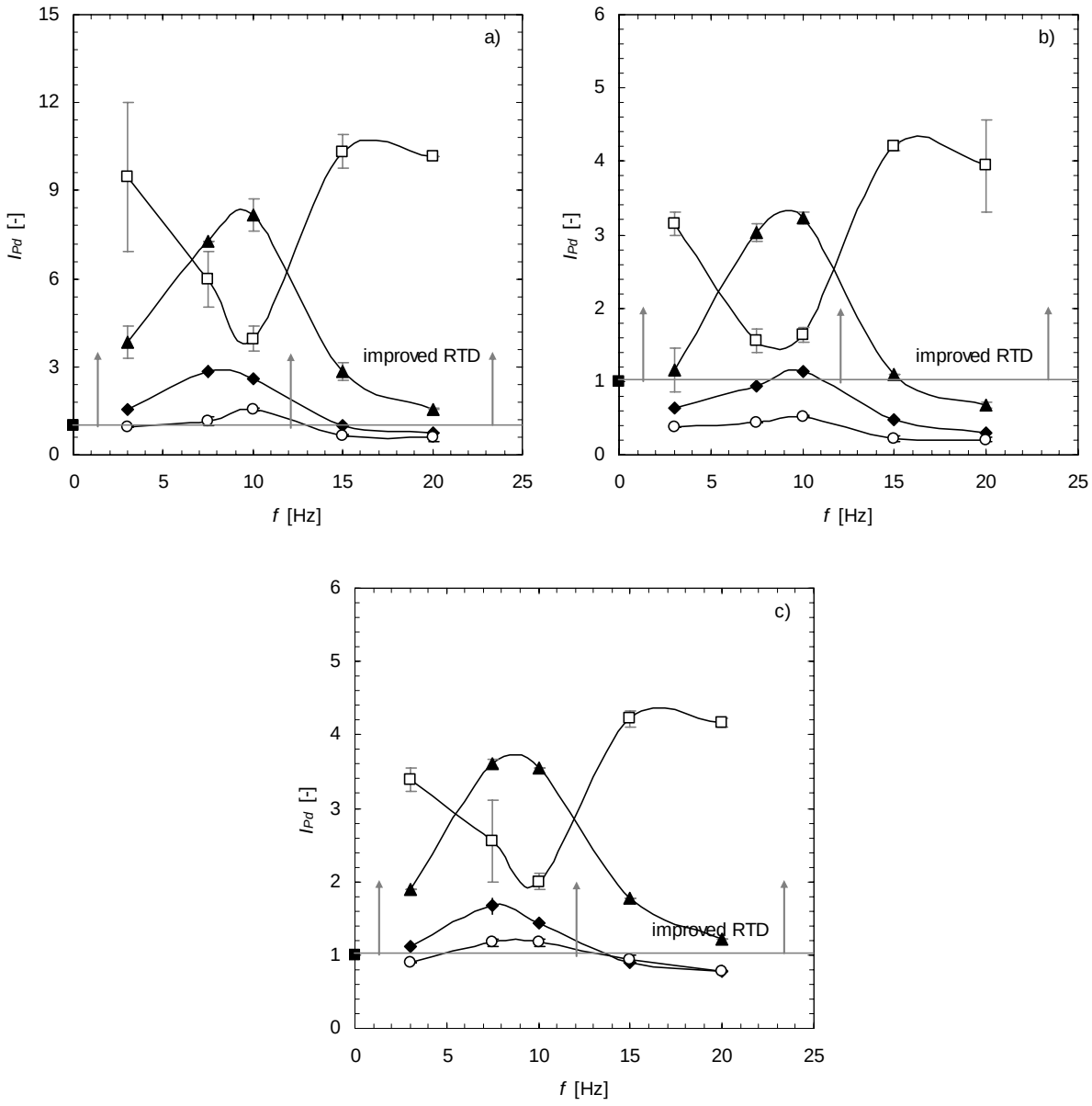

Figure 5-11. Effect of fluid oscillation frequency (f) on the dimensionless number I_{PD} for constant fluid oscillation amplitudes (x_0), using values of D_p estimated by different methods. ■ 0 mm, □ 0.5 mm, ▲ 1.0 mm, ♦ 2.0 mm, ○ 3.0 mm; (a) I_{PD} found by the moments method; (b) I_{PD} found by fitting of $g_{out}(\bar{t})$ to $g(\bar{t})$; (c) I_{PD} found by direct nonlinear regression of the analytical equation of axial dispersion model presented by Levenspiel (1972) Vertical error bars represent spread (standard deviation) of values for different experiments. Net flow rate of 1.94 ml/min. Area not shaded corresponds to the region where an improvement of RTD is achieved, i.e. where dispersion becomes less significant than convection.

Figure 5-11 shows similar values of I_{PD} derived from the values of P_D estimated by best-fitting of the washout data to the numerical Laplace transform (Figure 5-11b) and to the Levenspiel's equation (Levenspiel 1972) (Figure 5-11c), although higher values (~160 %) of I_{PD} were obtain by the moments technique (Figure 5-11a) in comparison with the values extracted by comparison of transfer function (Figure 5-11b). Such differences were found to be related with the underestimated (~57 %) values of $P_{D,0}$ by the moment's method (the value of $P_{D,0}$ affects directly the calculated values of I_{PD}, as shown in Equation (10)). The estimated absolute values of $P_{D,osc}$ were in fact in accordance for the different experiments (less than 15 % between the three parameter estimation methods), thus the high values of I_{PD} obtained are due to the wrongly extracted values of in $P_{D,0}$. Estimation of model parameters (and of P_D, in particular) was found very sensitive to the estimation method, especially for RTD at steady flow (mean $P_{D,0}$ = 6.03, with a standard deviation of 3.14). This is because the purely convective laminar flow (Levenspiel 1972) obtained at ν = 1.94 ml/min (as previously discussed in Figure 5-7a) generates an E_θ-diagram with a raising edge at θ = 0.5, followed by a long tail (up to θ = 3), which is difficult to fit with models that generate symmetrical E-curves with the flow approaching the tubular flow. Although the moments technique has the main advantage of easy computation from numerical integration this is overcome by serious drawbacks, as the emphasis given to the data in the tail of C-curves, which are commonly not very accurate and lack of knowledge of the quality of the fit of the model (Froment and Bischoff 1990). This undermines the confidence in the results obtained by this technique. On the other hand, the direct comparison of transfer functions (Figure 5-11b) gives the most stable results. A main advantage of this estimation method is the lower emphasis on the tail, as mentioned elsewhere (Froment and Bischoff 1990).

The values of I_{PD} found by comparison of F_θ-diagrams (Figure 5-11a) were found proportional (slope = 1.07; r = 0.983) to those found by comparison of transfer function (Figure 5-11b), however the first were translated by ~0.6. Such deviation is presumably related with the used boundary conditions of Levenspiel's equation (Levenspiel 1972), namely the through-the-wall measurements and the open-open boundaries.

Correlation between the model parameters of various single-phase models for OFM

Figure 5-12 presents the correlations of P_D with the estimated model parameter G (Figure 5-12a), N_{tis} (Figure 5-12b) and V_p/V (Figure 5-12c), accordingly the various estimation methods. Continuous lines in

Figure 5-12 represent the cross-correlation to the parameters estimated by fitting of moments and fitting of $g(\bar{t})$ to $g_{out}(\bar{t})$ of the models. Equations for all represented trend lines are summarised in Table 5-3.

Figure 5-12a) and Table 5-3 show that tanks-in-series with backflow and the plug flow with axial dispersion models are inter-convertible (Westerterp et al. 1963). The correlation G versus P_D estimated by direct fitting of transfer function very closely matches the theoretical one (Mecklenburgh and Hartland 1976), (obtained from mass balance of respective models) however when the estimation is made by direct comparison of moments, the deviation in slope may reach 12 %.

The tanks-in-series model (without backflow) (N_{tis}) fitted very well the experimental data (from micro-probe 2) at the lowest x_0 (as previously seen in Figure 5-10a) but it failed to represent the non-ideal washout response of SPC tube at the highest values of x_0 as shown in Figure 5-10b. This is undoubtedly related with the observed high backflow rate (improved at thigh x_0) which is not considered by that model.

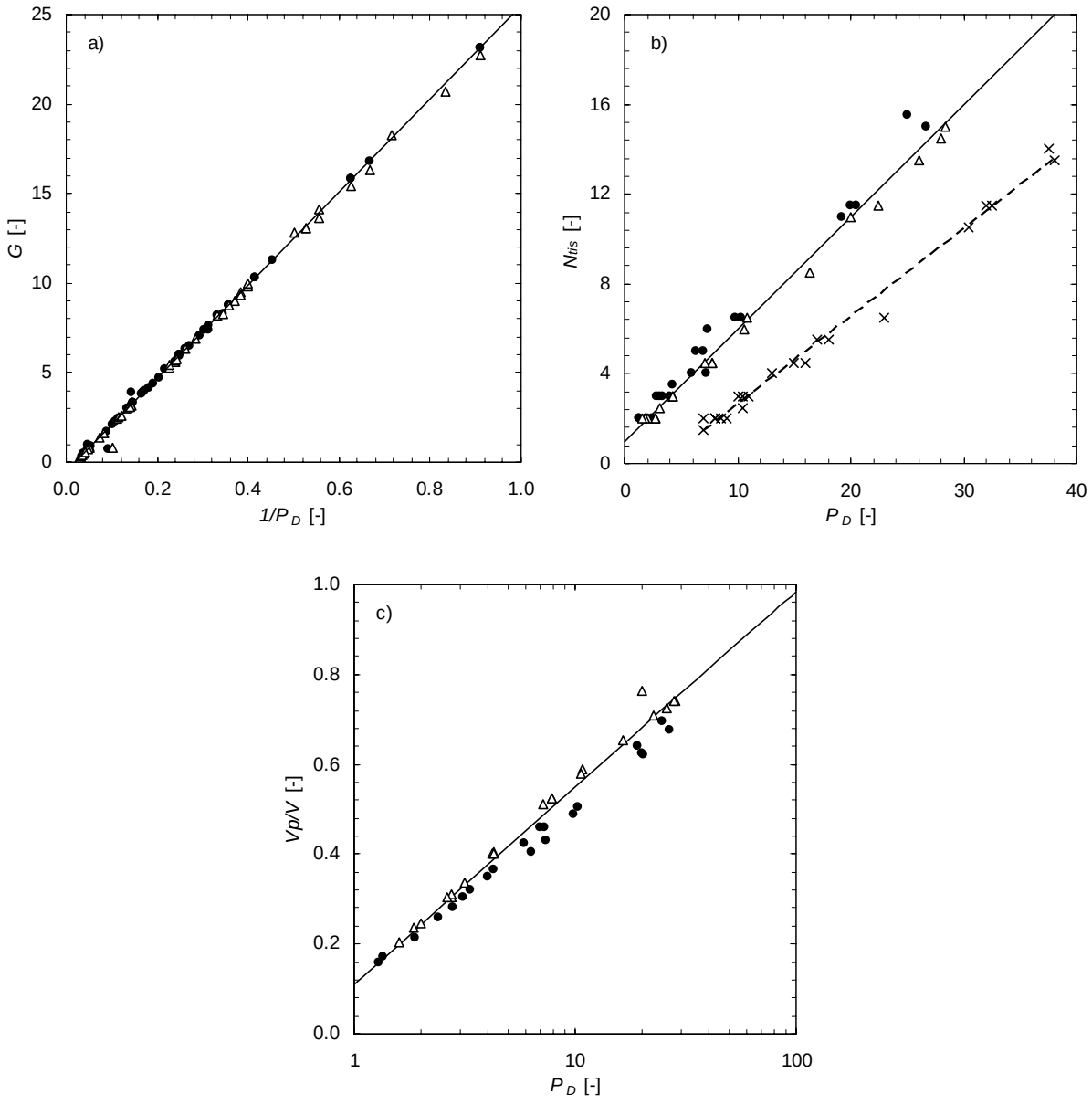

Figure 5-12. Cross-correlation of dimensionless axial dispersion number (P_D) with the backmixing (G), the number of tanks-in-series (N_{tis}) and the volume-fraction of ideal PFR (V_p/V), according the values of parameters estimated through different methods. (a) Linear plot of G vs. $1/P_D$; (b) linear plot N_{tis} vs. P_D; (c) log-plot of V_P/V vs. P_D; model parameters estimated through △ fitting of moments, ● fitting of $g_{out}(\bar{t})$ to $g(\bar{t})$ of the model. × fitting of F_θ-diagrams (Levenspiel 1972). Line in (a) represents the theoretical relation $G + 0.5 = N_{sw}/P_D$ (Mecklenburgh and Hartland 1976); continuous line in (b) represents the theoretical (Westerterp et al. 1963) relation: $N_{tis} = 0.5\ P_D + 1$; dash line in (b) shows relation of N_{tis} with the values of P_D estimated by fitting of experimental F_θ-diagram to that given by the Levenspiel's equation (Levenspiel 1972).

Table 5-3: Equations for cross-correlation of dimensionless axial dispersion number (P_D) with the backmixing (G), the number of tanks-in-series (N_{tis}) and the volume-fraction of PFR (V_p/V), using the values of parameter estimated through various techniques.

Parameter estimation method	G versus P_D	N_{tis} versus P_D	V_p/V versus P_D
Moments fitting	$G = 22.84 / P_D + 0.23$ $r = 0.9975$	$N_{tis} = 0.49 P_D + 0.90$ $r = 0.9976$	$V_p/V = 0.19 \text{ Ln}(P_D) + 0.12$ $r = 0.9900$
Fitting of $g(\bar{t})$	$G = 26.06 / P_D - 0.55$ $r = 0.9993$	$N_{tis} = 0.53 P_D + 1.17$ $r = 0.9881$	$V_p/V = 0.17 \text{ Ln}(P_D) + 0.11$ $r = 0.9936$
Fitting of F_θ-diagram	-	$N_{tis} = 0.39 P_D - 1.28$ $r = 0.9913$	-
Global trend	$G \approx 26/ P_D - 0.5$ (from Mecklenburgh and Hartland 1976).	$N_{tis} \approx 0.5 P_D + 1$ (from Westerterp et al. 1963)	$V_p/V \approx 0.2 \text{ Ln}(P_D) + 0.1$

For large values of N_{tis} (e.g. Figure 5-10a) the RTD curve becomes increasingly symmetrical and approaches the ideal flow case of PFR. Thus, a comparison between the tanks-in-series and the plug flow with axial dispersion models becomes possible (Figure 5-12b). Table 5-3 summarises the correlation of N_{tis} versus P_D, using the model parameters values found by the various methods, as well as the equation of overall trend shown in Figure 5-10a. Both the methods of fitting of moments and of direct comparison of transfer functions give a similar correlation, with a global trend (Westerterp et al. 1963): $N_{tis} = 0.5 P_D + 1$, and a cross correlation coefficient, $r = 0.9927$. This means that $P_D = 0$ for $N_{tis} = 1$, while $N_{tis} = 26$ for $P_D = 50$ (a typical PFR threshold (Levenspiel 1972)), and confirms the existence of a general tendency of each cavity to behave as a single stage (number of cavities in SPC tube = 26). Nevertheless, the method of direct comparison of F_θ-diagrams gives a negative value (-1.28) for N_{tis} when $P_D \rightarrow 0$ (i.e. for an ideal CSTR), which is not of physical understanding. This is presumably related either with a typical disadvantage of this parameter estimation method (the objective functions often have local, in addition to global, minima and/or long ridges because of correlation between the parameters, both of these causing difficulties in finding the real axial dispersion parameter (Froment and Bischoff 1990)) or with an inappropriate fitting of Levenspiel's equation (Levenspiel 1972).

Figure 5-12c shows correlation between the model parameters V_p/V and P_D. A high r (> 0.99) was obtained (Table 5-3) and a an overall trend was detected: $V_p/V \approx 0.2 Ln(P_D) + 0.1$, with $r = 0.9854$ and $V_p/V \rightarrow 1$ for values of $P_D \geq 100$.

In summary, the various non-ideal, single-phase flow models tested together with different methods for estimation of model parameters clearly demonstrated that the introduction of OFM (in comparison with the steady flow) successfully allows the control of RTD in a 350-mm-long SPC tube (i.e., the micro-bioreactor) to ideal flow cases of either PFR and CSTR, through the control of convection/dispersion fraction. In particular, the different estimation methods show a least favourable 4.2 to 10.2–fold increase of P_D, a 3.1 to 7.5–fold increase of N_{tis}, a 1.6 to 2.5–fold increase of V_p/V and an 83 to 96 % decrease of G in approaching the flow behaviour of an ideal PFR. On the other hand, the ideal completely back-mixed limit was better approximated at x_0 = 3 mm and f = 20 Hz. This resulted in a 60, 80 and 60 % decrease of N_{tis}, P_D and V_p/V, respectively, and a 5.5-fold increase of G. Table 5-4 summarises the calculated values of I_{Ntis}, I_{PD}, I_G and $I_{Vp/V}$ (where $I_{Ntis} = I_{Ntis,osc}/I_{Ntis,0}$, $I_G = I_{G,osc}/I_{G,0}$ and $I_{Vp/V} = I_{Vp/V,osc}/I_{Vp/V,0}$, in analogy with I_{PD}, defined in Equation (5-8)) clarifying the better approach of non-ideal flow to convective (i.e., ideal PFR) and dispersive (i.e., ideal CSTR) systems, achieved through introduction of OFM (i.e. in comparison with the steady flow situation).

Table 5-4: Summary of maximum and minimum values of dimensionless parameters I_{Ntis}, I_{PD}, I_G and $I_{Vp/V}$ obtained with the introduction of OFM, towards the ideal convective or dispersive systems, respectively. * Ideal flow case for convective flow is a PFR; ideal case for dispersive flow is a CSTR.

	Convective system*				Dispersive system*			
Maximum or minimum values	I_{Ntis}	I_{PD}	I_G	$I_{Vp/V}$	I_{Ntis}	I_{PD}	I_G	$I_{Vp/V}$
Moments fitting	7.5	10.3	0.04	2.5	1.0	0.6	1.9	0.7
Fitting to $g(T)$	3.1	4.2	0.13	1.6	0.4	0.2	5.5	0.4
Direct regression of F_θ-diagram	7.0	4.2	-	-	0.8	0.8	-	-

Prediction of conversion for a first-order homogeneous reaction in the SPC tube

RTD may be directly applied to predict chemical reactor behaviour as follows (Westerterp et al. 1963):

$$\overline{C}_A = \int_0^\infty C_A(\theta) E_\theta d\theta \qquad (5.9)$$

which becomes for a first-order reaction

$$1 - \overline{X} = \frac{\overline{C}_A}{C_{A_{in}}} = \int_0^\infty e^{-k\theta} E_\theta d\theta \qquad (5.10)$$

The above integral is in fact the definition of Laplace transform with respect to θ of E_θ, but with k substituted by T. Thus, the exit concentration for a first-order reaction is found from the transforms of any E_θ by merely replacing k for T, as shown elsewhere (Froment and Bischoff 1990). The 1st-order reaction is the only case where the reduced residence curve (E-diagram) gives all the information required for the prediction of the conversion of a homogeneous isothermal reaction; for high order reactions an extra information of mixing (micromixing or macromixing) is required.

Figure 5-13 compares the prediction of conversion ($\overline{X}$) for a 1st-order isothermal reaction running in the SPC tube for: *i*) steady flow in SPC tube (i.e. $Re_o = 0$) at $\nu = 1.94$ ml/min; *ii*) unsteady flow, at two combinations of f and x_o with maximum I_{PD}, i.e. $x_o = 1$ mm and $f = 10$ Hz, $x_o = 0.5$ mm and $f = 15$ Hz; *iii*) unsteady flow at $x_o = 3$ mm and $f = 20$ Hz (i.e. maximum backmixing); *iv*) completely segregated flow (CSTR); *v*) tubular flow (PFR).

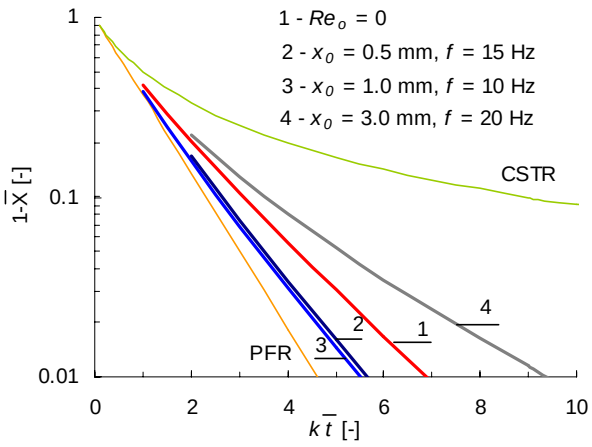

Figure 5-13. Predicted deviation on conversion ($\overline{X}$) in a 350-mm-long SPC tube (micro-bioreactor) for a homogeneous, isothermal chemical reaction as determined directly from the E_θ-diagram in the SPC tube, at $\nu = 1.94$ ml/min.

Analysis of Figure 5-13 was based on deviations of $\overline{X}$ from PFR for a reference value of $k\bar{t}$ = 4, as summarised in Table 5-5.

Table 5-5: Predicted conversions and respective deviations from conversion in a PFR, calculated from the experimental RTD (E_θ-diagrams) in the 350-mm-long SPC tube, for a continuous, homogeneous, isothermal first-order reaction, at ν = 1.94 ml/min.

Per cent conversion for	CSTR	3 mm, 20 Hz	Re_o = 0	0.5 mm, 15 Hz	1 mm, 10 Hz	PFR
Predicted conversion	80.0	92.0	94.4	96.6	97.0	98.2
Difference in conversion	-18.2	-6.2	-3.8	-1.6	-1.2	0

Table 5-5.shows that deviation of predicted ($\overline{X}$) for the SPC geometry is very small (1.2 %) in relation to $\overline{X}$ obtained for a perfect flow reactor. Even for the experiments with the maximum backmixing tested in this study (i.e. 3 mm and 20 Hz) the predicted deviation is 6.2 %, which is about 1/3 of the reduction of $\overline{X}$ predicted for the completely segregated flow (i.e. in a CSTR). Actually, such small deviations are coupled with the good radial mixing and suspension in the SPC geometry (Reis et al. 2005), thus micro-bioreactor presents as a promising scale-down system for continuous screening tasks.

5.3.2 Analysis of RTD of liquid phase in the meso-reactor

Experiments carried out in the continuous meso-reactor allowed to assess the effect of τ at fixed values of Re_os. Figure 3 shows normalised E_θ-distributions for two values of τ (60 and 10 minutes), at increasing values of Re_o (i.e., from 0 to 639), monitored at three axial distances from meso-reactor inlet.

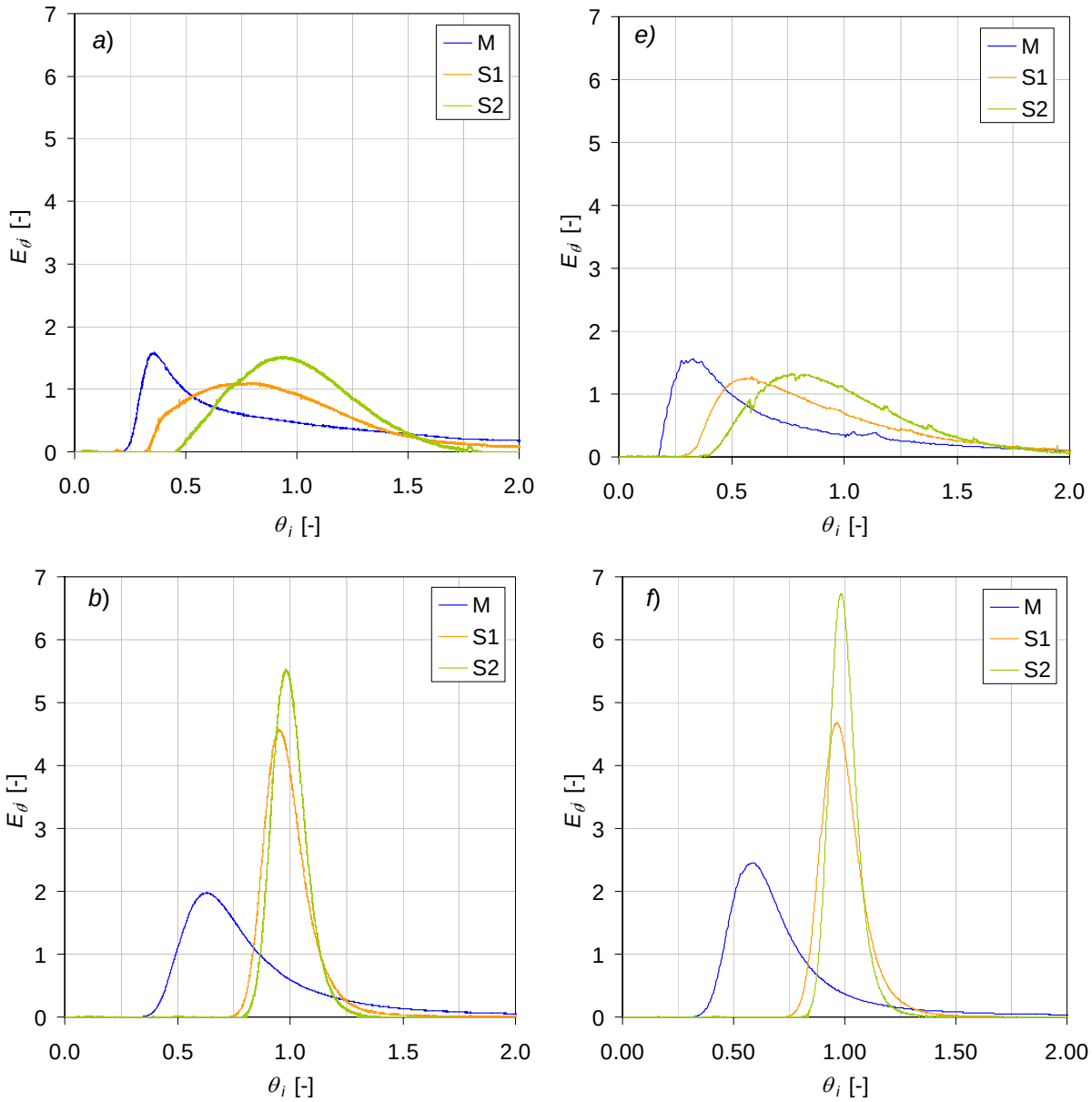

Figure 5-14. Reduced RTD curves at three axial distances of the meso-reactor, operated at eight combination of hydraulic mean residence times (τ) and oscillatory flow Reynolds number (Re_o). *M* – micro-probe 3; *S1* – microprobe 4; *S2* – microprobe 5; (a) τ = 60 min, steady flow (i.e. Re_o = 0); (b) τ = 60 min, x_o = 1 mm, f = 10 Hz, Re_o = 312; (c) τ = 60 min, x_o = 2 mm, f = 10 Hz, Re_o = 625; (d) τ = 60 min, x_o = 3.5 mm, f = 6 Hz, Re_o = 657; (e) τ = 10 min, Re_o = 0; (f) τ = 10 min, x_o = 1 mm, f = 10 Hz, Re_o = 312; (g) τ = 10 min, x_o = 2 mm, f = 10 Hz, Re_o = 625; (h) τ = 60 min, x_o = 3.5 mm, f = 6 Hz, Re_o = 657. Note that $\theta = t/\bar{t}$, where $\bar{t}$ was determined from tracer response in micro-probe 3 (i.e. located at the higher axial distance).

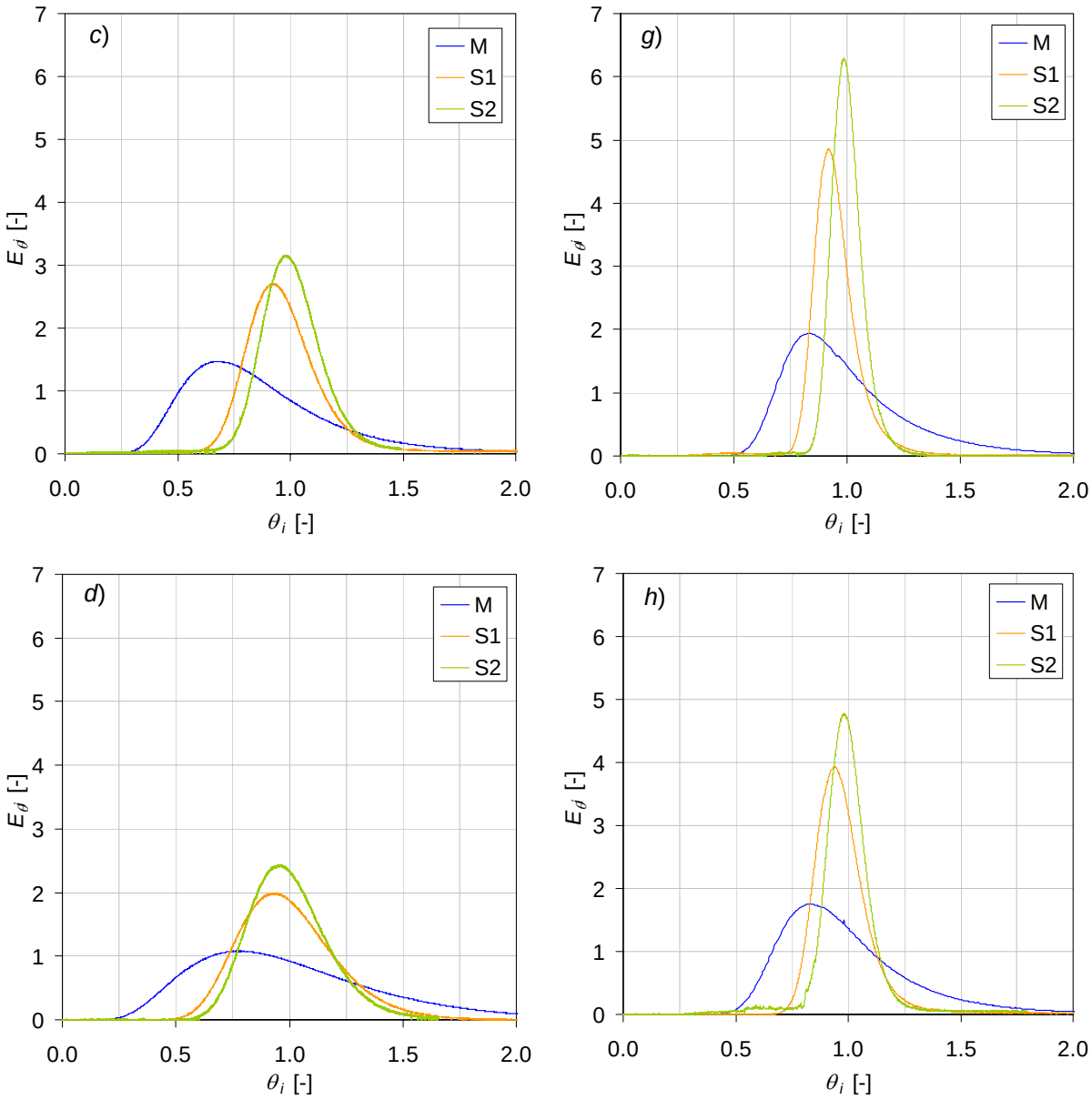

Figure 5-14. (Continued).

Figure 5-14a to Figure 5-14d show an improvement of RTD (as seen from the narrower E_θ-curves) for the higher τ = 60 min (and a respective ν = 2.28 ml/min) at the lower Re_o, in comparison with the RTD at continuous, steady flow. However, when τ is decreased by 6 times (τ = 10 min – Figure 5-14e to Figure 5-14h) the effect of f and x_o over the RTD becomes insignificant as all E_θ-curves monitored under OFM become very similar and very close to the narrowest one. This is well demonstrated by the direct comparison of estimated flow model parameters.

Figure 5-15a summarises the number of tanks-in-series (N_{tis}) extracted by direct comparison of experimental E_θ-distribution (only for micro-probe 5) with a cascade of tanks-in-series. Note that tanks-in-series model is not sensitive to the type of boundary conditions of the system, thus allowing the direct comparison of N_{tis} estimated for the 350-mm-long tube (micro-bioreactor). It is clear that increasing Re_n (in the range of 9-113) at unsteady flow conditions drives the RTD towards the plug flow in the SPC geometry (up to a maximum $N_{tis} \approx 125$). This is presumably related with the lower backflow of fluid elements at the higher v during the flow through the SPC tube. From all the studied combinations of v, f and x_0, it becomes clear that RTD is highly affected by f or x_0 only for low values of Re_n (i.e. $Re_n < 56$).

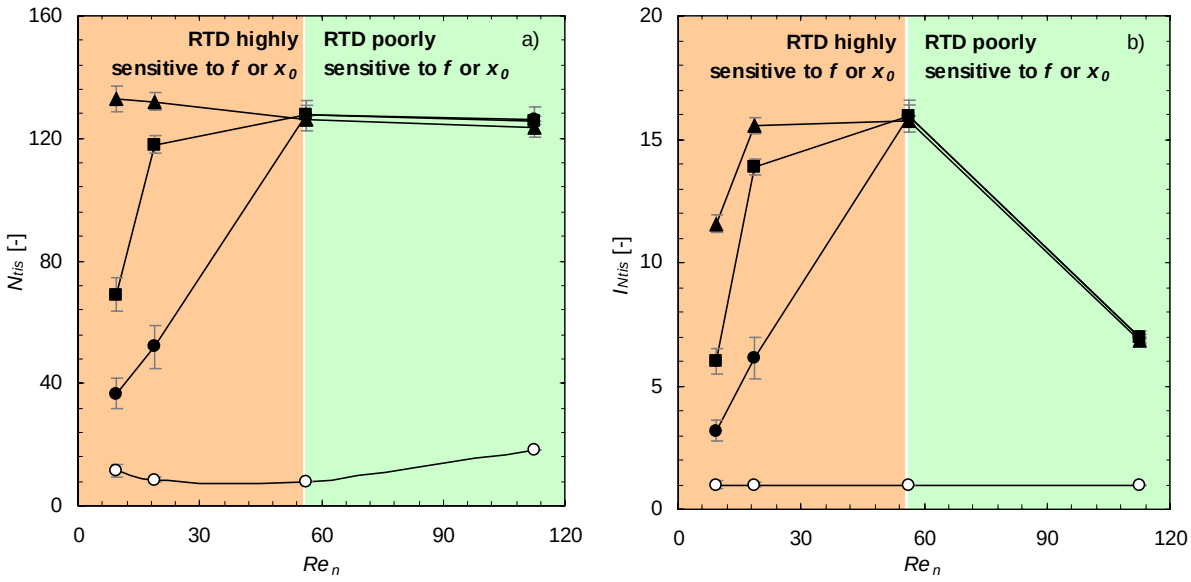

Figure 5-15. Number of tanks-in-series (N_{tis}) estimated by direct comparison of E_θ-curve of micro-probe 5 response for increasing values of net flow Reynolds number (Re_n). ○ Steady flow, i.e. $Re_o = 0$; ● $x_0 = 3.5$ mm, $f = 6$ Hz, $Re_o = 312$; ■ $x_0 = 2$ mm, $f = 10$ Hz, $Re_o = 625$; ♦ $x_0 = 1$ mm, $f = 10$ Hz, $Re_o = 657$. Error bars shows standard deviation of values extracted for different experiments.

In comparison with the steady flow (i.e. $Re_o = 0$), the increase of N_{tis} at OFM conditions (i.e. I_{Ntis}) becomes significant, as illustrated by Figure 5-15b. It is observed that I_{Ntis} is highly sensitive to both f and x_0 for low values of Re_n (below 56) and that I_{Ntis} improves with the increase of Re_n up to a critical value of $Re_n = 56$. Above that critical value, parameter I_{Ntis} decreases as a result of N_{tis} enhancement at steady, continuous flow (presumably due to flow reversing associated with the flow separation).

5.3.3 Determination of mixing times fro batch operation of micro-bioreactor at different combinations of f and x_o

Two hundred different experiments were carried out in batch mode and at different oscillation conditions. From the monitored concentration along the experimental time (Figure 5-16a) a mixing time parameter, t_U, was obtained. It is defined as the time to achieve a certain level of uniformity, U (usually 90, 95 or 99 %). However, a different approach allowed correlating t_U with U and an empirical mixing coefficient, k_m [T^{-1}]. A mass balance performed to the tracer concentration x in the cavity of the bottom of the tube (the cavity which is at farthest distance from the injection point) yields, after integration along the experiment time t

$$ln\left(\frac{1/x_{inf} - 1/x_i}{1/x_{inf} - 1/x_{ini}}\right) = -k_m t \qquad (5.11)$$

where x_{inf} is the concentration at infinite time, x_{ini} is the initial concentration and x_i is tracer concentration at time t_i. Equation (5-11) allows the determination of k_m directly from the experimental data. The main advantage of this procedure is that mixing times are not limited to defined levels of uniformity but to a wide range of U. Equation (5-11) works very well for $0.5 < U < 0.99$, with correlation coefficients, R, above 0.99 (results not shown here).

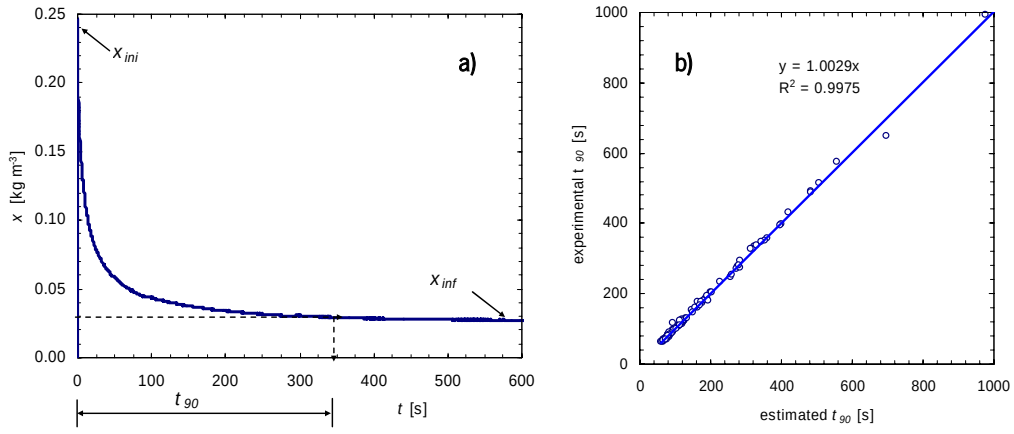

Figure 5-16. a) determination of mixing time t_{90} parameter from experimental data at 20 Hz and 1 mm; b) comparison of experimental t_{90} parameter with estimated values with Eq. (5-14).

As for the cavity at the top (where x_i was monitored) U is given by:

$$U = \frac{x_{inf}}{x_i} \tag{5.12}$$

it can be demonstrated that the general equation for t_U is:

$$t_U = -\frac{1}{k_m} ln\left[\frac{1-U}{1-x_{inf}/x_{ini}}\right] \tag{5.13}$$

When x_{inf} is very small when compared with x_{ini} (the most usual situation), the logarithm term simplifies to $ln(1-U)$.

In Figure 5-17 it is presented the variation of k_m with the x_0 and f in the studied range. It is clear that both x_0 and f affects k_m and thus the mixing time is in a non-linear way. The following dependency of t_U (in seconds) was obtained from experimental data fitting:

$$t_U = \frac{1}{0.0072\, ln\left(\frac{x_0^{2.35} f}{2.75}\right)} ln[1-U] \tag{5.14}$$

This equation is valid only for values that satisfies $x_0^{2.35} f > 2.75$ and are restricted to the SPC geometry. Otherwise, Eq. (5-14) cannot be applied and data from batch experiments (Figure 5-17) suggests that a near null axial dispersion is reached, thus approaching a plug flow behaviour.

The comparison of parameter t_{90} ($U = 90$ %) estimated from Eq. (5.14) with experimental values led to a maximum error of 5.7 % in all studied range of oscillation frequencies and amplitudes (0 to 20 Hz and 0 to 3 mm, respectively), showing a very good fit (Figure 5-16b).

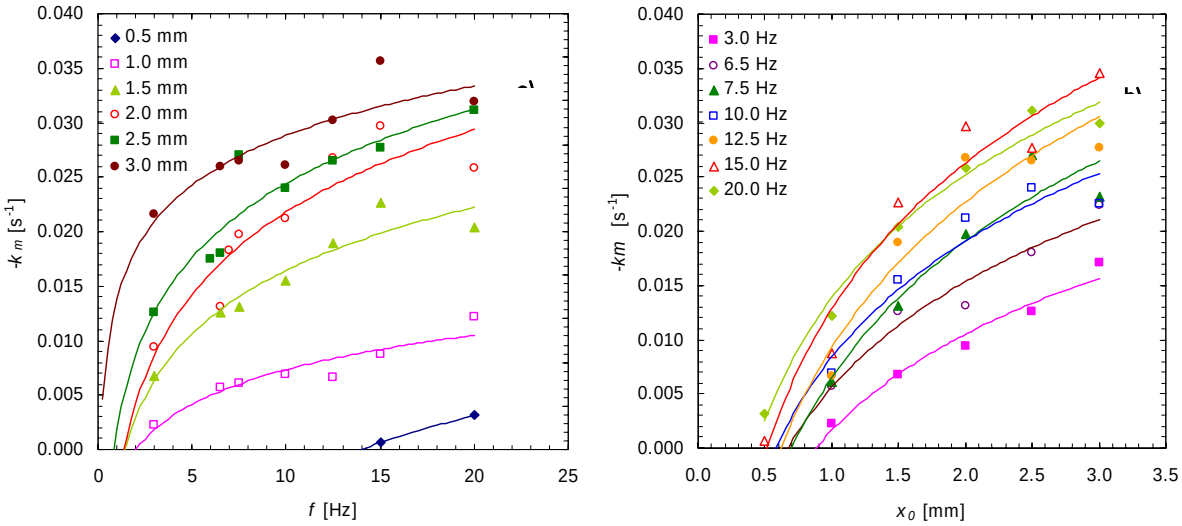

Figure 5-17. Variation of the mean values of mixing coefficient k_m with fluid oscillation (a) frequency and (b) amplitude at different oscillation conditions.

The mixing time correlation given by Eq. (5.14) shows that k_m is more sensitive to x_0 than f. Presumably, this relates with the effect that x_0 has on the nature of the eddies formed and thus dispersion along the tube. This confirms *PIV* observations and *CFD* simulations previously reported in Harvey et al. (2003) and Reis et al. (2005). The increase of f leads essentially to an increase of mixing intensity inside each cavity and thus not necessarily to an increase of the axial dispersion. This allows to conclude that in the screening reactor: *i)* the increase of x_0 (at constant f) leads essentially to an increase of the mixing length (thus increasing the axial dispersion) and *ii)* the increase of f (at constant x_0) leads essentially to an increase of the radial mixing. This has been shown with the RTD experiments.

5.3.4 Matching of numerical simulations of RTD in the SPC tube for steady flow

The effect of the flow rate on fluid dispersion was studied by performing experiments in the absence of oscillations (Figure 5-18). The mean residence times intended for future industrial applications are in the order of minutes to hours. This means very low flow rates, namely below 1 ml/min. Numerical simulations (Reis et al. 2005) showed that flow separation (development of counter flow, leading to vortex rings) occurs in the screening reactor at a Re_n about 10, i.e. for a flow rate of ca. 2 ml/min.

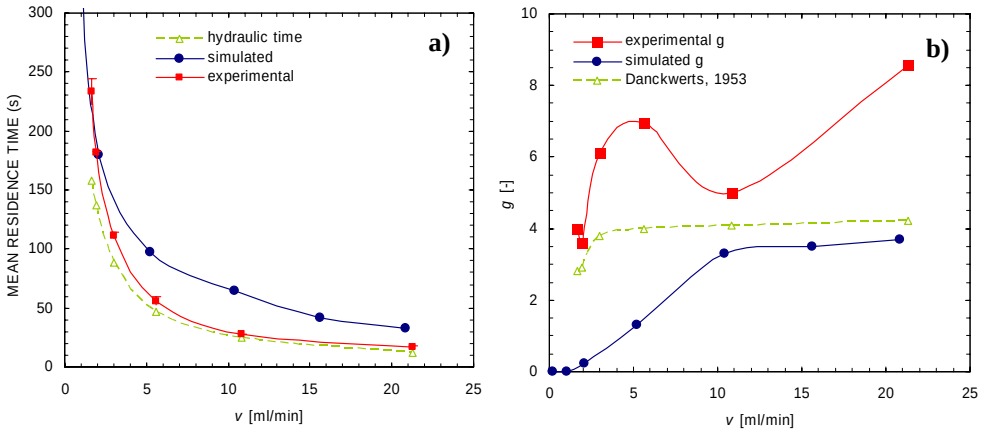

Figure 5-18. Effect of net flow rate over a) tracer mean residence time and b) backmixing, *g,* assuming a perfect step input at steady flow (no fluid oscillations). A comparison is presented between experimental (■) and simulated values (●) using a 2D-axisymmetric model.

Estimated values of backmixing *G* (by direct fitting of $g_{out}(\bar{t})$ to $g(\bar{t})$ of the tank-in-series model with backflow) were compared with the value of *G* predicted by the *CFD* simulations, using a 2D-axisymmetric model. A comparison with laminar flow in an unbaffled tube (with same mean internal diameter) is also shown (Danckwerts, 1953) in Figure 5-18. Differences between simulated and experimental results (Figure 5-18b) can be explained by differences in $\bar{t}$: knowing that *g* is a best fitted parameter based on the experimental dimensionless times ($\theta = t/\bar{t}$), differences between experimental and simulated $\bar{t}$ (Figure 5-18a) consequently led to different best fitted *g* (Figure 5-18b)). In fact, simulations using a 2D-axisymmetric model tend to over-estimate the mean residence time of the tracer (Figure 5-18a). This can be due to two different reasons: 1) used CFD model does not predict correctly the mixing process; 2) some tracer is lost through the symmetry axis boundary due to the nature of a 2-D axisymmetric model. In any case, used 2-D axisymmetry model has shown to be not suitable for *RTD* predictions. Strategies for matching of RTD simulations may involve the optimisation of time step or the use of a 3-D mesh (requiring extended computation times).

Estimated values of backmixing *G* were found higher than those values fitted to a *C-curve* of a laminar flow in a tube in the absence of oscillations. This means that the existence of constrictions contributes itself to an increase of the axial dispersion but such increase can globally be overcome eliminated when imposing the OFM component, as previously demonstrated by *RTD* of liquid phase.

5.4 Conclusions

This study has demonstrated that residence time distribution (RTD) of liquid phase in a small-scale tube geometry (whose inner walls are provided with smooth periodic constrictions – SPC tube) can effectively be controlled using oscillatory flow mixing (OFM).

RTD experiments performed in a 350-mm-long SPC tube (micro-bioreactor) in the presence of a laminar, steady liquid flow rate (ν) of 1.67-21.30 ml/min showed that flow is convective for ν = 1.67 ml/min, but becomes highly dispersive as values of $\nu \geq$ 2.99 ml/min are used.

Further experiments carried out at a continuous (ν = 1.94 ml/min) and unsteady (reciprocating) flow rate (f = 0 - 20 Hz; x_0 = 0 - 3 mm) demonstrated that macroscopic flow patterns within the SPC tube might be driven towards the ideal flow cases of either plug flow or completely back-mixed limits by correctly setting f and x_0. Macroscopic fluid mixing was quantified by comparing the non-ideal washout response data with the responses of various single-phase flow models (tanks-in-series with and without backflow, plug reactor with axial dispersion, and a combined model consisting of an ideal PFR and CSTR in series) where the respective flow model parameters (G, N_{tis}, P_D and V_P/V) were estimated by various methods.

The model parameters N_{tis}, P_D, V_P/V (e.g., estimated with the Laplace transfer functions) were increased up to 3.1, 4.2 and 1.6 times and G decreased up to 87 % when SPC operation was changed from steady to unsteady (reciprocating) flow at a ν = 1.94 ml/min, revealing an enhancement of convection/dispersion ratio in the OFM situation. On the other hand, maximum dispersive flow (achieved at x_0 = 3 mm and f = 20 Hz) resulted in a 60, 80 and 60 % decrease of modelled N_{tis}, P_D, V_P/V parameters, respectively, and a 5.5-fold increase of G.

The tanks-in-series model with backflow (i.e. stagewise reactor (Mecklenburgh and Hartland 1976)) is considered the one better representing RTD in the 350-mm-long SPC tube due to i) the physical analogy and ii) the ability of best fitting the non-ideal washout data with the backmixing parameter G.

Conversion ($\overline{X}$) predicted directly from the RTD for a first-order, homogeneous, isothermal, chemical reaction demonstrated that $\overline{X}$ in SPC tube may successfully approach the value obtained in a PFR, with a small deviation of 1.2 % (for a reference value of $k\bar{t}$ = 4). These promising results will support the design of scale-down systems based on the novel SPC geometry, addressing e.g. the continuous screening of homogeneous catalysts.

Further RTD experiments carried at unsteady flow in an array of 10 SPC tubes 800-mm-long (continuous meso-reactor) at v = 2.28 - 27.40 ml/min demonstrated that the effect of f and x_0 on RTD is highly reduced by operating at high values of v (ideally at v = 27.4 ml/min), presumably by decreasing the fluid backflow. In particular, the operation of meso-reactor at unsteady flow and a Re_n = 56 is appreciated as the macroscopic fluid mixing simultaneously meet two requirements of a convective system (i.e. PFR): i) maximum improvement of estimated tanks-in-series (N_{tis}) in relation to the steady flow in the SPC geometry; ii) expected single-phase flow conversion is practically not dependent of OFM (f or x_0). The coupling of OFM allowed an improvement of estimated number of tanks-in-series (without backflow) (as given by parameter I_{Ntis}) of ~16 times in relation to the steady flow.

Additionally, batch mixing data presented in terms of a mixing coefficient k_m in a 350-mm-long SPC tube (micro-bioreactor) has shown anticipated that mixing time depend of both oscillation amplitude and frequency and that oscillation amplitude has a stronger effect than frequency.

For last, the RTD experiments for steady flow reported in this paper offered the opportunity to compare experimental data with numerical simulations using Fluent software, but an incomplete agreement was achieved.

5.5 Notation

A	*light absorbance, dimensionless*
C_A	*concentration of chemical specie 'A', kg/m³*
d	*mean internal tube diameter, m*
d_0	*internal tube diameter in the constriction, m*
$\bar{d}$	*mean internal diameter, m*
D_z	*axial dispersion coefficient, m²/s*
E	*normalised tracer concentration, dimensionless*
f	*oscillation frequency, Hz*
F	*cumulative concentration function, dimensionless*
$g(T)$	*transfer function, dimensionless*
G	*backmixing ratio, dimensionless*
k_m	*mixing coefficient, s⁻¹*

h_p	*axial piston position, m*
I	*improvement parameter, dimensionless*
k	*first-order kinetic constant, 1/s*
L	*inter-constrictions distance, m*
N_{sw}	*total number of stages, dimensionless*
N_{tis}	*number of tanks-in-series, dimensionless*
P	*power radiation, W*
P_D	*axial dispersion number (= u_{LS} Z/D_z), dimensionless*
P_0	*power radiation for water, W*
r	*cross-correlation coefficient, dimensionless*
Re_n	*net flow Reynolds number, dimensionless*
Re_o	*oscillatory Reynolds number (= $2\pi f x_0 \rho d / \mu$, with x_0 in mm), dimensionless*
St_r	*Strouhal number, dimensionless*
t	*time, s*
$\bar{t}$	*mean residence time of the tracer, s*
T	*Laplace's variable, dimensionless*
U	*uniformity level (U = 0 to 1), dimensionless*
u_{LS}	*superficial liquid velocity, cm/s*
v	*volumetric flow rate, m^3/s*
V	*vessel volume, m^3*
V_p/V	*volume-fraction of PFR, dimensionless*
$w(t)$	*washout function, dimensionless*
x	*tracer concentration, kg/m^3*
$\bar{x}$	*Laplace's transform of the pulse response, dimensionless*
x_0	*oscillation amplitude, mm*
$\overline{X}$	*reaction conversion, dimensionless*
Z	*reactor length, m*
z	*dimensionless distance*

Greek symbols

α	*cross-free section area, dimensionless*

δ	*constriction length, m*
λ	*light wavelength, nm*
μ	*fluid viscosity, kg/(m s)*
θ	*dimensionless time = $t/\bar{t}$*
ρ	*density of the fluid, kg/m³*
σ^2	*variance, s²*
τ	*mean hydraulic time (= V/v), s*

Subscripts/superscripts

in	*incoming (x)*
out	*outgoing (x)*
osc	*oscillatory*
ref	*reference*
0	*steady flow*
t	*time*
θ	*dimensionless time*

5.6 References

Andersse AS, White ET. 1971. Parameter Estimation by Weighted Moments Method. Chemical Engineering Science 26(8):1203-&.

Boyer C, Duquenne AM, Wild G. 2002. Measuring techniques in gas-liquid and gas-liquid-solid reactors. Chemical Engineering Science 57(16):3185-3215.

Briens CL, Margaritis A, Wild G. 1995. A New Stochastic-Model and Measurement Errors in Residence Time Distributions of Multiphase Reactors. Chemical Engineering Science 50(2):279-287.

Danckwerts PV. 1953. Continuous Flow Systems - Distribution of Residence Times. Chemical Engineering Science 2(1):1-13.

Fitch AW, Ni X. 2003. On the determination of axial dispersion coefficient in a batch oscillatory baffled column using laser induced fluorescence. Chemical Engineering Journal 92(1-3):243-253.

Froment GF, Bischoff KB. 1990. Chemical Reactor Analysis and Design. New York: John Wiley & Sons.

Gangwal SK, Hudgins RR, Bryson AW, Silvesto.Pl. 1971. Interpretation of Chromatographic Peaks by Fourier Analysis. Canadian Journal of Chemical Engineering 49(1):113-&.

Harvey AP, Mackley MR, Reis N, Vicente AA, Teixeira JA. The fluid mechanics relating to a novel oscillatory flow micro reactor. Proceeding of the 4th European Congress of Chemical Engineering - ECCE4; 2003 21st - 25th September; Granada. p 0-6.4-004.

Hatch RT. 1973. Experimental and theoretical studies of oxygen transfer in the airlift reactor [PhD thesis]. Massachusetts: Massachusetts Institute of Technology.

Hewgill MR, Mackley MR, Pandit AB, Pannu SS. 1993. Enhancement of Gas-Liquid Mass-Transfer Using Oscillatory Flow in a Baffled Tube. Chemical Engineering Science 48(4):799-809.

Levenspiel O. 1972. Chemical reaction engineering. New York: John Wiley & Sons, Inc.

Lu W, Hwang S, Chang C. 1994. Liquid mixing in internal loop airlift reactors. Industrial Engineering and Chemical Research 33:2180-2186.

Mackley MR, Ni X. 1991. Mixing and Dispersion in a Baffled Tube for Steady Laminar and Pulsative Flow. Chemical Engineering Science 46(12):3139-3151.

Mecklenburgh JC, Hartland S. 1976. The Theory of Backmixing. New York: John Wiley & Sons, Inc.

Mills PL, Dudukovic MP. 1989. Convolution and Deconvolution of Nonideal Tracer Response Data with Application to 3-Phase Packed-Beds. Computers & Chemical Engineering 13(8):881-898.

Nauman EB, Buffham BA. 1983. Mixing in Continuous Flow Systems. New York: Wiley Intersciences.

Ni XW, de Gelicourt YS, Neil J, Howes T. 2002. On the effect of tracer density on axial dispersion in a batch oscillatory baffled column. Chemical Engineering Journal 85(1):17-25.

Ni XW, Gao SW, Pritchard DW. 1995. Study of Mass-Transfer in Yeast in a Pulsed Baffled Bioreactor. Biotechnology and Bioengineering 45(2):165-175.

Ni XW, Pereira NE. 2000. Parameters affecting fluid dispersion in a continuous oscillatory baffled tube. Aiche Journal 46(1):37-45.

Reis N, Gonçalves CN, Águedo M, Gomes N, Teixeira JA, Vicente AA. In press. Application of a novel oscillatory flow micro-bioreactor to the production of g-decalactone in a two immiscible liquid phase medium. Biotechnology Letters.

Reis N, Harvey AP, Vicente AA, Teixeira JA, Mackley MR. 2005. Fluid Mechanics and Design Aspects of a Novel Oscillatory Flow Meso-Reactor. Chemical Engineering Research & Design 83(A4):357-371.

Verlaan P, Vaneijs AMM, Tramper J, Vantriet K, Luyben KCAM. 1989. Estimation of Axial-Dispersion in Individual-Sections of an Airlift-Loop Reactor. Chemical Engineering Science 44(5):1139-1146.

Wen CF, Fan LT. 1975. Models for flow systems and chemical reactors. New York: Marcel Dekker.

Westerterp KR, van Swaaij WPM, Beenackers AACM. 1963. Chemical Reactor Design and Operation. New York: John Wiley & Sons.

Chapter 6 Correlating the macroscopic fluid mixing and axial dispersion with the fluid mechanics of the micro-bioreactor

This chapter is concerned with the evaluation of the magnitude of radial velocities in the micro-bioreactor in the presence of oscillatory flow mixing (OFM) conditions.

Particle Image Velocimetry (PIV) technique was used to obtain 2-dimensional velocity vector maps in a cavity centrally located in the SPC tube, at different combinations of fluid oscillation amplitude (centre-to-peak), x_0 and frequency, f. Macroscopic flow patterns were analysed at different stroke positions and throughout at least three consecutive oscillation cycles. Average values of velocities and standard deviation of radial and axial velocities were calculated from PIV vector data. Such calculations were performed in each velocity vector map (i.e. instantaneous-average V_{radial}, V_{axial}, σ_{Vx}, σ_{Vy}) and throughout the oscillation cycles (i.e. cycle-average $\overline{V}_{radial}$, $\overline{V}_{axial}$, σ_{radial}, σ_{axial}).

Maps of V_{radial} and V_{axial} were drawn and two cycle-average ratios determined: a ratio of cycle-average radial velocity over the axial velocity, $R_V = \overline{V}_{radial} / \overline{V}_{axial}$, and a ratio of macroscopic mixing based on the standard deviation in the radial over the radial velocities components, $R_S = \sigma_{radial} / \sigma_{axial}$.

It was found that both R_V and R_S may drive the macroscopic flow patterns in the tube towards either the ideal plug-flow or completely backmixed limits. In order to reduce deviations from plug-flow, both R_V and R_S should approach the ratio of mean internal tube diameter over the constrictions spacing, $\overline{d}/L$ = 0.294 for this particular SPC geometry. In addition, when operating at a constant $x_0 \approx 1$ mm, a critical value of ~3.9 for the products $R_V \cdot f$ and $R_S \cdot f$ marks a sudden transition between the ideal plug-flow and the backmixed behaviour. These findings were demonstrated by correlating R_V and R_S with the best-fitted coefficients expressing the axial dispersion coefficients (a dimensionless axial dispersion parameter, P_D backmixing coefficient, G and number of tanks in series, N_{tis}) and with a mixing parameter, k_m, respectively.

Keywords: oscillatory flow mixing; mixing enhancement; fluid mechanics; chaotic advection; periodically constricted tube; axial dispersion.

6.1 Introduction

The 4.4 mm internal diameter, smooth-walled, periodically constricted (SPC) tube (Reis et al., 2005) represents a step towards the scale-down design of conventional oscillatory flow reactors (OFRs). Constrictions are smooth rather than the sharp-edged baffles found in conventional OFRs, while holding a superior ratio baffle length to tube diameter, d/L and a higher constriction free-section, α. As applications of SPC tube geometry are foreseen both in batch and continuous operation mode the control of macroscopic fluid mixing within this tube is a *sine qua non* condition for e.g. the prediction of selectivity and conversion.

Fluid mixing within a SPC tube was evaluated directly from the macroscopic flow patterns, aspect by post-processing the magnitude of radial and axial velocities generated at different combinations of fluid oscillation amplitude centre-to-peak, x_0 and frequency, f. Velocity vector data previously obtained (Reis et al., 2005) by Particle Image Velocimetry (PIV) was mathematically manipulated to measure the velocity vector maps at different stroke positions and allowing the determination of instantaneous and cycle-

average properties at the tested range of f and x_o. Axial and radial velocities are correlated with the experimentally measured residence time distributions (RTDs) and mixing times studies (e.g. Reis et al., 2004).

6.2 Materials and Methods

Experimental setup

The 350-mm-long SPC tube (micro-bioreactor) geometry and the Particle Image Velocimetry (PIV) system were previously described elsewhere (Reis et al., 2005). This study addresses experiments carried out in batch mode at Re_o values between 85 and 630 (Table 6-1), covering the expected axisymmetric and non-axisymmetric regimes (Howes, Mackley, & Roberts, 1991; Mackley, 1991; Mackley & Ni, 1991; Mackley, Tweddle, & Wyatt, 1990).

Table 6-1: Experimental conditions (f, x_o and Re_o) used for PIV measurement of flow patterns in SPC tube (from Reis et al. 2005). Experiments run (a) are those performed at a constant value of $x_o \approx 1$ mm, while experimental run (b) comprises experiments performed at further values of x_o. u_{peak} is the maximum theoretical axial velocity of the fluid (i.e. equal to $2 \pi f x_0$), while $\overline{V}_{axial,theo}$ is the (theoretical) cycle-average axial velocity throughout a complete oscillation cycle (i.e. $\overline{V}_{axial,theo} = \int_{3/4f}^{5/4f} 2\pi f x_0 \cos(2\pi f t) \Big/ 1/2f$); these values will be used for comparison of experimental data in Figure 6-2 and Figure 6-9

	approx. x_0 [mm]	f [s^{-1}]	Re_o [-]	u_{peak} [mm s^{-1}]	$\overline{V}_{axial,theo}$ [mm s^{-1}]
(a)	1	4.1	117	26.6	17.4
	1	5.1	203	46.3	30.4
	1	10.1	259	59.0	38.7
	1	11.1	348	79.3	52.0
	1	15.1	430	98.0	64.3
	1	20.1	630	143.5	94.1
(b)	5	2.1	305	69.5	45.5
	4	1.1	116	26.4	17.3
	11	1.1	342	77.8	50.9
	3	2.1	168	38.2	25.0
	0.1	30.1	86	19.0	12.8

Post-processing of PIV velocity data

After building of velocity vector maps with VidPIV (using the procedure presented by Reis et al. 2005), velocity data was exported to an Excel spreadsheet. Then, vector data was filtered and averaged firstly for each velocity vector map (instantaneous-average) and then for all the velocity vector maps composing 3 consecutive full-oscillation cycles (cycle-average). Several parameters expressing the macroscopic mixing intensities in the cavity were determined. The procedure may be summarised as follows:

a) **The velocity vector data** were initially filtered out for the region corresponding to one single cavity of the SPC tube. Then, all velocity vectors $\vec{V}$ were decomposed into the radial (x) and axial (y) velocity components, such that $\vec{V} = V_x.\vec{i} + V_y.\vec{j}$, where $\vec{i}$ and $\vec{j}$ are the unitary vectors in the x and y direction, respectively (Figure 6-1a);

b) **Instantaneous-average velocities** and **standard deviations** were determined by averaging the velocity data in each velocity vector map as follows:

   a. **Cross-section weighted velocities** were determined by a mass balance across the surface (Perry, Green, & Maloney, 2002):

$$v_i = \frac{1}{A}\int_A v(t)dA \qquad (6.1)$$

   where A is the flow cross-section. Velocity vectors maps were mapped through the PIV technique with the same interrogation size (16 x 16 pixels), thus all cells were presenting the same size in both y and x directions and therefore no area-averaged integration of Eq. (6.1) was required and the calculation was reduced to the simple case of determining the average of a population of a finite number n of cells (Figure 6-1b). However, either the arithmetic mean or the Eq. (6.1) would lead to an averaged velocity expressed in relation to the mean diameter of the grid, i.e. about 3.82 mm ($\bar{d}$) rather than 4.40 mm (diameter of the tube in the straight zone, d). Therefore, the averaged velocity v_i found by Eq. (6.1) must be multiplied by a correction factor, $C_f = \left(\bar{d}/d\right)^2$ in order to express v_i in relation to the inlet cross section (with diameter d).

   By averaging all the axial vectors (V_y) in each velocity vector map an instantaneous-average axial velocity V_{axial} was obtained. The average of vectors with positive V_y and V_x components separately provides the instantaneous-average V^{pos}_{axial} and V^{pos}_{radial}, respectively,

while the average of vectors with a negative V_y and V_x components allowed the determination of parameters V^{neg}_{axial} and V^{neg}_{radial}, respectively.

b. **Standard deviations** of V_x and V_y (i.e. σ_{Vx} and σ_{Vy}, respectively) were determined as follows:

$$\sigma(t) = \sqrt{\frac{\sum_{i=1}^{n} n_i . v(t)_i^{\,2}}{N} - \bar{v}(t)^2} \qquad (6.2)$$

where n_i is the weight of the cross-sectional area or volume of the cell i, and was determined by dividing the cross-section by the minimum cross-section of the two-dimensional grid; $v(t)$ is the velocity value in the cell i, and $\bar{v}(t)$ is the area-average velocity value at the time instant t.

c) V_{axial} and V_{radial} were averaged throughout three consecutive complete oscillation cycles allowing the determination of a **cycle-average** axial velocity, $\overline{V}_{axial}$, and a cycle-average radial velocity, $\overline{V}_{radial}$ (Figure 6-1c). However, as fluid oscillations are a reversible process (i.e. with cycle-average equal to zero), the cycle-average values of positive and negative velocity components alone were firstly obtained, namely: $\overline{V}^{pos}{}_{axial}$, $\overline{V}^{neg}{}_{axial}$, $\overline{V}^{pos}{}_{radial}$ and $\overline{V}^{neg}{}_{radial}$ (Figure 6-1d). Afterwards, a ratio $R_v = \overline{V}_{radial} / \overline{V}_{axial}$ was determined by finding the mean value of the following ratios: *i)* $\overline{V}^{pos}{}_{radial} / \overline{V}^{pos}{}_{axial}$, *ii)* $\overline{V}^{pos}{}_{radial} / \overline{V}^{neg}{}_{axial}$, *iii)* $\overline{V}^{neg}{}_{radial} / \overline{V}^{pos}{}_{axial}$ and *iv)* $\overline{V}^{neg}{}_{radial} / \overline{V}^{neg}{}_{axial}$. This procedure might be simplified by using absolute values of V_x and V_y, but the presented procedure has the advantage of allowing to confirm (or not) the axisymmetry of flow patterns.

d) **Cycle-average standard deviation** of axial and radial velocities (i.e. σ_{axial} and σ_{radial}, respectively) were determined by applying Eq. (6.2) to all V_y and V_x data, respectively, and for all the velocity vector maps composing the three consecutive oscillation cycles of each experiment. This allowed to define another parameter, $R_S = \sigma_{radial} / \sigma_{axial}$.

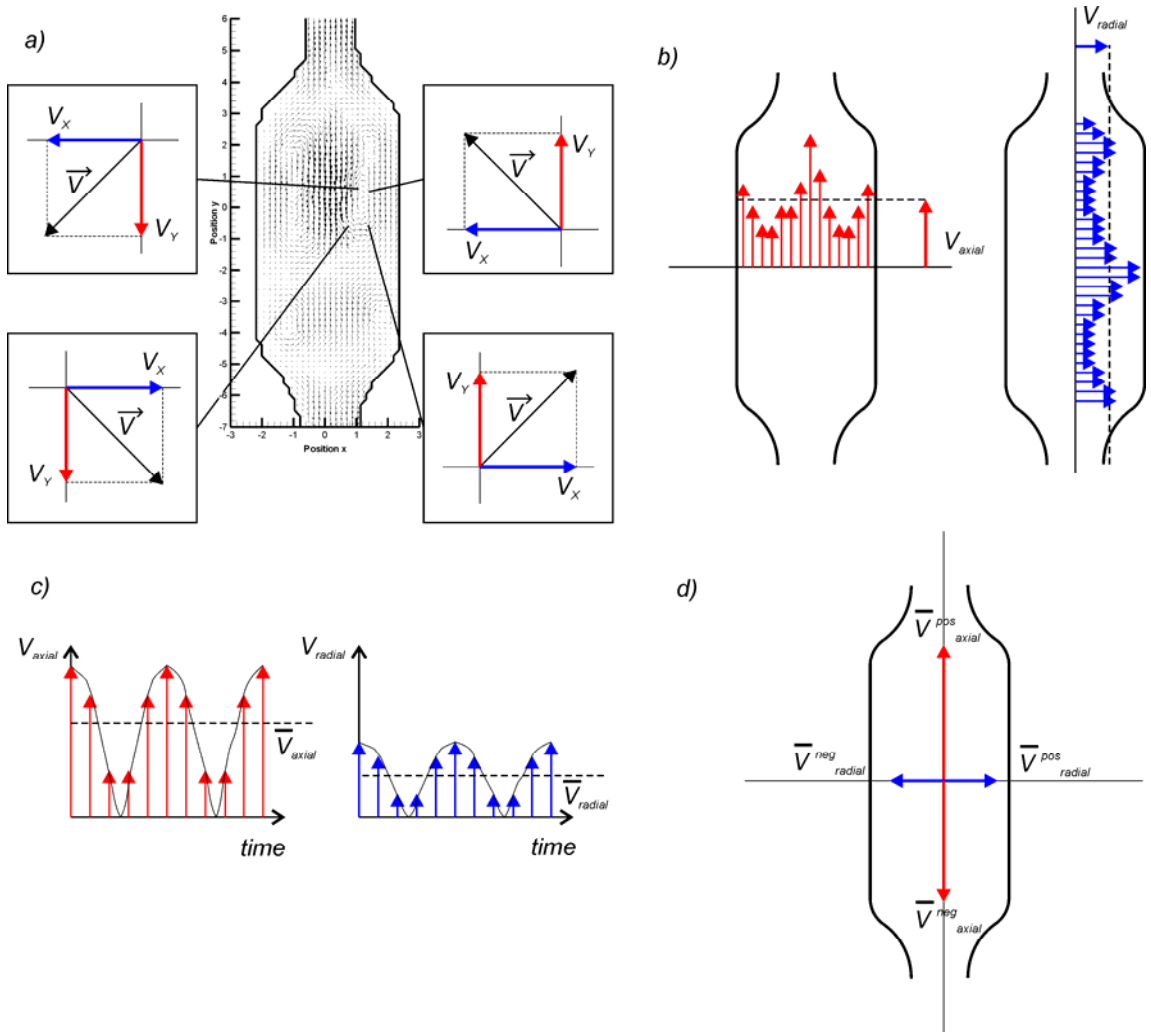

Figure 6-1. Illustration of the procedure applied to the determination of instantaneous-average (V_{radial}, V_{axial}) and cycle-average velocities ($\overline{V}_{axial}$, $\overline{V}_{radial}$).

6.3 Results and discussion

Analysis of the magnitude of radial velocities at increasing f and $x_0 \approx 1$ mm

Maps of instantaneous-average radial velocities (V_{radial}) throughout 3 complete fluid oscillation cycles are presented in Figure 6-2 as a function of instantaneous-average axial velocity, V_{axial}, for increasing f (from 4.1 to 20.1 s^{-1}) and a constant $x_0 \approx 1$ mm. Radial velocities are illustrated in terms of instantaneous-average of positive and negative V_x components, thus values of V^{pos}_{radial} and V^{neg}_{radial} are represented in the right hand and left hand side of Figure 6-2, respectively.

It is possible to observe in Figure 6-2 that the magnitude of both radial and axial velocities increases with the increase of *f*. The non-zero V_{radial} recorded at $x_0 \approx 1$ mm throughout the piston stroke, especially during flow reversal (when the piston velocity is equal to zero, i.e. $V_{radial} = 0$) is a consequence of the presence of eddy structures under OFM. The co-existence of constrictions and a periodic flow movement of fluid actually leads to significant changes in the flow patterns, compared to laminar flow: the oscillatory motion of fluid through the constriction leads to its detachment and reattachment at a neighbouring constriction, with formation of vortex rings in the zone between the constrictions (cavity), which act to reduce the boundary layer effect (Mackley & Ni, 1991). It is believed that vortex rings are formed primarily during deceleration of fluid which has been subjected to pulsation, and are subsequently ejected during acceleration (Bellhouse 1978). In fact, the V_{radial} at flow reversal generally increased with *f*, due to the contribution of inchoate vortex rings during the deceleration. The combination of OFM with the periodic constrictions is actually a mean by which effective mixing can be achieved even in laminar flow conditions without turbulence.

Maps of V_{radial} throughout the oscillation cycles at $x_0 \approx 1$ mm appear symmetric in relation to the line $V_{axial} = 0$ as seen in Figure 6-2, meaning that events on the left hand side of cavity are similar to those in the right hand side. This also suggests that there is no significant secondary flow at such fluid oscillation conditions. However, some differences are seen between the flow structures at the different values of *f* in Figure 6-2. For example, the V_{radial} *versus* V_{axial} representation profile in Figure 6-2a differs from those in Figure 6-2b to Figure 6-2f as the radial motion is far more pronounced in the latter cases. That switch in V_{radial} *versus* V_{axial} profile is coincident with the observed brake of flow axisymmetry when *f* is increased from 4.1 to 5.1 s^{-1}.

The radial velocities of a small order of magnitude (i.e. 0.5 to 1.5 mm s^{-1}) obtained at $f = 4.1$ s^{-1} are replaced by the one order of magnitude higher (i.e. above 10 mm s^{-1}) radial velocities at higher f (≥ 5.1 s^{-1}). This suggests that *f* has a fundamental effect on the control of V_{radial}, and it is associated with the observed axisymmetric nature of flow. This higher radial mixing results into the radial homogeneity in the SPC tube at $f \geq 5.1$ s^{-1}, as the conditions at the wall and centre of the tube become very similar. This was observed in the velocity vector maps and was also concluded by Mackley and Ni (1991) when operating a conventional OFR at $f = 2$ s^{-1} ($Re_o = 377$).

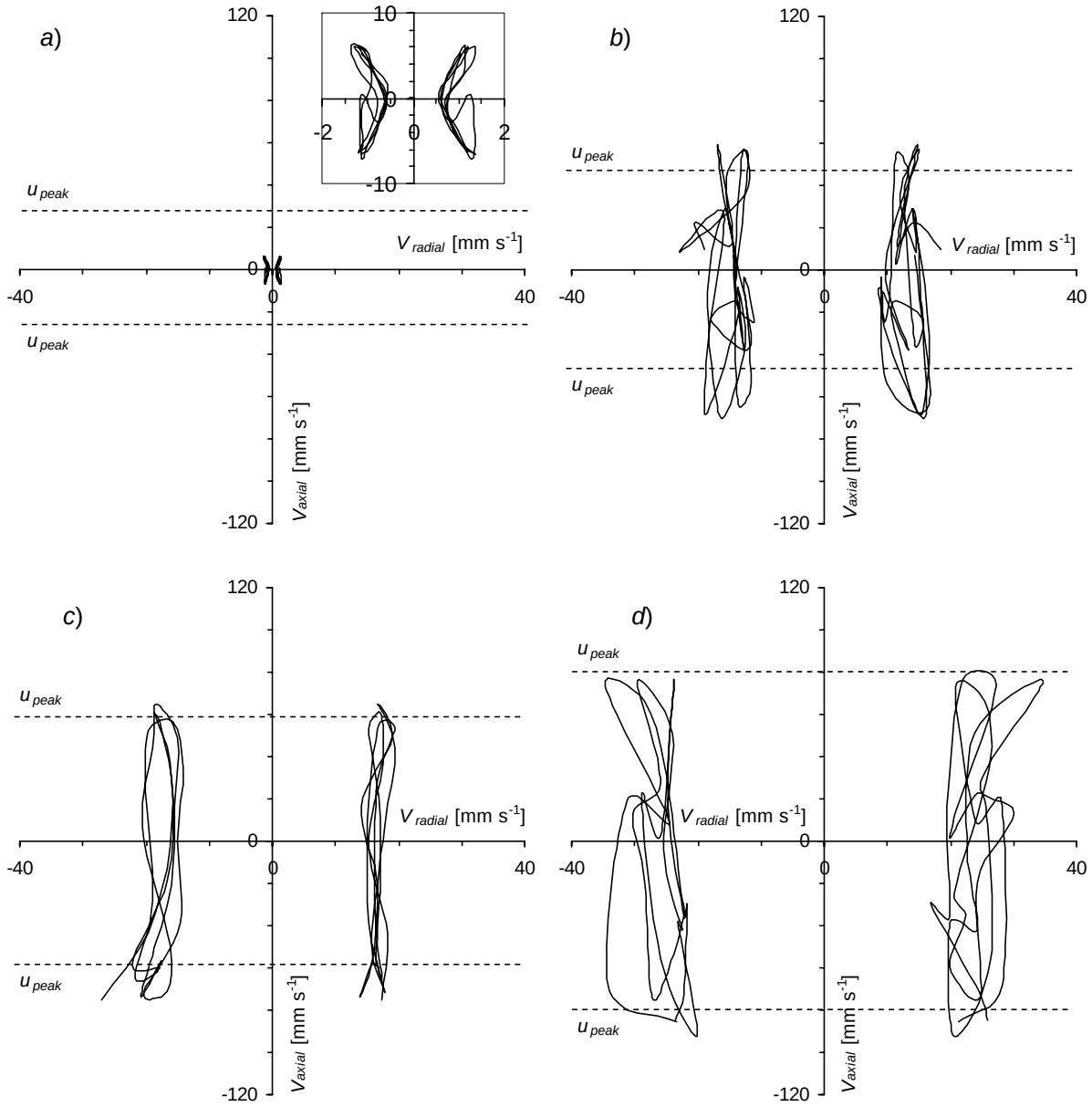

Figure 6-2. Maps of instantaneous-average radial velocity (V^{neg}_{radial} in left hand side of figures and V^{pos}_{radial} in right hand side) and of axial velocity (V_{axial}), through three complete fluid oscillation cycles, when the fluid is oscillated in batch mode at: (*a*) 4.1 s^{-1} and 1 mm, Re_o = 117; (*b*) 5.1 s^{-1} and 1 mm, Re_o = 203; (*c*) 10.1 s^{-1} and 1 mm, Re_o =259; (*d*) 11.1 s^{-1} and 1 mm, Re_o = 348; (*e*) 15.1 s^{-1} and 1 mm, Re_o = 430; (*f*) 20.1 s^{-1} and 1 mm, Re_o = 630.

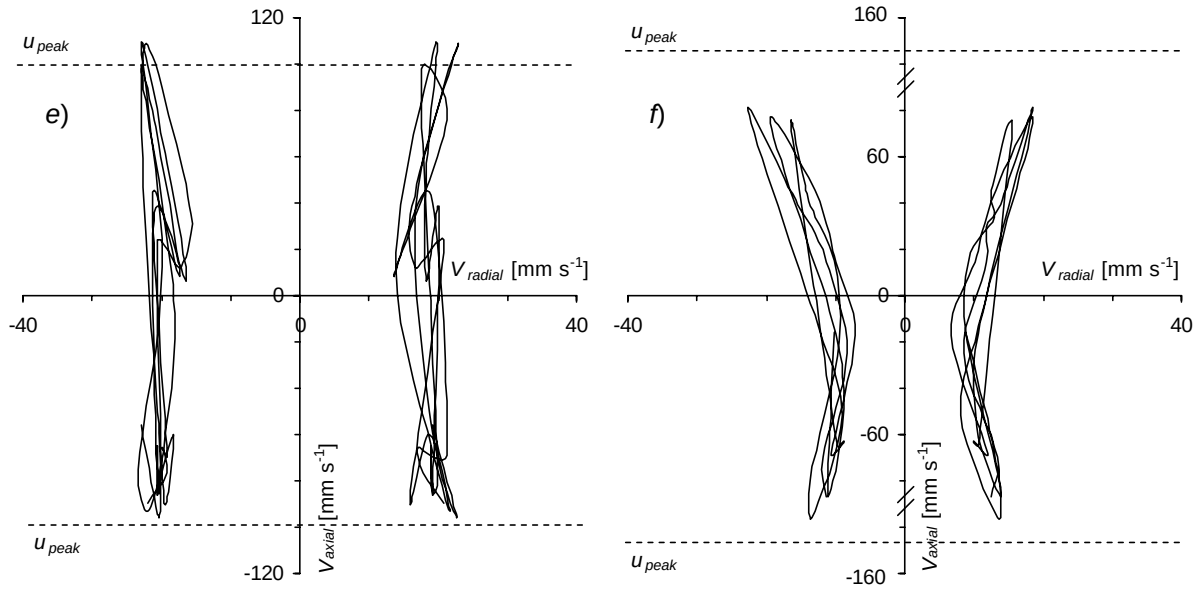

Figure 6-2. (Continued).

Generally, Figure 6-2 shows that fluid oscillations at low x_o (such as 1 mm) and low f (below 5.1 s^{-1}) results in radial velocities very small during the flow reversal and highly variable throughout the oscillation cycle, as they depend upon the axial velocities to generate the vortex rings (by flow separation). At higher oscillation frequencies (f > 5.1 s^{-1}), high radial velocities persist at the flow reversal, indicating that eddy structures are much more intensive at higher f. In particular, the operation at $f \geq$ 10.1 s^{-1} causes improved radial velocities and independent of the phase angle (i.e., roughly constant throughout the oscillation cycle).

According to Perry (2002), differences between the velocity-time profiles are very important in mixing processes. For e.g. a given impeller flow and diameter, lower powers have the smallest velocity fluctuations and smallest micro-scale shear rates; higher powers correspondingly have the highest velocity fluctuations and highest micro-scale shear rates. On the other hand, the velocity at a given point in time can be expressed as an averaged velocity, v, plus a fluctuating component v'. Such fluctuation in time can be quantified using the standard deviation, σ. Thus, in completion to axial and radial velocities, an analysis of σ may be very useful. Maps of standard deviations of both the radial (σ_{vx}) and axial (σ_{vy}) velocities are presented in Figure 6-3, for the same experiments above presented in Figure 6-2.

Figure 6-3 shows that the spread of axial and radial velocities (i.e. σ_{Vx} and σ_{Vy}, respectively) increases with increasing f (except for the higher tested f of 20 s^{-1}) at a constant $x_o \approx 1$ mm. This increase is due to increasing oscillation intensity (i.e. Re_o), leading to increased *mixing* intensity. Also, for $f \geq 5.1$ s^{-1}, both σ_{Vx} and σ_{Vy} are significantly high in comparison with the values of V_{radial} and V_{axial}, respectively, demonstrating the good mixing obtained through the oscillation of fluid in the SPC tube.

Globally, the value of f = 11.1 s^{-1} (at $x_o \approx 1$ mm) was the more favourable oscillatory flow condition for maximum radial mixing, because at such oscillation conditions the spread of radial velocities (as measured by σ_{Vx}) is maximised in relation to the spread of axial velocities (as measured by σ_{Vy}).

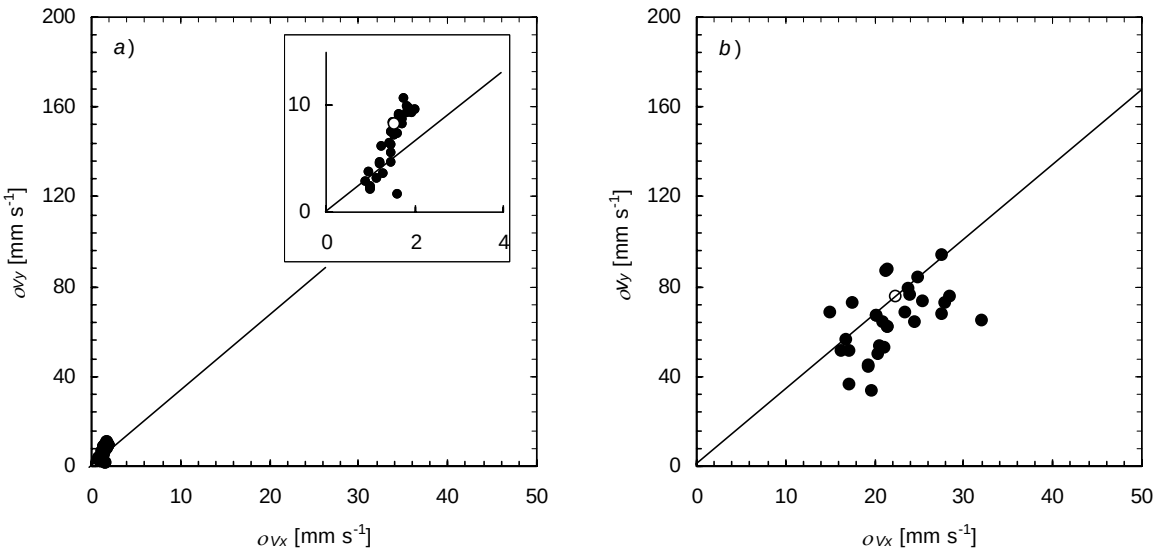

Figure 6-3. Maps of standard deviation of radial velocities (σ_{Vx}) and axial velocities (σ_{Vy}) as obtained from PIV velocity vector maps for three complete fluid oscillation cycles, when the fluid is oscillated in batch mode at: (*a*) 4.1 s^{-1} and 1 mm, Re_o = 117; (*b*) 5.1 s^{-1} and 1 mm, Re_o = 203; (*c*) 10.1 s^{-1} and 1 mm, Re_o = 259; (*d*) 11.1 s^{-1} and 1 mm, Re_o = 348; (*e*) 15.1 s^{-1} and 1 mm, Re_o = 430; (*f*) 20.1 s^{-1} and 1 mm, Re_o = 630. White dots represents the cycle-average parameter $R_s = \sigma_{radial}/\sigma_{axial}$, while the sloping-dashed line represents the relationship $\sigma_{Vx}/\sigma_{Vy} = \bar{d}/L = 0.294$.

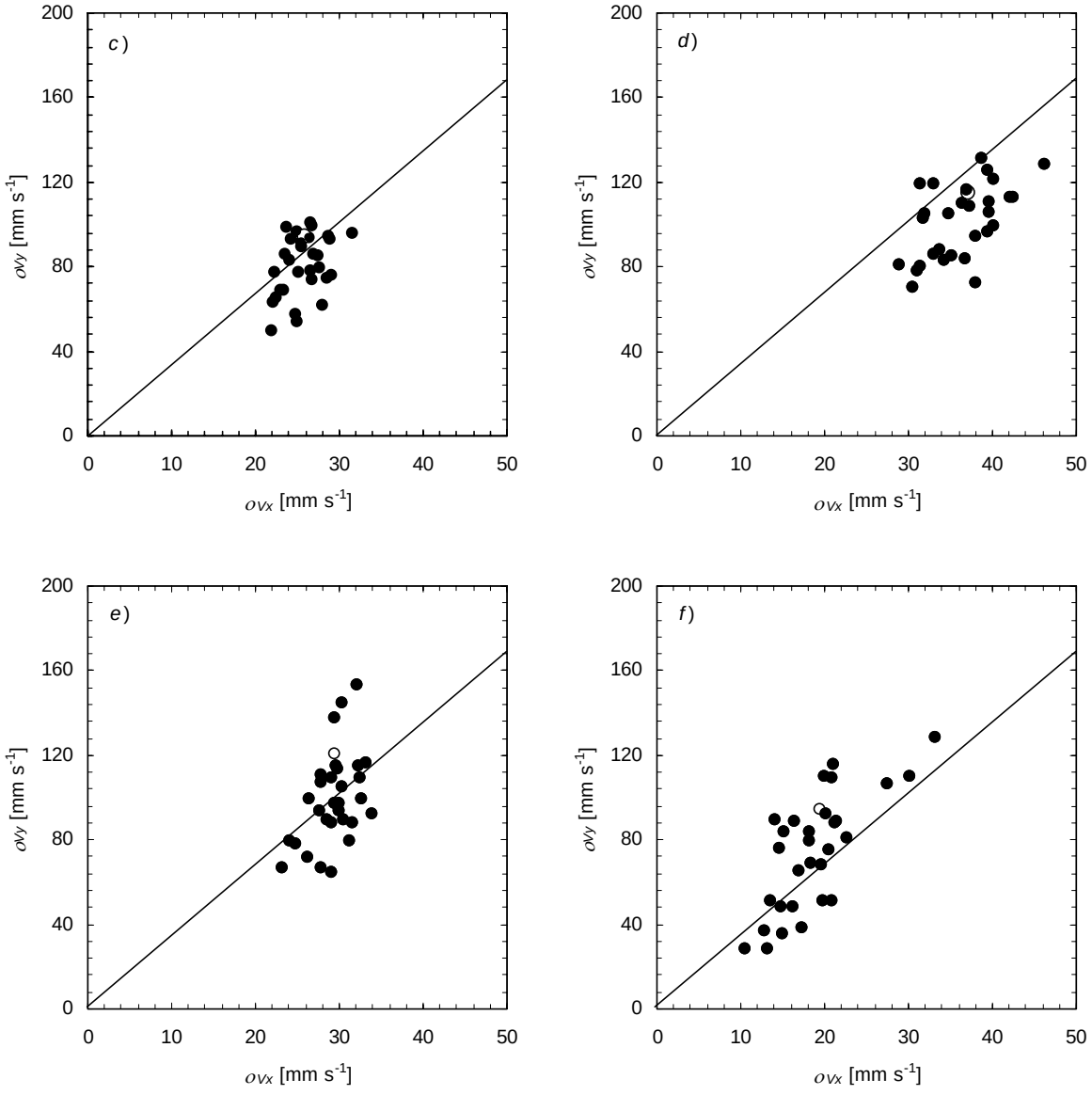

Figure 6-3. (Continued).

Cycle-average velocity vector maps at increasing f and $x_0 \approx 1$ mm

The intensity of mixing, showing the extension of radial and axial circulation of the fluid, can be easily observed in the cycle-average velocity vector maps of Figure 6-4. These vector maps were obtained by averaging the velocity vector maps of three consecutive oscillation cycles and represent an actual picture of the cycle average flow patterns. Break of flow axisymmetry was clearly seen when *f* was increased from 4.1 to 5.1 s^{-1} (Figure 6-4a and 5b, respectively), and cycle-average maps clearly demonstrate it. Note the similarity of cycle-average flow patterns with those typically observed in a stirred tank (Figure 6-4g).

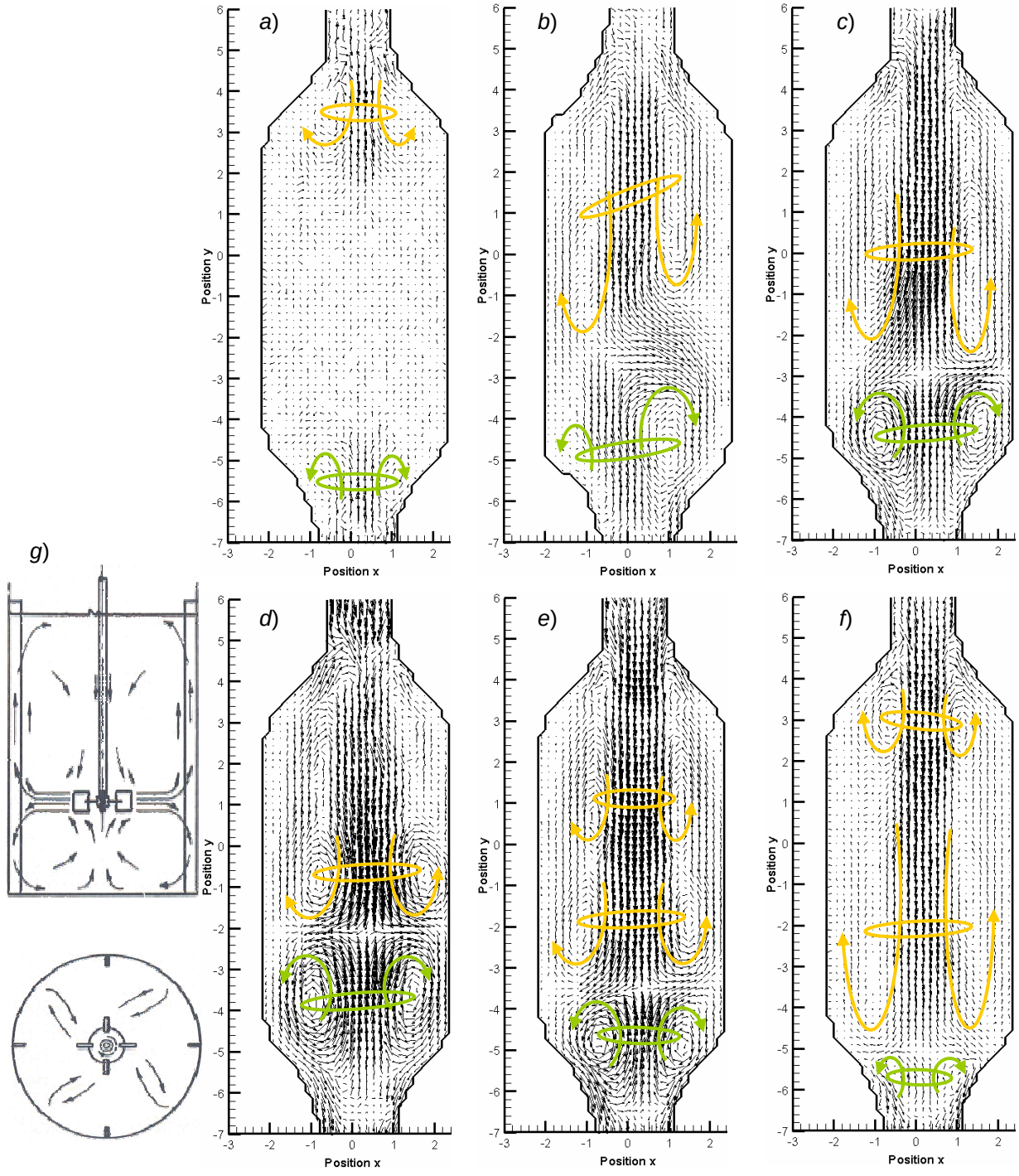

Figure 6-4. Cycle-average velocity vector maps as seen in PIV measurements. (*a*) Re_o = 117, x_0 = 1 mm, f = 4.1 s^{-1}; (*b*) Re_o = 203, x_0 = 1.4 mm, f = 5.1 s^{-1}; (*c*) Re_o = 259, x_0 = 0.9 mm, f = 10.1 s^{-1}; (*d*) Re_o = 348, x_0 = 1.1 mm, f = 11.1 s^{-1}; (*e*) Re_o = 430, x_0 = 1.0 mm, f = 15.1 s^{-1}; (*f*) Re_o = 630, x_0 = 1.1 mm, f = 20.1 s^{-1}; (*g*) Typical flow patterns in a stirred tank reactor (side and bottom view) when a propeller and wall baffles are used (*adapted from J. H. Rushton and J. Y. Oldshue, Chem. Eng. Prog., 49, 161 (1953)*).

In particular, compare the typical flow patterns in a baffled tank (Figure 6-4g), with a centrally positioned turbine, with the cycle-average flow patterns obtained in SPC tube at a Re_o of 348, x_o of 1.1 mm and f of 11.1 s^{-1} (Figure 6-4d). The similarity is clear: two axial circulation zones are formed above and below the (virtual) position of the stirrer.

The eddy motion generated within the SPC tube (Figure 6-4) not only enhances the radial motion, producing similar magnitudes of velocity components in both axial and radial directions (as previously shown in Figure 6-2), but also results in net vortex convection after each cycle of oscillation. These results are significant as they show the transport phenomena or convective motion of eddies experienced at each cycle of oscillation within such a tube. This means that on the completion of every cycle of oscillation, particles and fluids have convected both across and along the tube. As stated by Ni et al. (1999), it is such a net convective motion that is responsible for mixing particles/fluids evenly throughout the constricted tube; particles/fluids at the top may constantly reach all parts of tube, and vice-versa. This explains the good performance of SPC tube in the suspension of catalyst particles as reported before (Reis et al., 2005).

Baird & Rao (1995) working in a conventional OFR concluded that fluid patterns are not strongly affected by operating f except that the fluid motion was speeded up at higher f. This seems to be not valid for the SPC tube, meaning that the macroscopic fluid mechanics within this novel geometry may be significantly different from that in the conventional OFR, presumably due to the higher value of α and the consequent higher power input.

Determined cycle-average radial velocities at increasing f and $x_o \approx 1$ mm

Many previous works have reported that high radial velocities are achieved in conventional OFRs, but apart from Fitch *et al.* (2005), no study has quantified such magnitude of cycle-average radial velocities. Figure 6-5a summarises the ratio of cycle-average radial over the axial velocities ($R_V = \overline{V}_{radial} / \overline{V}_{axial}$) at increasing f and $x_o \approx 1$ mm in SPC tube. The ratio mean internal diameter over the constriction length, $\overline{d}/L$, which is equal to 0.294 for this particular geometry, is also represented. Because standard deviation is usually a good indication of mixing power, a second ratio is presented also in Figure 6-5, a ratio of cycle-average variance of radial velocities over the axial velocities, $R_S = \sigma_{radial} / \sigma_{axial}$.

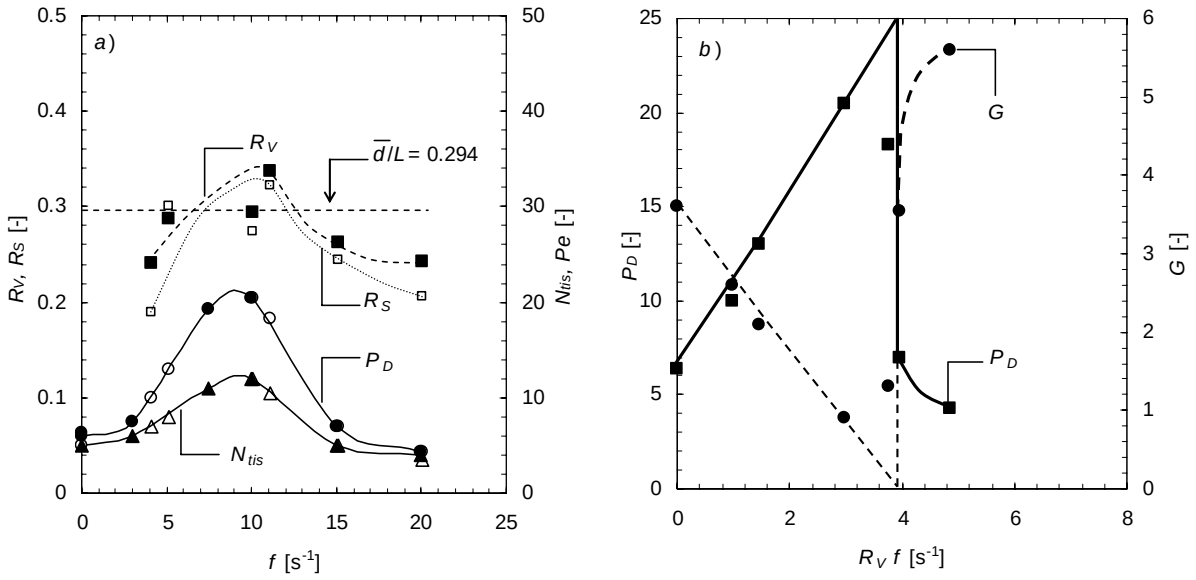

Figure 6-5. Effect of f on the best-fitting of G, P_D and N_{tis} dispersion parameters at a constant fluid oscillation, x_0 = 1 mm. (*a*) Effect of f on R_v, R_s, P_D and N_{tis} (white dots in P_D and N_{tis} curves represent interpolated data); (*b*) Correlation of P_D and G with the products $R_V f$. Axial dispersion data is from Reis et al. (2004), using a net flow rate of 1.94 ml min^{-1}.

It is clear from Figure 6-5 that both R_v and R_s are somehow associated with the control of RTD in the SPC tube. OFM leads to a maximum ratio of R_v to be achieved at f = 11.1 s^{-1} (at a $Re_o \approx 348$) at a constant x_0 of 1 mm. A decrease in f leads to a decrease of R_v towards a critical Re_o for non-axisymmetric flow (observed for Re_o > 100 in this study, for values of x_0 higher than 1 mm), meaning that an increase of f from 5.1 to 11.1 s^{-1} (at least) contributes to the radial mixing enhancement. On the other side, for values of f > 11.1 s^{-1} R_v decreases presumably due to the axial extension of vortex rings as a consequence of the small diameter of the tube, which leads to enhanced axial velocities instead of radial ones.

The effect of f over R_s is very similar to the above mentioned effect of f on R_v, thus meaning that an enhancement of radial mixing is accompanied by an enhancement in mixing power.

Correlating the cycle-average velocities, mixing and axial dispersion at $x_0 \approx 1$ mm

This section intends to identify the mechanism through which the macroscopic flow patterns are driven to ideal cases of either plug-flow or completely back-mixed limits in this novel SPC tube geometry. Thus, the cycle-average values of R_v and R_s are compared with results of (batch) mixing and with best-fitted axial dispersion parameters (dimensionless axial dispersion parameter, P_D; backmixing ratio, G; number of tanks-in-series, N_{tis}) extracted from RTD experiments performed in continuous running of SPC geometry at the same value of x_0 (1mm). Because the ratio Re_n/Re_o used is very small (i.e. below 0.1), the macroscopic flow patterns during the continuous running of a net flow rate of 1.94 ml min^{-1} (i.e. $Re_n \approx 9$, as used in RTD experiments) were not significantly different from those found by PIV in batch mode for the same f and x_0, according to previous studies in conventional OFRs (Harvey, Mackley, & Stonestreet, 2001).

Figure 6-5a also shows the variation of best-fitting dimensionless parameters N_{tis} and P_D at increasing f and x_0 = 1 mm. The narrower RTD (i.e. the maximum P_D) was obtained at f = 10 s^{-1}, at an R_v ratio equal to ~0.29 (not at the maximum value, i.e. ~0.34 found for f = 11.1 s^{-1}). Data is interpreted as follows (illustrated in Figure 6-6): in the absence of OFM (i.e. f = 0 s^{-1} - Figure 6-6a), the RTD in the SPC tube presents some 'shortcuts' and 'dead zones' due to the existence of constrictions. The coupling of OFM (Figure 6-6b) leads to an improvement of radial mixing (thus of R_v and R_s) from f = 0 s^{-1} to ~10 s^{-1} through 2 main steps: *i*) by forming vortex ring as a result of flow separation in the constrictions' surface; *ii*) by increasing the intensity and acceleration of ejected vortex rings. Thus, RTD becomes narrower as seen in F-diagrams (e.g. Figure 6-6c). The increase of f above ~10 s^{-1} (Figure 6-6d) improves the radial mixing (thus increasing R_v) but it also increases the backflow rates. In addition, spreads of axial velocities are increased (Figure 6-3) which also contributes for axial dispersion of fluid (with a decrease of P_D). For f above ~13 s^{-1} the high axial velocities at the input lead to a reduction of R_v, thus high backflow rates lead to high extent of axial dispersion (thus small P_D).

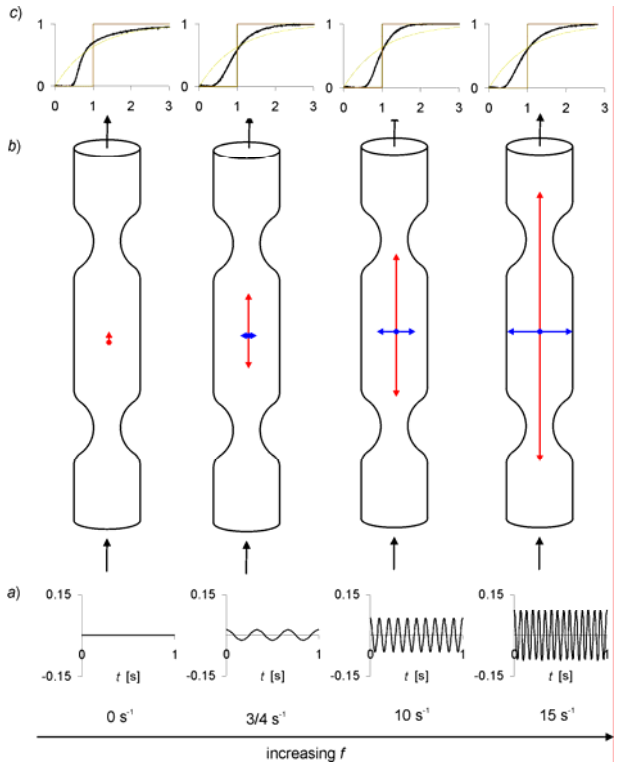

Figure 6-6. Illustration of the effect of R_v on the RTD (net flow rate of 1.94 ml min^{-1}) at increasing f (from 0 to 15 s^{-1}) and x_0 = 1 mm. (a) Oscillatory velocity (in mm s^{-1}) at input; (b) Cycle-average axial and radial velocities within the cavities of SPC tube; (c) Experimental $F(\theta)$-diagram (comparison with ideal plug-flow and stirred tank).

In order to correlate R_v with the axial dispersion it should be noted that the dimensionless parameter R_v does not consider the time dependency of the mixing process. As an example, for the same value of R_v a solute will be more dispersed in the same time interval when oscillating at 20 s^{-1} than at 10 s^{-1}, because it was subjected to twice the oscillation cycles and twice the backflow rate. This is easily understood by correlating both P_D and G parameters with the product $R_V f$, therefore considering the backflow ratio (Figure 6-5b). A narrower RTD was effectively obtained at lower values of the product $R_V f$. A linear increase of P_D (thus a linear decrease of G) was obtained with increasing values of $R_V f$, up to a critical value of ~3.9. For values of $R_V f$ above that value, the flow presents a sudden change from scarcely-dispersed to highly-dispersed: the increase of the product $R_V f$ above 3.9 leads indeed to a backmixed state (i.e. to a low value of P_D) in all the SPC tube. Similar results were obtained when using $R_S f$ instead of $R_V f$ (results not shown).

In terms of fluid dispersion it is always necessary to consider that the eddy mixing convection produced by the OFM leads to some extent of axial dispersion along the length of the tube, thus the axial dispersion is naturally a function of R_V (or R_S) and f. This explains why the hydrodynamic models considering some degree of backmixing give good accuracy in describing the RTD in chaotic advected flow regime (for an OFR, it means a Re_o above 120 according to Mackley & Ni (1991).

Despite of the presence of backflow, the chaotic advected flow regime shows some advantages, such as the great enhancement of global mixing within the constricted tube, similar events in the wall to those at the centre of the tube and improvement of RTD (towards plug-flow), heat and mass transfer, among others (Mackley & Ni, 1991). This statement is complemented by Ni & Pereira (2000) who concluded that good radial mixing is achieved by vortex formation and shedding in the constricted tube, with the main consequence being the negligible radial concentration gradient.

Because the extent of backflow at x_0 of 1 mm is very low, the tanks-in-series model also gave reasonable results, thus the relation of R_V with N_{tis} was very similar to that discussed for P_D (results not shown).

In summary, the correlation of axial dispersion with cycle-average radial and axial velocities and standard deviations as presented in this study allows to improve the actual understanding of OFM. Firstly, it is suggested that the visualisation of flow non-axisymmetry is associated with an increase of the ratio cycle-average radial over the axial velocities (R_V). Secondly, the introduction of OFM from 0 to 10 s^{-1} mainly results (apart from the enhancement in Re_o) in an enhancement of R_V and R_S ratios, thus improved radial mixing, with the RTD approaching the plug-flow. Thirdly, the operation at f > 10 s^{-1} leads to increased products $R_V f$, and the macroscopic flow patterns experiment a sudden transition to completely backmixed. This summarises the different ways of having f affecting the radial mixing under OFM, which are actually not included in Re_o relation (Eq. (1)).

For correlation with mixing times (*mixing time* is the time necessary to achieve a specific homogeneity level U, and usually U > 95 %) the ratio R_S was chose as it presented a better correlation coefficient with the mixing coefficient k_m (a coefficient allowing to predict the mixing time in SPC tube) than with R_V (results not shown). Because mixing in batch also depends on the mixing time, the product $R_S \ f$ was used to express the mixing dissipation as determined from the macroscopic flow patterns. Figure 6-7 shows the relationship of product $R_S \ f$ and batch mixing coefficient k_m (for x_0 = 1 mm) with Re_o. As clear correlations

are observed, it is also clear a direct proportionality $R_S\ f$ and k_m, confirming that the liquid homogeneity does correlate with the macroscopic flow patterns.

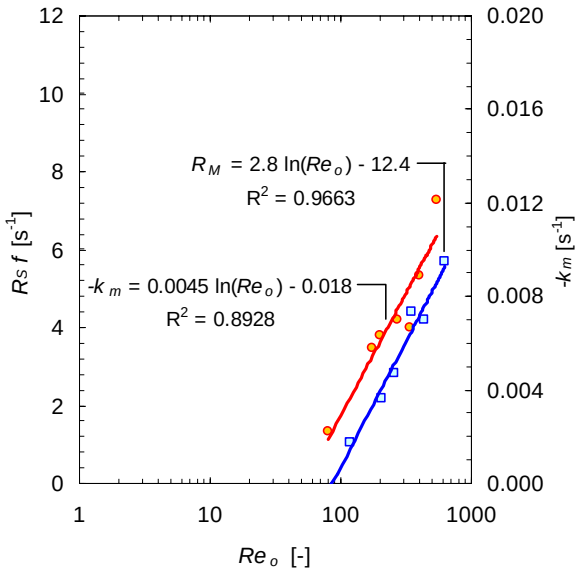

Figure 6-7. Effect of Re_o on mixing coefficient k_m and comparison with the effect of Re_o on the product $R_S\ f$.

The values of the product $R_S f$ also did correlate those of the product $R_V f$ (Figure 6-8): products of $R_S f$ exponentially increases with $R_V f$, meaning that the mixing power increases exponentially with the enhancement of the product 'radial mixing × oscillation period frequency'. In practice, this means that the macroscopic flow pattern predicts (through the values of R_s and R_v) a positive correlation of 'mixing intensity' with the backflow rate, which is coherent with a long time scale model for a real-batch stirred tank (see Levenspiel 1972).

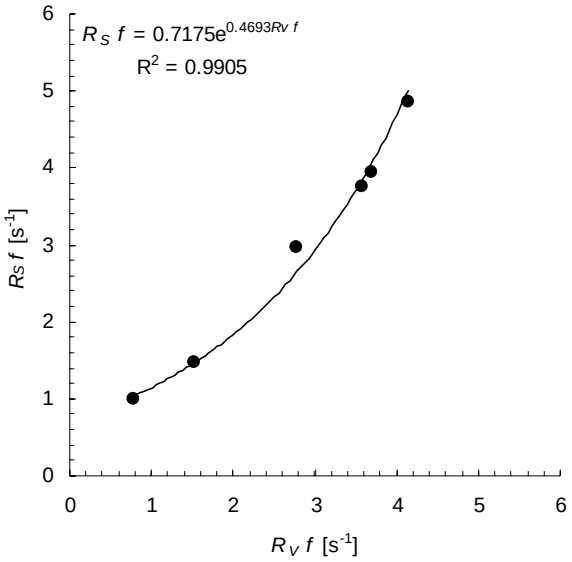

Figure 6-8. Correlation between the product s $R_S f$ and the products $R_V f$.

Analysis of cycle-average radial and axial velocities for Re_o = 85 to 630

The further experiments performed in this study at values of x_o other than 1 mm allowed to determine the cycle-average parameters $\overline{V}_{axial}$ and $\overline{V}_{radial}$ for different combinations of f and x_o. Results for all experiments in run a) and run b) (as seen in Table 6-1) are shown in Figure 6-9.

It is clearly seen from Figure 6-9 that a small $\overline{V}_{axial}$ is accompanied by low intensity $\overline{V}_{radial}$. Moreover, the break of flow axisymmetry observed for Re_o > 100 was coincident with a ~10-fold increase in $\overline{V}_{radial}$, suggesting that the visualized flow non-axisymmetry is induced by the higher radial velocities. For the two higher values of f tested (15 and 20 s^{-1}), a decrease of mixing intensity in the x-y plane (plane monitored by PIV) was observed, presumably indicating the formation of a secondary flow in the z direction. This indicates the formation of tangential flow at high values of Re_o (above 360 for x_o of 1 mm).

Up to a Re_o of about 360 it was found that $\overline{V}_{radial}$ increases linearly (Figure 6-9b) with Re_o, according to the relation: $\overline{V}_{radial} \approx 0.26\ \overline{V}_{axial,theo}$, where $\overline{V}_{axial,theo}$ is the cycle-average axial velocity as determined from the time (t) integration of the relation $V_{axial,theo}(t) = 2\pi\ f\ x_0\ cos(2\pi\ f\ t)$. It means the radial

velocities reach, on average, 26 % of the order of magnitude of input axial velocities ($\overline{V}_{axial,theo}$) in each cavity of the SPC tube, in the studied range of Re_o = 86 - 630.

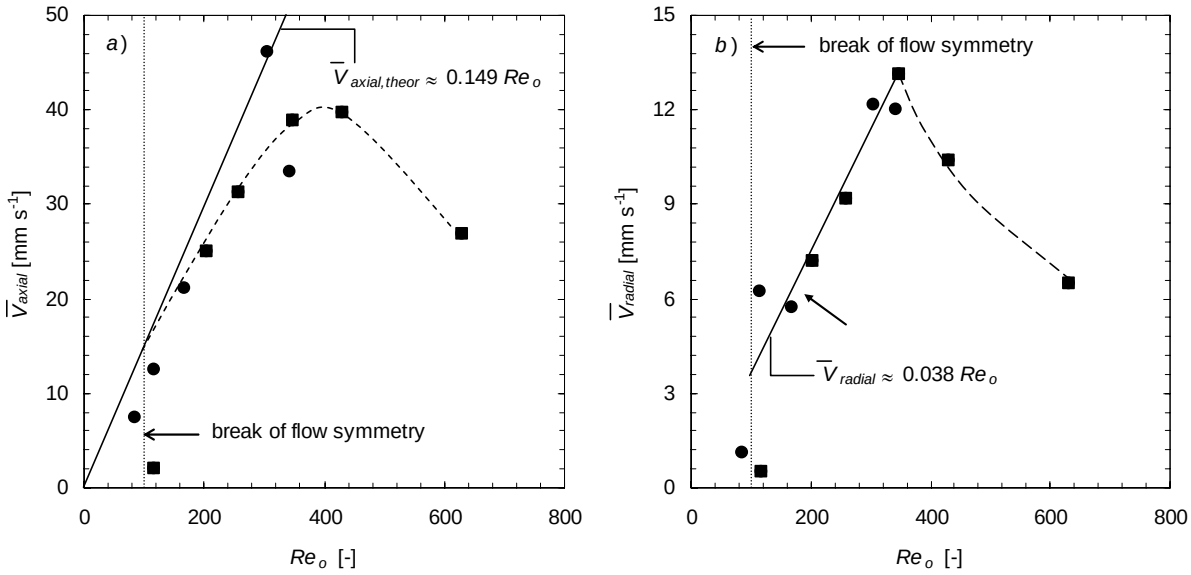

Figure 6-9. Cycle-average $\overline{V}_{axial}$ and $\overline{V}_{radial}$ as a function of Re_o at different combinations of f and x_o, i.e. Re_o. (*a*) cycle-average axial velocities, $\overline{V}_{axial}$. (*b*) cycle-average radial velocities, $\overline{V}_{radial}$. (■) experiments at constant x_o of ~1 mm, i.e. run a); (●) experiments at different combinations of f and x_o, i.e. run b). Vertical dashed line represents the critical Re_o where break of flow symmetry was detected.

Velocity vector maps of the experiments performed at a x_o different from 1 mm (run b) (results not shown) demonstrated that the dependency of flow behaviour on x_o was different from the previously discussed dependency on f, differing from the behaviour reported in studies on larger conventional OFRs with sharp-edged baffles (e.g. Mackley & Ni, 1993; Ni & Pereira, 2000). Increase of x_o to values above 1 mm leads to a higher ratio $\overline{V}_{radial} / \overline{V}_{axial}$ (i.e. R_v) but to a smaller $\sigma_{Vradial}$ (results not shown), resulting in a decrease of radial mixing power in some phases of the oscillation cycle. Moreover, because $\overline{V}_{radial}$ is enhanced (Figure 6-9) the non-axisymmetry of flow is accentuated, as seen from the velocity vector maps Figure 6-4. In fact, the experimental PIV velocity vector maps demonstrated that the increase of x_o leads to a greater vortex ring propagation length. The consequence is an overall increase of V_y in the tube when compared to V_x. Ni et al. (2000) concluded that x_o could be the governing factor in determining the length to which a

vortex propagates through the fluid; eddies formed at higher x_0 are larger and occupy a greater percentage of the volume between the constrictions (cavity). That conclusion was confirmed in the SPC geometry.

6.4 Conclusions

The macroscopic flow patterns generated in a novel 4.4 mm internal diameter, smooth, periodically constricted (SPC) tube were experimentally studied with the PIV technique. Velocity vector maps have shown an improved mixing performance of this novel SPC geometry for three main reasons: *i*) an intensive radial mixing is generated by the axial oscillation of fluid; *ii*) high (axial) circulation rates are generated; *iii*) no tangential flow is apparently produced.

Cycle-average radial and axial velocities ($\overline{V}_{radial}$ and $\overline{V}_{axial}$, respectively) have correlated with the experimental axial dispersion (from RTD studies) and with mixing time measurements. In particular, an increase of the ratios $R_v = \overline{V}_{radial} / \overline{V}_{axial}$ and $R_s = \sigma_{Vradial} / \sigma_{Vaxial}$ was found to make the RTD move towards the ideal case of a plug-flow reactor, especially when both R_v and R_s approach the geometry ratio $\overline{d}/L$ = 0.294. Nevertheless, a maximum value of R_v = 0.34 was obtained for f = 11.1 s^{-1} and x_0 = 1 mm. Moreover, the products $R_V \ f$ and $R_S \ f$ successfully correlated the axial dispersion (represented by the best-fitted P_o, G and N_{tis} parameters), and a mixing coefficient k_m, respectively; a value of product $R_V \ f$ of ~3.9 marks a sudden transition from plug-flow to completely backmixing states and explains the good control of RTD and mixing times usually reported by OFM studies.

PIV experiments at increasing values of f and a constant x_0 = 1 mm demonstrated that it affects the OFM by controlling the magnitude of axial and radial velocities and the respective standard deviation, σ of velocities (which is a direct measure of the mixing power). Experiments at higher values of x_0 showed that this parameter may govern the length of vortex rings propagation through the fluid in a cavity of the SPC tube, thus promoting the axial motion of fluid while assuring a good radial homogeneity (i.e. high R_v ratios).

6.5 References

Baird, M.H.I. & Rao, N.V.R. (1995). Power dissipation and flow patterns in reciprocating baffle-plate columns. Canadian Journal of Chemical Engineering, 73(4), 417-425.

Bellhouse, B.J. (1978). Method for effecting heat or mass transfer, United States Patent. USA: National Research Development Corporation, London England.

Fitch, A.W., Jian, H.B., & Ni, X.W. (2005). An investigation of the effect of viscosity on mixing in an oscillatory baffled column using digital particle image velocimetry and computational fluid dynamics simulation. Chemical Engineering Journal, 112(1-3), 197-210.

Harvey, A.P., Mackley, M.R., & Stonestreet, P. (2001). Operation and optimization of an oscillatory flow continuous reactor. Industrial & Engineering Chemistry Research, 40(23), 5371-5377.

Howes, T., Mackley, M.R., & Roberts, E.P.L. (1991). The simulation of chaotic mixing and dispersion for periodic flows in baffled channels. Chemical Engineering Science, 46(7), 1669-1677.

Levenspiel, O. (1972). Chemical reaction engineering (1st edition ed.). New York: John Wiley & Sons, Inc.

Mackley, M.R., Tweddle, G.M., & Wyatt, I.D. (1990). Experimental heat-transfer measurements for Pulsative flow in baffled tubes. Chemical Engineering Science, 45(5), 1237-1242.

Mackley, M.R. (1991). Process innovation using oscillatory flow within baffled tubes. Chemical Engineering Research & Design, 69(3), 197-199.

Mackley, M.R. & Ni, X. (1991). Mixing and dispersion in a baffled tube for steady laminar and Pulsative flow. Chemical Engineering Science, 46(12), 3139-3151.

Mackley, M.R. & Ni, X. (1993). Experimental fluid dispersion measurements in periodic baffled tube arrays. Chemical Engineering Science, 48(18), 3293-3305.

Ni, X., Zhang, Y., & Mustafa, I. (1999). Correlation of polymer particle size with droplet size in suspension polymerisation of methylmethacrylate in a batch oscillatory-baffled reactor. Chemical Engineering Science, 54(6), 841-850.

Ni, X.W., Nelson, G., & Mustafa, I. (2000). Flow patterns and oil-water dispersion in a 0.38 m diameter oscillatory baffled column. Canadian Journal of Chemical Engineering, 78(1), 211-220.

Ni, X.W. & Pereira, N.E. (2000). Parameters affecting fluid dispersion in a continuous oscillatory baffled tube. Aiche Journal, 46(1), 37-45.

Perry, R.P., Green, D.W., & Maloney, J.O. (2002). Perry's chemical engineer', platinum edition. New York: McGraw-Hill.

Reis, N., et al. (2004). Residence times and mixing of a novel continuous oscillatory flow screening reactor. Chemical Engineering Science, 59(22-23), 4967-4974.

Reis, N., et al. (2005). Fluid mechanics and design aspects of a novel oscillatory flow meso-reactor. Chemical Engineering Research & Design, 83(A4), 357-371.

Chapter 7 Oxygen mass transfer rates for gas-liquid flow in the micro-bioreactor

This chapter deals with the determination of air-water oxygen mass transfer rates within the continuous micro-bioreactor. A state-of-the-art fibre-optical micro-probe (oxygen micro-optrode) was applied in the on-line monitoring of O_2 saturation levels at different combinations of fluid oscillation frequency (f) and amplitude (x_0). Volumetric oxygen mass transfer rates (k_La) of up to 0.05 s^{-1} were estimated for the range of x_0 from 0 to 3 mm (centre-to-peak) and f from 0 to 20 s^{-1}, where a thirteen-fold increase was obtained in comparison with the predictable k_La for gas-sparging in a conventional bubble column at the same gas superficial velocity (0.37 mm s^{-1}), according to Deckwer's correlation. An average 70 % increase was obtained with this system when compared with the k_La values reported for a 50 mm i.d. oscillatory flow reactor (OFR) within the same range of f and x_0.

It was shown that the reversing nature of oscillatory flow mixing (OFM) in the presence of these small-scale smooth periodic constrictions (SPC) effectively enhances the k_La with both f and x_0. Due to the smaller scale of the reactor and to the existence of SPCs the gas hold-up could be controlled, which was found to play a major effect on the global enhancement of k_La in the studied range of OFM regimes.

Keywords: novel screening reactor; oscillatory flow; mass transfer; multiphase flow; mixing; fluid mechanics.

7.1 Introduction

A novel continuous small-scale reactor (micro-bioreactor) based on the Oscillatory Flow Mixing (OFM) technology (e.g. Mackley, 1991) is being developed for applications at specialist chemicals manufacture and high throughput screening, as recently presented by Reis et al. (2005). This novel micro-bioreactor is able to perform continuous multiphase reactions, namely those involving the suspension of catalyst beads. Its extensive use in chemistry, biological and pharmaceutical research laboratories is envisaged. Optimum operation conditions for applications at the bioengineering field are being established in relation to four parameters: 1) fluid mixing, 2) residence time distributions, 3) suspension of catalyst particles and 4) (oxygen) mass transfer rates. The first three parameters were previously reported in previous works (e.g. f Reis et al. 2005; 2004), being the determination of O_2 mass transfer rates the subject of this work.

Gas-liquid O_2 mass transfer coefficient (k_La) is an important parameter when considering the application of a reactor for O_2 dependent processes (e.g. many biological reactions) and has been widely studied in conventional reactors.

The measurements of k_La have been reported for many devices, from high power rotary agitators to bubble columns, for many processes and using different methods. The most used measurement techniques for estimation of k_La can be classified in different classes: 1) dynamic methods (e.g. dynamic O_2 electrode and start-up methods); 2) steady-state sulphite method; 3) dynamic pressure method (DPM); 4) peroxide methods and 5) response methods. A fine survey of the various methods mostly employed at the industrial scale is presented by Gogate and Pandit (1999). Reported works cover a wide range of reactor types (e.g., see Baird & Garstang, 1967, 1972; Blakebro & Sambamur, 1966; Linek, Sinkule, & Benes, 1991, 1992; Serieys, Goma, & Durand, 1978). In terms of applicability of these techniques to oscillatory flow reactors

(OFRs), Hewgill et al. (1993) considered the nitrogen purge method as an accurate method for measurement of k_La. The same technique has been also recommended by Linek et al. (1987). However, this method might lead in some circumstances to wrong values of k_La, as pointed out by Hewgill et al. (1993). Ni et al. (1995) used the dynamic gassing-out technique to determine k_La values in a conventional OFR. In a subsequent work Ni and Gao (1996) identified a pitfall of the gassing-out method: a well-mixed state needs to be achieved within a reactor if this method is to be used for k_La determination in a batch OFR. It is generally accepted that the application of all above referred methods (essentially dynamic and response methods) to determine k_La is limited to the assumption of perfect liquid mixing state (Gogate & Pandit, 1999).

O_2 measuring devices may limit the determination accuracy of k_La. Van't Riet (1979) concluded that the use of commercially available probes enables a k_La of up to 0.1 s^{-1} to be measured with little losses of accuracy and without the need to use response models if the response time of the probe is 2 to 3 seconds. In most commercial O_2 dissolved (OD) probes this is not the case, thus being essential to use a method to compensate for different time response of probes, even when the mean response time is as short as 3 seconds (X. Ni & Gao, 1996; X. W. Ni, Gao, & Pritchard, 1995).

In comparison with OD electrodes, O_2 optrodes (the optical equivalent of electrodes) seem more suitable for bioengineering applications. Firstly, sensing does not consume oxygen. Secondly (and as a consequence of that) the partial pressure of oxygen in the optrode where a fluorescent dye is located is in equilibrium with the partial pressure outside the optrode. As the optrode response is directly related to O_2 concentration, and not to flow of O_2, a modification of the diffusion properties of the optrode should only alter the response time. Furthermore, optrodes offer many advantages due to the utilisation of fibre optical technology, such as remote sensing, small size and sensor networking (Gouin et al., 1997).

Little attention was given to gas-liquid mass transfer enhancement using OFM until the nineties, with a few exceptions (Baird & Garstang, 1967, 1972; Bellhouse et al., 1973). The growing interest in OFR during the nineties led to some novel important results concerning mass transfer in this type of reactors. Mass transfer of O_2 into water was reported by Hewgill et al. (1993) for an OFR. A six-fold increase in k_La was obtained in comparison with the k_La values for a bubble column. Ni et al. (1995; 1995) obtained 75 % higher values of k_La working in OFR when compared to a stirred tank reactor (STR) with similar power inputs. The first explanation for this effect could be an increase in gas hold-up (and hence in a term), as reported by Baird and Gargstand (1967) and Serieys et al. (1978). A second possibility mentioned by Ni et

al. (1995) was that k_La improvement experienced in OFRs might be associated with the more even distribution of shear rate in the OFR which on average leads to thinner liquid films (hence increasing the k_L term).

The effect of aeration rate (U_G) over k_La in OFRs was reported by Ni et al. (1996). Mackley et al. (1998) tested the performance of a self-aerated OFR using the nitrogen-sparger method thus reporting a maximum k_La value of 0.008 s^{-1}. Oliveira and Ni (2001) investigated which characteristics of the gas phase in the OFR provide enhancements to k_La: bubbles' mean residence time (τ_G), gas hold-up (ε_G) and bubble size distribution were studied at f from 1 to 5 s^{-1} and x_0 from 2 to 8 mm (centre-to-peak), with U_g from 1.06×10^{-3} to 4.24×10^{-3} m s^{-1} (i.e. 0.05 to 0.2 vvm, where vvm is the volume of air per volume of reactor per minute). The conclusion was that at low Re_o (up to 5,000) oscillation has little effect on the mean bubble diameter (d_b). The consequence of OFM is an increased bubble breakage, resulting in a higher number of smaller bubbles, higher τ_G and higher ε_G. Changes in ε_G played a more significant role over k_La values than changes in d_b but it is the mutual effect of smaller d_b and their corresponding (high) τ_d the responsible feature for enhanced k_La values.

The main objective of this work is to demonstrate that the novel continuous micro-bioreactor is able to achieve oxygen transfer rates (OTRs) enough to support the growth of oxygen-dependent cultures, therefore being able to support applications as a screening device for fast parallel bioprocessing. It is expected that both fluid hydrodynamics and gas-hold up (proportional to bubble mean residence times) in the reactor contribute to enhance k_La.

Previous PIV measurements and CDF simulations demonstrated high radial rates of flow exchange between the walls and the centre of the tube during the complete oscillation cycle, coupled with high degrees of velocity gradients (as illustrated in Figure 7-1, where the dashed arrows represent vortex rings position while dotted arrows represent locations of main fluid net stream; for simplicity, no attempt was made to represent non-axisymmetry of flow). Accordingly, enhancements of heat and mass transfer rates are expectable with this reactor (Perry, Green, & Maloney, 2002), in addition to an increase of bubbles breakage (leading to a decrease of d_b, i.e. an increase of the specific bubble area, a, and also of ε_G), leading to a significant improvement of k_La.

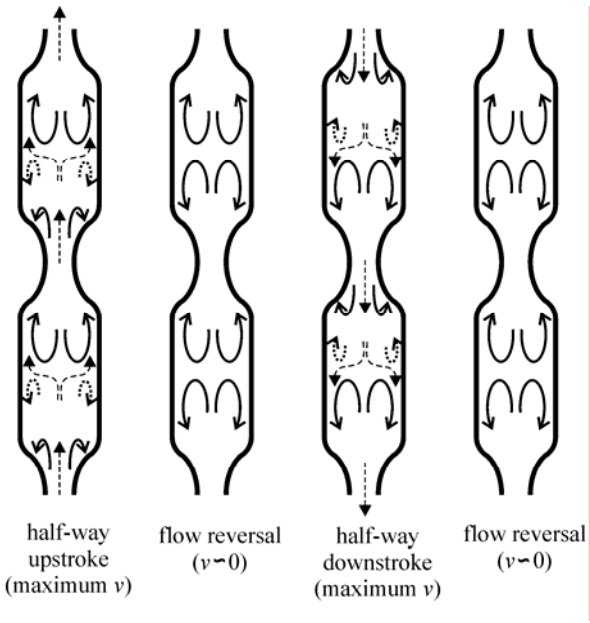

Figure 7-1. Typical flow patterns within a SPC-tube's geometry (Reis et al., 2005).

7.2 Materials and Methods

The Continuous SPC tube Geometries

The SPC tube geometry has been introduced by Reis et al. (2005). This particular study involved the use of two SPC tubes of different lengths: 350-mm-long (tube SPC1 – micro-bioreactor) and 75 mm (tube SPC2), as shown in Figure 7-2 and detailed in Table 7-1. OFM intensity was controlled by setting up f and x_0. The studied range for f and x_0 was 0 to 20 s^{-1} and 0 to 3 mm (centre-to-peak), respectively. The SPC tube may be used as a batch-wise reactor but it also allows continuous operations by coupling a fluid net flow.

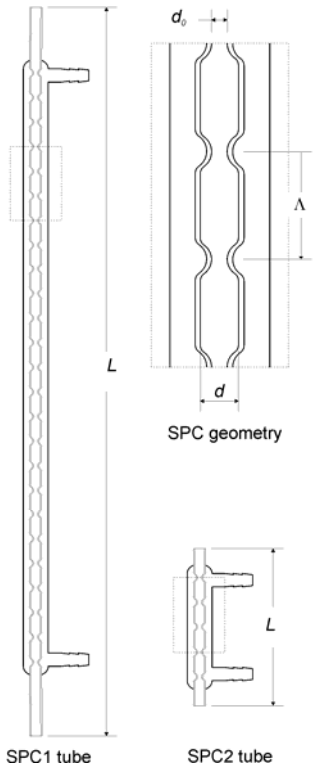

Figure 7-2. Geometry of a 350-mm-long SPC tube (SPC1 – micro-bioreactor) and a 75 mm length tube (SPC2); details of SPC geometry. All distances are in mm.

Table 7-1: Dimensions and constants used in the experiments with tubes SPC1 and SPC2

	SPC1	SPC2
SPC tube length, L, mm	350	75
Distance between gas-sparger and micro-optrode, mm	346	100
Volume of a single tube, V, ml	4.4	~1.0
Maximum internal diameter of SPC tube, d, mm	4.4	
Mean internal diameter of SPC tube, mean d, mm	4.0	
Fluid oscillation frequencies, f, s^{-1}	0 - 20	
Fluid oscillation amplitudes, x_0, mm	0 – 3.0	
Volumetric fluid rate, v, ml min^{-1}	1.58	
Volumetric airflow rate, v_g, ml min^{-1}	0.28	
Mean superficial fluid velocity, U, mm s^{-1} *	2.1	
Mean superficial gas velocity, U_g, mm s^{-1} *	3.7×10^{-4}	
Experiments temperature, °C	20	

* based on mean d = 4.0 mm

Experimental apparatus

In this work k_La was determined using a variation of the dynamic O_2 method, permitting the estimation of an averaged mass transfer coefficient using a continuous gas and a continuous liquid phase. Previous studies clearly demonstrated that flow within a single 350-mm-long SPC tube may approach a plug behaviour (essentially at low f and x_o) therefore the use of batch methods for k_La determination is not advisable. Thus, all experiments were run with fluid oscillations in the presence of a continuous liquid net flow. Air was continuously sparged through a syringe needle at a flow rate of 0.28 ml min^{-1} in the inlet of the tube and the O_2 saturation level was monitored at the outlet, until a new steady-state in the saturation level of OD was reached in the outlet flow. No other gas distribution method was tried since under OFM the mass transfer is dominated by the fluid flow patterns and is independent of the gas distributor, as concluded by Oliveira and Ni (2004). Figure 7-3 shows a typical profile of O_2 concentration at the outlet of the tube during the experiment duration. Typical time to achieve final steady-state (Figure 7-3a) was about 10-15 hydraulic residence times (Figure 7-3b). As mentioned before, two main advantages of this variant of the dynamic method when compared with the conventional dynamic methods are (Gogate & Pandit, 1999): 1) the system dynamics is considered in this case and 2) the estimation of k_La is only based on O_2 saturation levels at the initial and the final steady-states (Figure 7-3a). Actually, it means that estimated values of k_La become independent of the response time of the O_2 probe (optrode), as long as the attainment of the steady-state is assured.

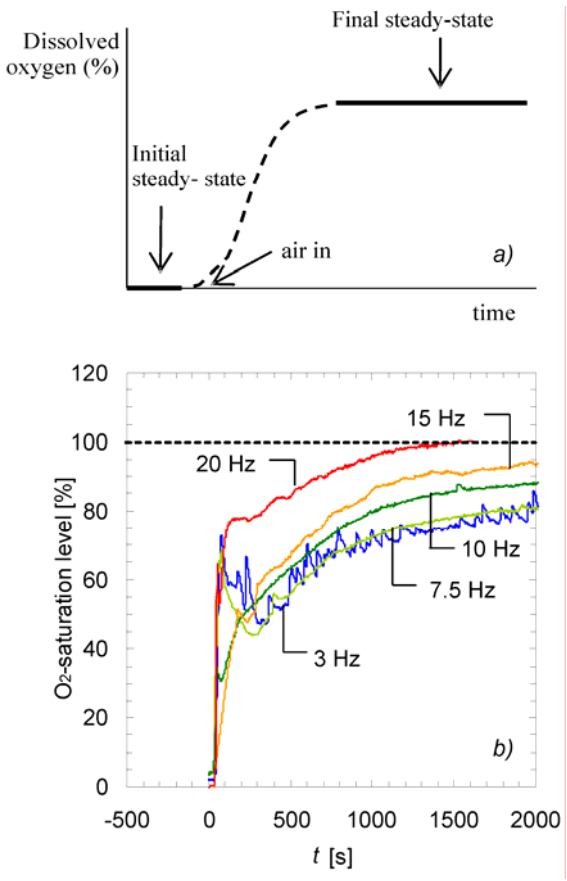

Figure 7-3. *a)* Illustration of the variation of the dynamic O_2 method used in this work; *b)* experimental time profiles of O_2 dissolved saturation level using the proposed modification of the dynamic method (SPC1 tube, x_0 = 1 mm and f = 3 to 20 s^{-1}).

Experimental setup

A SPC tube was fixed vertically and mounted according to Figure 7-4. A continuous fluid flow rate with a zero O_2 concentration was coupled to the OFM component using a peristaltic pump. The inlet stream from the peristaltic pump was passed through a reservoir in order to eliminate propagation of fluid pulsations. Fluid oscillations were achieved by a rotating ceramic piston pump (CKCRH0, Fluid Metering Inc., New York), working in closed-loop. The design of such pump (valveless rotating and reciprocating piston) allowed good sinusoidal oscillations of the fluid. The control of x_0 was possible by turning an easy-grip flow control ring in the pump head. The relationship between piston position (h_p) and x_0 (in the maximum internal tube diameter, i.e. 4.4. mm) was: x_0 (mm) = 7.3074E-3 × hp. f was controlled through the angular

rotation velocity of a motor. Typical values obtained were x_0 from 0 to 3 mm and f from 0 to 20 s^{-1}. In all, a precise and independent control of both x_0 and f was obtained with this setup.

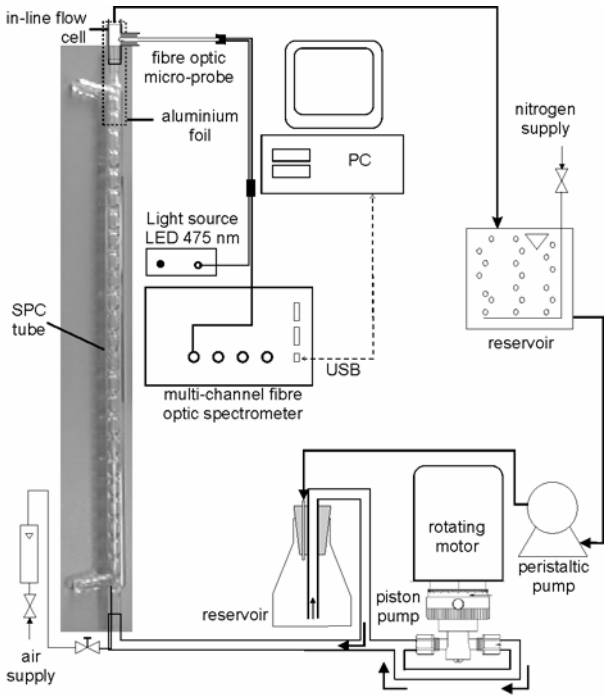

Figure 7-4. Experimental setup used in k_La studies.

Measurement of O_2 dissolved concentration

O_2 dissolved (OD) saturation level was measured on-line at the outlet of the SPC tube using a special fibre optic fluorescence micro-probe (O_2 micro-optrode) provided with SMA connectors (Avs-oxyprobe-1.5, Avantes, Eerbeek, The Netherlands). The working tip of the micro-optrode (1.5 mm diameter) was dip-coated with a ruthenium complex immobilised in a sol-gel matrix. When this complex is excited to fluorescence by a blue led (475 nm output peak), the level of the fluorescence (at about 600 nm) is inversely related to the concentration of the oxygen through the Stern-Volmer equation (Gouin et al., 1997; Wang et al., 1999):

$$\frac{I_0}{I} = 1 + K_{SV}\, x_{o_2} \qquad (7.1)$$

where I_0, I are the intensities in the absence or presence of O_2, respectively; K_{SV} is the Stern-Volmer constant; x_{O2} is the O_2 concentration (Gouin et al., 1997).

Reading of the light coming from the micro-optrode was made on-line using the master channel of a 4-channel optical spectrometer (AvaLights-2048, Avantes, Eerbeek, The Netherlands). The 2,048 pixels CCD detector was connected to an electronic board with 14 bit AD converter and USB/RS-232 interface. Data transfer between the optic spectrometer and a personal computer was controlled by AvaSoft full software (Avantes, Eerbeek, The Netherlands).

The micro-optrode was attached to a flow cell installed at the exit of SPC tube. Since at some oscillation conditions the diameter of the micro-optrode is of the same magnitude of the bubbles' diameter, the problem of direct impingement of bubbles was minimized by using a plain pipe section in the flow cell with an internal diameter slightly higher (5.0 mm) than that of the SPC tube (4.4 mm). It avoided the adsorption of bubbles to the micro-optrode tip, which might complicate the attainment of a steady-state. From previous hydrodynamic studies (e.g. Reis et al. 2004) it was observed that the volume within each single cavity of a SPC tube is well-mixed using OFM on this range of f and x_0, thus the O_2 concentration was taken as uniform around the micro-optrode tip.

Prior to the beginning of the experiments, the micro-optrode was calibrated by running a O_2 free (0 % O_2 saturation level) and a O_2 saturated (100 % O_2 saturation level) continuous water stream, in the presence of smooth fluid oscillations (say 10 s^{-1} and 1 mm). The O_2 free water was obtained by continuously bubbling nitrogen in an external reservoir until an O_2 saturation level of 0 % (12 mm O_2 probe, Mettler-Toledo, Switzerland), while the O_2 saturated solution was achieved by bubbling of compressed air until the O_2 electrode readout was 100 %. Values of K_{SV} and I_0 from Eq. (7-1) were determined by Avasoft full software (Avantes, Eerbeek, The Netherlands).

Experiments started by filling the apparatus volume with oxygen-free water re-circulated until a constant and null O_2 saturation level was measured in the micro-optrode (i.e. 0 %). Then, pump was set to a constant fluid net flow (ν = 1.58 ml min^{-1}) of oxygen-free water and a constant airflow (ν_g) of 0.28 ml min^{-1} (i.e., $U_g = 3.7\times10^{-4}$ m s^{-1} or 0.064 vvm in a 350-mm-long SPC tube) was injected by a syringe's needle through the bottom of the SPC tube, at time t = 0. Injection and O_2 measuring points were separated by the distance described in Table 7-1. An integration time of 450 milliseconds was used and 10 consecutive measurements were averaged in order to obtain more stable readings (and thus eliminating signal

oscillations), allowing an experimental measurement of O_2 saturation level every 4.5 seconds. All experiments were performed at room temperature (20 °C) using distilled water as main fluid.

The SPC tube was covered with aluminium foil at the measuring point (at the top – outlet – of the reactor) to reduce the noise due to environmental light. PVC tubes were used in all the setup and fitted with rigid PVC-connectors to minimise gas diffusion through the tube walls. Experiments were performed in duplicate at x_0 of 0, 0.5, 1.0, 2.0 and 3.0 mm and f of 0, 3.0, 7.5, 10.0, 15.0 and 20.0 s^{-1}, covering different OFM regimes with Re_o = 0 to ~1,607.

Determination of O_2 mass transfer coefficients

Air-water O_2 mass transfer coefficient, k_La, was estimated from an O_2 mass balance to the liquid stream in a SPC tube at initial and final steady states. This can be done because flow is tubular. Considering a differential (plug flow) reactor, a mass balance to all SPC tube volume yields:

$$\frac{dx_{O_2,i}}{dt} = k_L a \left(x_{o_2,sat} - x_{o_2,i}\right) \tag{7.2}$$

Considering that $t_i = l_i\ \tau / L$, then $dt = \tau\ dl / L$. Therefore, Eq. (7.2) can be re-written as follows:

$$\frac{dx_{O_2,i}}{dl} = \frac{\tau}{L} k_L a \left(x_{o_2,sat} - x_{o_2,i}\right) \tag{7.3}$$

The spatial boundary conditions are for the inlet

dl = 0 and $x_{O2,i} = x_{O2,in}$ (7.4)

and for the outlet

$dl = L$ and $x_{O2,i} = x_{O2,out}$ (7.5)

Rearranging and considering a null O_2 concentration in the inlet stream, i.e. $x_{O2,in}$ = 0, yields:

$$k_L a = -\frac{1}{\tau} ln\left(1 - \frac{x_{o_2,out}}{x_{o_2,sat}}\right) \tag{7.6}$$

This equation allows the estimation of averaged k_La values in the SPC tube volume, assuming a near plug flow situation. Note that Eq. (7.6) can only be applied for outlet O_2 concentrations under 100 % of saturation, i.e. $x_{O2,out} < x_{O2,sat}$.

Experimental measurement of ε_G

The gas hold-up, ε_G, was measured at batch and continuous flow of liquid-phase by recording the changes in the liquid height from SPC1 tube using a fine scaled (± 0.5 mm) plain pipe with 6 mm internal diameter fitted to the outlet of the SPC tube, similarly to the procedure followed by Oliveira and Ni (2001). The precision of this setup allowed an estimation of ε_G in most experiments with a final error ≤ 5 %. A 6 mm diameter was chosen for the plain pipe to avoid bubble retention after the outlet of the SPC tube, thus allowing a more accurate measuring of ε_G within the SPC tube. The procedure involved measuring the liquid level in the fine scale plain pipe in the absence of gas, h_0, and the corresponding level, h, when gas was continuously introduced at a given flow rate (0.28 ml min^{-1}). At batch operation mode (no fluid net flow) the liquid surface is initially fixed at a stable level (h_0). Then, the gas inlet valve is opened and the final steady-state liquid level (h) measured. This final steady-state is achieved after some minutes for the majority of the combinations of f and x_0 but it may take much longer when f is either very low (≤ 3 s^{-1}) or very high (≥ 15 s^{-1}). In continuous operation (with a fluid net flow), a reverse proceeding setup was applied: the reactor was operated for 5 to 10 minutes at the desired f, x_0, ν and ν_g. Then, simultaneously the fluid level was fixed (h) and both fluid and gas streams stopped. After rinsing of all bubbles, the final liquid level (h_0) was measured.

In both continuous and batch mode, hold-up (ε_G) was calculated from the volume variation (ΔV) by:

$$\varepsilon_G = \frac{\Delta V}{V} \tag{7.7}$$

where $\Delta V = (h - h_0)\frac{\pi}{4}0.006^2$.

The main advantage of this procedure is its easy implementation. The batch mode determination was also adopted due to the major importance of knowing the gas-phase behaviour when this novel reactor is operated in a batch mode under aerobic (aerated) conditions.

7.3 Results and discussion

k_La for continuous flow as a function of f and x_0

Enhanced mass transfer rates are expected (according to Perry, Green, & Maloney, 2002) from previous hydrodynamic studies using the SPC geometry, whereas PIV and numerical simulations were included (e.g. Reis et al., 2005). High outflow rates were observed throughout an overall oscillation cycle (as illustrated above in Figure 7-1). Thus, air-water experiments were conducted and reported in this work to quantify the efficiency of gas-liquid mass transfer of O_2 expressed by the k_La coefficient. Several experiments were run at different f (0 to 20 s^{-1}) and x_0 (0 to 3 mm) while keeping a constant liquid flow rate of 1.58 ml min^{-1} and a volumetric airflow of 0.28 ml min^{-1} (i.e. $U_g = 3.7\times10^{-4}$ m s^{-1}). In SPC1 (350 mm length) tube saturation was effectively achieved at $f > 7.5$ s^{-1} and $x_0 > 0.5$ mm (results not shown), suggesting k_La values of 0.03 s^{-1}, or above, according to Eq. (7.6). However, it was not possible to estimate k_La with SPC1 tube at all the desired combinations of f and x_0 and at the present mean residence time of liquid-phase, τ, because Eq. (7.6) is not applicable when $x_{O2,out} = x_{O2,sat}$. As v and v_g were fixed the option was to work with a SPC tube with a smaller length, thus all air-water mass transfer experiments were repeated with a second, shorter SPC tube (SPC2), 75 mm length. This length has demonstrated to be suitable to avoid O_2-saturation at the tested combination of experimental conditions of v_g, v, f and x_0. All experimental conditions were kept constant as shown in Table 7-1. A similar behaviour was found between experiments performed with SPC1 and SPC2 tubes (results not shown) in terms of the increase of O_2 saturation level with the increase of f and x_0. Mean values of O_2 saturation levels obtained at such experimental conditions with SPC2 tube are shown in Figure 7-5.

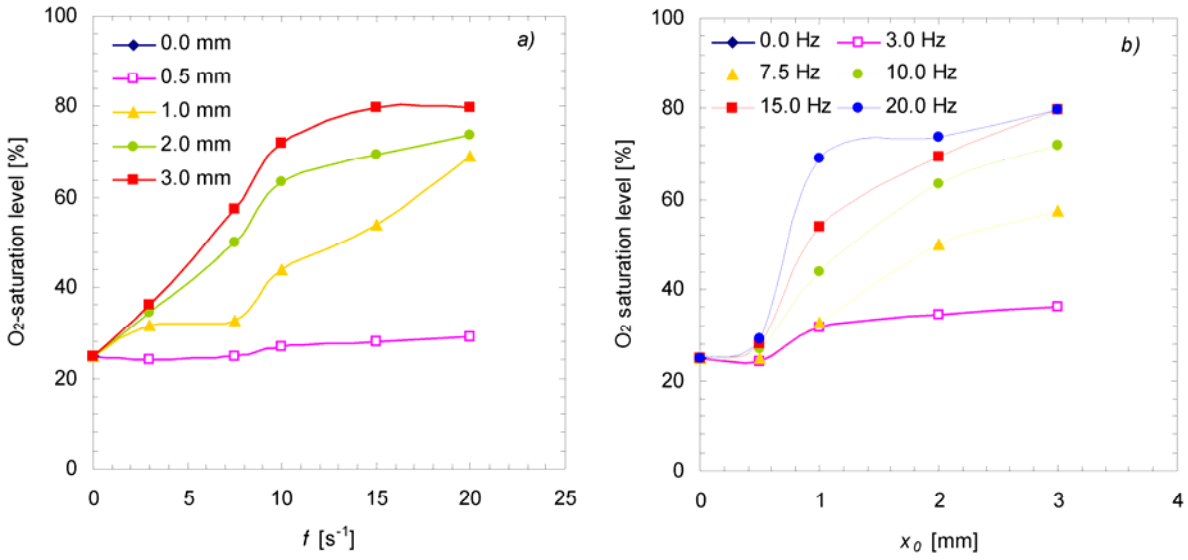

Figure 7-5. Effect of OFM on the mean value of O_2 saturation levels at the outlet of SPC2 tube: *a)* effect of *f*; *b)* effect of x_0.

It may be concluded from Figure 7-5 that oscillation conditions (*f* and x_0) affect the O_2 saturation level at the exit of the SPC2 tube, suggesting different air-water O_2 mass transfer rates or/and a different behaviour of the bubbles inside the tube at different oscillation conditions. The variation in O_2 saturation level caused by an increase of *f* was found to be different from the variation caused by an increase of x_0 (Figure 7-5a and Figure 7-5b). Saturation levels were maximised for *f* of 20 s^{-1} and x_0 of 3 mm, presumably due to the higher power input at such oscillation conditions.

Experimental k_La values were estimated from O_2 saturation levels in SPC2 tube using Eq. (7-5), and are displayed in Figure 7-6.

Figure 7-6 shows k_La increasing with both *f* and x_0 for all tested fluid oscillation conditions. Again, the effect of x_0 over k_La appears to be more significant than that of *f*: doubling x_0 induces a greater increase in k_La than doubling *f*; in fact, the same increase in k_La may be obtained by increasing x_0 only from 0 to 3 mm whereas an increase of *f* from 0 to 20 s^{-1} is needed. Considering the same value of Re_o corresponds to similar fluid mechanics (which is believed to be truth up to this date), it is evident that k_La can not be directly correlated with that dimensionless number. This is an evidence indicating that x_0 controls the length of eddy generation along the column and is in agreement with studies on mass transfer in a

conventional OFR, as reported by Ni et al. (1995). This result is also in agreement with studies of mixing time and liquid residence time distribution previously reported for the SPC geometry (e.g. Reis et al., 2004). Actually, such variance is already suggested by the different exponent terms in the two time-average power consumption power input prediction models usually considered for OFR: the acoustic model (Baird & Stonestreet, 1995) and the quasi-steady flow model (Jealous & Johnson, 1955).

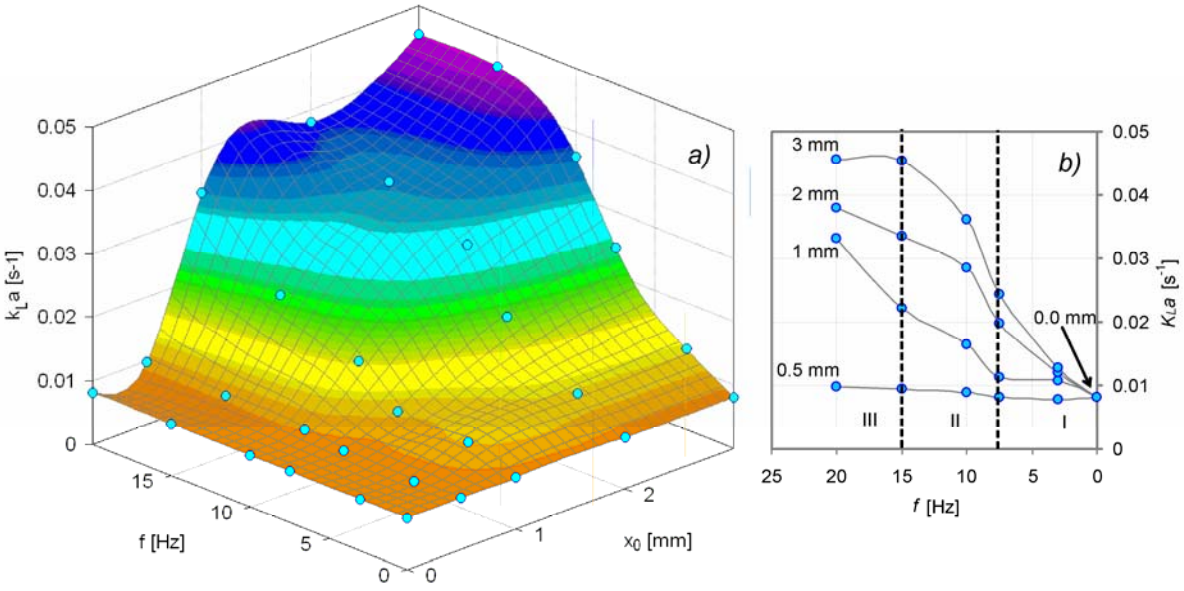

Figure 7-6. Estimated k_La values for the SPC2 tube. *a)* 3-D representation of the effect of f and x_0; *b)* plot of k_La regimes.

In addition, Figure 7-6 allowed the identification of three different k_La regimes (represented by vertical dotted lines), also confirmed in k_La results for the SPC1 tube (results not shown). In regime I (right-hand side of Figure 7-6b) k_La shows a small increase with the increase of f. In regime II (central zone of Figure 7-6b) k_La shows a logarithmic increase with increasing f. It suggests that for those oscillation conditions (f of 7.5 and 10 s^{-1}) k_La is essentially dependent on the mixing intensity, i.e. the k_La is enhanced as a direct result of an improvement on OFM. This is in agreement with the logarithmic dependency of mixing times with increasing f found in mixing time studies performed for this SPC geometry. In the right-hand side of Figure 7-6b (regime III) an irregular behaviour of k_La is observed with increasing f: at extreme values of x_0 (0.5 and 3.0 mm) an increase of f has no effect over k_La while for intermediate values of x_0 the increase of f leads to an increase of k_La values.

Results shown in Figure 7-6 are to some extent similar to those reported by Ni et al. (1995) in a conventional OFR. These authors assessed the k_La values in a sparged OFR for f of 3 to 12 s^{-1} and x_0 ranging from 4 to 14 mm. The observed effect of f over k_La is similar and fits in regime II meaning that in this range fluid flow patterns in both OFR and novel reactor are similar (Reis et al., 2005).

Globally, the maximum value of k_La obtained in this work was of ca. 0.05 s^{-1}, for v_g = 0.28 mm s^{-1} and at a Re_o of about 1,600. It is significantly higher than the maximum values reported for work in OFRs: a value of 0.01 s^{-1} was reported by Hewgill et al. (1993) at a similar Re_o and a maximum value of 0.02 s^{-1} was achieved at a Re_o of 5,000. This improvement is remarkable, especially considering that the work of Hewgill et al. (1993) was performed with four-fold higher values of v_g (1.1 mm s^{-1}). Also, Oliveira and Ni (2004) reported maximum values of k_La of 0.017 s^{-1} at 1.06×10^{-3} m s^{-1} or 0.04 s^{-1} at 4.24×10^{-3} m s^{-1} for a value of x_0 of 4 mm and f of 8 s^{-1}. In terms of the effects of f and x_0 over k_La a comparison is shown in Figure 7-7 between the present work and that of Oliveira and Ni (2004).

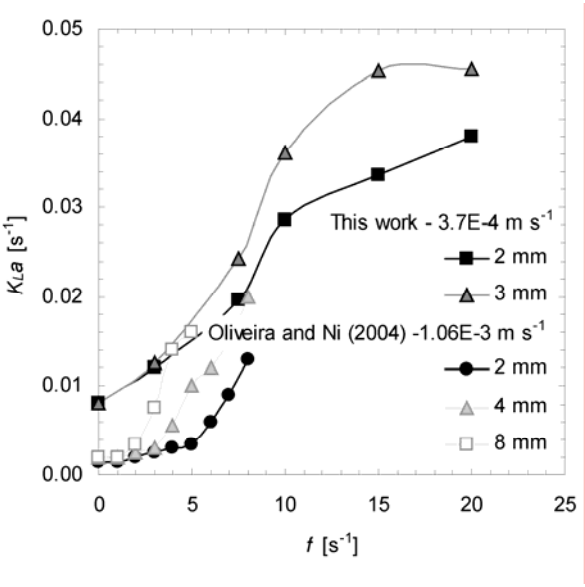

Figure 7-7. Comparison of k_La values obtained with SPC2 tube and with the work of Oliveira and Ni (2004) using a conventional 50 mm internal diameter OFR for similar fluid oscillation conditions.

A coarse best-fitting to experimental averaged k_La values of Figure 7-6 leads to the following equation:

$$k_L a = 7.63\times10^{-3}\ f\ x_0 \qquad (7.8)$$

where f is in SI units (s^{-1}) while x_0 is in millimetres. Using a similar equation, results of Oliveira and Ni (2004) shown in Figure 7-7 is fitted by:

$$k_L a = 4.3 \times 10^{-3} \; f \; x_0 \tag{7.9}$$

Results in Figure 7-7 demonstrate the high performance of this screening reactor for O_2 mass transfer. The higher term in Eq. (7.8) when compared to Eq. (7.9) means that the SPC tube geometry is about 77 % more efficient in terms of the O_2 mass transfer process than the OFR, when both are operated at the same x_0 and f.

Experimental measurement of ε_G

There are a number of parameters directly related to O_2 mass transfer, including gas hold-up (ε_G), interfacial area, as well as bubbles' size and rising velocity. While performing O_2 mass transfer experiments, the behaviour of the gas-phase within a single SPC tube was carefully observed in order to identify significant changes when altering the fluid oscillation conditions. Therefore, ε_G was determined for the same combination of f and x_0 and the same operational conditions (i.e. ν = 1.58 ml min^{-1} and ν_g = 0.28 ml min^{-1}). For these experiments, the 350-mm-long (SPC2) tube was used instead of SPC2 tube to minimise the measuring error. Further experiments allowed assessing ε_G in a gas-liquid system when the reactor is run in the absence of a continuous flow of liquid-phase (i.e., at batch mode and ν_g = 0.28 ml min^{-1}). Results of ε_G measurement are presented in Figure 7-8. Note the one order magnitude higher values in y-axis at Figure 7-8a) in comparison with values in Figure 7-8b).

The value of ε_G is in fact very small (≤ 5 %) in the presence of the continuous liquid-phase (Figure 7-8a). All ε_G values were found to be at least three times smaller than the $\nu_g/(\nu_g+\nu)$ ratio (i.e. ~16 %). This means a lower residence time of gas-phase in comparison with the residence time of the liquid-phase within the reactor volume, thus reducing the contacting time of bubbles (τ_d); note that τ_d is given by (Baird & Stonestreet, 1995):

$$\tau_d = \frac{H \, \varepsilon_G}{U_g} \tag{7.10}$$

where U_g is the mean superficial gas velocity (based on d).

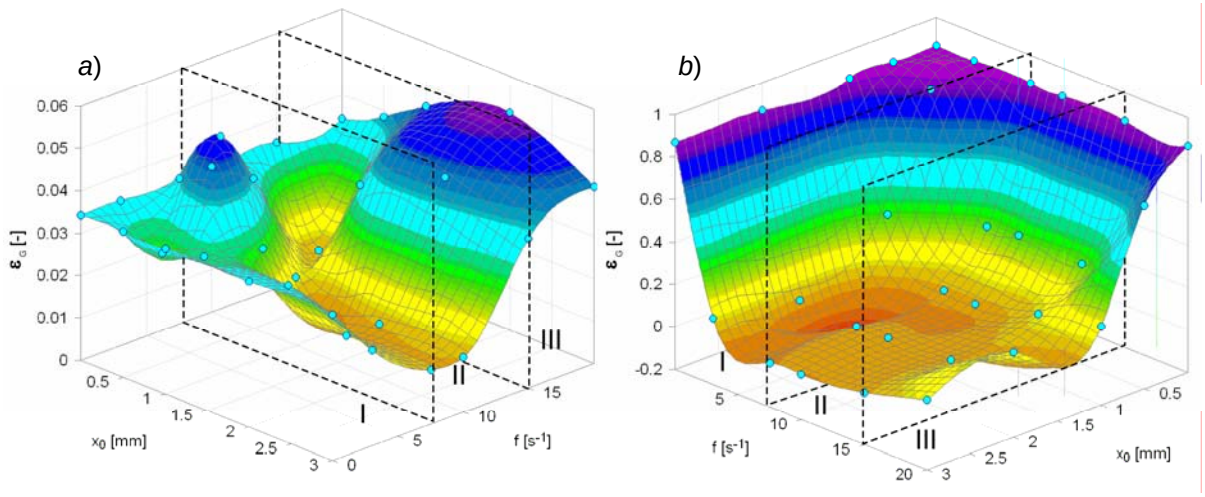

Figure 7-8. Effect of f on ε_G when operating the SPC1 tube under OFM and *a)* a continuous fluid net flow (v = 1.58 ml min^{-1}) or *b)* in batch mode (i.e. v = 0 ml min^{-1}).

The net flow of fluid facilitates the upward movement (rising) of bubbles, facilitating the gas disengagement at the top of the tube.

ε_G determined at batch (Figure 7-8b) demonstrated that very high gas-fractions (up to 90 %) may be obtained through the continuous sparging of a gas into this novel reactor due to its geometry, essentially when small values of x_0 (0.5 mm) are used. This is generally undesirable and may be overcome by operation at higher x_0 values, preferably 3 mm, resulting in ε_G values between 1 and 30 %.

Despite the above mentioned differences between continuous and batch operation, ε_G results share some similarities demonstrating that ε_G is in fact controlled by the OFM in the novel reactor. Figure 7-8 shows that imposition of fluid oscillation leads initially to a decrease of ε_G with the increase of f. Indeed, for all x_0 considered in this study (0 to 3 mm) ε_G was minimized for f of 7.5 and 10 s^{-1} (regime II). The minimum ε_G registered was 0.013 ± 0.003 (i.e. ~1.3 %) for both modes of operation, when running at 10 s^{-1} and 3 mm. The different behaviour of ε_G with the variation of f below 7.5 s^{-1} (regime I) and above 10 s^{-1} (regime III) confirms the division of the effect of f over ε_G in three regions as represented in Figure 7-8 by the vertical dotted lines. These three regions are perceptible in both Figure 7-8 and Figure 7-6, meaning that ε_G is affected by oscillation conditions in the same way as k_La. This correspondence between k_La and ε_G is supported by the work of Oliveira and Ni (2004) and is discussed below in more detail.

Comparison with conventional gas-liquid systems

In this section, k_La values obtained in this work with the screening reactor are compared with published work with conventional reactors, such as the bubble column. Deckwer et al. (1974) modelled k_La in a simple bubble column as:

$$k_L a = b U_g^n \tag{7.11}$$

where n and b are empirical constants. Hewgill et al. (1993) working with an OFR yielded results of n = 1.01 and b = 10.1 m^{-1}, consistent with Deckwer's results. Extrapolating such results for the present case and attending to the fact that Hewgill's work was performed for a range of U_G from 0.42 to 2.4 mm s^{-1} and that in the present study U_G is very close to Hewgill's minimum value (0.37 mm s^{-1}), a value of k_La of 0.00345 s^{-1} is estimated with Eq. (7.11). Comparison with Figure 7-6 shows a 2.3-fold enhancement of k_La in continuous flow with this novel reactor, while coupling of an unsteady motion component (f = 20 s^{-1} and x_0 = 3 mm) permits to achieve a thirteen-fold increase of k_La. A broader comparison of the performance of the screening reactor with further vessel designs for O_2 mass transfer in a gas -liquid system is summarised in Table 7-2. Note that despite of the very low v_g used in this study (0.37 mm s^{-1}), an O_2 mass transfer efficiency of up to 21 % (w/w) was registered with this novel reactor, which can be considered very satisfactory when compared with works in OFRs (e.g., Oliveira & Ni, 2001; Oliveira & Ni, 2004) and in more standard reactors such as STR, airlift and bubble columns.

Table 7-2: Comparison of performance of the SPC geometry for O_2 mass transfer in a gas-liquid system with further reported works in literature

Vessel	Air feed	k_La [s^{-1}]	Conditions	Reference
Screening reactor	U_g = 0.37 mm s^{-1} (0.064 vvm in SPC1; 0.282 vvm in SPC2)	ca. 0.05	Re_O = 1,600	This work
		0.008	Re_O = 0	
OFR	U_g = 1.1 mm s^{-1} (0.06 vvm)	0.003	Re_O = 0	Hewgill et al. (1993)
		0.004	Re_O = 959	
		0.006	Re_O = 2,510	
		0.017	Re_O = 5,200	
OFR	U_g = 1.06 mm s^{-1} (0.05 vvm)	0.017	Re_O = 9,743	Oliveira and Ni (2004)
OFR	U_g = 4.24 mm s^{-1} (0.20 vvm)	0.04	Re_O = 9,743	Oliveira and Ni (2004)
STR	U_g = 7.84 mm s^{-1} (0.54 vvm)	0.098	-	Vasconcelos et al. (2003)
Airlift reactor	Ug = 8.3 mm s^{-1} (0.20 vvm)	0.095	-	Vasconcelos et al. (2003)
Bubble column	Ug = 0.37 mm s^{-1}	0.00345	estimated Eq. (7.11)	Deckwer et al. (1974)
Bubble column	Ug = 22 mm s^{-1} (1.31 vvm)	0.066	-	Vasconcelos et al. (2003)

Empirical correlation for k_La

A coarse correlation such as Eq. (7.8) was found to be not suitable to predict k_La in this novel reactor with a small error (say, below 10 %). Equation (7.8) assumes a linear effect of f and x_0 over k_La, which was previously shown in this work to be untruthful. Thus, a (semi)-empirical correlation was formulated for modelling k_La in the SPC tube. The procedure used was as follows: the difference in k_La values obtained in the absence and in the presence of OFM (representing the enhancement of k_La due to oscillatory motion) was represented as a function of x_0. Then, experimental points were best fitted by a natural logarithmic function of the type: $k_La = a \ln(x_0) + b$, at each constant f. Afterwards, parameters a and b were determined as a function of f. Three different functions were obtained, corresponding to each of the three regimes previously identified (regime I, II and III), and resulting in Eq. (7.12) for estimation of k_La in the SPC tube.

$$k_L a\,(s^{-1}) = 0.0081 + \begin{cases} 0.0015\ (f - 1.33)\ln(x_0) + (0.0007\ f + 0.00003) & f \in [0 - 7.5\ s^{-1}[\\ 0.0144\ (\ln(f) - 1.33)\ln(x_0) + (0.0128\ln(f) - 0.02) & f \in [7.5 - 15\ s^{-1}] \\ 0.0191\ \ln(x_0) + (0.0008\ f + 0.0016) & f \in [15 - 20\ s^{-1}] \end{cases} \quad (7.12)$$

Equation (7.12) fitted quite well experimental data, as shown in Figure 7-9a (r^2 = 0.979). In Figure 7-9 it is also clear the better accuracy of Eq. (7.12) when compared to the coarse fitting achieved with Eq. (7.8).

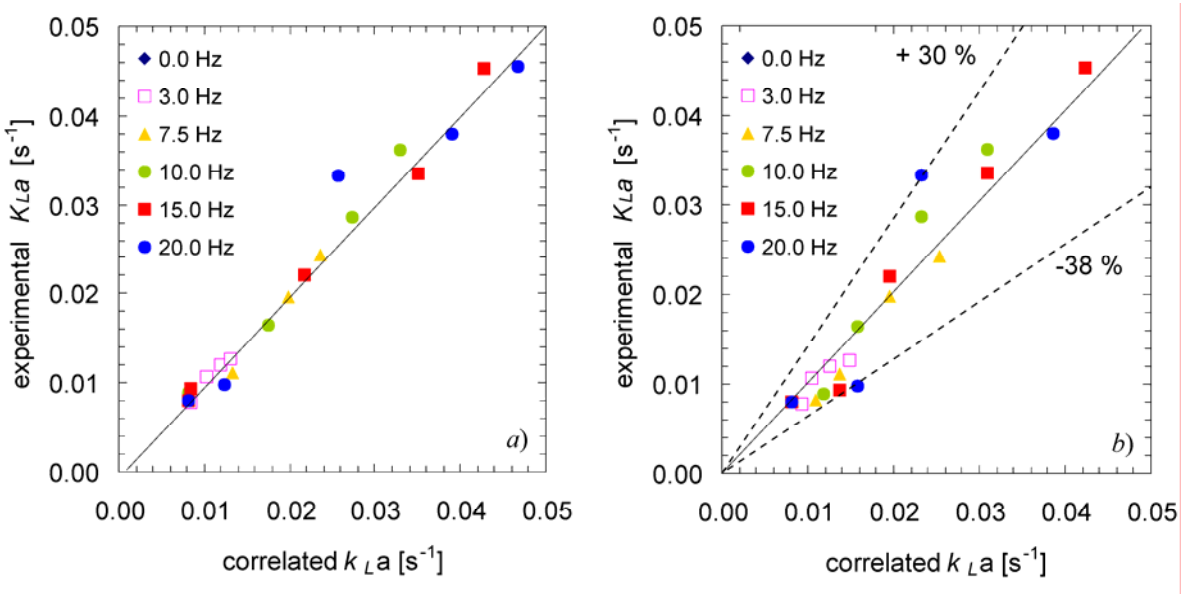

Figure 7-9. Comparison of experimental $k_L a$ values with estimated ones, using: *a)* the semi-empirical correlation shown in Eq. (7.12); *b)* the coarse correlation presented in Eq. (7.8). The solid line represents $y = x$.

The logarithmic dependency of $k_L a$ *versus* x_0 is similar to that obtained in the mixing/residence time studies using the 350-mm-long SPC tube (SPC1). In fact, at the fluid oscillation conditions of regime II, $k_L a$ enhancement was found to be essentially the result of the improvement of fluid mechanics within the screening reactor, as demonstrated in Figure 7-10. Values of $k_L a$ found for regime II (f of 7.5 and 10 s^{-1}) effectively correlates with the OFM intensity, as expressed by the best-fitted backmixing parameter, G (Mecklenburgh & Hartland, 1976). In our previous residence time studies, parameter a was found to be constant and equal to 0.0169 while parameter b was found to be of the type: $b = c \ln(f) + d$, with c = 0.0072 and d = -0.0073. These values are of the same order of magnitude as the parameters obtained for

k_La correlation in the range of 7.5 to 10 s^{-1}, according to Eq. (7.12), thus confirming the relation between k_La and the OFM in regime II. One point in each of the curves f = 7.5 and 15 s^{-1} (determined at x_0 = 0.5 mm) is outside the considered fitting in Figure 7-10 because they were obtained at an OFM state (below a critical Re_o) different than that of the remaining points.

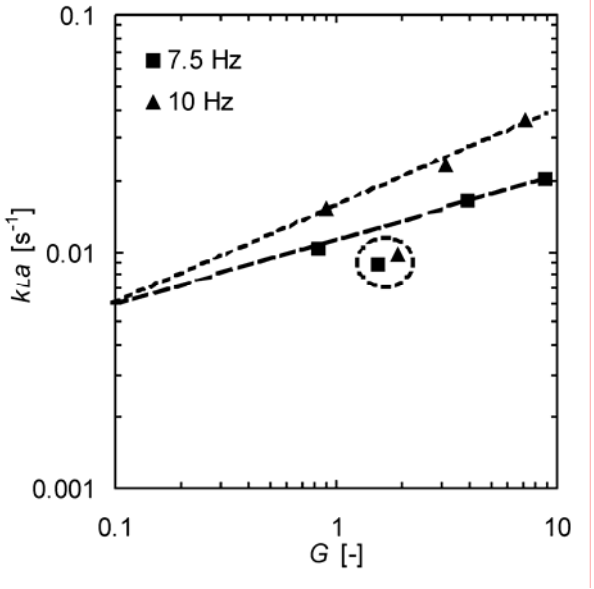

Figure 7-10. Correlation between the experimental k_La values and of the best-fitted backmixing parameter (G) of liquid phase (from Reis et al., 2004) for f in regime II (7.5 to 15 s^{-1}).

Understanding k_La enhancement in the novel screening reactor

Based on experimental observations of bubbles behaviour and k_La values above presented in this work the main processes responsible for enhancement of k_La in SPC geometry at each of the identified three regimes may be summarised as follows:

a) **regime I** (f from 0 to 7.5 s^{-1}): high diameter (d_b) bubbles are formed in the sparger and are effectively lagged by periodic constrictions. The main consequence is a high value of ε_G and thus an increased τ_G; when compared with the situation of gas sparged in a vertical (unbaffled) bubble column, at the same v_g. This generally results is a small enhancement of k_La;

b) **regime II** (f of 7.5 and 10 s^{-1}): increased shear rates lead to bubbles breakage and to a decrease of d_b to a value below that of the internal diameter of the tube in the constricted zone (i.e. < 1.6 mm). Thus, bubbles achieve a free upward motion. Consequently, ε_G is minimised leading to a small τ_G. The coupling of high bubbles interfacial area a (due to small d_b) with

increased OFM (due to the existence of intensive vortex rings) leads to a significant k_La enhancement, when compared with the situations of regime I and the gas sparging in a vertical bubble column;

c) **regime III** (*f* of 15 and 20 s^{-1}): high shear rates caused by very intensive OFM lead to the coexistence of bubbles breakage and coalescence as well as to a particular characteristic of OFRs: bubbles retention. The consequence is an increased ε_G and τ_d (when compared with regime II) and small *a* (when compared with the situation of regime I), which coupled with an intensive fluid mixing results in a significant general k_La improvement.

Figure 7-11 illustrates that the reported increase of k_La in regime III is essentially achieved due to an increase of ε_G (thus τ_d by means of bubbles retention capacity of this reactor), while in regime II the k_La increase is attached to a decrease of τ_d. In this last case, the overall k_La enhancement is related with the fluid flow patterns generated inside the reactor.

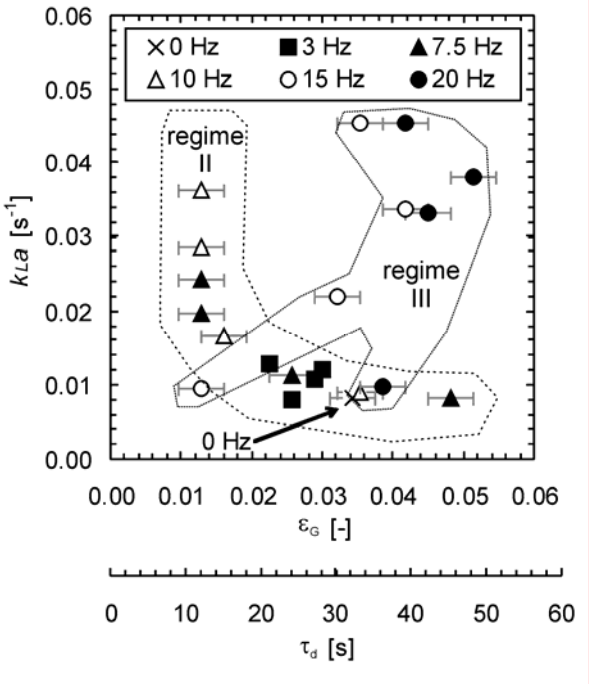

Figure 7-11. Variation of k_La with ε_G at different *f*. Dotted lines represents the general tendency. 0 to 7.5 s^{-1}: regime I; 7.5 to 15 s^{-1}: regime II; 15 to 20 s^{-1}: regime III.

Regimes I and II are in some extent equivalent to a bubble column, being analogue to the sparging of bubbles in a vertical tube. On the other hand, regimes II and III are similar to those identified in

conventional OFRs (e.g., Oliveira & Ni, 2004). In terms of OFRs, regime I is particular of this novel reactor due to its small-scale: because of the ratio d_b/d_0 is ~1, bubbles experience a drag when crossing each constriction which lag their progress towards the exit, therefore increasing their τ_d. A schematic summary of the main processes involved in k_La enhancement within SPC geometry is presented in Figure 7-12. The first row in Figure 7-12 summarises the bubbles behaviour experimental observed while the second row summarises the main consequences and the phenomenon leading identified as the major responsible to the obtained general k_La enhancement.

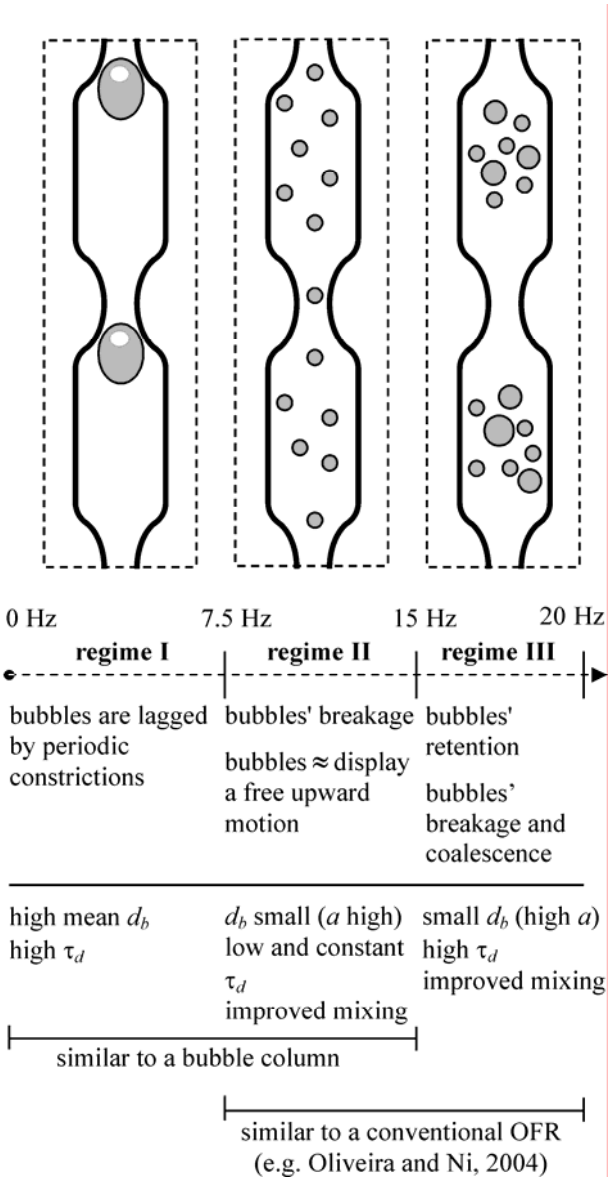

Figure 7-12. Schematic representation of bubbles behaviour in the three identified regimes, in the studied range of *f*.

The bubble breakage phenomenon experienced at regime II is demonstrated in Figure 7-13, showing the movement of a single bubble inside a cavity of the SPC tube for a sequence of ten frames at a rate of 24 frames per second, at a fluid oscillation conditions of 12 s^{-1} and 4 mm. White arrows in the bottom pictures in Figure 7-13 represent the piston stroke direction. Pictures were captured with a digital handy camera at a frame rate of 24 frames per second. Bubble shows a chaotic movement denoting a very intensive mixing. Note the smaller size of the bubble when compared to the internal diameter of the tube. Bubble breakage is perceptible at the seventh frame.

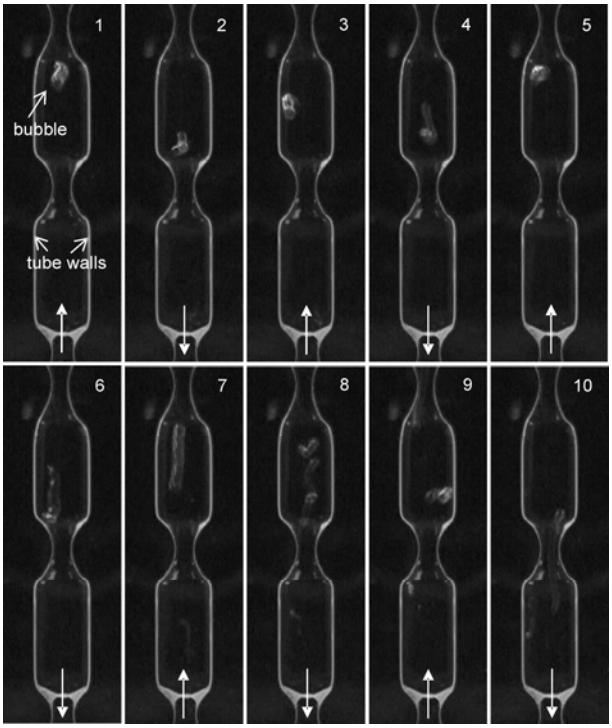

Figure 7-13. Ten frames sequence showing the bubble breakage phenomenon under OFM at 12 s^{-1} and 4 mm.

7.4 Conclusions

Experimental air-water O_2 mass transfer rates were estimated in a novel continuous scale-down oscillatory flow (micro-bioreactor) reactor through the on-line measurement of O_2 saturation level with an O_2 micro-optrode. Further experiments were run towards the assessment of gas hold-up (ε_G) in the reactor volume.

The volumetric mass transfer coefficient (k_La) was successfully demonstrated to be governed by the OFM conditions within the reactor: k_La increased considerably with both oscillation amplitude (x_0) and frequency (f), thus an empirical correlation was obtained. In addition, experimental k_La values for continuous flow were correlated with ε_G and the axial backflow (G parameter) in the reactor, whereas three k_La and ε_G regimes were identified (regime I, II and III) with increasing f from 0 to 20 s^{-1}. Triggering of bubble breakage was found to be responsible for transition from regime I to regime II, while the transition from regime II to regime III was associated with the bubble retaining capacity of this novel reactor, parallel to the reported capacity for catalyst particles' suspension (Reis et al., 2005). Due to the small-scale of the reactor and to the existence of tube constrictions, the mean residence time of rising bubbles (τ_d) was found to play a major effect in the global enhancement of k_La in the studied range of OFM regimes (i.e., f up to 20 s^{-1} and x_0 up to 3 mm, centre-to-peak).

In particular, the experimental k_La values obtained with this novel reactor represented a thirteen-fold increase in comparison with the predicted k_La values for a conventional bubble column operating the same gas superficial velocity (0.37 mm s^{-1}), according to the correlation of Deckwer et al. (1974). Such improvement is a great step forward for the application of this reactor e.g. to bioprocesses where mass transfer of a solute (e.g. O_2) from a gas into the liquid phase is often the rate-controlling step. Overall, it was concluded that the k_La values obtained in this work are in the same order of magnitude of those reported for the most efficient reactor designs applied in cell cultures, and that coupling of OFM effectively leads to an enhancement of k_La, thus forecasting the successful application of this scale-down reactor as a bioprocess screening unit. This will be the subject for future works.

7.5 Notation

d *tube internal diameter, m*

d_0 *internal constriction diameter, m*

d_b *bubble mean diameter, m*

f *oscillation frequency, s^{-1}*

G *best-fitted backmixing parameter*

h *gas-liquid dispersion level, m*

h_0 *liquid height, m*

I_0 *fluorescence intensity in the absence of oxygen, counts*

I *fluorescence intensity in the presence of oxygen, counts*

k_La *oxygen mass transfer coefficient,* s^{-1}

K_{SV} *Stern-Volmer constant,* $m^3\ mol^1$

l *micro-optrode location, m*

L *total tube length, m*

Re_o *oscillatory Reynolds number, dimensionless*

U *mean superficial velocity,* $m\ s^{-1}$

v *volumetric flow rate,* $m^3\ s^{-1}$

V *volume,* m^3

x_0 *oscillation amplitude, m*

x_{O2} *oxygen concentration,* $mol\ m^{-3}$

Subscripts

f *fluid*

g *gas*

in *inlet*

out *outlet*

sat *saturation*

Greek symbols

α *constriction free-area, dimensionless*

ε_G *gas hold-up, dimensionless*

Λ *distance between consecutive constrictions, m*

μ *fluid viscosity,* $kg\ m^{-1}\ s^{-1}$

ρ *density of the fluid,* $kg\ m^{-3}$

τ *mean hydraulic time, s*

τ_d *mean residence time of bubbles, s*

7.6 References

Baird, M.H.I. & Garstang, J.H. (1967). Power consumption and gas hold-up in a pulsed column. *Chemical Engineering Science*, 22(12), 1663-&.

Baird, M.H.I. & Garstang, J.H. (1972). Gas absorption in a pulsed bubble column. *Chemical Engineering Science*, 27(4), 823-&.

Baird, M.H.I. & Stonestreet, P. (1995). Energy-dissipation in oscillatory flow within a baffled tube. *Chemical Engineering Research & Design*, 73(A5), 503-511.

Bellhouse et al. (1973). High-efficiency membrane oxygenator and pulsative pumping system, and its application to animal trials. *Transactions American Society for Artificial Internal Organs*, 19, 72-79.

Blakebro, N. & Sambamur, K. (1966). Mass transfer and mixing rates in fermentation vessels. *Biotechnology and Bioengineering*, 8(1), 25-&.

Deckwer, W.D., Burckhar.R, & Zoll, G. (1974). Mixing and mass-transfer in tall bubble columns. *Chemical Engineering Science*, 29(11), 2177-2188.

Gogate, P.R. & Pandit, A.B. (1999). Survey of measurement techniques for gas-liquid mass transfer coefficient in bioreactors. *Biochemical Engineering Journal*, 4(1), 7-15.

Gouin, J.F., et al. (1997). A fibre-optic oxygen sensor for oceanography. *Sensors and Actuators B-Chemical*, 39(1-3), 401-406.

Hewgill, M.R., et al. (1993). Enhancement of gas-liquid mass-transfer using oscillatory flow in a baffled tube. *Chemical Engineering Science*, 48(4), 799-809.

Jealous, A.C. & Johnson, H.F. (1955). Power requirements for pulse generation in pulse columns. *Industrial and Engineering Chemistry*, 47(6), 1168-1169.

Linek, V., Vacek, V., & Benes, P. (1987). A critical-review and experimental-verification of the correct use of the dynamic method for the determination of oxygen-transfer in aerated agitated vessels to water, electrolyte-solutions and viscous-liquids. *Chemical Engineering Journal and the Biochemical Engineering Journal*, 34(1), 11-34.

Linek, V., Sinkule, J., & Benes, P. (1991). Critical-assessment of gassing-in methods for measuring kLa in fermenters. *Biotechnology and Bioengineering*, 38(4), 323-330.

Linek, V., Sinkule, J., & Benes, P. (1992). Critical-assessment of the dynamic double-response method for measuring kla - experimental elimination of dispersion effects. *Chemical Engineering Science*, 47(15-16), 3885-3894.

Mackley, M.R. (1991). Process innovation using oscillatory flow within baffled tubes. *Chemical Engineering Research & Design*, 69(3), 197-199.

Mackley, M.R., et al. (1998). Evaluation of a novel self-aerating, oscillating baffle column. *Canadian Journal of Chemical Engineering*, 76(1), 5-10.

Mecklenburgh, J.C. & Hartland, S. (1976). *The theory of backmixing* (1st edition ed.). New York: John Wiley & Sons, Inc.

Ni, X., et al. (1995). A comparative-study of mass-transfer in yeast for a batch pulsed baffled bioreactor and a stirred-tank fermenter. *Chemical Engineering Science*, 50(13), 2127-2136.

Ni, X. & Gao, S. (1996). Scale-up correlation for mass transfer coefficients in pulsed baffled reactors. *Chemical Engineering Journal*, 63(3), 157-166.

Ni, X.W., Gao, S.W., & Pritchard, D.W. (1995). Study of mass-transfer in yeast in a pulsed baffled bioreactor. *Biotechnology and Bioengineering*, 45(2), 165-175.

Oliveira, M.S.N. & Ni, X. (2001). Gas hold-up and bubble diameters in a gassed oscillatory baffled column. *Chemical Engineering Science*, 56(21-22), 6143-6148.

Oliveira, M.S.N. & Ni, X.W. (2004). Effect of hydrodynamics on mass transfer in a gas-liquid oscillatory baffled column. *Chemical Engineering Journal*, 99(1), 59-68.

Perry, R.P., Green, D.W., & Maloney, J.O. (2002). *Perry's chemical engineer', platinum edition*. New York: McGraw-Hill.

Reis, N., et al. (2004). Residence times and mixing of a novel continuous oscillatory flow screening reactor. *Chemical Engineering Science*, 59(22-23), 4967-4974.

Reis, N., et al. (2005). Fluid mechanics and design aspects of a novel oscillatory flow meso-reactor. *Chemical Engineering Research & Design*, 83(A4), 357-371.

Serieys, M., Goma, G., & Durand, G. (1978). Design and oxygen-transfer potential of a pulsed continuous tubular fermentor. *Biotechnology and Bioengineering*, 20(9), 1393-1406.

Vant'riet, K. (1979). Review of measuring methods and results in nonviscous gas-liquid mass-transfer in stirred vessels. *Industrial & Engineering Chemistry Process Design and Development*, 18(3), 357-364.

Wang, W., et al. (1999). Applying fiber-optic sensors for monitoring dissolved oxygen. *Sea Technology*, 40(3), 69-+.

Chapter 8 Aerobic and anaerobic growth on glucose of *Saccharomyces cerevisiae* in the micro-bioreactor

The experimental performance of the micro-bioreactor has been tested in the presence of a fermentation with *Saccharomyces cerevisiae*. Several batch fermentations with a flocculent *Saccharomyces cerevisiae* strain were carried out under oscillatory flow mixing (OFM) at a range of initial glucose concentrations (S_0) of ~5-20 g/L and compared to yeast growth kinetics in a stirred tank (ST) bioreactor. Aerobic fermentations were monitored *ex-situ* in terms of pH, DO, glucose consumption and biomass and ethanol production (wherever applicable). An average biomass production increase of 83 % was obtained in the micro-bioreactor when compared with the ST, with less 93.6 % air requirements. It also corresponded to a 214 % increase on biomass production when compared with growth in a shaken flask (SF) at S_0 = 20 g/L.

Further anaerobic fermentations at the same initial glucose concentration ranges gave the opportunity to use state-of-the-art fibre optics technology for *on-line* and real-time monitoring of this bioprocess. Time profiles of biomass concentration (measured as optical density (OD)) were very similar in the ST bioreactor and in the micro-bioreactor, with a highly reproducible yeast growth in these two scale-down platforms.

Keywords: novel micro-bioreactor; scale-down; oscillatory flow mixing; biomass production; fermentations; *Saccharomyces cerevisiae*.

8.1 Introduction

Bioprocess development is currently hampered by a paucity of high-throughput techniques to evaluate the effect of operational/nutritional parameters on cells growth (*Escherichia coli*, yeast, CHO, BHK, and other workhorses) and product formation in a systematic and statistically significant manner (Kostov et al. 2001). Bioprocesses development/optimisation in the pharmaceutical industry often calls for significant numbers of fermentations under varying environmental and nutritional conditions. That is expensive and time-consuming in practice, as this type of research is typically performed in shake flasks or in small (1-3 L) bioreactors (Tholudur et al. 1999). Thus, a technology for fast, reliable and inexpensive parallel bioprocessing is strongly desirable. The idea may be to scale-down the volume of a bioreactor system while preserving its control capabilities.

Shake flask fermentation (typical working volumes 50 - 500 mL) has been used with very little change for over five decades for cell growth culture, media screening and cell expansion, but they present very little capacity to control the bioprocess parameters (Buchs 2001; Maier and Buchs 2001; Rhodes and Gaden 1957). Plate readers offer the opportunity for studies of parallel bioprocesses (Li et al. 2000), but they can read one or two parameters (absorbance and/or fluorescence) and are not equipped with chemical sensors or actuators for bioprocess control. The automated shaken microwell system has been used to obtain process information on biological materials, including on bacterial fermentations (Duetz et al. 2000; Duetz and Witholt 2001), animal cell cultures (Girard et al. 2001), and biotransformation (Doig et al. 2002; Weiss et al. 2002). However, the limited data available indicate that the volumetric mass transfer coefficient in a shaken microwell (Weiss et al. 2002) is lower at least by a factor of 10, compared to a conventional scale fermenter.

Walther et al. (1994) have described a miniature bioreactor with a working volume of 3 mL for cell culture in a space laboratory. Later on, Kostov et al. (2001) introduced the design of a 2 mL working volume microbioreactor provided with an optical sensing system. An *E. coli* fermentation in both the microbioreactor and a standard 1-L bioreactor showed similar pH, dissolved oxygen, and optical density profiles. Mixing was achieved by the action of a magnetic stirrer placed at the bottom of the well. Girard et al. (2001) also presented a small-scale bioreactor system for process development and optimization, based on agitated (by a rotational shaker) 12-well microtiter plates with a working volume of 2 mL. Such reactor improved maximum mammalian cells (CHO and HEK 293 cell lines) density and pH stability. Its automation and application to high throughputs is possible by running several hundred small-scale bioreactor experiments in parallel. Lamping et al. (2003) also presented the design of a new miniature bioreactor with a diameter equal to that of a single well of a 24-well plate, for high throughput automated bioprocessing. Mixing was provided by a set of three impellers mechanically driven via a microfabricated electric motor and aeration was achieved with a single tube sparger. Such design features resulted in measured volumetric mass transfer coefficients in the miniature reactor in the range 100-400 h^{-1}, typical of those reported for large-scale fermentation. Fibre optic probes were applied to the continuous monitoring of dissolved oxygen tension and cell biomass concentration during fermentations of *E. coli*. More recently, Doig et al. (2005a) presented a novel miniaturised bubble column bioreactor for high throughput cell cultivation. The miniature bioreactor (2 mL) consists of static deep well microtiter plate. Air was supplied to each well assuring a volumetric mass transfer coefficient for oxygen, k_La, of up to 220 h^{-1} and was used to optimise the growth conditions of *Bacillus subtilis*, a strict aerobic microorganism. The system was not shaken and allowed installation of miniature optical probes.

A key requirement for any process is the ability to measure process parameters, as well as to supply nutrients, oxygen, and pH correctors. Typically, pH, dissolved oxygen (DO) and optical density (OD) are monitored continuously. In small volumes (1-2 mL or less) it is difficult to use standard industrial probes because of their dimensions. This problem may be overcome using the emerging technology of optical sensing (Lamping et al. 2003).

When the yeast *Saccharomyces cerevisiae* is grown in a batch culture under aerobic conditions with glucose as sole energy and carbon source, ethanol can be released into the culture liquid as a by-product. In a first growth phase, biomass is formed and ethanol is accumulated at the expense of glucose consumption. The ethanol is assimilated only in the subsequent growth phase, which begins after glucose

is completely exhausted and the cells have adapted to the new carbon source (Rieger et al. 1983; Sonnleitner and Kappeli 1986). The model for yeast growth presented by Sonnleitner and Kappeli (1986) considers three pure metabolic routes involved in (aerobic and anaerobic) glucose breakdown: i) oxidative and ii) reductive glucose catabolism as well as iii) ethanol utilisation. Under anaerobic conditions, the glucose reduction (fermentation) is the only mode of energy production but alcoholic fermentation may occur even under aerobic conditions (Vandijken and Scheffers 1986) if the glucose concentration surpasses a critical threshold value (Sonnleitner and Kappeli 1986; Verduyn et al. 1984).

Cell cultures studies in conventional oscillatory flow reactors (OFRs) were limited to the experimental determination of mass transfer of oxygen into a yeast suspension. Ni et al. (1995) reported the study of ressuspended *S. cerevisiae* (from frozen baker's) in an aerated 50-mm internal diameter OFR with an 11 % increase in the k_La, compared to those obtained in a ST. Such trends in k_La were consistent with the fluid mechanics observed within both systems. Lee et al. (2002; 2001) considered the OFR a viable reactor for protein refolding via direct dilution; as the mixing characteristics of the OFR are well described and controllable (e.g., Mackley, 1991) and also suggested that OFR can be scaled-up to process scale without loss of mixing efficiency.

In this work, proof-of-concept experiments of a novel micro-bioreactor recently designed (Reis et al. 2005) is presented by running several batch fermentations with a flocculent *S. cerevisiae* strain, both under aerobic and anaerobic conditions. The objective is to show that the novel reactor can be used with advantages over the more traditional SF and ST bioreactors. The possibility of using fibre optical technology for *on-line* and real-time monitoring of the bioprocesses going on the reactor has also been demonstrated by monitoring the biomass concentration through OD measurements.

8.2 Materials and methods

Proof-of-concept experiments have been established by carrying out fermentations in the micro-bioreactor system using as workhorse a flocculent *S. cerevisiae* strain at four different initial glucose concentrations in the range of ~5 - 20 g/L, under aerobic and anaerobic growth conditions. The results were compared with those from fermentations in a lab-scale stirred tank (ST) bioreactor.

Experimental operation of Micro-bioreactor

The experimental micro-bioreactor setup is shown in Figure 8-1. This novel micro-bioreactor was designed to offer sterile conditions with sufficient mass-transfer capability so as to support, for example, the fermentation of commercially-important recombinant organisms (Reis et al. 2004a). Each SPC tube is temperature controlled and it can be coupled to a fibre optics system to achieve online monitoring and control of e.g. OD, DO or pH.

In this work the micro-bioreactor was operated as follows: a single sterilised (at 110 °C for 40 minutes) SPC tube (4.5 ml operating volume) was positioned vertically (Figure 8-1), and the fluid oscillated at a f and x_0 of 18 s^{-1} and 3 mm, respectively, where the flow is turbulent like (Reis et al. 2005). In aerobic yeast growth experiments, the reactor was continuously aerated through the bottom (Figure 8-1A, C) with sterile air at an average superficial gas velocity, U_g = 0.37 mm/s (equivalent to a gas flow rate of 0.064 vvm, where vvm is the volume of gas-phase per volume of reactor per minute). The aeration rate was controlled using a needle micro valve. In all fermentations, the temperature was maintained at 25 °C by circulating water at that temperature through the jacket of the SPC tube.

5-L ST bioreactor geometry

A 5-L ST bioreactor – Model microDCU system, installed with Twin and MCU-200 controllers (B. Braun Biotech International, Melsungen, Germany) with a working volume of 4.7 L was used in the aerobic fermentations of *S. cerevisiae*. The ST bioreactor was sterilised at 121 °C during 30 minutes with 4.23 L of YPD medium. After stabilisation of temperature and dissolved oxygen it was inoculated with the 470 mL seed culture. The ST bioreactor was aerated with sterile air at an aeration rate of 1.1 vvm and the agitation speed was controlled at 150 rpm. The aeration rate was controlled using a Hastings (Hampton, Virginia, USA) mass-flow controller. A minimum O_2 concentration of 30 % was assured throughout the fermentation by means of a cascade controller using aeration as master and agitation as slave controller. pH was analysed on-line using a pH probe connected to the microDCU system.

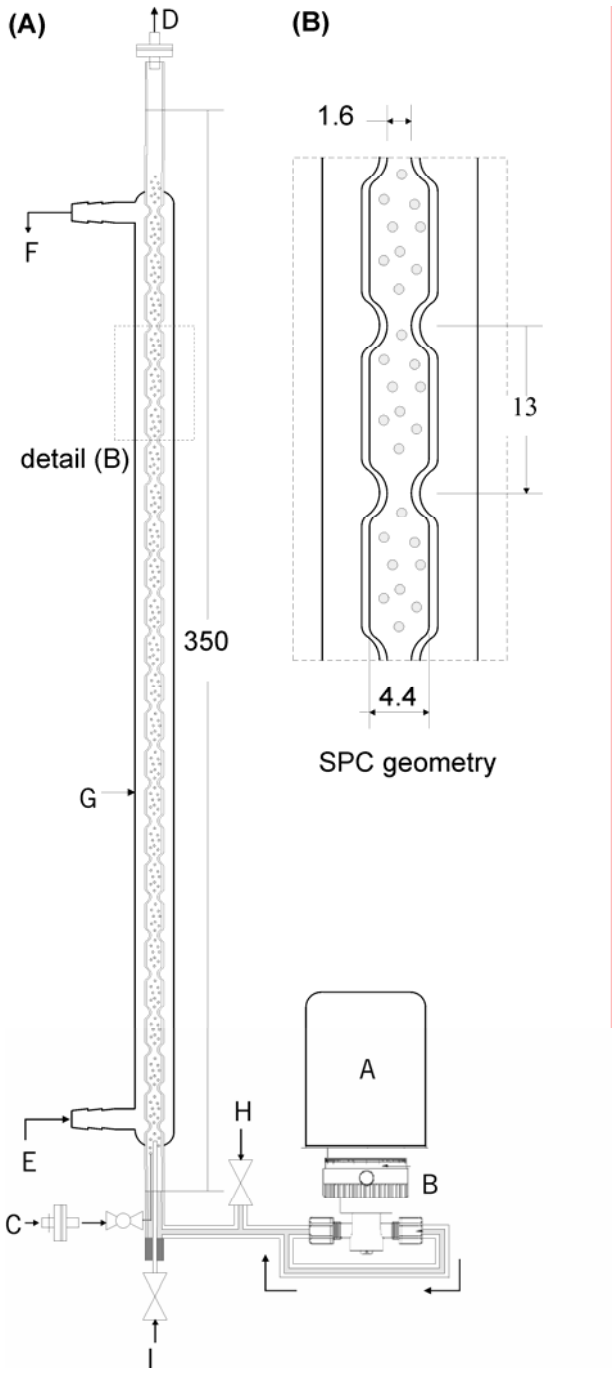

Figure 8-1. (A) Experimental setup used in batch fermentations of *S. cerevisiae*: A- rotary motor; B- piston pump; C- gas inlet; D- gas outlet; E- fluid heating inlet; F- fluid heating outlet; G- SPC tube; H- purging port; I- sampling port. (B) Detail of SPC (Smooth Periodic Constricted) tube geometry, which composes the novel, designed oscillatory flow Micro-bioreactor. All dimensions are in mm.

2-L ST bioreactor geometry

A 2-L ST bioreactor – Model Biostat M (B. Braun Biotech International, Melsungen, Germany) with a working volume of 1.5 L was used for yeast growth at anaerobic conditions. The ST bioreactor's agitation speed was set to 150 rpm and the reactor containing 1.5 L of YPD medium was sterilized at 121 °C during 20 minutes.

Aerobic growth of S. cerevisiae

S. cerevisiae yeast was selected due to its high industrial relevance (Kappeli 1986). *S. cerevisiae* RIBM 655 was preserved at 4 °C on YPD (10 g/L yeast extract (Merck Co., Darmstadt, Germany), 20 g/L peptone (Bacto™ peptone, Quilaban, Le Pont de Claix, France) and 20 g/L D-glucose anhydrous (HiMedia Laboratories, Pvt. Ld., Mumbai, India) agar slants. One agar slant was washed with sterile YPD medium and the obtained cell suspension was transferred to a 1000 mL Erlenmeyer flask (working volume of 470 ml). That culture was then incubated overnight at 27 °C (Certomat® H) under orbital shaking at 150 rpm (Certomat® R) (both from B. Braun Biotech International, Melsungen, Germany). Cells for the inoculation of the SF, the 5-L ST bioreactor and the micro-bioreactor were harvested at the end of the exponential growth phase (after 16-17 hours from inoculation), which was estimated by measuring the OD of a sample at = 620 nm. Four different initial glucose concentrations (ranging from 5 to 20 g/L) were tested in both the 5-L ST bioreactor and in the micro-bioreactor (Table 8-1).

Fermentation temperature was controlled at 25 °C. To avoid foaming formation due to mixing 1 ppm of antifoam O-30 (Sigma Aldrich, Steinheim, Germany) was added to the fermentation media in the micro-bioreactor.

Samples were collected from each fermentation vessel (5-L ST bioreactor, SF and micro-bioreactor) at every hour and centrifuged 15,000 rpm for 10 min (centrifuge model Sigma 112, B. Braun Biotech International, Melsungen, Germany). The precipitate was afterwards used for determining the biomass by spectrophotometry, while the supernatant (from 5-L ST bioreactor and micro-bioreactor) was used for determination of the glucose and ethanol by HPLC.

Biomass determination: The precipitate from each centrifuged sample was treated with de-flocculation solution (washed three times with NaCl 1.5 % (Merck Co., Darmstadt, Germany), pH adjusted to 3.0 with HCl). After ressuspension in de-flocculation solution, the OD was measured at 620 nm using a Jasco's V-560 spectrometer (Jasco, Tokyo, Japan). The cell dry weight was obtained from a calibration curve, which was found linear up to cell dry weights (X) of 330 mg/L, corresponding to cell turbidity (absorbance) of 0.802 at 620 nm.

Glucose and Ethanol determination: Glucose and ethanol concentrations were determined using a HPLC system (830-RI detector, pump 830-PU, both from Jasco, Tokyo, Japan), installed with a Chrompack Organic Acids Column (Varian Inc., Palo Alto, CA, USA). The mobile phase was H_2SO_4 (0.01 N) at a flow rate of 0.6 mL/min. Temperature was maintained at 60 °C with an oven Chrompack column thermostat (Varian Inc., Palo Alto, CA, USA). Under these conditions, distinct peaks of glucose and ethanol were resolved within 20 min. The mean retention time was 7.17 (± 0.03) minutes for glucose and 15.38 (± 0.07) minutes for ethanol.

Anaerobic growth of S. cerevisiae

S. cerevisiae RIBM 655 was preserved at 4 °C in a water solution. Cells were ressuspended and then transferred to a small container. Apart, in a 5-L Erlenmeyer, sterilised YPD medium (10 g/L yeast extract (Merck Co., Darmstadt, German), 20 g/L peptone (Bacto™ peptone, Quilaban, Le Pont de Claix, France) and 20 g/L D-glucose anhydrous (HiMedia Laboratories, Pvt. Ld., Mumbai, India) previously degassed for 30 min with N_2 was inoculated with ~10 % (v/v) of ressuspended cells such that the turbidity (OD measured with a V-560 spectrometer (Jasco, Tokyo, Japan) at 620 nm) was ~0.5. Finally, this 'initial culture' was aseptically transferred (pumped) to the fermentation vessels (2-L ST bioreactor and micro-bioreactor) with the desired volumes. The fermentation temperature was controlled at 25 °C and pH was not controlled. Four different initial glucose concentrations were tested: 5, 10, 15 and 20 g/L.

Monitoring of medium OD along the anaerobic growth: OD of cell growth media was *on-line* and real-time measured in the 2-L ST bioreactor and in the micro-bioreactor by means of reflectance optical micro-

probes connected to a multi-channel optic spectrometer system (Avantes, Eerbeek, The Netherlands). Due to the different vessel geometries, two different probes were used. In the micro-bioreactor, a reflection probe (FCR-7UV200-1.5x100-2) with a small tip (1.5 mm) was installed in the top, in contact with the fermentation media. In the 2-L ST bioreactor, a standard reflection probe provided with a mirror at 45 degrees (FCR-7UV200-2-45-ME) was installed inside through the top. In both cases, great attention was taken with probes installation, namely to avoid contact with light's reflectance surfaces (walls or impellers). Reading of the light coming from both probes was made *on-line* and simultaneously using a 4-channel optical spectrometer AvaLights-2048. The CCD detector was connected to an electronic board with 14 bit AD converter and USB/RS-232 interface. Data transfer between the optic spectrometer and a personal computer was controlled by AvaSoft full software. A tungsten halogen light source (AvaLight-HAL) was connected to FCR-7UV200-2-45-ME while a 475 nm LED light source (AvaLigh-LED-475) was attached to FCR-7UV200-1.5x100-2. Thus, the integrals of the measured medium absorbance between 610 and 630 nm (for FCR-7UV200-1.5x100-2) and 465 and 485 nm (for FCR-7UV200-2-45-ME) were ten times averaged and recorded at every 5 minutes using suitable integration times. The measured OD (absorbance) values were found to change linearly with the dry cell weight in all experiments (results not shown). Being absorbance a logarithmic function of an amount, I_0/I (where I_0 and I are the reference and the sample reflected light, respectively), which is proportional to the quantity of biomass in the medium, this means that the function 'OD *versus* time' is a direct measure of the exponential growth phase, being its slope proportional to the specific growth rate (μ).

8.3 Results and discussion

Aerobic growth of S. cerevisiae on glucose

The effects of S_0 on the yeast growth metabolism at aerobic growth conditions were investigated in the range of ~5 – 20 g/L (see Table 8-1). Several experiments were performed in a 5-L ST bioreactor and in the micro-bioreactor. All experiments were run under well controlled conditions of temperature, agitation and aeration, as previously defined in Materials and Methods section. Variations in biomass, glucose and ethanol concentrations of the strain during the fermentation time were monitored *ex-situ*. The end of fermentations was identified by the stabilization of biomass curve and a pH increase (results not shown). Once the fermentation was stopped, these observations were confirmed with the determination of

substrate (glucose) concentration in the collected samples, demonstrating the effective glucose depletion. Figure 8-2 shows an example of the time course of biomass and ethanol productions using glucose as the sole substrate at ca. 15 g/L, in 5-L ST and in micro-bioreactor vessels. The higher biomass production (equal to $X - X_0$, where X_0 is the initial biomass concentration) achieved with the novel micro-bioreactor can be clearly observed, especially when taking into account the lower S_0 in the micro-bioreactor at the start of batch culture. In particular, this means the yield of biomass growth on glucose is enhanced in the micro-bioreactor.

In both culture vessels (Figure 8-2), the kinetics of glucose consumption and biomass and ethanol production followed the expected patterns for these fermentation conditions. In the initial stage of fermentation, the glucose consumption was generally low due to the initial low cell density, but glucose concentration markedly decreased during batch fermentation after 200-400 minutes for both fermentation vessels. The resulting cell growth curve obtained from batch experiments has a typical sigmoidal shape (S-shape). The glucose consumption kinetics is apparently similar in both fermentation vessels. However very different biomass amounts were measured at the end of the fermentation: a 79 % higher biomass production was obtained in the micro-bioreactor in comparison with the biomass production in the 5-L ST bioreactor. Such biomass enhancement reveals a higher yield of biomass on glucose in the micro-bioreactor, suggesting that the growth of *S. cerevisiae* on glucose in this reactor is mainly through the oxidative (respiratory) metabolic pathway, accordingly the model of Sonnleitner and Kappeli (1986). Glucose inhibits the uptake of ethanol as a substrate for growth while present in measurable concentrations, thus growth on ethanol is not considered. Because the oxidative glucose catabolism is a respiratory process (oxygen dependent), presumably such improvement in biomass production is due to the higher mass transfer rate of oxygen achieved with this novel micro-bioreactor, as shown by Reis et al. (2004a).

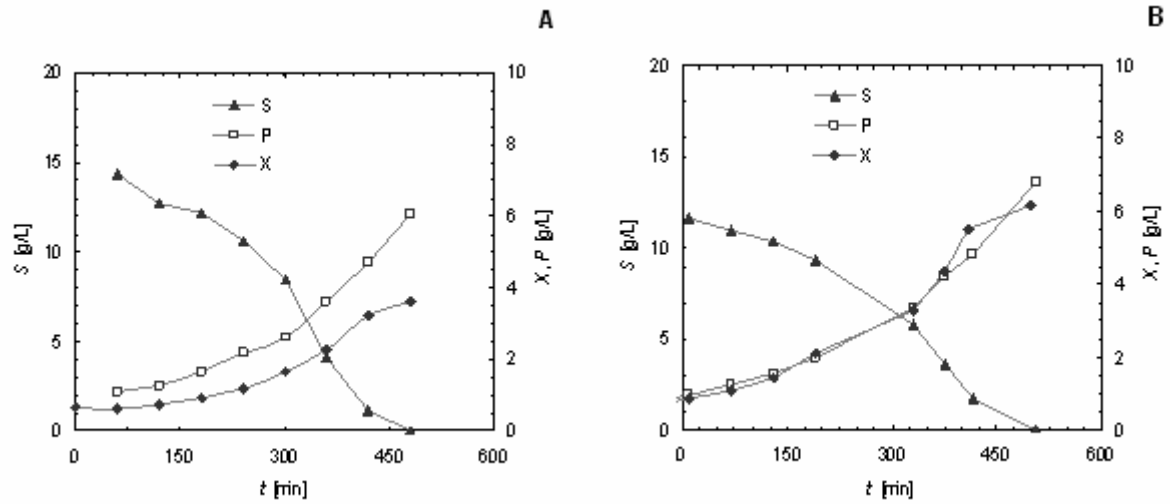

Figure 8-2. Time course of glucose concentration (*S*), cell dry weight (*X*) and ethanol concentration (*P*) in batch aerobic-growth on glucose of *S. cerevisiae* (bioprocess IIIa and IIIb – see Table 8-1). Fermentations in the 5-L stirred tank bioreactor (A), with an aeration rate of 1.1 vvm and in the micro-bioreactor (B) with an aeration rate of 0.064 vvm.

A comparison of the dry cell weight concentration obtained under aerated conditions is shown in Figure 8-3A (ST) and Figure 8-3B (micro-bioreactor), for bioprocesses I to IV. For the three higher initial glucose concentrations (bioprocesses II to IV) it is possible to observe the higher (up to 79 %) biomass production obtained with the micro-bioreactor, when compared to that produced in the 5-L ST bioreactor. In general, the biomass exponential growth phase was time-extended in the micro-bioreactor. The consequence is a 70 % and a 203 % increase of biomass production in the ST and micro-bioreactor, respectively, as compared to the SF (Figure 8-3C). Figure 8-3 presents a comparison of time profiles of dry cell weight in aerated vessels (A and B) with the micro-aerobic growth in a SF at 27 °C (C) and also confirms the exponential phase of seed cultures after 16 h (the overnight incubation time).

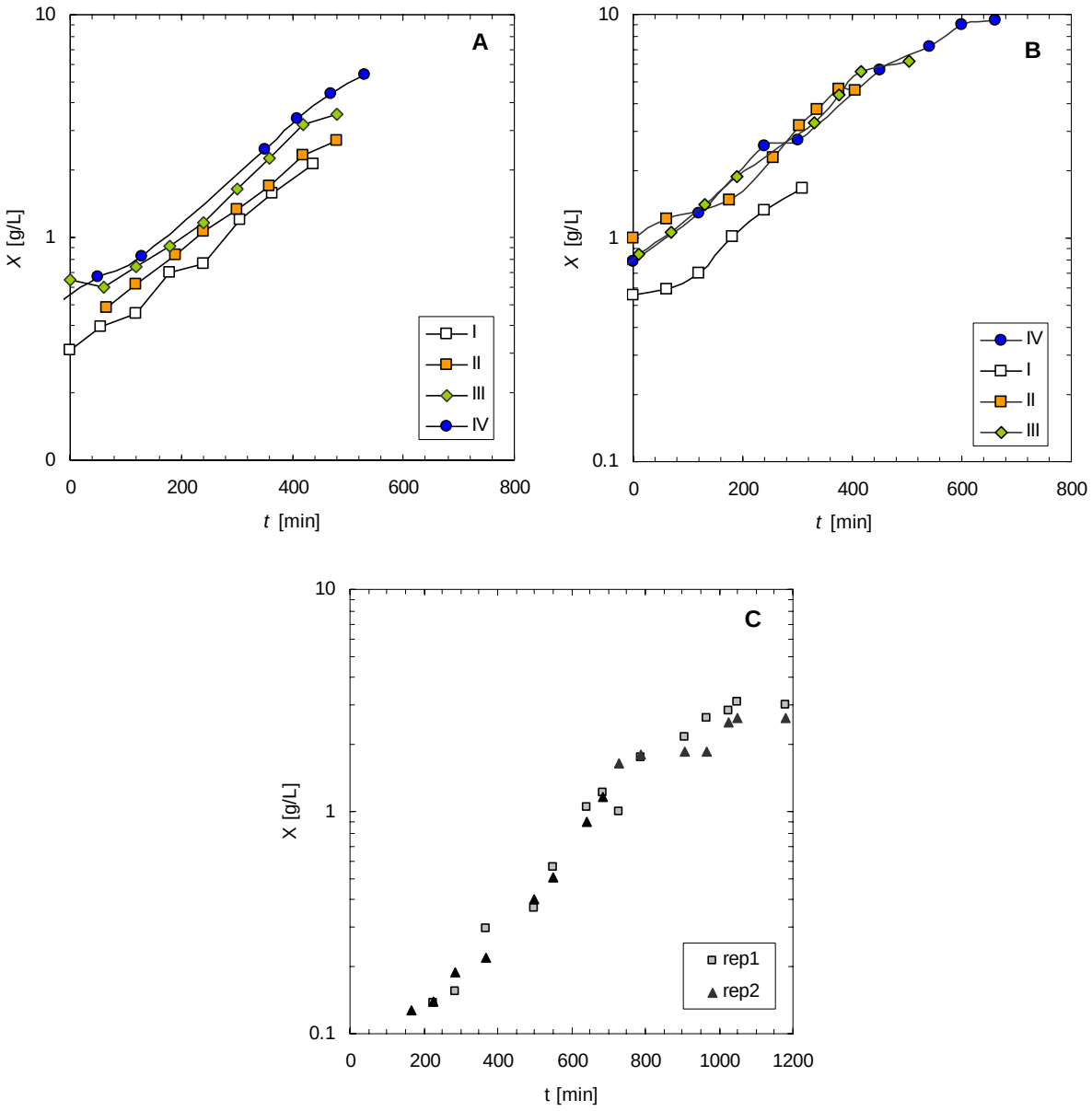

Figure 8-3. Time profiles of cell dry weight, *X* (log scale) in aerobic-batch glucose-growth of *S. cerevisiae* (bioprocesses I to IV). Fermentations in the 5-L stirred tank (ST) bioreactor (A) and in the micro-bioreactor (B) with an aeration rate of 1.1 vvm for the 5-L ST and 0.064 vvm for the micro-bioreactor. (C) Time profiles of dry cell weight in two replicates of *S. cerevisiae* growth in a shake flask (SF) starting with a glucose concentration of 20 g/L (bioprocess IVc – see also Table 8-1); yeast was cultivated at 27 °C and agitated in an orbital shaker at 150 rpm (these experiments correspond to the seed culture's growth).

Residual glucose concentrations along the batch growth are summarised in Figure 8-4 for both the 5-L ST bioreactor and the micro-bioreactor. The biomass (Figure 8-3) and ethanol (results not shown) production

were found to cease as the glucose concentration reaches exhaustion (Figure 8-4), and therefore biomass and ethanol production were consistent with the time period of glucose catabolism in both reactor systems.

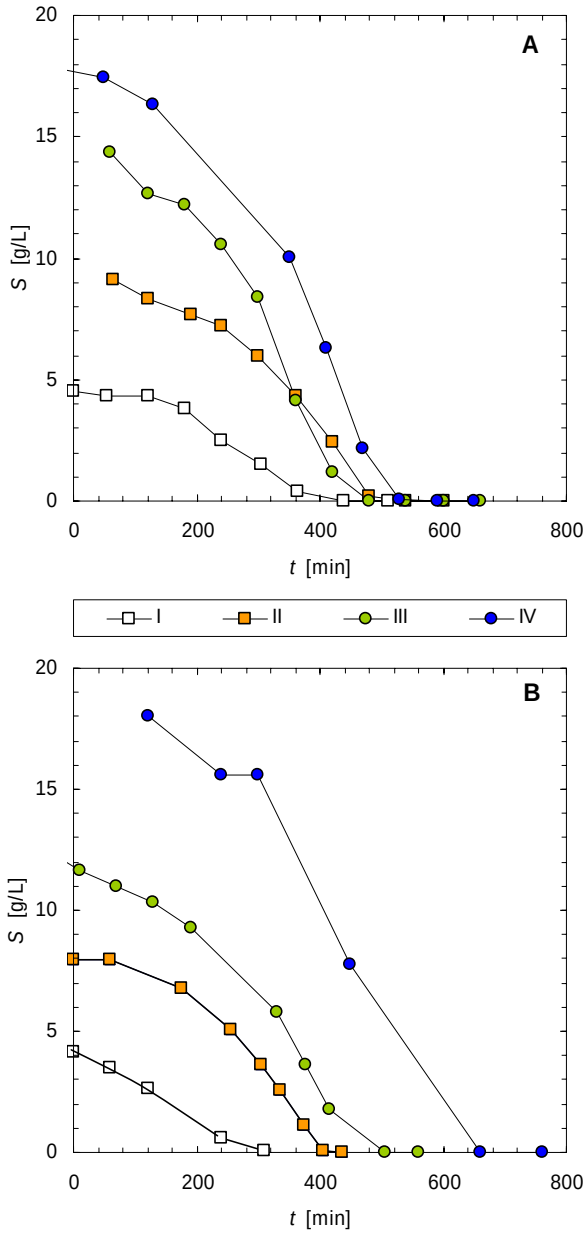

Figure 8-4. Time profiles of residual glucose concentrations (*S*) in the aerobic batch growth on glucose of *S. cerevisiae* in bioprocesses I to IV (see Table 8-1). Fermentations running in the 5-L stirred tank (ST) bioreactor (A) and in the micro-bioreactor (B).

pH was not controlled during batch growth but it was monitored (results not shown) being above 5.0 in all the experiments with the ST, SF and micro-bioreactor systems. At such pH values typically both cell growth and ethanol productivity are not inhibited (Yu and Zhang 2004).

Modelling the aerobic batch growth of S. cerevisiae on glucose

Yeast growth kinetics. The kinetics involved in the batch growth of *S. cerevisiae* strain was characterised by its specific growth rate (μ), as suggested by Marin (1999). Kinetic studies have demonstrated that growth depends on the concentration of nutrients in the medium (see e.g. the review of Marin 1999) but it was concluded that substrate concentration is not growth limiting in the tested range of concentrations (~5 - 20 g/L) for this *S. cerevisiae* strain (Figure 8-5), where all the experiments showed an μ around an average value of 0.303 ± 0.040 h^{-1} for the micro-bioreactor, and 0.288 ± 0.025 h^{-1} for the 5-L ST bioreactor.

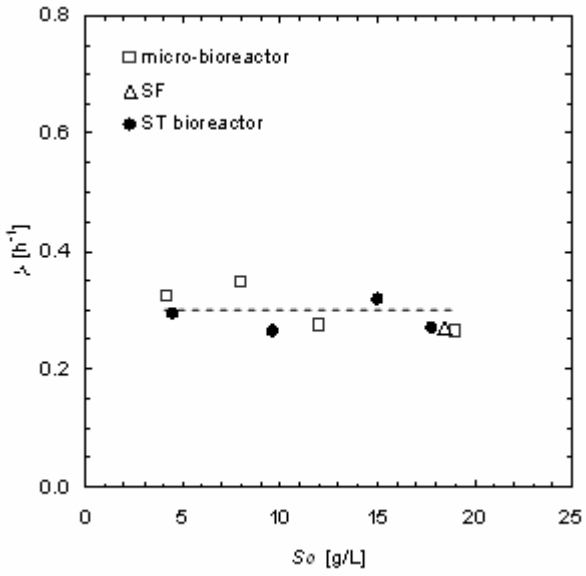

Figure 8-5. Specific growth rates (μ) for batch growth on glucose of *S. cerevisiae* at 25 °C and different initial glucose concentrations (S_0) in the 5-L stirred tank (ST) bioreactor and in the micro-bioreactor. The specific growth rate presented for the SF was the averaged μ found for the seed culture growth, incubated at 27 °C and 150 rpm.

For the SF, an average growth rate of 0.268 h^{-1} was calculated for a S_0 of 20 g/L, which is in agreement with the other systems' results. These μ values are smaller than that reported by Beck and Vonmeyen (1968) (μ = 0.42 for S_0 = 9.2 g/L), but in the last case the fermentation conditions were controlled to pH = 5.5 and 30 °C, thus favouring the yeast growth.

The increase of the dry cell weight (X-X_0) of *S. cerevisiae* was correlated with the initial glucose concentration S_0, as shown in Figure 8-6. The correlation slope gives an averaged-global yield coefficient $\Delta X/S_0$, which revealed that biomass production in the S_0 range of ~5 - 20 g/L is increased by 83 % and 214 % in the micro-bioreactor in comparison with the 5-L ST and the SF, respectively. Substrate degradation during the exponential growth is therefore mostly achieved *via* respiratory metabolism instead of fermentative pathway in both ST and micro-bioreactor vessels. It may be suggested that, given the yields shown in Figure 8-6, the metabolism in the micro-bioreactor (with an average biomass production yield = 0.44) is closer to pure-oxidative (with a typical average yield of 0.50) (Pamment et al. 1978).

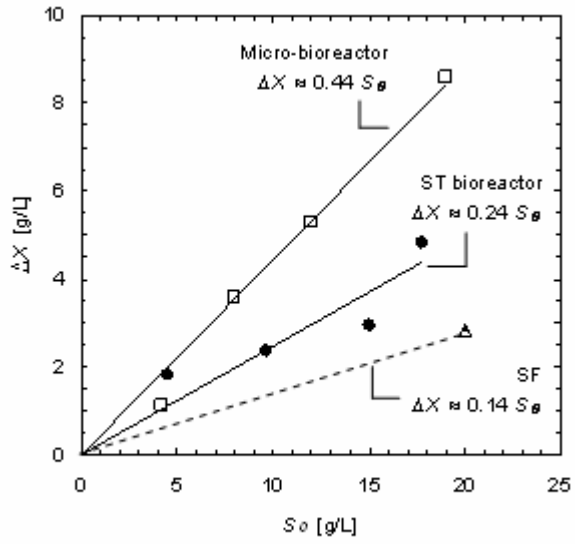

Figure 8-6. Increase in dry cell weight, $\Delta X = X - X_0$, obtained until complete depletion of glucose in the aerobic batch growth of *S. cerevisiae* on glucose in bioprocesses I to IV, for initial glucose concentrations S_0 of ~ 5 - 20 g/L.

Substrate consumption kinetics. Glucose can be metabolised both aerobically (through the oxidative pathway) and anaerobically (via the reductive or fermentative pathway), however, with different rates and different efficiencies (Sonnleitner and Kappeli 1986). The yield coefficient $Y_{X/S}$ (on a mass basis) is the most reliable measurable (empirical) coefficient to summarise the substrate (S) consumption for biomass (X) formation. Typical values of $Y_{X/S}$ for *S. cerevisiae* are 0.47-0.50 and 0.05-0.10 for oxidative and reductive glucose breakdown pathways, respectively, at T = 30 °C and pH = 5.0 (Sonnleitner and Kappeli 1986). In the present work a global (oxidative plus reductive) $Y_{X/S}$ was determined for the exponential phase of yeast growth, as summarised in Table 8-1.

Table 8-1: Averaged yields of biomass on substrate ($Y_{X/S}$) and specific substrate uptake rate ($q_s = \mu / Y_{X/S}$) during the exponential phase of the aerobic growth of *S. cerevisiae* in bioprocesses I to IV and in three different small-scale vessels: 5-L stirred tank (ST) bioreactor, micro-bioreactor and shake flask (SF). S_0 is the initial glucose concentration, as measured after inoculation with 10 % v/v of seed culture

	Bioprocess	S_0 [g/L]	$Y_{X/S}$ [$g_{cells}/g_{glucose}$]	q_s [$g_{glucose}/g_{cells}/h$]
5-L ST bioreactor[a]	Ia	4.5	0.27	-1.10
	IIa	9.6	0.27	-0.98
	IIIa	15.0	0.20	-1.59
	IVa	17.8	0.26	-1.06
Micro-bioreactor[a]	Ib	4.2	0.36	-0.91
	IIb	8.0	0.54	-0.64
	IIIb	12.0	0.42	-0.68
	IVb	19.0	0.40	-0.65
Shake flask[b]	IVc	20.0	0.16	-
Literature		40.0[c]	0.11[c]	-
		-	0.50[H]	-

[a] experimental results from aerobic growth at 25 °C inoculated with 10 % seed culture. [b] results from seed culture kinetics at 27 °C and shaking at 150 rpm. [c] data from Haack et al. (2004). [H] data from Pamment et al. (1978).

It is straightforward to conclude that higher $Y_{X/S}$ values were obtained with the micro-bioreactor. During the exponential growth, $Y_{X/S}$ was increased by up to 110 % on the micro-bioreactor in comparison with the 5-L ST, also corresponding to more than a 3-fold increase in comparison with data from Haack et al. (2004).

The $Y_{X/S}$ values for the fermentations in the micro-bioreactor are in all cases above 72 % of the reported value ($Y_{X/S} \approx 0.50$) for pure-oxidative (aerobic) growth of *S. cerevisiae* (Pamment et al. 1978), meaning that batch yeast growth in this reactor is achieved mostly through the respiratory pathway. Because respiration itself depends on the dissolved oxygen (Sonnleitner and Kappeli 1986) such improvement on $Y_{X/S}$ values suggests enhanced dissolved oxygen availability in the micro-bioreactor due to the reciprocating nature of OFM. Also, the existence of inhomogeneities in the extremities of the ST vessel and its inherent oxygen gradients (Hadjiev et al. 2006) may be in the base for the lower performance of ST bioreactor.

The kinetics of substrate (glucose) consumption may be summarised in relation to the specific substrate uptake rate, q_s (Table 8-1). Glucose flux was not differentiated between oxidative and reductive pathways, thus q_s represents the glucose uptake by both ways.

The batch aerobic growth of *S. cerevisiae* in the novel reactor presented lower values of q_s (30 % lower) in parallel with the higher $Y_{X/S}$ values, as compared with the ST. In both ST and micro-bioreactor systems the *S. cerevisiae* yeast is growing at a rate near μ_{max} as shown previously. However, q_s is lower in the micro-bioreactor, thus the amount of glucose exceeding the bottleneck and being metabolised according to the reduction pathway is decreased. This results in enhanced biomass formation per unit of substrate consumed, i.e. higher $Y_{X/S}$ values. In summary, the respiro-fermentative flux distribution of *S. cerevisiae* in ST bioreactor is redirected with the micro-bioreactor towards the oxidative pathway, allowing e.g. the optimisation of industrial production of *S. cerevisiae*.

Anaerobic growth of S. cerevisiae on glucose

Anaerobic growth of *S. cerevisiae* was monitored with the *on-line* and real-time OD of the culture media in both the 2-L ST and the micro-bioreactor using dip-optical reflectance probes, for initial glucose concentrations in the range 5-20 g/L. As no gas bubbles were present, a constant relation was obtained between the on-line OD signal and the biomass concentration.

Under anaerobic conditions, glucose is metabolised by the reductive (fermentative) pathway with the consequent formation of ethanol.

A comparison of batch anaerobic growth of *S. cerevisiae* for S_0 between 5 and 20 g/L is presented in Figure 8-7 for both ST bioreactor and micro-bioreactor vessels.

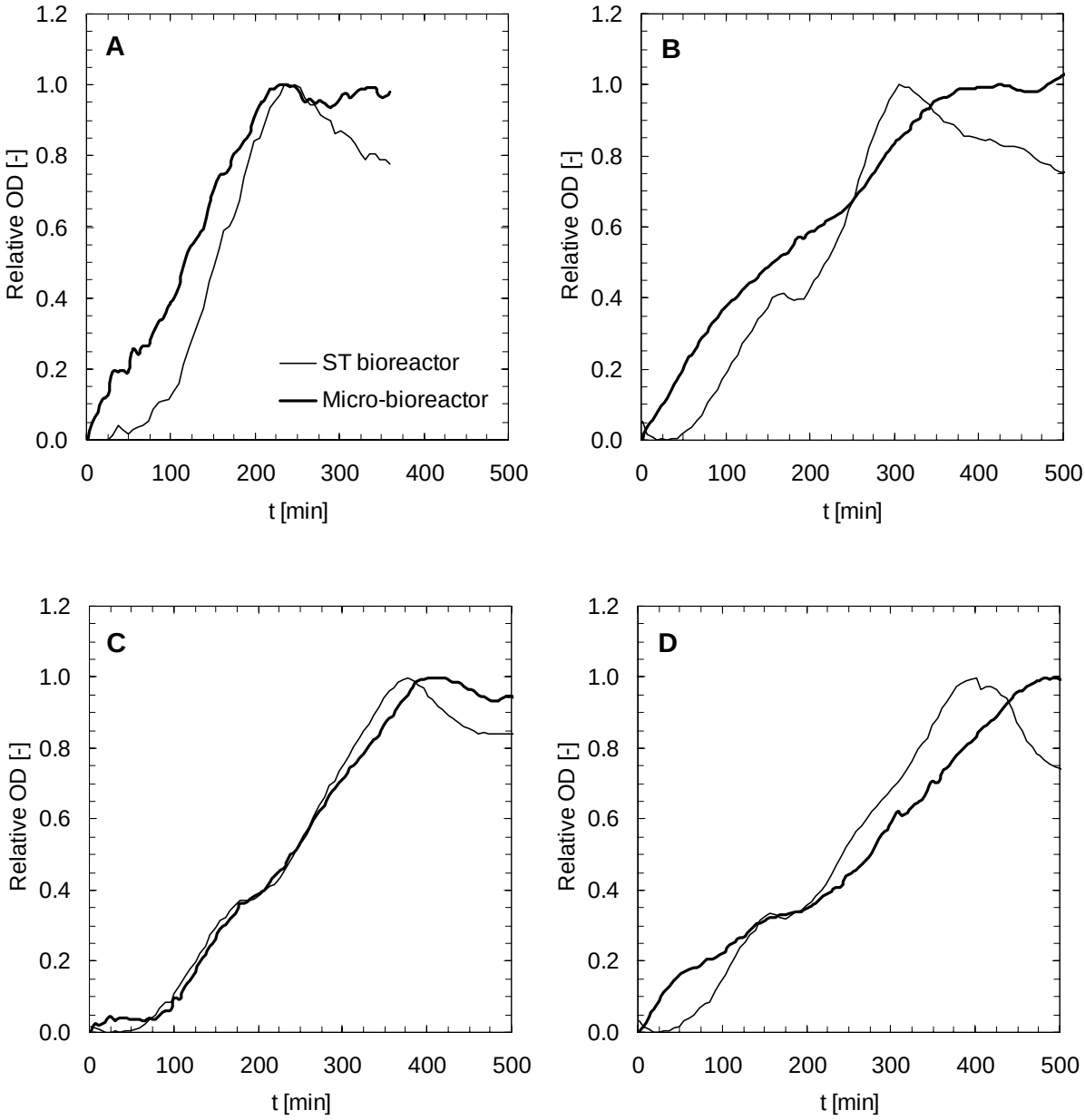

Figure 8-7. Time course of anaerobic batch growth on glucose (expressed as a relative function of the OD) of *S. cerevisiae* in the 2-L stirred tank (ST) reactor and in the micro-bioreactor. Experiments were run in parallel and started with glucose concentrations of 5 g/L (A), 10 g/L (B), 15 g/L (C) and 20 g/L (D). No seed culture was prepared and fermentation temperature was controlled at 25 °C. Note that OD was turned dimensionless with the OD peak obtained at the end of growth phase (i.e. at the instant of glucose depletion, as indicated from pH measurements).

The OD increase along the fermentation time was very similar in both the 2-L ST and the micro-bioreactor, which means similar growth behaviour of the yeast in these two vessels. However, in the 2-L ST bioreactor's experiments a decrease in OD was observed after the end of fermentation (OD peak), which was coincident with the observed biomass flocculation. This phenomenon is due to the glucose exhaustion: under these circumstances, the *S. cerevisiae* strain tends to flocculate, thus reducing the absorbance of the fermentation broth. In fact, the ideal brewing yeast (as the *S. cerevisiae* strain used in this work) grows as discrete cells and flocculates after sugar depletion from the media, leaving clear beer (Stewart and Russell 1981). The differences found between ST and micro-bioreactor after glucose depletion mean that although stirred, the intensity of mixing provided by the 150 rpm in the 2-L ST was insufficient to keep all the biomass suspended, while the micro-bioreactor proved to be a better device to keep cells in suspension.

8.4 Conclusions

As a proof-of-concept several aerobic fermentations were carried out with a novel micro-bioreactor system using as workhorse a flocculent *S. cerevisiae* strain at four different initial glucose concentrations (~5 - 20 g/L). Average 83 % and 214 % increases on biomass production were obtained with the micro-bioreactor when compared with a stirred-tank (ST) bioreactor and the seed culture growth in a shake flask (SF), respectively. It was postulated that the respiro-fermentative flux distribution of *S.cerevisiae* from the ST bioreactor was redirected in the micro-bioreactor towards the oxidative pathway. This was explained by the enhanced mass transfer rates achieved with this novel scaled-down platform, as demonstrated elsewhere (Reis et al. 2004a). Anaerobic fermentations at the same initial glucose concentration ranges (5-20 g/L) gave the opportunity to use state-of-the-art fibre optics technology for *on-line* and real-time monitoring/control of bioprocesses within this novel micro-bioreactor. A time profile of optical density (OD) was observed to be very similar in the ST and in the micro-bioreactor, with a highly reproducible yeast growth in the two platforms.

The higher efficiencies of biomass production obtained as well as the much lower air-inlet requirements turn this novel micro-bioreactor also a potential platform for upstream development of animal cells derived bioprocesses. Moreover, the linear scale-up of reactors based on the oscillatory flow mixing (OFM) technology anticipates a parallel screening/optimisation of bioprocesses with this novel micro-reactor at

similar conditions to those at industrial scale. Future work will be focused in the development of a multiple-SPC tube unit allowing the high-throughput bioprocess optimisation in a single unit volume.

8.5 References

Beck C, Vonmeyen.Hk. 1968. Enzyme Pattern and Aerobic Growth of Saccharomyces Cerevisiae under Various Degrees of Glucose Limitation. Journal of Bacteriology 96(2):479-&.

Buchs J. 2001. Introduction to advantages and problems of shaken cultures. Biochemical Engineering Journal 7(2):91-98.

Doig SD, Diep A, Baganz F. 2005a. Characterisation of a novel miniaturised bubble column bioreactor for high throughput cell cultivation. Biochemical Engineering Journal 23(2):97-105.

Doig SD, Ortiz-Ochoa K, Ward JM, Baganz F. 2005b. Characterization of oxygen transfer in miniature and lab-scale bubble column bioreactors and comparison of microbial growth performance based on constant k(L)alpha. Biotechnology Progress 21(4):1175-1182.

Doig SD, Pickering SCR, Lye GJ, Woodley JM. 2002. The use of microscale processing technologies for quantification of biocatalytic Baeyer-Villiger oxidation kinetics. Biotechnology and Bioengineering 80(1):42-49.

Duetz WA, Ruedi L, Hermann R, O'Connor K, Buchs J, Witholt B. 2000. Methods for intense aeration, growth, storage, and replication of bacterial strains in microtiter plates. Applied and Environmental Microbiology 66(6):2641-2646.

Duetz WA, Witholt B. 2001. Effectiveness of orbital shaking for the aeration of suspended bacterial cultures in square-deepwell microtiter plates. Biochemical Engineering Journal 7(2):113-115.

Girard P, Jordan M, Tsao M, Wurm FM. 2001. Small-scale bioreactor system for process development and optimization. Biochemical Engineering Journal 7(2):117-119.

Haack MB, Eliasson A, Olsson L. 2004. On-line cell mass monitoring of Saccharomyces cerevisiae cultivations by multi-wavelength fluorescence. Journal of Biotechnology 114(1-2):199-208.

Hadjiev D, Sabiri NE, Zanati A. 2006. Mixing time in bioreactors under aerated conditions. Biochemical Engineering Journal 27(3):323-330.

Kappeli O. 1986. Regulation of Carbon Metabolism in Saccharomyces-Cerevisiae and Related Yeasts. Advances in Microbial Physiology 28:181-209.

Kostov Y, Harms P, Randers-Eichhorn L, Rao G. 2001. Low-cost microbioreactor for high-throughput bioprocessing. Biotechnology and Bioengineering 72(3):346-352.

Lamping SR, Zhang H, Allen B, Shamlou PA. 2003. Design of a prototype miniature bioreactor for high throughput automated bioprocessing. Chemical Engineering Science 58(3-6):747-758.

Lee CT, Buswell AM, Middelberg APJ. 2002. The influence of mixing on lysozyme renaturation during refolding in an oscillatory flow and a stirred-tank reactor. Chemical Engineering Science 57(10):1679-1684.

Lee CT, Mackley MR, Stonestreet P, Middelberg APJ. 2001. Protein refolding in an oscillatory flow reactor. Biotechnology Letters 23(22):1899-1901.

Li JC, Wang S, VanDusen WJ, Schultz LD, George HA, Herber WK, Chae HJ, Bentley WE, Rao G. 2000. Green fluorescent protein in Saccharomyces cerevisiae: Real-time studies of the GAL1 promoter. Biotechnology and Bioengineering 70(2):187-196.

Mackley MR. 1991. Process Innovation Using Oscillatory Flow within Baffled Tubes. Chemical Engineering Research & Design 69(3):197-199.

Maier U, Buchs J. 2001. Characterisation of the gas-liquid mass transfer in shaking bioreactors. Biochemical Engineering Journal 7(2):99-106.

Marin MR. 1999. Alcoholic fermentation modelling: Current state and perspectives. American Journal of Enology and Viticulture 50(2):166-178.

Ni XW, Gao SW, Pritchard DW. 1995. Study of Mass-Transfer in Yeast in a Pulsed Baffled Bioreactor. Biotechnology and Bioengineering 45(2):165-175.

Pamment NB, Hall RJ, Barford JP. 1978. Mathematical-Modeling of Lag Phases in Microbial-Growth. Biotechnology and Bioengineering 20(3):349-381.

Reis N, Harvey AP, Vicente AA, Teixeira JA, Mackley MR. 2005. Fluid Mechanics and Design Aspects of a Novel Oscillatory Flow Meso-Reactor. Chemical Engineering Research & Design 83(A4):357-371.

Reis N, Vicente AA, Teixeira JA, Mackley MR. Enhanced mass transfer rates of a novel oscillatory flow screening reactor. Summaries of the 16th International Congress of Chemical and Process Engineering; 2004a 22nd - 26th August; Praha, Czech Republic. p 898-899.

Reis N, Vicente AA, Teixeira JA, Mackley MR. 2004b. Residence times and mixing of a novel continuous oscillatory flow screening reactor. Chemical Engineering Science 59(22-23):4967-4974.

Rhodes RP, Gaden EL. 1957. Characterization of Agitation Effects in Shaken Flasks. Industrial and Engineering Chemistry 49(8):1233-1236.

Rieger M, Kappeli O, Fiechter A. 1983. The Role of Limited Respiration in the Incomplete Oxidation of Glucose by Saccharomyces-Cerevisiae. Journal of General Microbiology 129:653-661.

Sonnleitner B, Kappeli O. 1986. Growth of Saccharomyces-Cerevisiae Is Controlled by Its Limited Respiratory Capacity - Formulation and Verification of a Hypothesis. Biotechnology and Bioengineering 28:927-937.

Stewart GG, Russell I. 1981. Yeast flocculation. In: Pollock JRA, editor. Brewing Science. Toronto: Academic Press. p 61-92.

Tholudur A, Ramirez WF, McMillan JD. 1999. Mathematical modeling and optimization of cellulase protein production using Trichoderma reesei RL-P37. Biotechnology and Bioengineering 66(1):1-16.

Vandijken JP, Scheffers WA. 1986. Redox Balances in the Metabolism of Sugars by Yeasts. Fems Microbiology Reviews 32(3-4):199-224.

Verduyn C, Zomerdijk TPL, Vandijken JP, Scheffers WA. 1984. Continuous Measurement of Ethanol-Production by Aerobic Yeast Suspensions with an Enzyme Electrode. Applied Microbiology and Biotechnology 19(3):181-185.

Walther I, Vanderschoot BH, Jeanneret S, Arquint P, Derooij NF, Gass V, Bechler B, Lorenzi G, Cogoli A. 1994. Development of a Miniature Bioreactor for Continuous-Culture in a Space Laboratory. Journal of Biotechnology 38(1):21-32.

Weiss S, John GT, Klimant I, Heinzle E. 2002. Modeling of mixing in 96-well microplates observed with fluorescence indicators. Biotechnology Progress 18(4):821-830.

Yu ZS, Zhang HX. 2004. Ethanol fermentation of acid-hydrolyzed cellulosic pyrolysate with Saccharomyces cerevisiae. Bioresource Technology 93(2):199-204.

Chapter 9 Biotechnological production of γ-decalactone by the strict aerobic yeast *Yarrowia lipolytica* in the micro-bioreactor

This chapter describes the application of the micro-bioreactor to the scale-down of the biotechnological production of γ-decalactone. A decrease up to 50 % of the time required to obtain the maximum concentration of the compound was observed, when compared with other scaled-down platforms (stirred tank bioreactor or shake flask). A three-fold increase in γ-decalactone productivity was obtained by increasing oscillatory mixing intensity from a Re_o of ~482 to a Re_o of ~1,447. This was presumably related to the effective contribution of both the reactor geometry and the oscillatory flow mixing (OFM) to enhance the mass transfer rates between the two immiscible liquid phases involved in the process by increasing the interfacial area of the dispersed phase.

Keywords: γ-decalactone; micro-bioreactor; mixing; oscillatory flow; screening; two immiscible liquid phases; *Yarrowia lipolytica*.

9.1 Introduction

Rapid development of bioprocesses and their scale-up are key issues in e.g. the biopharmaceutical industry but, before one can get to commercial (large scale) fermentations of microorganisms, their growth conditions have to be tested and refined (Kumar et al. 2004).

To carry out a vast number of development fermentations, the use of controlled high-performance parallel reactor systems is required in order to speed up the process. Traditional cell cultures platforms (e.g. stirred tank - ST - bioreactors, shake flasks) are inappropriate to perform high-quality cell culture optimisation experiments in high-throughput mode for reasons of scale, reproducibility, price and available automation (e.g. Dilsen et al. 2001). Thus, microscale bioprocessing is emerging as an important high-throughput screening tool in upstream bioprocessing research.

The needs for scale-down systems resulted in the last decade in the development of successful novel micro-bioreactor (~2 – 3 ml) designs, such as those described by Walther *et al.* (1994), Kostov (2001), Girard *et al.* (2001) and some others in the tens of millilitres scale (e.g. Puskeiler et al. 2005). Platform technologies can effectively decrease the time required to develop high-producing cell lines for biotherapeutics, as well discussed in two recent reviews (Lye *et al.*, 2003, Kumar *et al.*, 2004. Micro-reactors offer a cheap and fast tool to achieve an optimisation by a screening approach, of course not only in the pharmaceutical industry, but also possibly in other areas, such as the degradation of hydrophobic pollutants and food technology.

In the present work, an innovative micro-bioreactor based on oscillatory flow, recently presented by Reis *et al.* (2005; 2004b), is foreseen as a novel scale-down technology for fast parallel bioprocessing. The micro-bioreactor's design offers sterile conditions and sufficient mass-transfer rates so as to support, for example, the fermentation of commercially-important recombinant organisms. The main innovations of this micro-bioreactor are the very good control of mixing and mass transfer rates, simply by setting the fluid oscillation conditions (e.g., Reis et al. 2005). Furthermore, studies with bench-scale oscillatory flow reactors demonstrated the linear scale-up of baffled reactors based on oscillatory flow (e.g., Ni and Gao 1996; Ni et al. 2001), thus optimisations achieved here can be applied at industrial scale.

As a proof-of-concept, this reactor was applied to the biotechnological production of γ-decalactone, which consists on the biotransformation of methyl ricinoleate by the yeast *Yarrowia lipolytica* (Aguedo et al.

2004). γ-Decalactone is a fruity (peach-like) aroma compound, thus of great interest for the flavour industry, as illustrated by the numerous existing patents (Fickers et al. 2005). *Y. lipolytica* is a strict aerobic species, particularly adapted to hydrophobic substrates. In the present system, the substrate forms an immiscible liquid phase and it is presented as an emulsion.

The feasibility and screening performance of the micro-bioreactor in bioprocesses involving immiscible liquids was assessed in the present work by monitoring *ex-situ* the number of cells and the γ-decalactone concentration in four aerobic biotransformations at increasing oscillatory mixing intensities.

9.2 Materials and Methods

The experimental biotransformation setup

In these trials a single sterilised micro-bioreactor (Reis et al., 2005) was positioned vertically, and the fluid oscillated at f from 0 to 20 s^{-1} and x_0 from 0 to 3 mm (centre-to-peak). Four experiments were carried out at different combinations of f and x_0, as shown in Table 9-1 At least two reproducible replicates were obtained for each experiment.

Table 9-1: Fluid oscillation conditions used in the four biotransformations carried out in this work, at different combinations of fluid oscillation frequency (f) and amplitude (x_0) (expressed as centre-to-peak); Re_o is the oscillatory Reynolds number and is a measure of mixing intensity.

Experiment	x_0 [m]	f [s^{-1}]	Re_o [-]
I	1	18	482
II	2	10	536
III	2	18	965
IV	3	18	1447

Pre-cultured cells of *Yarrowia lipolytica* W29 (ATCC20460; CLIB89) in the late growth-phase (19 h) were washed (6,000 g, 5 min) three times with water and transferred to the biotransformation medium, consisting of: 10 g methyl-ricinoleate l^{-1}, 2.5 g NH_4Cl l^{-1}, 6.7 g YNB l^{-1} and 1 g Tween80 l^{-1} (Aguedo et al.

2004). Initial ~1-2 x 10^8 cells ml^{-1} was pumped to a SPC tube and the biotransformations were carried out in batch mode and controlled at 27 °C. Air was continuously injected through the bottom of the SPC tube at an aeration rate of 0.064 vvm and 300 μl samples were collected every two hours for cells counting and γ-decalactone quantification. The experimental apparatus is shown in Figure 9-1.

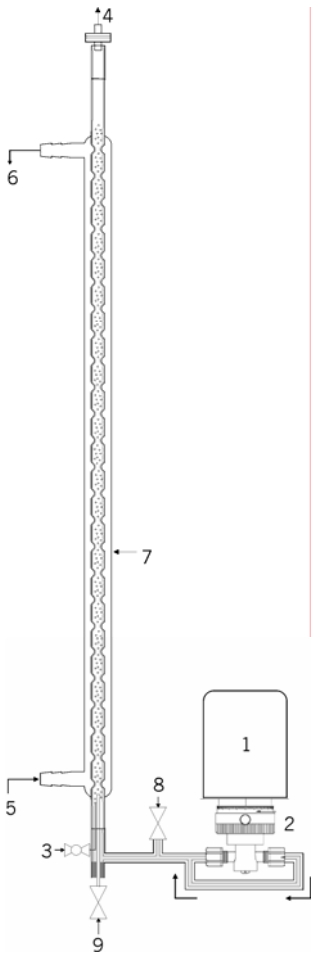

Figure 9-1. Experimental setup used in batch biotransformations. 1- rotary motor; 2- piston pump; 3- air inlet; 4- air outlet; 5- fluid heating inlet; 6- fluid heating outlet; 7- SPC tube; 8- purging port; 9- sampling port.

9.3 Results and discussion

γ-Decalactone production and *Y. lipolytica* cells counts along the biotransformation time are given in Figure 9-2 and Figure 9-3, respectively.

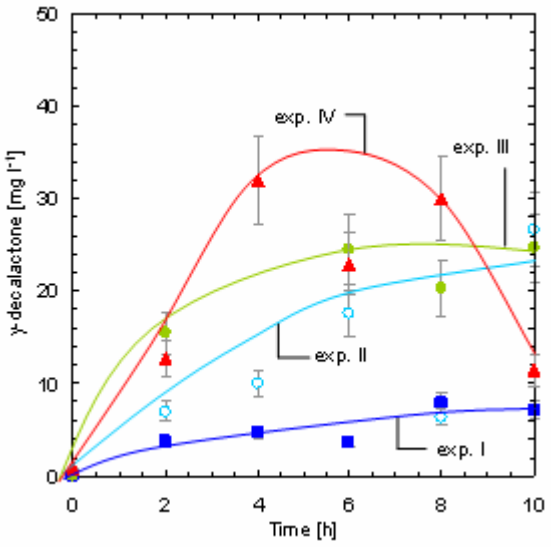

Figure 9-2. Concentration of γ-decalactone experimentally obtained with a SPC tube in the four biotransformations carried out in this study (details given in

Table **2-1**): ■ - experiment I; ○ - experiment II; ● - experiment III; ▲ - experiment IV. Biotransformations started with ~0.5-2 x 10^8 cells ml^{-1} and were controlled at 0.064 vvm and 27 °C. The initial pH was 5.6 and it was not controlled. The fluid was subjected to different oscillation conditions, as mentioned in

Table **2-1**. The concentration of γ-decalactone was assessed by *L-L* extraction with diethyl ether followed by GC analysis (Aguedo et al. 2004). Error bars correspond to standard deviation of samples during replicated GC assessment.

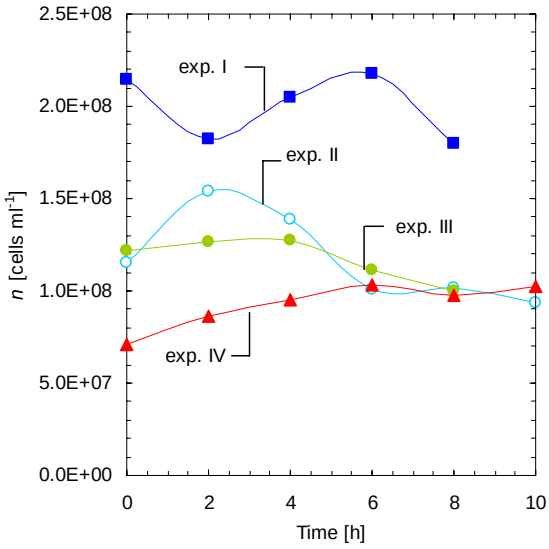

Figure 9-3. Evolution of the number of cells (*n*) of *Y. lipolytica* in suspension within a SPC tube in the four biotransformations carried out in this study (details given in Table **2-1**): ■ - experiment I; ○ - experiment II; ● - experiment III; ▲ - experiment IV. Cell counting was assessed with a Neubauer cell, with a reproducibility of 80 to 90 %.

The aroma compound production presented a maximum for the higher value of Re_o (exp. IV) followed by a decay of its concentration (Figure 9-2). This is a consequence of the substrate exhaustion at that maximum point, as confirmed by gas-chromatography analysis (results not shown): when no other carbon source is available, yeast degrades the γ-decalactone present in the medium. The production of the aroma compound was increased in a linear way by the oscillatory flow mixing (as measured by Re_o) (Figure 9-4), demonstrating the beneficial effect of increasing Re_o. The time necessary to reach the maximum concentration of γ-decalactone (around 6 hours) at highly axial-dispersed conditions (i.e. x_0 = 3 mm) (exp. IV in Figure 9-2) was reduced to about 50 % of that obtained in traditional scale-down systems, such as ST bioreactors (Aguedo *et al.* 2005) or shake flasks. This was confirmed with further experiments carried out at the same conditions (data not shown).

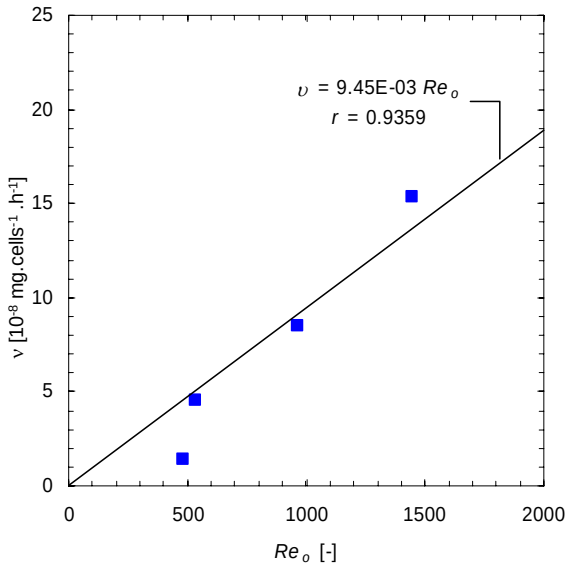

Figure 9-4. Evolution of the specific rate of production of γ-decalactone (υ) with the oscillatory mixing intensity (i.e. oscillatory Reynolds number, Re_o).

The cell concentration along the biotransformation time did not vary significantly, as seen in Figure 9-3. However, in some experiments the cell concentration slightly decreased, as a consequence of cells entrapment inside the loop connecting the SPC tube to the piston pump (see Figure 9-1). This tube section (with ~20 % of operating volume) was not provided with constrictions, thus cells tended to accumulate initially inside it. This problem requires the re-designing of the oscillatory unit, namely by using an oscillating piston and/or a diaphragm directly fitted to the bottom of SPC tube.

Experiment I in Figure 9-3 was intentionally started with a higher cell concentration, to check the eventual effect of this factor on the γ-decalactone production. The final effect was a decrease of the specific production rate of the metabolite.

γ-Decalatone concentrations obtained in this work were of similar order of magnitude of those reported for ST bioreactors, while using an aeration rate corresponding only to 6.4 % of the typical value in ST bioreactors (1 vvm). This demonstrates the high performance of this micro-bioreactor not only for strictly aerobic processes but also for two immiscible liquid phase bioprocesses. It is clear that, at this low aeration rate, oxygen supply is enough to satisfy the demands of the strain used, which is an obvious advantage of this system in what concerns aeration associated costs. The k_La values of up to 0.05 s^{-1}

found in this micro-reactor for a non-coalescing system (f from 0 to 20 s^{-1} and x_o from 0 to 3 mm, centre-to-peak) at an aeration rate as low as 0.064 vvm compare favourably with values from lab-scale bioreactors (ST bioreactors and shake flasks) (Reis et al. 2004a). An oxygen transfer rate (OTR) up to ~350 mmol O_2 l^{-1} h^{-1} may be achieved with this reactor for aerobic cultures, which is a significant improvement in relation to OTRs of other micro-reactor systems such as e.g. deep square wells, with typical OTR values of 16 – 33 mmol O_2 l^{-1} h^{-1} (Lye et al. 2003).

In the present case this is beneficial to the metabolism of *Y. lipolytica* which is a strictly aerobic yeast species. O_2 also indirectly participates in the metabolic pathway leading to the formation of the lactone (peroxisomal β-oxidation), however, no direct relation between oxygen supply and the rate of γ-decalactone production was evidenced (Aguedo *et al.* 2005).

Another factor susceptible of modifying the metabolite production and that can be influenced by the hydrodynamic behaviour of the SPC tube is the size of the substrate lipidic droplets. As the substrate is emulsified, droplet size may exert a limitation in the biotransformation process, where the interfacial area between the organic and aqueous phases is important for mass transfer: not only to favour the access of yeast to substrate but also to extract the produced γ-decalactone (Aguedo et al. 2004).

It is known that the use of oscillatory flow leads to a stable, fine emulsion in which the size of the oil droplets is effectively controlled by changing the fluid oscillation conditions (f or x_o). This effect has been observed also in other systems, e.g. a linear decrease of the mean particle size of methylmethacrylate polymer with Re_o was reported by Ni *et al.* (1999). The hydrodynamic behaviour of the liquid phase within a SPC tube was intensively characterised in previous studies (see Reis et al. 2005; Reis et al. 2004a; Reis et al. 2004b) and similar results to those of e.g. Ni *et al.* (1999) were obtained meaning that the mixing intensity of this reactor allows for an effective control of the droplet size in the bioconversion medium. This improves the available surface area for phase contact, increasing the overall reaction rate, as confirmed by the linear relation observed between the specific production rate of γ-decalactone (as well as productivity, once biomass concentration is of the same order of magnitude in all experiments) and mixing intensity, as defined by Reynolds number (Figure 9-4).

All these features suggest the use of this micro-bioreactor as a suitable device for biotransformations involving immiscible liquid phases, as confirmed by the results presented in this work.

9.4 Conclusions

As demonstrated with the case-study of biotechnological production of γ-decalatone, this novel micro-bioreactor, due to its very modest size, constitutes a valuable tool for screening purposes of bioprocesses involving microorganisms within immiscible liquid phases.

One of the main conclusions of the present work is that γ-decalactone productivity can be enhanced within this micro-bioreactor by generating an intensive mixing. Due to the oscillatory flow such mixing is achieved at laminar flow conditions, thus avoiding high stresses usually experimented by cells in traditional scale-down vessels, such as ST bioreactors.

New advances could now be achieved by the use of state-of-the art fibre optics technology (for on-line and real-time monitoring and/or control of dissolved O_2, biomass, substrate, pH, metabolites...) and the construction of a micro-bioreactor unit composed of a single unit with several SPC tubes running in parallel, allowing the automation of screening procedures. In addition, the possibility of continuous running presented by this micro-bioreactor is a great step forward in the field of high-throughput bioprocess designs.

9.5 References

Aguedo M, Gomes N, Escamilla Garcia E, Waché Y, Mota M, Teixeira JA, Belo I (2005) Decalactone production by *Yarrowia lipolytica* under increased O_2 transfer rates. *Biotechnol. Lett.* **27:** 1617-1621.

Aguedo M, Wache Y, Coste F, Husson F, Belin JM (2004) Impact of surfactants on the biotransformation of methyl ricinoleate into gamma-decalactone by *Yarrowia lipolytica*. *J. Mol. Catal. B-Enzym.* **29**: 31-36.

Dilsen S, Paul W, Herforth D, Sandgathe A, Altenbach-Rehm J, Freudl R, Wandrey C, Weuster-Botz D (2001) Evaluation of parallel operated small-scale bubble columns for microbial process development using *Staphylococcus carnosus*. *J. Biotechnol.* **88**: 77-84.

Fickers P, Benetti PH, Wache Y, Marty A, Mauersberger S, Smit MS, Nicaud JM (2005) Hydrophobic substrate utilisation by the yeast *Yarrowia lipolytica*, and its potential applications. *FEMS Yeast Res.* **5**: 527-543.

Girard P, Jordan M, Tsao M, Wurm FM (2001) Small-scale bioreactor system for process development and optimization. *Biochem. Eng. J.* **7**: 117-119.

Kostov Y, Harms P, Randers-Eichhorn L, Rao G (2001) Low-cost microbioreactor for high-throughput bioprocessing. *Biotechnol. Bioeng.* **72**: 346-352.

Kumar S, Wittmann C, Heinzle E (2004) Minibioreactors. *Biotechnol. Lett.* **26**: 1-10.

Lye GJ, Ayazi-Shamlou P, Baganz F, Dalby PA, Woodley JM (2003) Accelerated design of bioconversion processes using automated microscale processing techniques. *Trends Biotechnol.* **21**: 29-37.

Mackley MR (1991) Process innovation using oscillatory flow within baffled tubes. *Chem. Eng. Res. Des.* **69**: 197-199.

Ni X, Gao S (1996) Scale-up correlation for mass transfer coefficients in pulsed baffled reactors. *Chem. Eng. J.* **63**: 157-166.

Ni X, Zhang Y, Mustafa I (1999) Correlation of polymer particle size with droplet size in suspension polymerisation of methylmethacrylate in a batch oscillatory-baffled reactor. *Chem. Eng. Sci.* **54**: 841-850.

Ni XW, de Gelicourt YS, Baird MHI, Rao NVR (2001) Scale-up of single phase axial dispersion coefficients in batch and continuous oscillatory baffled tubes. *Can. J. Chem. Eng.* **79**: 444-448.

Puskeiler R, Kusterer A, John GT, Weuster-Botz D (2005) Miniature bioreactors for automated high-throughput bioprocess design (HTBD): reproducibility of parallel fed-batch cultivations with *Escherichia coli*. *Biotechnol. Appl. Biochem.* **42**: 227-235.

Reis N, Harvey AP, Vicente AA, Teixeira JA, Mackley MR (2005) Fluid mechanics and design aspects of a novel oscillatory flow meso-reactor. *Chem. Eng. Res. Des.* **83**: 357-371.

Reis N, Vicente AA, Teixeira JA, Mackley MR. (2004a) Enhanced mass transfer rates of a novel oscillatory flow screening reactor. In: *Summaries of the 16th International Congress of Chemical and Process Engineering*, 22nd - 26th August, Praha, Czech Republic, pp 898-899. ISBN 80-86059-40-5

Reis N, Vicente AA, Teixeira JA, Mackley MR (2004b) Residence times and mixing of a novel continuous oscillatory flow screening reactor. *Chem. Eng. Sci.* **59**: 4967-4974.

Walther I, Vanderschoot BH, Jeanneret S, Arquint P, Derooij NF, Gass V, Bechler B, Lorenzi G, Cogoli A (1994) Development of a miniature bioreactor for continuous-culture in a space laboratory. *J. Biotechnol.* **38**: 21-32.

Chapter 10 Lysozyme Dilution Refolding

Continuous dilution refolding of lysozyme (50 μg/ml) was assessed in the meso-reactor under continuous operation, presenting an enhanced selectivity, while controlled convection and fluid dispersion was assured through the use of oscillatory flow mixing (OFM). Batch, small-scale refolding experiments were run in beakers (~5 ml) and in a 5 mm i.d. × 350-mm-long SPC tube, using different procedures of dilution/mixing of denatured lysozyme (in 8 M urea, 32 mm DTT) in the refolding buffer (4 mM Gluthanione oxidised) and different injection times. These basic experiments allowed the study of the effect of mixing intensity and OFM nature in the aggregation and refolding yield (Y_{ref}) in dilution refolding. Finally, continuous lysozyme dilution refolding was assessed in the meso-reactor, using a mean hydraulic residence time of 79 minutes.

It has been experimentally demonstrated that the improvement of Y_{ref} due to mixing is actually limited to the first moments of refolding kinetics. In particular, the positive effect of OFM on Y_{ref} is observed only during the initial stage of the batch refolding process, by assuring from the very beginning of the process a good dispersion and mixing of denatured lyszoyme. The continuous refolding of lysozyme through dilution with a refolding buffer has shown not to take place within a meso-reactor operated under OFM (even for very gentle OFM conditions, e.g. 1 mm and 1 Hz).

Keywords: dilution refolding; continuous; micro-bioreactor; meso-reactor; oscillatory flow mixing.

10.1 Introduction

Proteins are actually a product of genes and a target for drugs. They are very interesting to biopharmaceutical industry for their potential therapeutic use (e.g. insulin, EPO, tPA, hGH, antibodies, etc) or to be merely used for screening, for developing and optimisation of low-molecular-weight drugs (receptors, proteases, kinases, ion-channels) (Lubiniecki 1990). Therapeutic proteins may be accessed as native or recombinant, but native proteins are limited in humans to blood proteins. Recombinant proteins may be expressed in several types of host cells: bacteria (*Escherichia coli*), yeast (*Saccharomyces cerevisiae*, *Pichia pastoris*), mammalian cells (C127, CHO, DON, HEK, BHK, COS), insect cells (High-five, Sf 9, Sf 21), transgenic plants/animals (e.g. sheep, goat, cow). Protein expression from bacteria and yeast hosts are a very fast, very cheap, well characterised, easy scale-up, and usually with a final high expression level. *E. coli* retains its dominant position as the first choice of hosts, although a key disadvantage is the formation of insoluble inclusion bodies for some gene sequences.

Inclusion bodies are dense aggregates of misfolded polypeptide (e.g., Dobson 2003), usually located at the bacterial cytoplasm, although secreted proteins can form inclusion bodies in the periplasmic space. The protein must therefore be released from the inclusion body and 'refolded' or 'renatured' to return to its native 3D structure. Batch and fed-batch refolding through dilution/mixing with a refolding agent is a default step for biopharmaceutical production of recombinant proteins, but the design of a continuous refolding system would allow the full integration of the bioprocess.

Purification and separation of proteins from culture broths usually cross three main stages (Middelberg 2002): *i*) isolation of the inclusion bodies; *ii*) removal of contaminants; *iii*) solubilization of inclusion bodies

using a concentrated chemical denaturant, such as urea or guanidinium chloride (also usually designated by chaotropes). In addition, reducing agents are often coupled to the denaturant, such as DTT or 2-mercaptoethanol (the last being harmful, thus DTT is preferred). Urea (6 – 8 M) is usually preferred in industry as it is cheaper, however having the disadvantage of degrading when in aqueous solution. Guanidine chloride is a stronger denaturant than urea and has the advantage of not degrading when in solution, however it is more expensive than urea and toxic (thus requiring a separation from the final solution) (Buswell 2002).

After dissolution, proteins must be refolded (to achieve its native 3D structure) and the denaturants in excess must be removed. This is usually run through two main ways (Middelberg 2002): *i*) by dilution into an appropriate refolding buffer (dilution method); *ii*) using packed columns (column-based method).

Dilution is the most common method of initiating the refolding process, and it consists in the mixing of the unfolded protein with a buffer solution. It is simple and enables the easy screening of additives and redox agents (Middelberg 2002). Previous small-scale studies have run dilution refolding in different reactor systems (Clark 2001): *i*) batch; *ii*) multiple steps (pulse refolding); *iii*) semi-continuous (fed-batch); *iv*) continuous. The use of batch and fed-batch systems is frequently reported, continuous systems are limited to the work of Terashima *et al.* (1996): lysozyme refolding by dilution in a flow-type reactor.

Oscillatory flow reactors (OFRs) were also successfully applied in the fed-batch refolding of lysozyme, using a final lysozyme concentration of 1 mg/ml (Lee et al. 2002; Lee et al. 2001). Values of refolding yield (Y_{ref}) after 3 hours of mixing were found similar in the OFR (at oscillatory flow Reynolds number, Re_o = 250 and 1580) and in a stirred tank reactor (STR) working at different rotor speeds (Re_T = 726, 3267 and 6353), thus OFR was strongly suggested as a viable reactor for protein refolding via direct dilution. Furthermore, the same two studies have brought important observations: *i*) dilution and dispersion significantly affect Y_{ref}; *ii*) mixing affects Y_{ref}; *iii*) aggregation occurs within a seconds-scale. The true impact of mixing on dilution refolding was recently assessed by Mannal *et al.* (2006), by stating that the effect of mixing only on Y_{ref} is limited to the time period ranging from the addition of denatured protein to the short period immediately after that addition.

Proteins with free disulphide bonds require oxidising agents with redox-couples, e.g. oxidised and reduced gluthanione (1 - 5 mM). For protein concentrations above 10 μg/ml (Middelberg 2002), there is an irreversible formation of protein aggregates, because refolding occurs through a competitive 1st order

reaction, while aggregation is of 2nd or higher order kinetics (Figure 10-1). For lysozyme, aggregation is best predicted with 3rd order kinetics, accordingly Hevehan and Clark (1997). The degree of aggregation is mostly affected by the concentration of protein, thus refolding is generally conducted at flow protein concentrations, namely 10-100 μg/ml. However, it significantly affects the overall economics of the refolding process due to increased solution volumes required for the industrial production of correctly refolded proteins (Middelberg 1996).

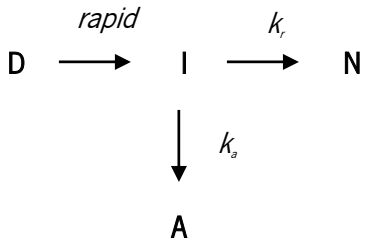

Figure 10-1. Simplified kinetic scheme showing first-order refolding competing with higher-order aggregation, where k_r is the refolding rate constant and k_a is the aggregation rate constant (Hevehan and Clark 1997).

Recently, Buswell and Middelberg (2003) based on fed-batch and 'snapshot' batch refolding reactions have suggested a novel kinetic model for lysozyme refolding and aggregation, which allows for aggregation via a sequential mechanism, considering that monomeric lysozyme in different states, including native, is able to aggregate with intermediates. The subsequent work of Gu *et al.* (2004) supported the role of intermediate state *I* in the dilution refolding process by demonstrating that intermediate states are very important in determining the fate of refolded proteins.

This work tests the novel meso-reactor as a scale-down system for continuous refolding of proteins through the dilution method. The macroscopic flow patterns within the meso-reactor are driven towards an ideal plug flow through flow detachment and convection within the smooth periodic contricted (SPC) tubes, thus permitting the prediction of a maximized volumetric productivity and refolding yields in relation to the batch and fed-batch operations. Refolding is initiated by mixing denatured-reduced lysozyme (in 8 M urea and 32 mM of DTT) with a refolding agent (oxidised gluthanione, 4 mM), being Y_{ref} followed through the residence time in the meso-reactor. Further basic, small-scale batch experiments run in small beakers (~5

ml) and in a 4.9 ml SPC tube operating under OFM, allowed a good initial understanding of the effects of dilution and mixing upon Y_{ref}.

10.2 Materials and methods

The procedure and conditions for denaturing-reducing of lysozyme, batch refolding of lysozyme and analytical methods were based on those reported in Buswell (2002).

Materials

Chicken egg white lysozyme, lyophilized powder ~100,000 Units/mg protein was purchased from Sigma-Aldrich Company Ltd., (Poole, UK). L-glutathione oxidised (GSSG), urea, Tris buffer, ethylenediaminetetraacetic acid (EDTA), HCl, NaOH and Trifluoroacetic Acid (TFA) were sourced from Sigma-Aldrich Company Ltd. (Poole, UK), and were ACS reagent grade, except TFA which was HPLC quality grade (> 99 %). Dithiothreitol (DTT) was from Melford Laboratories (Chelsworth, UK) and *Micrococcus lysodeikticus* ATCC No. 4698 dried cells were obtained from Sigma-Aldrich Company Ltd. (Poole, UK). All solutions were prepared using distilled water and pH readjustments were done with NaOH or HCl, 4 M.

Denaturation-Reduction of Lysozyme

Native lysozyme was incubated for at least 1 h (preferably for 3-4 h), at 37 °C, in an orbital shaker (set at 120 rpm) in a denaturing-reducing buffer (typical volume was 10 ml). Composition of denaturing-reducing buffer was: 8 M urea, 32 mM DTT, 50 mM Tris, 1 mM EDTA; pH 8.0. The loss of enzymatic activity following denaturation confirmed the absence of residual native protein. Denatured lysozyme was used for experiments at the same day.

Refolding of Lysozyme

Lysozyme refolding experiments were run at room temperature (20 °C) by adding a small volume of denatured-reduce lysozyme (with a micro-pipette) to a refolding buffer, in a dilution ratio of 1:15, thus

giving a lysozyme concentration after dilution of 50 μg/ml. Composition of refolding buffer was: 4 mM GSSG, 50 mM Tris, 1mM EDTA, pH 8.0, 20 °C. Samples (135 μl) were taken at regular times and immediately quenched with 15 μl of TFA (10 %) (dilution ratio = 9:10), thus giving a final protein concentration lower than 0.1 mg/ml (which fits in the linear range of enzyme activity calibration curve). When needed, samples were kept under refrigeration (4 °C) overnight, but were preferably analysed for enzyme activity on the same day.

Micrococcus Lysodeikticus Lysozyme Assay

Enzymatic activity was conducted by following the decrease in absorbance of a cell suspension (0.15 mg/ml *Micrococcus lysodeikticus*, 0.067 M sodium phosphate, pH 6.0) at ambient temperature (20 °C). An aliquot of 20 μl of diluted sample was added to 980 μl of cell suspension (ratio of 1:50) in a disposable cuvette, briefly mixed for 5 seconds, and the absorbance was measured at 450 nm (Unicam UV1 Spectrophotometer, UK) for 30 seconds. Samples were analysed in triplicate for enzyme activity. Percentage of refolded (native) protein in each sample was given by the ratio of the slope of absorbance decay of the sample to the slope of absorbance decay of a native lysozyme standard (diluted in the same original buffer). The above procedure was found to give a linear correlation for lysozyme concentration in the range of 0 - 0.8 mg/ml in the sample (i.e. protein concentration before quenching with TFA) (Figure 10-2).

Assessment of the effect of mixing and injection time upon batch lysozyme refolding yield

Several small-scale (~5 ml) refolding experiments were firstly run in small beakers. These experiments consisted in the batch dilution of 213 μl of denatured-reduced lysozyme within 5 ml of refolding buffer, at room temperature (20 °C). Three batch, mixing procedures were tested: i) addition of denatured-reduced lysozyme to the refolding buffer through a sharp stroke of micropipette, followed by a brief mixing (10 s in a vortex mixer) and then leaved unstirred; ii) sharp-injection of reduced lysozyme to the refolding buffer which was kept mixed (with a magnetic stirrer, ~120 rpm) during all the refolding experiment; iii) slow addition (injection time = 30 seconds) of denatured-reduced lysozyme to the refolding buffer in a mixed container. Samples were collected after 2, 4, 8, 16, 32, 64 and 128 minutes.

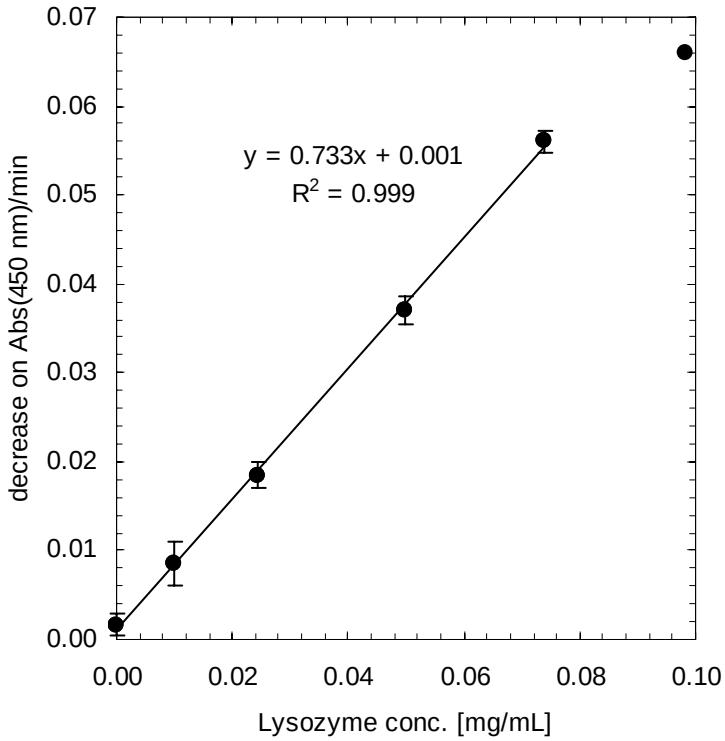

Figure 10-2. Relation between lysozyme concentrations (before dilution with TFA) and slope of decrease on absorbance (450 nm) of a cell suspension (0.15 g/l *Micrococcus lysodeikticus*).

Assessment of the effect of oscillatory flow mixing and injection time upon batch-lysozyme refolding yield

A 5 mm internal diameter × 350-mm-long SPC tube was vertically fixed and the bottom of the tube was fitted (sealed) to a Teflon cylinder case, holding a small piston (5.0 mm external diameter). Fluid was oscillated reciprocally by moving the piston up and down stroke through a magnetic oscillator, as shown elsewhere (Reis et al. 2005). Fluid oscillation frequency (f) and amplitude (x_o) were controlled by setting the signal frequency and signal power, respectively, in a signal generator unit supplying the magnetic oscillator.

The total batch volume of the system (4.9 ml) was overfilled with fresh, refolding buffer and fluid oscillations started (at a defined f and x_o) at ambient temperature (20 °C). Then, 327 μl of buffer were removed and the same volume of denatured-reduced lysozyme injected (corresponding to a 1:15 dilution of reduced lysozyme) with a HPLC syringe, about 10 cm below the top of the fluid surface. Two modes of injection were used: i) a fast injection of reduced lysozyme (corresponding to a sharp movement of syringe

piston) and ii) a slow addition of reduced lysozyme (injection time of 2 and 4 minutes). Samples (22.5 μl) were taken in triplicate after 2, 4, 8, 16, 31, 64 and 128 minutes, immediately quenched with 2.5 μl of TFA (10 %) and kept in the fridge (4 °C).

Assessment of continuous refolding of lysozyme in the meso-reactor

Due to the high density of denatured-reduced lysozyme solution (containing 8 M of urea), the operation of meso-reactor at smooth OFM conditions (i.e. low x_0 and f) was found to be incompatible with a good and rapid mixing (with a time-scale of few milliseconds). Thus, the meso-reactor was run downstream a 3 ml stirred tank (where dilution of denatured-reduced lysozyme solution and the refolding buffer would take place) as described below.

Fresh denatured-reduced lysozyme (6.9 ml/h) and refolding buffer (97 ml/h) were continuously fed through two capillary tube to a 3 ml stirred container (continuously stirred with a magnetic stirrer), thus giving a dilution ratio of 1:15 and a residence time in the container of ~2 min. Then, the diluted lysozyme solution was continuously injected in the mixing chamber of the meso-reactor unit (working at a defined f and x_0) at a flow rate of 103.9 ml/h, through a non-return valve. The meso-reactor was run for at least 3 mean residence times (> 4 hours) (i.e., until stabilisation of enzyme activity) and samples were collected at the end of each 800-mm-long tube (through sealed, sampling ports installed in U-bends) with a 0.5 mm i. d. syringe needle, corresponding to residence times of: 14, 22, 30, 39, 47, 55, 63, 71 and 79 minutes. A sample volume of 135 μl was quenched with 15 μl of TFA (10%) and analysed for enzyme activity.

10.3 Results and discussion

Effect of mixing conditions upon batch lysozyme refolding yield

This part of the work was related with the understanding of refolding process by the dilution method and in particular with the study of the eventual effect of mixing and dilution in the overall refolding yields (Y_{ref}).

Figure 10-3 shows the results of Y_{ref} for a refolding initiated with the addition of denatured lysozyme to 3 ml of refolding buffer, in a Falcon tube left unstirred during the reaction time (solution briefly mixed at the beginning, after a sharp addition of denatured-reduced lysozyme). This procedure closely reproduces the

refolding procedure used by Buswell and Middelberg (2003), thus both experimental results are very similar. In particular, in both cases the maximum value of Y_{ref} obtained was about 80 %.

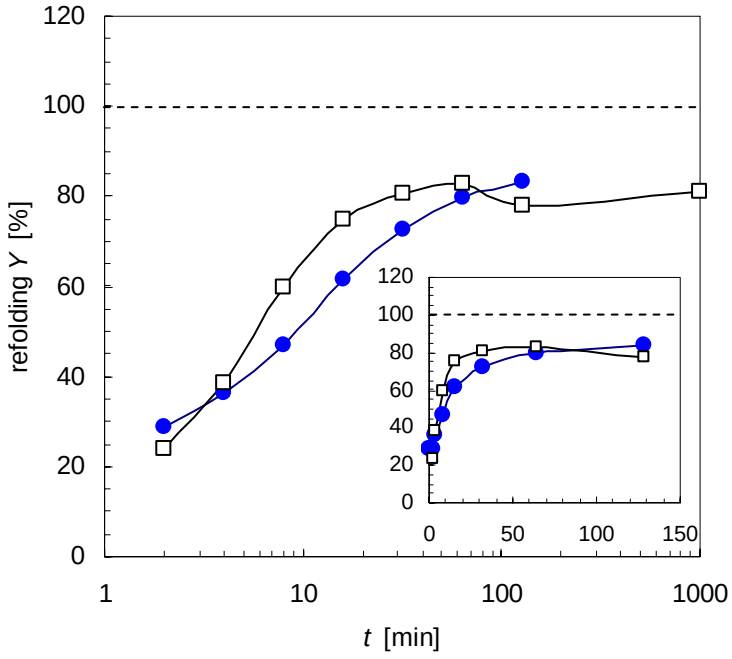

Figure 10-3. Refolding yield (Y_{ref}) of lysozyme in a batch, unstirred Falcon tube (denatured-reduced lysozyme added with a sharp micropipette stroke and solution briefly mixed); ● this work; □ results from Buswell & Middelberg (2003).

Subsequently, refolding experiments were run in a ~5 mL stirred beaker (Figure 10-4). Refolding was initiated by adding the denatured lysozyme to 5 mL of refolding buffer through a sharp micropipette stroke. In comparison with the unstirred situation (Figure 10-3), Y_{ref} is slightly increased (by about 10 %), thus suggesting that mixing has an effect on dilution refolding and aggregation.

When refolding was initiated through an injection time of 30 s, the final value of Y_{ref} successfully reached 100 % after ~30 minutes (Figure 10-5), thus demonstrating that injection time strongly affects the overall value of Y_{ref}. This is thought to be related with the non-ideal mixing of the stirred systems: because competitive aggregation reaction is of higher order than the refolding reaction, the existence of high concentrations of denatured-reduced lysozyme (as occurs in an unstirred system or during the fast-injection of lysozyme to the refolding buffer) favours the aggregation process, thus decreasing the overall

Y_{ref}. In practice, by using higher injection times the occurrence of volume fractions with high lysozyme concentrations (Figure 10-5) is avoided, thus justifying the improvement of final Y_{ref}.

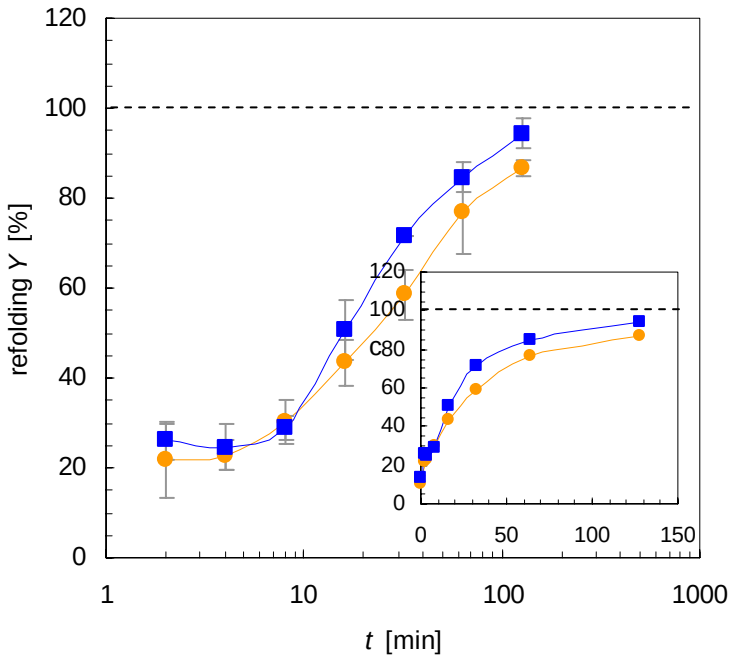

Figure 10-4. Refolding yield (Y_{ref}) of lysozyme in a batch, small stirred beaker (refolding initiated with a sharp addition of denatured lysozyme); two parallel experiments are shown. Vertical bars represent standard deviation of Y_{ref}.

In summary, the batch lysozyme refolding reaction in a small beaker (~5 ml) allows to conclude that mixing is in fact very important to the overall Y_{ref}, but such effect is presumably limited to the first instants of the refolding reaction, in particular with the dilution and dispersion of denatured-refolded lysozyme solution (with 8 M of urea). These conclusions are in accordance with the recent findings of Mannal *et al.* (2006).

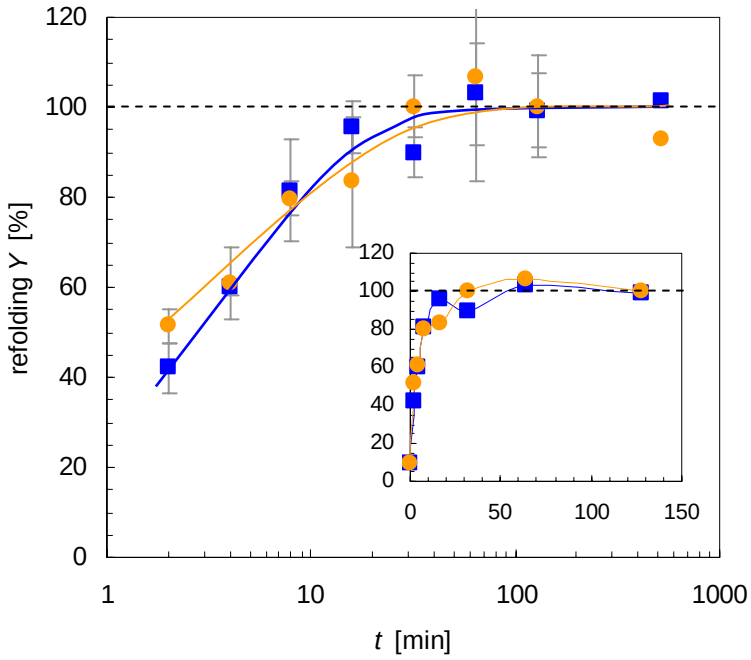

Figure 10-5. Refolding yield (Y_{ref}) of lysozyme in a batch, small stirred beaker; refolding initialled through a slow addition (30 s) of denatured-reduced lysozyme solution (average injection rate = 0.7 ml/min).

Effect of OFM upon batch lysozyme refolding yield

The batch refolding experiments presented above have demonstrated the vital importance of a good initial dispersion of the denatured-reduced lysozyme (in 8 M urea solution). In consequence, several experiments were run in a batch SPC tube, operating under oscillatory flow mixing (OFM), at a constant x_0 of 3 mm and varying fluid oscillation frequency (f). This value of x_0 ensures a good initial dispersion of lysozyme throughout the SPC tube length as previously shown in mixing time studies (Reis et al. 2004). Different injection times and mixing procedures were tested, and the obtained value of Y_{ref} is shown in Figure 10-6.

Experiments performed under OFM clearly demonstrated that SPC batch system is not viable for dilution refolding at the tested operation conditions. In comparison with the experiment performed at x_0 = 3 mm, f = 10 Hz, and using a sharp-injection of denatured-reduced lysozyme, a slight increase of Y_{ref} (16.2 %) was obtained through the increase of injection time (from 2 to 4 minutes), while a 23.3 % increase was obtained by decreasing f from 10 to 3 Hz and using an injection time of 2 minutes. In fact, the higher values of Y_{ref} were obtained by starting the refolding with an injection time of 2 minutes and running the SPC tube at 10 Hz and 3 mm just for 4 minutes (with OFM being afterwards stopped).

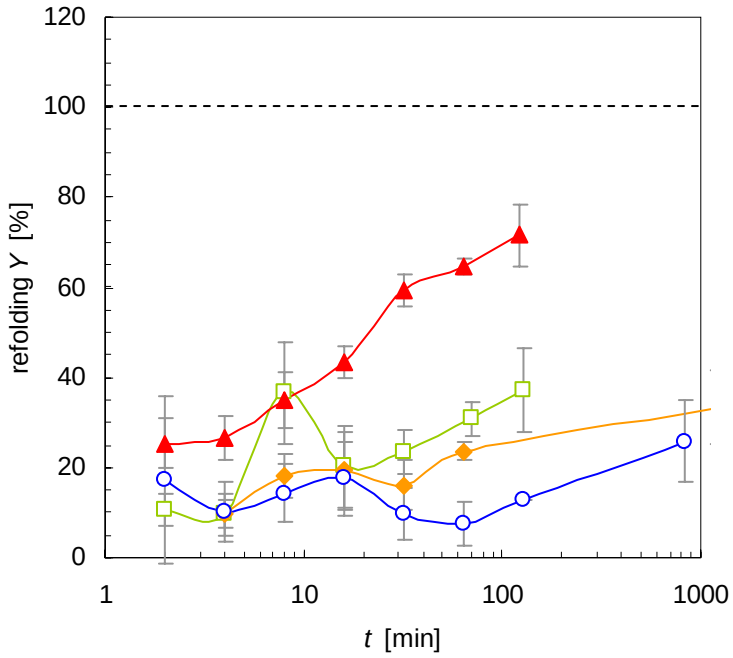

Figure 10-6. Refolding yield (Y_{ref}) of lysozyme in a batch, 350-mm-long SPC tube at a constant x_0 = 3 mm and varying f and injection procedures. ○ f = 10 Hz, sharp injection; ♦ f = 10 Hz, injection time = 4 min; □ f = 3 Hz, injection time = 2 min; ▲ f = 10 Hz, injection time = 2 min and OFM stopped at t = 4 min.

The use of OFM during the first 4 minutes assured a high initial dispersion and avoided high concentrations of lysozyme near the injection point. This suggests that mixing (at least that provoked by OFM) is not necessary (its presence being even a drawback) to the refolding reactor after a complete dilution of protein is achieved.

Assessment of continuous lysozyme refolding yield in the meso-reactor

Dilution refolding experiments of lysozyme were continuously run in the meso-reactor. Several combinations of f and x_0 were tested, but the higher values of Y_{ref} where obtained at 1 Hz and 1 mm (Figure 10-7). Different OFM conditions led to a great extent of protein aggregation (as observed through the glass walls of the reactor).

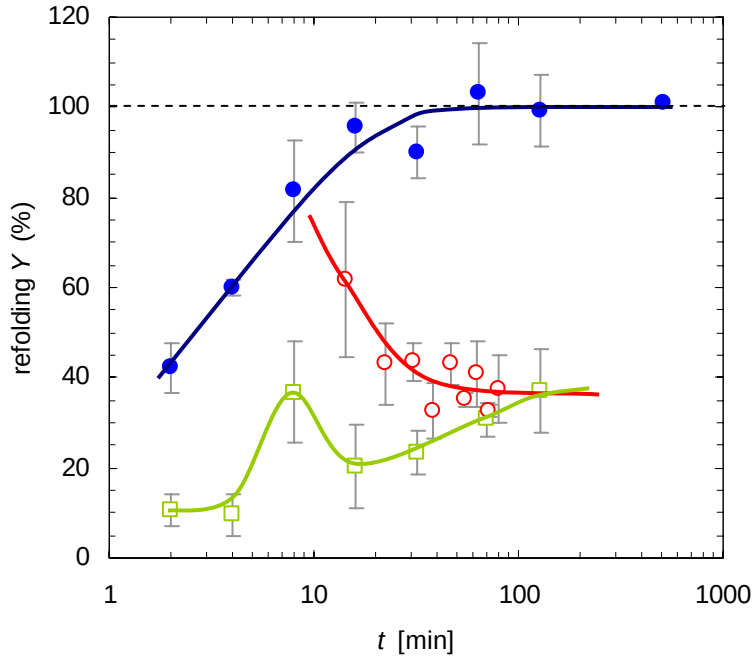

Figure 10-7. Comparison of refolding yields (Y_{ref}) of lysozyme in the continuous meso-reactor (along the residence time, t) with the values of Y_{ref} in batch dilution refolding. ● batch refolding in a small stirred beaker, with injection time >> 0 s; ○ continuous refolding in a meso-reactor at x_0 = 1 mm, f = 1 mm, Re_o = 30; □ batch refolding in the SPC tube, x_0 = 3 mm, f = 3 Hz, injection time = 2 min.

The meso-reactor was run in series with a (~5 mL) stirred glass beaker (τ = 2 min), thus the values of Y_{ref} presented in Figure 10-7 correspond to samples taken at different axial positions along the meso-reactor length, which is of course related with the residence time. The continuous meso-reactor was not successful in achieving the performance of the batch stirred glass beaker (shown in Figure 5), but it achieved values of Y_{ref} similar to those obtained for the batch SPC tube (i.e., $Y_{ref} \approx 40$ %). The major conclusion from Figure 10-7 is the impossibility to obtain lysozyme refolding (i.e. increase of Y_{ref}) within the meso-reactor, as Y_{ref} decreased all along the reactor length up to $t \approx 30$ min. In fact, an increasing aggregation was observed along the reactor, and it could be concluded that OFM in the meso-reactor further favours the aggregation reaction pathway (which is already favoured by the higher order of the reaction for longer reaction times) instead of the formation of the native lysozyme. This is presumably related with the fluid mechanics of OFM, as its reciprocating nature improves the 'probability' of having two lysozyme molecules contacting each other, thus aggregating through an irreversible pathway accordingly the kinetic model of Buswell and Middelberg (2003). The backflow rate introduced by the OFM

may bring upstream some native proteins, thus decreasing the value of Y_{ref} by aggregating with intermediate states of lyszoyme.

10.4 Conclusions

Small-scale (~5 ml) dilution refolding experiments run in a glass beaker have demonstrated that batch refolding yield (Y_{ref}) is optimum when the dilution of reduced lysozyme is done through to its slow addition (during 30 seconds) and under well mixed conditions (stirred tank). Such procedure allowed the achievement of a value of Y_{ref} = 100 % within 30 minutes. The further batch experiments run in a 5 mm i. d. × 350-mm-long SPC tube have turned clear that enhancement of dilution refolding through oscillatory flow mixing (OFM) is limited to the initial stage of the refolding process (first 2 – 4 minutes), with the use of OFM assuring a good dispersion and mixing of solutions from the very beginning. Unfortunately, the continuous lysozyme dilution refolding experiments run in the meso-reactor at OFM conditions as gentle as 1 mm and 1 Hz suggests that aggregation (and not refolding) is the main pathway improved on that continuous system. This is presumably due to the reciprocating nature of OFM, as it increases the probability function of contact of unfolded lysozyme molecules.

10.5 References

Buswell AM. 2002. Protein renaturation and aggregation during dilution refolding. Cambridge: University of Cambridge.

Buswell AM, Middelberg APJ. 2003. A new kinetic model for lysozyme refolding and aggregation. Biotechnology and Bioengineering 83(5):567-577.

Clark ED-B. 2001. Protein refolding for industrial processes. Current Opinion in Biotechnology 12:202-207.

Dobson CM. 2003. Protein folding and misfolding. Nature 426(18/25):884-890.

Gu Z, Zhu X, Ni S, Su Z, Zhou H-M. 2004. Conformational changes of lysozyme refolding intermediates and implications for aggregation and renaturation. The International Journal of Biochemistry & Cell Biology 36:795-805.

Hevehan DL, Clark ED-B. 1997. Oxidative renaturation of lysozyme at high concentrations. Biotechnology and Bioengineering 54(2):221-230.

Lee CT, Buswell AM, Middelberg APJ. 2002. The influence of mixing on lysozyme renaturation during refolding in an oscillatory flow and a stirred-tank reactor. Chemical Engineering Science 57(10):1679-1684.

Lee CT, Mackley MR, Stonestreet P, Middelberg APJ. 2001. Protein refolding in an oscillatory flow reactor. Biotechnology Letters 23(22):1899-1901.

Lubiniecki AS. 1990. Large-Scale Mammalian Cell Culture Technology. New York.: Marcel Dekker Inc. 688 p.

Mannal GJ, Tiitchener-Hooker NJ, Chase HA, Dalby PA. 2006. A critical assessment of the impact of mixing on dilution refolding. Biotechnology and Bioengineering 93(5):955-963.

Middelberg APJ. 1996. The influence of protein refolding strategy on cost for competitive reactions. The Chemical Engineering Journal 61:41-52.

Middelberg APJ. 2002. Preparative protein refolding. Trends in Biotechnology 20(10):437-443.

Reis N, Harvey AP, Vicente AA, Teixeira JA, Mackley MR. 2005. Fluid Mechanics and Design Aspects of a Novel Oscillatory Flow Meso-Reactor. Chemical Engineering Research & Design 83(A4):357-371.

Reis N, Vicente AA, Teixeira JA, Mackley MR. 2004. Residence times and mixing of a novel continuous oscillatory flow screening reactor. Chemical Engineering Science 59(22-23):4967-4974.

Terashima M, Suzuki K, Katoh S. 1996. Effective Refolding of Fully Reduced Lysozyme with a Flow-Type Reactor. Process Biochemistry 31(4):341-345.

Chapter 11 General conclusions and suggestions for future work

Two novel scale-down reactors were developed and herein presented, being both based on a novel small-scale tube geometry, whose inner walls are provided with Smooth Periodic Constrictions (SPC): a micro-bioreactor and a meso-reactor (adjusted for continuous operation). Both micro-bioreactor and micro-bioreactor operated under oscillatory flow mixing (OFM) and differ essentially on the tube length. It was concluded that fluid mechanics within the SPC tube geometry are similar to those generated in conventional OFRs, but with decreased critical Re_o numbers (about 50 %) for flow separation and breakage of flow axisymmetry, which is found related with the smaller cross-free section of the constrictions in the SPC geometry. Numerical simulations with a 2-D axisymmetric laminar model have matched the flow patterns within the SPC tube geometry for situations with small interaction between fluid elements (axisymmetric flow), while a 3-D model (laminar or LES) was necessary to match the breakage of flow axisymmetry observed for higher values of Re_o.

The turbulent model, LES, presented some advantages over the pure-laminar model as the first requires less computational resources and overcomes grid dependency in coarser grids by simulating a sub-grid. Further characterisation of macroscopic flow patterns and mass transfer within the micro-bioreactor demonstrated that both f and x_0 affect the fluid mechanics, mixing times, RTDs, k_La and ε., but the effect of x_0 was found to differ from that of f. In particular, f was found to control the intensity of the vortex rings (which mainly results in the increasing of radial mixing) while the increasing of x_0 mainly results in the increase of the backflow (thus of axial dispersion). Globally, the dimensionless Re_o number is not truly adapted to represent the flow patterns within the SPC geometry, and the formulation of a new dimensionless parameter (attributing different weights to f and x_0) should be considered.

The macroscopic flow patterns within both the micro-bioreactor and the meso-reactor are driven towards the ideal cases of a plug flow reactor or a completely back-mixed reactor simply by setting f and x_0. In particular, the reactor conversion may closely approach the ideal case of a plug flow reactor through OFM, with the great advantage of having a good radial mixing presumably decreasing the mass-transfer phenomena and improving the reactor's selectivity in single or multiphase reactions.

Small-scale bio-transformations with the micro-bioreactor have demonstrated that bioprocesses productivity is optimized with the SPC geometry, and that this reactor presents excellent features as a scale-down platform for bioprocess screening.

Guidelines for future work:

a) the (batch) application of the micro-bioreactor to the screening of fermentation media and growth conditions, mainly those under development in the biopharmaceutical industry (recombinant proteins from yeast and bacterial hosts and vaccines and other therapeutic proteins from animal workhorses) should be implemented;
b) as processes involving the suspension of catalyst or biocatalyst particles are also highly improved by the oscillatory flow mixing (OFM), work could be done concerning e.g. the anaerobic waste-water digestion using suspended, aggregated microorganisms;
c) screening of bioprocesses involving immiscible phases are also suggested due to the good contact between different phases promoted by the reciprocating OFM;

d) applications of the meso-reactor are mainly attractive for residence times of minutes to 1 – 2 hours, thus e.g. the continuous production of nano-particles, crystallization, screening of chemical drugs may also be considered;

e) work could also be done in the *on-line* monitoring of bioprocesses within both the micro-bioreactor and the meso-reactor, being such work in fact crucial for high-throughput screening tasks.

In terms of fundamental characterisation of scale-down reactors (micro-bioreactor and meso-reactor) or in general of the SPC geometry, the study of multiphase flows, namely on the modification of flow patterns in the presence of one or several phases could also be considered.